UCLA
UCLA Electronic Theses and Dissertations

Title

Advances in Hybrid Nanolithography: Wafer-Scale Fabrication of 1D to 3D Micro- and Nanostructures

Permalink
https://escholarship.org/uc/item/9zk77593

Author
Liu, Wenfei

Publication Date
2022

Peer reviewed|Thesis/dissertation

eScholarship.org Powered by the California Digital Library
University of California

UNIVERSITY OF CALIFORNIA

Los Angeles

Advances in Hybrid Nanolithography:

Wafer-Scale Fabrication of 1D to 3D Micro- and Nanostructures

A dissertation submitted in partial satisfaction of the

requirements for the degree of Doctor of Philosophy

in Chemistry

by

Wenfei Liu

2022

© Copyright by

Wenfei Liu

2022

ABSTRACT OF THE DISSERTATION

Advances in Hybrid Nanolithography:

Wafer-Scale Fabrication of 1D to 3D Micro- and Nanostructures

by

Wenfei Liu

Doctor of Philosophy in Chemistry

University of California, Los Angeles, 2022

Prof. Anne M. Andrews, Co-Chair

Professor Paul S. Weiss, Co-Chair

Nanolithography is a critical step in the patterning and fabrication process of sub-micron and nanoscale structures, which can be integrated into electronic, optical, and biomedical devices for improved performance, sensitivity, and efficiency. State-of-the-art methods for advanced high-resolution lithographic techniques (*e.g.*, extreme ultraviolet photolithography, electron-beam lithography) are limited by high equipment costs and/or time-consuming serial writing processes. I have focused on developing hybrid nanolithographic techniques with high throughput, low cost, and large scale, for patterning and fabrication of one-, two-, and three-dimensional (1D-3D) sub-micron and nanoscale structures that can be used for emerging applications.

As a novel soft lithographic method, chemical lift-off lithography (CLL) was developed for high-throughput and wafer-scale nanopatterning. To lower the cost and improve the accessibility of CLL, we used commercially available digital versatile discs (DVDs) as templates to prepare elastomeric stamps for nanopatterning. Combined with thin-film etching and material sputtering, CLL was used to fabricate ultrathin 1D In_2O_3 nanoribbons to assemble field-effect-transistor (FET) biosensors. Integrated with a double-patterning strategy, CLL was used to pattern 2D gold nanodisks, which provided a new opportunity for photothermal intracellular delivery.

Combined with material deposition and silicon etching, nanosphere lithography (NSL) was used to fabricate various 2D and 3D silicon nanostructures with high periodicity and structural integrity. We developed a strategy that combined NSL with silicon anisotropic etching, for scalable fabrication of ordered nanopyramid structures. This strategy, with adaptability and expansibility, provides theoretical guidance for the design and fabrication of periodic perovskite nanoarrays with enhanced light absorption and photoelectric sensitivity for high-performance photodetectors.

To improve the resolution limit and to build on the practicality of conventional photolithography, we developed a derivative of conventional photolithography, dual-layer photolithography (DLPL), for nanoscale patterning. Utilizing the photoresponsivity variation of positive and negative photoresists, DLPL enabled patterning "outline-like" features (~180 nm) 25 times smaller than the photomask feature size (5 μm) with a single exposure. Combined with material deposition and silicon etching, DLPL can be used to fabricate 3D nanostructures for applications in electronics and biology.

The dissertation of Wenfei Liu is approved.

William M. Gelbart

Richard B. Kaner

Hsian-Rong Tseng

Anne M. Andrews, Committee Co-Chair

Paul S. Weiss, Committee Co-Chair

University of California, Los Angeles

2022

To my beloved parents, Hongfang Ma and Zhibao Liu

Table of Contents

List of Figures and Tables viii

List of Abbreviations and Symbols xxiii

Acknowledgments xxvi

Biographical Sketch xxviii

Chapter 1. Introduction

1.1 Development of Nanolithography 2
1.2 Hybridication of Chemical Lift-Off Lithography 6
1.3 Hybridization of Nanosphere Lithography 10
1.4 Hybridization of Conventional Photolithography 12
1.5 References 15

Chapter 2. Single-Step Dual-Layer Photolithography for Tunable and Scalable Nanopatterning

2.1 Abstract 36
2.2 Introduction 37
2.3 Materials and Methods 39
2.4. Results and Discussions 41
2.5 Conclusions and Prospects 55
2.6 Supplementary Materials 56
2.7 References 61

Chapter 3. Sub-200-nm Patterning by Self-Aligned Dual-Layer Photolithography

3.1 Abstract 71
3.2 Introduction 72
3.3 Materials and Methods 74
3.4. Results and Discussions 76
3.5 Conclusions and Prospects 84
3.6 Supplementary Materials 85
3.7 References 88

Chapter 4. Large-Area Periodic Organic–Inorganic Hybrid Perovskite Nanopyramid Arrays for High-Performance Photodetector and Image Sensor Applications

4.1 Abstract 94
4.2 Introduction 95
4.3 Materials and Methods 97
4.4. Results and Discussions 99
4.5 Conclusions and Prospects 110
4.6 Supplementary Materials 111
4.7 References 117

Chapter 5. Narrower Nanoribbon Biosensors Fabricated by Chemical Lift-off Lithography Show Higher Sensitivity

5.1 Abstract 126
5.2 Introduction 127
5.3 Materials and Methods 129
5.4. Results and Discussions 133
5.5 Conclusions and Prospects 149
5.6 Supplementary Materials 150
5.7 References 160

Chapter 6. Photothermal Intracellular Delivery Using Gold Nanodisk Arrays

6.1 Abstract 174
6.2 Introduction 175
6.3 Materials and Methods 178
6.4. Results and Discussions 181
6.5 Conclusions and Prospects 193
6.6 Supplementary Materials 194
6.7 References 197

Chapter 7. Conclusions and Future Prospects

List of Figures and Tables

Figure 1.1. Schematics illustrating the contact reaction in chemical lift-off lithography. Reproduced with permission from reference 116. Copyright 2018, American Association for the Advancement of Science..........7

Figure 1.2. (a) Schematic illustration of self-collapse lithography (SCL). Reproduced with permission from reference 121. Copyright 2017, American Chemical Society. (b) Schematic illustrations of polymer-pen chemical lift-off lithography (PPCLL) using pyramidal (top) and V-shaped (bottom) polymer-pen arrays. Reproduced with permission from reference 122. Copyright 2017, American Chemical Society. (c) Molecular patterning on the surface of different substrates *via* chemical lift-off lithography. Reproduced with permission from reference 123. Copyright 2020, American Chemical Society. (d) The chemical lift-off process on a self-assembled monolayer of Au nanoparticles. Reproduced with permission from reference 124. Copyright 2021, American Chemical Society..........8

Figure 1.3. (a) Schematic architecture of a high-definition digital versatile disc (HD-DVD): layer I, polycarbonate protective layer; layer II, mirror-like metal film; layer III, data recording film; layer IV, polycarbonate layer containing concentric rings with typical widths of 250 nm and periodicities of 400 nm. Photographs of a HD-DVD, a HD-DVD master (layer IV), and a patterned polydimethylsiloxane (PDMS) stamp, respectively. (b) Atomic force micrographs of a representative HD-DVD master (left) and a patterned PDMS stamp (right). Scale bars are 2 μm. (c) Fabrication scheme for producing In_2O_3 nanoribbons using chemical lift-off lithography. (d) (top) Topographic images measured using atomic force microscopy (AFM) and (bottom)

schematic illustrations of SAM/Au/Ti/ In_2O_3 and bare In_2O_3 nanoribbons, respectively, with line widths of ~200 nm. Reproduced with permission from reference 125. Copyright 2018, American Chemical Society..9

Figure 1.4. Schematics illustrating the self-assembly process of polystyrene (PS) micro /nanospheres *via* the Langmuir-Blodgett method. (a) Addition of the PS sphere solution using a glass slide in water to form a self-assembled monolayer. (b) Drying process of the PS spheres on a substrate. (c) Scanning electronic microscopy (SEM) image of PS sphere close-packed monolayer on the substrate. Reproduced with permission from reference 129. Copyright 2020, American Chemical Society..11

Figure 1.5. (a) Resolution improvement in conventional photolithography *via* a double exposure and patterning technique. Reproduced with permission from reference 141. Copyright 2013, ITRS. (b) Resolution improvement in nanoimprint lithography *via* a double patterning technique. Reproduced with permission from reference 142. Copyright 2013, Elsevier...13

Figure 2.1. Fabrication schematics of SiO_2 nanorings by single-step dual-layer photolithography (DLPL). Top, overall process; bottom, cross-sectional view. (a) One-time UV exposure on dual-layer photoresists. (b) Postbaking after removing photomask. (c) First development of negative photoresist layer. (d) Second development of positive photoresist. (e) Deposition of SiO_2 thin film *via* magnetron sputtering. (f) Removal of dual-layer photoresists and generation of SiO_2 nanorings. PR: photoresist...42

Figure 2.2. Systematic study of the pattern size dependence on the exposure time (or exposure energy) in dual-layer photolithography (DLPL). Scanning electron microscopy (SEM) images of single-layer photolithography for (a) positive photoresist and (b) negative photoresist with exposure times of 18, 26, and 34 s. Scale bar: 5 μm. (c) Histogram of the size changes of features on positive and negative photoresists in the single-layer photolithography (SLPL) as the exposure time or corresponding exposure energy increased. (d) SEM top and side view images of the dual-layer structure after the development in DLPL with 30 s of exposure and the photomask feature sizes of 5 and 10 μm. Scale bar: 10 μm. PR: photoresist..44

Figure 2.3. Scanning electron microscopy images of the nanopatterns fabricated by dual-layer photolithography with independent control of pattern parameters (*i.e.*, size, line width, material, and shape): (a) SiO_2 nanorings with inner diameter of 10 μm and width of 900 nm; (b) SiO_2 nanorings with inner diameter of 4.8 μm and width of 800 nm; (c) SiO_2 nanorings with inner diameter of 4.7 μm and width of 300 nm; (d) Cr nanorings; (e) Ag nanorings; (f) metal patterns in number-shaped outlines with a line width of ~10 μm; (g) metal patterns in letter-shaped outlines with a line width of ~10 μm. Original AutoCAD photomask designs of number and letter patterns are provided in (f) and (g)..47

Figure 2.4. (a–c) Time-driven KOH anisotropic etching process of Si(100) substrates with a dual-layer-photolithography-fabricated SiO_2 nanoring as the etching mask. Scanning electron microscopy images of morphologic transition of Si complex 3D nanostructures with etching times of (d) 2, (e) 3, (f) 5, and (g) 7 min. Top view of a

single Si complex 3D nanostructure, and 45° tilt view of complex 3D nanostructure arrays..........50

Figure 2.5. (a) Schematics of the $MAPbI_3$ film coating and interdigital electrode fabrication processes for the 2 min KOH-etched Si/SiO_2 3D complex nanostructures. (b) Scanning electron microscopy (SEM) image of the 2 min KOH-etched Si complex 3D nanostructures coated with SiO_2 for isolation. (c) Top view and side view SEM images of the $MAPbI_3$ film coated on the Si/SiO_2 substrate. (d) Time-resolved light response curve of $MAPbI_3$-based photodetector on the 2 min KOH-etched Si/SiO_2 nanostructure under a Xe lamp (10 mW/cm^2)..........53

Figure S2.1. Top view optical microscopy image of 5 μm hollow nanorings fabricated by the modified dual-layer photolithography on chromium film..........56

Figure S2.2. Top view scanning electron microscopy image of fabricated Si complex structure (inverted pyramid inside) with 5-min KOH anisotropic etching. Image was taken with a 45° tilt angle..........57

Figure S2.3. Top view scanning electron microscopy images of large-scale Si complex structure arrays fabricated with the KOH anisotropic etching time of (a) 2 min and (b) 5 min..........57

Figure S2.4. Scanning electron microscopy image of Si complex structures with 7-min KOH anisotropic etching before the removal of SiO_2 nanoring. Image was taken with a 45° tilt angle..........58

Figure S2.5. Optical image of a single $MAPbI_3$-based photodetector on SiO_2/Si substrate that was fabricated with 2-min KOH anisotropic etching..........58

Figure S2.6. Top view scanning electron microscopy image of the $MAPBI_3$ film coated on Si/SiO_2 (a) single complex structure and (b) arrays of complex structure fabricated with 7-min KOH anisotropic etching....59

Table S2.1. Data of Fig. 2.2c....60

Scheme 3.1. Schematic fabrication process of (top) single-step dual-layer photolithography (DLPL) and (bottom) DLPL with optimized photoresist thickness....76

Figure 3.1. (a-d) Schematic diagrams and scanning electron microscopy images of dual-layer photolithography patterns prepared with negative photoresist (-PR) under different dilution ratios (-PR : γ-butyrolactone). From top to bottom: schematic diagram; top view; 45° view, cross-sectional view. Scale bars: whole view 10 μm; zoom-in view 5 μm. (e) Histogram of photoresist thicknesses under different dilution ratios. (f) Histogram of inner and outer diameters under different dilution ratios....78

Figure 3.2. Cross-sectional scanning electron microscopy images of patterned (a) single layer positive photoresist, (b) single layer negative photoresist (-PR), and (c) dual layer photoresist at different spin-coating speeds. (d) Histogram of positive and -PRs thicknesses under different spin-coating speeds. (e) Histogram of photoresists thickness under different spin-coating speeds....80

Figure 3.3. Schematic diagrams of the impact of (a) exposure and (b) development time on feature size in dual-layer photolithography. (c) Schematic of the fabrication process for SiO_2 microrings. (d) Scanning electron microscopy images of SiO_2

microrings prepared at different exposure and development times. Scale bars: whole view 10 μm; zoom-in view 2 μm......82

Figure 3.4. (a) Patterning scheme of dual-layer photolithography (DLPL) followed by reactive ion etching of Si (left) and metal deposition (right). Scanning electron microscopy (SEM) images of (b) Si recessed microrings (upper: 5-μm recessed square microrings, lower: 3-μm recessed triangular microrings), (c) DLPL patterned dual photoresist layers (zoom-in left: 45° view, zoom-in right: top view), and (d) metal microrings (upper: Cr square microrings, lower: Ni triangular microrings). (e) Fabrication scheme for Si microtubes using Cr (yellow) or SiO_2 (blue) microrings as etching masks. (f-i) Si microtubes etched for (f) 2 min or (g) 7 min using Cr square microrings as etching masks and silicon microtubes etched for (h) 2 min or (i) 10 min using SiO_2 circular microrings as etching masks. Scale bars: whole view 5 μm; zoom-in view 2.5 μm......83

Figure S3.1. Negative photoresist (-PR) patterns prepared *via* single-layer phototlithography with different dilution ratios (-PR : γ-butyrolactone): (a) Undiluted; (b) 3:1 dilution; (c) 2:1 dilution; (d) 1:1 dilution. (e) Histogram of negative photoresist thicknesses and feature size under different dilution ratios. Scale bars: whole view 5 μm; zoom-in view 2.5 μm......85

Figure S3.2. Histograms of feature sizes of the SiO_2 microrings prepared at different exposure time (30-38 s) and development time: (a) 20 s, (b) 15 s, and (c) 10 s......86

Figure S3.3. (a) Schematic illustration of the photodetector based on a $CsPbI_3$ film spin coated on the microtube arrays. (b) Scanning electron microscopy image of the coated

$CsPbI_3$ thin film on the microtube arrays. (c) Dark/photocurrent of the photodetectors under a Xe lamp (1 mW/cm^2). (d) Time-resolved light response curve of $CsPbI_3$-based photodetector..87

Figure 4.1. Schematic fabrication process of inverted-pyramid arrays by nanosphere lithography and related scanning electron microscopy (SEM) images. Step 1: A monolayer of close-packed polystyrene (PS) nanospheres was prepared on a Si substrate. Step 2: The sizes of PS nanospheres were reduced by O_2 plasma etching. Step 3: A 30 nm-thick Cr film was deposited followed by removal of PS nanospheres. Step 4: KOH-anisotropic etching of exposed Si and selective etching of Cr to form inverted-pyramid arrays of Si. Step 5: Thermal vapor deposition of silicon oxide film (~200 nm) on inverted-pyramid arrays of Si. Scale bars = 2 μm......................................100

Figure 4.2. (a) Schematic coating process of $MAPbI_3$ film on inverted-pyramid arrays of SiO_2/Si. (b, c) Scanning electron microscopy (SEM) images of the $MAPbI_3$ film (top view). (d) Cross-sectional SEM image of the $MAPbI_3$ film (side view) 101

Figure 4.3. (a) Measured absorption spectra of $MAPbI_3$ films on SiO_2/Si nanopyramid substrates and flat substrates in the visible region. (b) Dark/photocurrent of the photodetectors. The incident light intensity is 1 mW/cm^2. (c) *I-V* curves of the photodetector (sample P-2, see text) measured in the dark and under illumination with a range of wavelengths. (d) Plots of responsivity of the photodetector (sample P-2) as a function of light wavelength. (e) Photocurrent-light intensity curve of the photodetector. The voltage was fixed at 5 V. (f) The rise time and decay time of the photodetector. (g, h) Time-resolved photoresponse of the photodetector at 340 and 920 nm, respectively. The incident light intensity is 3 $\mu W/cm^2$. (i) Finite-difference

time-domain (FDTD) simulations for $MAPbI_3$ films on SiO_2/Si nanopyramid substrates under light illumination at 600 and 900 nm. (j) The magnitude of the electric field obtained from FDTD simulations for $MAPbI_3$ films on flat substrate under light illumination at 600 and 900 nm........104

Table 4.1. Comparison of the key parameters of photodetectors based on different materials........106

Figure 4.4. (a) Schematic illustration of a photodetector array with 5 × 5 pixels. (b) Time-resolved photoresponse of the photodetector based on a $MAPbI_3$ film on a SiO_2/Si nanopyramid substrate (P-2 sample) under white light (1 mW/cm^2). (c, d) Output results of the photodetector array in darkness and under illumination, respectively........109

Figure S4.1. Scanning electron microscopy (SEM) images of: (a) polystyrene (PS) microspheres with 1 μm diameters, (b) size reduced PS microspheres, (c) inverted Si nanopyramid arrays........111

Figure S4.2. Typical scanning electron microscopy (SEM) images of: (a) polystyrene (PS) nanospheres with 500 nm diameters, (b) size reduced PS nanospheres, (c) inverted Si nanopyramid arrays........111

Figure S4.3. (a) Scanning electron microscopy (SEM) image of the nanopyramid array. (b) Cross-sectional SEM image of a single pyramid........112

Figure S4.4. Scanning electron microscope image of the photodetector based on a $MAPbI_3$ film on a SiO_2/Si nanopyramid substrate........112

Figure S4.5. Dark/Photocurrent of the photodetector based on a $MAPbI_3$ film on a SiO_2/Si nanopyramid substrate (a P-1 sample and a P-3 sample). The incident light intensity is 1 mW/cm......113

Figure S4.6. Noise power density of the photodetector based on a $MAPbI_3$ film on a SiO_2/Si nanopyramid substrate (a P-2 sample) 113

Figure S4.7. Plots of specific detectivity of the photodetector (a P-2 sample) as a function of light wavelength......114

Figure S4.8. Photocurrent of the photodetector based on a $MAPbI_3$ film on a SiO_2/Si nanopyramid substrate (a P-2 sample) under white light at different light intensities......114

Figure S4.9. Time-resolved photoresponse of the photodetector for a $MAPbI_3$ film on SiO_2/Si nanopyramid substrate (a P-2 sample) under white light. Enlarged views of the (a) rising edge and (b) decaying edge of the photodetector......115

Figure S4.10. Time-resolved photoresponse of the photodetector based on a $MAPbI_3$ film on a SiO_2/Si nanopyramid substrate (a P-2 sample) under light illumination at wavelengths of: (a) 400 nm, (b) 500 nm, (c) 1000 nm, and (d) 1100 nm. The light intensity was fixed at 3 μW/cm^2......116

Figure 5.1. Schematic illustration of the fabrication process for In_2O_3 nanoribbons. Step 1: A Au layer (30 nm) was deposited over Ti (30 nm) on Si/SiO_2 (100 nm). A monolayer of 11-mercapto-1-undecanol was then self-assembled on the Au surface. Step 2: An oxygen plasma “activated” polydimethylsiloxane (PDMS) stamp with micro- or nanoribbon features was brought into conformal contact with the substrate. Step 3: Stamp removal from the surface (chemical lift-off lithography, CLL) lifted off

self-assembled molecules in the contacted areas. Step 4: Selective etching processes removed Au and Ti in the unprotected (contacted) regions on the surface. Step 5: Sputtering was used to deposit In_2O_3 (20 nm) over the entire substrate. Step 6: The remaining Au/Ti structures were removed to obtain In_2O_3 nanoribbon arrays..134

Figure 5.2. Atomic force microscope (AFM) images of 350 nm nanoribbon substrates (a) before (Step 5, Figure 5.1) and (b) after removing underlying Au structures (Step 6, Figure 5.1). (c) Height profiles from the AFM images in (a,b) across the nanoribbons. (d) Photographs of In_2O_3 nanoribbons at different viewing angles. (e,f) Scanning electron microscope (SEM) images of 350 nm wide In_2O_3 nanoribbons. (g) Energy-dispersive X-ray mapping of indium corresponding to the SEM image in (f) 136

Figure 5.3. (a) Schematic illustration of the field-effect transistor (FET) configuration using In_2O_3 nanoribbons (or microribbons) as the channel material aligned perpendicular to source and drain electrodes. (b,c) Scanning electron microscope images of 350-nm-wide In_2O_3 nanoribbons with source and drain electrodes. (d,e) Scanning electron microscope images of 2-μm-wide In_2O_3 nanoribbons with source and drain electrodes. (f) Photograph (top) and schematic illustration (bottom) of the solid-state measurement setup for In_2O_3 nanoribbon (and microribbon) FETs, where p^{++} Si serves as the bottom gate. The lavender layer is SiO_2. Transfer (g) and output (h) characteristics of representative 350 nm In_2O_3 nanoribbon FETs..................................138

Figure 5.4. (a) Schematic illustration of a liquid state measurement where a Ag/AgCl electrode serves as the top gate. Transfer (b) and output (c) characteristics of

350-nm-wide In_2O_3 nanoribbon field-effect transistors (FETs) in the liquid-gate setup shown in (a). (d) Transfer curves of 350-nm-wide In_2O_3 nanoribbon FETs in solutions of pH 10 to 5. (e) Real-time current responses from a representative 350-nm-wide In_2O_3 nanoribbon FET exposed to commercial buffer solutions of pH 10 to 5. (f) Current responses relative to baseline for solutions of pH 10 to 5 using 350-nm- or 20-μm-wide ribbon In_2O_3 FETs. I/I_0 is current normalized to the baseline pH before the experiments (I_0, pH 7.4). Error bars are standard errors of the means with N = 3 FETs for each configuration........140

Figure 5.5. (a) Schematic illustration of serotonin detection using aptamer-functionalized In_2O_3 field-effect transistor (FET) biosensors. (b) Representative transfer curves for serotonin responses from 10 fM to 100 μM for 350-nm In_2O_3 nanoribbon FET biosensors. (c) Calibrated response curves for serotonin from 350-nm- *vs* 20-μm-wide In_2O_3 nanoribbon FET biosensors. Error bars are standard errors of the means for N = 3 350-nm-wide nanoribbon and N = 2 20-μm-wide nanoribbon devices. (d) Schematic illustration of DNA hybridization detection. (e) Representative transfer curves for responses for complementary DNA hybridization (10^6 to 10^{15} copies) for 350-nm In_2O_3 nanoribbon FET biosensors. (f) Calibrated responses for complementary DNA hybridization for 350-nm- *vs* 20-μm-wide In_2O_3 nanoribbon FET biosensors. Error bars are standard errors of the means for N = 2 350-nm-wide nanoribbon and N = 3 20-μm-wide microribbon devices........143

Figure S5.1. Elemental energy spectrum for In_2O_3 nanoribbons from energy-dispersive X-ray mapping........151

Table S5.1. Elemental quantification analysis of In_2O_3 nanoribbons by energy-dispersive X-ray mapping......152

Figure S5.2. Optical microscope image of interdigitated electrodes (yellow). Orientations of In_2O_3 nanoribbons are depicted in overlay (light blue) 153

Figure S5.3. Optical microscope images of 20-µm-wide In_2O_3 nanoribbons with source and drain electrodes......153

Figure S5.4. Solid-state transfer characteristics of In_2O_3 FETs with different nanoribbon widths, (a) 2 µm, (b) 20 µm, and (c) thin film......154

Figure S5.5. Gate leakage current (gate current to gate voltage) in buffer solution (pH = 7.4) at V_{DS} = 100 mV......154

Figure S5.6. Liquid-state transfer characteristics of In_2O_3 FETs with nanoribbon different widths, (a) 2 µm, (b) 20 µm, or (c) thin film......155

Figure S5.7. Schematic of nanoribbons for calculation of surface-to-volume ratio......156

Table S5.2. Surface-to-volume ratios calculated for different configurations of In_2O_3 FETs......157

Figure S5.8. COMSOL simulations of effects of nanoribbon width on surface-to-volume ratio. (a) Model used in the simulation, where nanoribbons are 20-nm-thick with widths varying from 5 nm to 20 µm. (b) Simulation results of the electrostatic potential due to the charge of the biomolecules. (c) Simulated normalized calibrated responses at different ribbon widths showing that the sensitivity of In_2O_3 nanoribbon FETs is predicted to increase at widths below 2 µm. Simulated calibrated response

values were normalized to responses for 20-μm microribbons. Simulated responses are not directly comparable with experimental results in the main text due to the nature of the simulation complexity for the semiconductor system under study....158

Table S5.3. Concentration-dependent field-effect transistor data were analyzed by two-way analysis of variance with nanoribbon sizes and target concentration as the independent variables....159

Figure 6.1. (a) Illustration of photothermal intracellular delivery enabled by localized surface plasmon resonance (LSPR) of gold nanodisks excited by a nanosecond laser. After cell seeding, the laser was rastered over cells seeded onto the nanostructures and cultured in a medium containing membrane impermeable biomolecules. Upon irradiation, the gold plasmonic structures heat up rapidly and generate cavitation bubbles, which facilitate the delivery of the biomolecular cargo into targeted cells by creating transient pores along nearby their outer membranes....183

Figure 6.2. Gold plasmonic disk arrays fabricated by double-patterning chemical lift-off lithography (CLL) 185

Figure 6.3. (a) Fluorescence microscope images of HeLa cells on 1-μm-wide gold (Au) nanodisk arrays labeled with a cell membrane-impermeable dye (Calcein AM). (b) Scanning electron microscope images of fixed cells on a substrate. (c) Overlay of the green-box-designated region seen in (b) with (a). (d) Fluorescence microscope images of HeLa cells on 2-μm-wide gold (Au) nanodisk arrays labeled with a cell membrane impermeable dye (Calcein AM). (e) Scanning electron microscope images of fixed cells

on a substrate. (f) Overlay of the green box-designated region seen in (b) with (a). (g) Scanning electron microscope image of single Hela cell on 2-μm-wide Au nanodisk array substrate. (h,i) Simulation results of surface temperature at the gold nanodisk array (1-μm wide) interface in water. Scale bars: (a-f) 100 μm, (g) 20 μm..188

Figure 6.4. (a) Delivery efficiency and cell viability testing. (a-d) Delivery of calcein to HeLa cells using gold nanodisk arrays (1 μm wide, 2 μm pitch, 30 nm thickness) under laser irradiation with 11 mJ/cm^2 fluence. (a) Representative image of delivery of calcein (green) to targeted cells. (b) Cell nuclei are stained with Hoechst 33342 to label both live and dead cells (blue). (c) Propidium iodide (PI) assay to identify dead cells (red). (d) Overlaid image of calcein, Hoechst 33342, and PI dyes. Efficiency was found to be 98 ± 1%, and viability to be 99 ± 1%. (e–h) Control experiment using flat gold thin film under the same laser irradiation of 11 mJ/cm^2 fluence, where (e) corresponds to the calcein channel, (f) is the Hoechst dye, (g) is the PI dye, and (h) is the overlaid image of (e–g). Scale bars: 100 μm...190

Figure 6.5. (a) Delivery efficiency and cell viability at different laser fluences and gold disk sizes are shown in overlaid images (a-d) of 0.6 kDa calcein delivery (green), Hoechst dye (blue), and PI dye (red). Delivery results under different laser fluence at (a) 7 mJ/cm^2, and (b) 21.2 mJ/cm^2, respectively, both on 1-μm wide nanodisk arrays. Delivery results using different sizes of gold nanodisk arrays of (c) 2 μm and (d) 10 μm widths, respectively, both under laser fluence of 7 mJ/cm^2. (e) Delivery efficiencies and viabilities after 90 min as a function of laser fluence on 1-μm wide nanodisk arrays. Error bars represented standard error mean (s.e.m.) (n = ~2,500 cells for all

tests). (f) Delivery efficiencies and viabilities with different sizes of gold nanodisk arrays at 7 mJ/cm^2. Error bars, s.e.m. (n = ~1,900 cells for all tests). (g) Delivery efficiencies and viabilities with different cargoes at 11 mJ/cm^2 on 1-μm-wide nanodisk arrays. Error bars, s.e.m. (n = ~2,000 cells for all tests). Scale bars: 100 μm..192

Figure S6.1. Optical microscope image of cells on 350-nm Au nanodisk arrays. The Au nanodisks are not visible in the optical microscope due to their sub-micron features..194

Figure S6.2. Simulation results for tip temperature on different dimensions of Au nanodisk arrays upon laser radiation of 11 mJ/cm^2..195

Figure S6.3. Schematic diagram of the optical setup..195

Figure S6.4. Delivery efficiency and cell viability results of 0.6 kDa calcein AM using a 1-μm-wide gold (Au) nanodisk arrays chip after five runs under 11 mJ/cm^2 laser fluence...196

List of Abbreviations and Symbols

(3-Aminopropyl)triethoxysilane (APTES)

(3-Aminopropyl)trimethoxysilane (APTMS)

Artificial cerebrospinal fluid (aCSF)

Atomic force microscopy (AFM)

Bovine serum albumin (BSA)

γ-Butyrolactone (GBL)

California Nanosystems Institute (CNSI)

Chemical lift-off lithography (CLL)

Chemical vapor deposition (CVD)

Chief Technology Officer (CTO)

Deep reactive ion etching (DRIE)

Deep ultraviolet photolithography (DUV)

Deionized (DI)

Deoxyribonucleic acid (DNA)

Digital versatile discs (DVDs)

Dimethylsulphoxide (DMSO)

Direct self-assembly (DSA)

Dual-layer photolithography (DLPL)

Dulbecco's modified essential medium (DMEM)

Electron-beam lithography (EBL)

Energy-dispersive X-ray (EDX)

Ethylenediaminetetraacetic acid disodium salt dihydrate (EDTA)

Extreme ultraviolet photolithography (EUV)

Fetal bovine serum (FBS)

Field-effect transistor (FET)

Finite-difference time-domain (FDTD)

Focused ion beam (FIB)

Hexamethyldisilazane (HMDS)

High-definition digital versatile disc (HD-DVD)

Integrated circuit (IC)

Ion-sensitive field-effect transistor (ISFET)

Linear dynamic range (LDR)

Localized surface plasmon resonance (LSPR)

3-Maleimidobenzoic acid *N*-hydroxysuccinimide ester (MBS)

Methylammonium lead iodide ($MAPbI_3$)

Microcontact printing (μCP)

Micro-electro-mechanical-system (MEMS)

Multiple-patterning nanosphere lithography (MP-NSL)

Nanoimprint lithography (NIL)

Nanoparticle chemical lift-off lithography (NP-CLL)

Nanosphere lithography (NSL)

Numerical aperture (NA)

Off-axis illumination (OAI)

One-dimensional (1D)

Phase-shifting masks (PSMs)

Phosphate-buffered saline (PBS)

Photoresist (PR)

Polydimethylsiloxane (PDMS)

Polymer-pen chemical lift-off lithography (PPCLL)

Polymer pen lithography (PPL)

Polystyrene (PS)

Propidium iodide (PI)

Reactive ion etching (RIE)

Ribonucleic acid (RNA)

Scanning electron microscopy (SEM)

Self-assembled monolayers (SAMs)

Self-collapse lithography (SCL)

Silicon nanowires (SiNWs)

Silicon-on-insulator (SOI)

Single-layer photolithography (SLPL)

Single-stranded DNA (ssDNA)

Small interfering RNA (siRNA)

Supramolecular nanoparticles (SMNPs)

Surface plasmonic resonance (SPR)

Three-dimensional (3D)

Trimethoxy(propyl)silane (PTMS)

Two-dimensional (2D)

Ultraviolet (UV)

Acknowledgments

As an old saying goes, all good things come to an end. I recall the beginning of this journey. In the summer of 2017, I came to the UCLA Chemistry department with passion and purpose. Five years later, I have learned and been rewarded so much in both academic research and personal development. I realize that the destination of this journey is not just the finale of my education, but the prelude to my career, with me now having stronger mindsets and greater capabilities. In this world-class institution, I am fortunate to work with so many great people and together, to solve important problems in the field of nanotechnology. At the end of this amazing journey, I would like to express my sincere gratitude to my advisors, colleagues, friends, and family for their unwavering support and help at every stage of my graduate research.

First, I would like to thank my advisors, Prof. Anne M. Andrews and Prof. Paul S. Weiss for their tremendous and continuous guidance and support. I am so fortunate to join the Andrews and Weiss labs, where I could work on diverse research projects and interdisciplinary studies. When I first met them, I was impressed by their enthusiasm for and meticulousness in science, and their charisma and dedication as mentors. During every meeting and conversation, Anne and Paul always encouraged and inspired me to explore new possibilities of my research and to think deeply about the big picture. During the COVID pandemic, Anne and Paul helped me build connections, provided me with resources, and most importantly, cared about me all the time. Words could not express how grateful I am for having them in my life. To me, they are my mentors, my elders, and my dearest friends. I

also want to thank my committee: Professor William M. Gelbart, Professor Richard B. Kaner, and Professor Hsian-Rong Tseng.

Secondly, I would like to thank my excellent colleagues in our groups: Dr. Chuanzhen Zhao, Prof. Xiaobin Xu, Dr. Qing Yang, Dr. Naihao Chiang, Yao Gong, Dr. Steven Jonas, Jun Shen, Dr. Tianhan Liu, Patrick Liu, Isa Frost, and all other members of our labs. Also, I want to acknowledge the efforts contributed by our collaborators at UCLA and all around the world.

Third, I would like to thank the staff in the Chemistry and Biochemistry Department, Semel Institute, California Nanosystems Institute (CNSI), and UCLA Nanolab. In addition, I want to thank the funding sources and agencies, including the National Science Foundation (CMMI-1636136), National Institute on Drug Abuse (DA045550), and Alex's Lemonade Stand Foundation, which make our research possible. I also want to thank UCLA Dashew Center, the Graduate Division, and the Chemistry Graduate Affairs Office for their help during the COVID pandemic.

Lastly, I want to say thank you from the bottom of my heart to all my family members. They always support my decisions and encourage me to overcome challenges. I want to thank my parents, Hongfang Ma and Zhibao Liu. It has been ten years since I left home for education in the US. Among those years, I did not take responsibility as a son. But you always loved me and believed in me unconditionally. I love you.

It is the time for departure. Besides saying goodbye, I take all the happy memories and beautiful stories from UCLA with me, to the next stage of my life. I have so many emotions for all my friends and this place. Until we see each other next time, please take care!

Biographical Sketch

Wenfei Liu attended the University of Illinois at Urbana-Champaign (UIUC) from 2013 to 2017 as an undergraduate in the Department of Chemistry. Besides excellent performance in coursework, he conducted research in Professor Jeffrey S. Moore's group at the Beckman Institute for three years. He developed numerous protocols for self-healing polymer synthesis and microcapsule encapsulation. In addition, he developed an innovative synthetic path for tetrahedral covalent organic cages with high yield and reproducibility. Outside the classroom and laboratory, Wenfei participated in various extracurricular activities. He served as a student ambassador in the Chemistry Department for three years and a high school tutor at Urbana High School for two years. At UIUC, he received several awards and honors, including the Fred S. Bailey Scholarship, the John Gieseking Scholarship, and the Minn Graduate Scholarship; he was on the Dean's List, and a James Scholar Honor. In 2017, Wenfei received a Bachelor of Science degree in Chemistry, and graduated with Higher Distinction in Curriculum.

In 2017, he flew to the west coast to the University of California, Los Angeles to pursue his graduate research career. He joined the Prof. Paul S. Weiss and Prof. Anne M. Andrews groups in the Department of Chemistry and Biochemistry. During his graduate career at UCLA, he: (1) developed hybrid nanolithographic techniques with high throughput, large area, and low cost; (2) fabricated wafer-scale one-, two-, and three-dimensional metal and semiconductor nanostructures for applications in electronics and biology. In 2019, he was awarded an SG Fellowship for excellence in graduate research. Besides making progress in research, he served as a teaching assistant throughout his graduate career, teaching more

than 13 undergraduate courses. He also volunteered at the UCLA TED Talk and Nanoscience Outreach Programs, contributing to campus diversity and public education.

Publications

1. **Liu, W.**; Wang, J.; Xu, X.; Zhao, C.; Xu, X.; Weiss, P. S. Single-Step Dual-Layer Photolithography for Tunable and Scalable Nanopatterning. *ACS Nano* 15, 12180-12188 (**2021**)
2. Xu, X.#; **Liu, W.#**; Ji, Z.; Hao, D.; Yan, W.; Ye, Z.; Hu, Y.; Fang, M.; Wang, C.; Ma, L.; Huang, J.; Xu, X.; Weiss, P. S. Large-Area Periodic Organic-Inorganic Hybrid Perovskite Nanopyramid Arrays for High Performance Photodetector and Image Sensor Applications. *ACS Materials Lett.* 3, 1189-1196 (**2021**)
3. Wang, B.#; Zhao, C.#; Wang, Z.; Yang, K. Y.; Cheng, X.; **Liu, W.;** Yu, W.; Lin, S.; Zhao, Y.; Cheung, K. M.; Lin, H.; Hojaiji, H.; Weiss, P. S.; Stojanivić, M. N.; Tomiyama, A. J.; Andrews, A. M.; Emaminejad, S. Wearable Aptamer Field-Effect Transistor Sensing System for Noninvasive Cortisol Monitoring. *Sci. Adv.* 8, eabk0967 (**2022**)
4. Zhang, D.#; Peng, R.#; **Liu, W.**; Donovan, M. J.; Wang, L.; Ismail, I.; Li, J.; Li, J.; Qu, F.; Tan, W. Engineering DNA on the Surface of Upconversion Nanoparticles for Bioanalysis and Therapeutics. *ACS Nano* 15, 17257–17274 (**2021**)
5. Zhao, C.; Liu, Q.; Cheung, K. M.; **Liu, W.**; Yang, Q.; Xu, X.; Weiss, P. S.; Zhou, C.; Andrews, A. M. Narrower Nanoribbon Biosensors Fabricated by Chemical Lift-Off Lithography Show Higher Sensitivity. *ACS Nano* 15, 904-915 (**2021**)

Chapter 1

Introduction

Part of the information in this chapter is adapted with permission from

Nano Lett. **2018**, *18*, 5590-5595. Copyright (2018) American Chemical Society

Authors: Zhao, C.; Xu, X.; Bae, S. H.; Yang, Q.; **Liu, W.**; Belling, J. N.; Cheung, K. M.; Rim, Y. S.; Yang, Y.; Andrews, A. M.; Weiss, P. S.

1.1 Development of Nanolithography

In 2020, Intel's Chief Technology Officer (CTO) Mike Mayberry gave a keynote presentation titled "The Future of Compute".[1] Within the talk, he discussed advanced designs and structures going beyond FinFET,[2,3] especially nanowire or nanoribbon transistors for improved electrostatics.[4,5] To fabricate advanced transistor architectures, to miniaturize functional components, and to build up structural complexity, nanolithography is the key driving force in integrated circuit (IC) manufacturing and the semiconductor industry.[6-12] Furthermore, over the past two decades, the continuous invention and development of nanolithographic methods have enabled many new applications, including energy storage and conversion devices,[13-22] optics and photonics,[23-27] cell regulation,[28-31] gene/drug delivery,[32-38] wearable and flexible electronics,[39-42] and sensing and monitoring devices.[43-52]

Although the development of nanolithography has only lasted 30-40 years so far, the development of printing methods has occurred over thousands of years. Primarily, about 2000-3000 years ago, ancient people carved their names or house symbols onto traditional seals, which were made of valuable stones such as jade, gold, or gems. Later, as art and religion flourished in the Tang dynasty (618 to 907 AD), woodblock printing emerged as a critical printing technique to help with the spread of art pieces and religious work. Compared to traditional seals, woodblock printing used easily fabricated molds (*i.e.*, wood panels) to enable large-scale printing, while reducing carving time. Later, as the popularity of literature reached a new level in the Song dynasty (960 to 1279 AD), movable type printing, also known as one of four landmark inventions in ancient China, appeared in the printing technique roadmap. Movable type printing creatively carved each Chinese character onto a tiny wooden square or metallic cube. The character pieces were assembled into a frame with the desired order, followed by printing and disassembly. The

efficiency of the entire printing process was significantly improved, and the cost was reduced. In the 19th century, lithography emerged in western Europe, which was based on the immiscibility of water and oil. The printing process was carried out on a planar surface (*i.e.*, stone and metal), where the printing pattern was ink-receptive whereas the blank area was ink-repellant. Due to the fast write/erase replication and pattern fidelity, lithography soon became the dominant printing method for art and media.

Nanolithography has developed along similar lines as ancient printing techniques: larger scale, higher efficiency, and lower cost.[11] Additionally, since nanolithography is a technique for printing patterns at the nanoscale, scientists and researchers also seek higher resolution as an ultimate pursuit. Generally, nanolithography can be categorized into three major types: **photolithography**, **direct-writing lithography**, and **unconventional lithography**. Based on the patterning styles, photolithography and unconventional lithography are considered parallel replication approaches with high throughput. Based on the lithographic mechanisms, photolithography and some direct-writing lithography methods use energetic beams (*i.e.*, photons, electrons, ions) to trigger chemical reactions on the organic resist, resulting in the desired patterns.[53] Below, I will discuss the mainstream nanolithographic techniques that fall into each category.

Photolithography is the most crucial nanolithographic technique in semiconductor manufacturing. Conventional photolithography, developed over 50 years ago, is a top-down large-area patterning process that replicates patterns from photomask to photoresist with ultraviolet (UV) light. However, optical diffraction and process factors limit the resolution of conventional photolithography.[54,55] To overcome the resolution limit and utilize photolithography for broader applications, advanced photolithographic techniques have been developed that use a shorter

wavelength of the incident light, such as X-ray lithography,[56-58] deep ultraviolet photolithography (DUV),[59,60] extreme ultraviolet photolithography (EUV).[61-63] Other approaches, such as immersion photolithography[64,65] (high-refractive-index media) and multiple patterning[66] (pattern subtraction), have also been widely applied in chip manufacturing. Although these techniques can push the resolution limit down to sub-10 nm, they are accessible only to a few top semiconductor companies due to high equipment costs. For example, the most advanced EUV photolithography system costs over $145 million. Moreover, the patterning substrates for current photolithographic techniques are hard silicon or silicon oxide wafer, which limit applications in flexible electronics.

The patterning mechanism of **direct-writing lithography**, as the name indicates, is like using a pen to "draw" patterns on the substrate. Electron-beam lithography (EBL)[29,67-69] and focused-ion beam (FIB) lithography[70-72] both utilize energetic beams to pattern electron-sensitive or ion-sensitive polymeric resist, with resolution limited to the beam spot size (sub-10 nm). These techniques are suitable for photomask fabrication and repair. Scanning probe lithography[73-75] also adopts the direct-writing process, often using an atomic force microscopy (AFM) probe or tip to "draw" patterns mechanically, thermally, or chemically. Common techniques include dip-pen lithography,[76] nanografting,[77] nanoshaving,[78] and beam-pen lithography.[79] Although direct-writing lithography has a high level of flexibility and high resolution, the serial writing process is time-consuming, and the pre-programmed writing procedure has a low fault-tolerance rate.[80] As a result, the low throughput and high cost limit applications in scalable fabrication and mass production.

Unconventional lithography is a series of benchtop patterning strategies that have been invented as alternative approaches to conventional photolithography, which are either based on master/stamp replication or self-assembly. Developed by Whitesides and coworkers, soft

lithography uses elastomeric stamps (usually polydimethylsiloxane, or PDMS) to replicate various patterns and structures at large scale and high throughput.[81,82] Based on this principle, several molecular patterning strategies were developed, such as microcontact printing (μCP),[83-86] replica molding,[87,88] polymer pen lithography,[89-91] nanotransfer printing,[92,93] decal transfer printing,[94] and edge spreading lithography.[95,96] Specifically, μCP is used to pattern "ink molecules" (*e.g.*, alkanethiols[84,97,98] and biomaterials[86,99,100]) at micro- and nanoscales. The ink molecules can serve as etch masks to assist pattern transfer to underlying substrates.[68,69] Nanoimprint lithography (NIL), as another type of master replication approach, is based on the mechanical deformation of a thin film in a thermo-mechanical or UV curing process.[101-103] While soft lithography and nanoimprint lithography require master and stamp fabrication before patterning, some unconventional lithographic strategies use self-assembly to generate desired patterns. For example, colloidal lithography,[104,105] nanosphere lithography (NSL),[106-108] and direct self-assembly (DSA) lithography.[109-111] Without the requirement of cleanroom facilities or high-cost equipment, unconventional lithography is economically available and accessible to research laboratories and startup companies. However, the pattern fidelity and uniformity highly rely on the quality of replica mold or the quality of self-assembly.

To meet the need for further advances, high-throughput, low-cost, and large-scale nanolithographic techniques must be developed for higher efficiency and universality. Instead of working on the improvement and optimization of a single patterning strategy, my graduate work focused on the development of hybridized nanolithographic techniques by combining the advantages of two or more nanopatterning and nanofabrication strategies. In the following chapters of my dissertation, I will introduce the hybridization advances of three nanolithographic techniques: chemical lift-off lithography, nanosphere lithography, and conventional photolithography.

1.2 Hybridization of Chemical Lift-Off Lithography

As one type of soft lithographic technique, μCP uses an additive patterning strategy to transfer ink molecules from fabricated PDMS stamps to target substrates *via* conformal contact, followed by the diffusion and self-assembly of ink molecules. The quality of the patterns produced by μCP is limited by diffusion of ink molecules and the deformation of stamp features.[82,98,112] For example, due to the physical contact and additive strategy, lateral diffusion of ink molecules enlarges feature sizes, resulting in poor pattern fidelity. This effect becomes more significant for patterning sub-micron features. To minimize lateral diffusion in μCP, our group developed several additive molecular patterning methods such as microdisplacement printing[113] and microcontact insertion printing.[114,115] To eliminate lateral diffusion, we further developed a subtractive molecular patterning method with straightforwardness and high fidelity, named chemical lift-off lithography (CLL).[116-119]

In a typical CLL process (**Figure 1.1**),[116] the Au substrates are first coated with self-assembled monolayers (SAMs) of hydroxyl-terminated alkanethiol or other reactive molecules.[120] The surfaces of PDMS stamps are made hydrophilic due to the generation of siloxyl groups *via* oxygen plasma treatment. When an activated PDMS stamp is brought into conformal contact with a substrate, a condensation reaction takes place between the siloxyl and hydroxyl groups, forming a covalent linkage. After a few hours, the PDMS stamp is lifted off from the substrate resulting in a complementary pattern on Au substrates. We previously reported that CLL could realize high-fidelity molecular patterning down to 20 nm.[117] With further refinements and optimizations, CLL achieved feature sizes down to ~15 nm.[118] In addition, the remaining molecules in the noncontacted regions serve as resists for wet etching,[84,97] resulting in 3D Au micro- and nanostructures.[49,120]

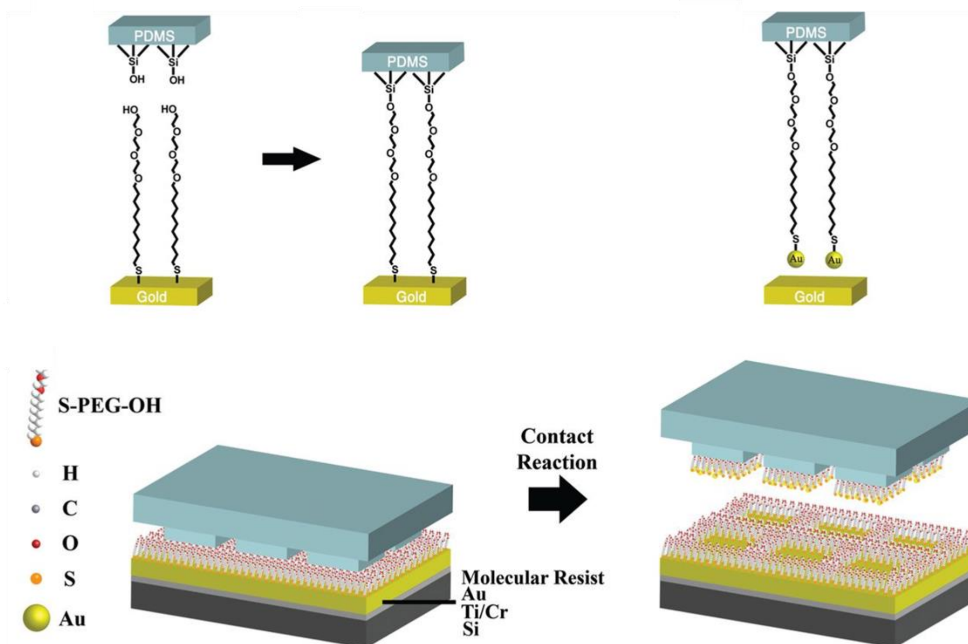

Figure 1.1. Schematics illustrating the contact reaction in chemical lift-off lithography. Reproduced with permission from reference 116. Copyright 2018, American Association for the Advancement of Science.

Advancing chemical interactions for high-fidelity nanopatterning in CLL, our group has developed multiple novel nanolithographic techniques by combining CLL with other nanopatterning strategies. For example, integrating the control of self-collapse behavior of PDMS stamps with CLL, self-collapse lithography (SCL) was developed to realize sub-30 nm features by tailoring the dimensions and stiffness of the PDMS stamps (**Figure 1.2a**).[121] Combined with polymer pen lithography (PPL), polymer-pen chemical lift-off lithography (PPCLL) utilized precisely controlled pyramidal and V-shaped polymer-pen arrays for large-scale patterning with resolution <50 nm (**Figure 1.2b**).[122] Combined with metal deposition and wet etching, CLL can be used as a technique to pattern a variety of materials with different functionalities (*e.g.*, Pt, Pd, Ag, Cu, Ni, Ti, Al, Ge) (**Figure 1.2c**).[123] Combined with colloidal nanochemistry and lithographic

patterning, nanoparticle chemical lift-off lithography (NP-CLL) was developed for scalable fabrication of functional plasmonic materials (**Figure 1.2d**).[124]

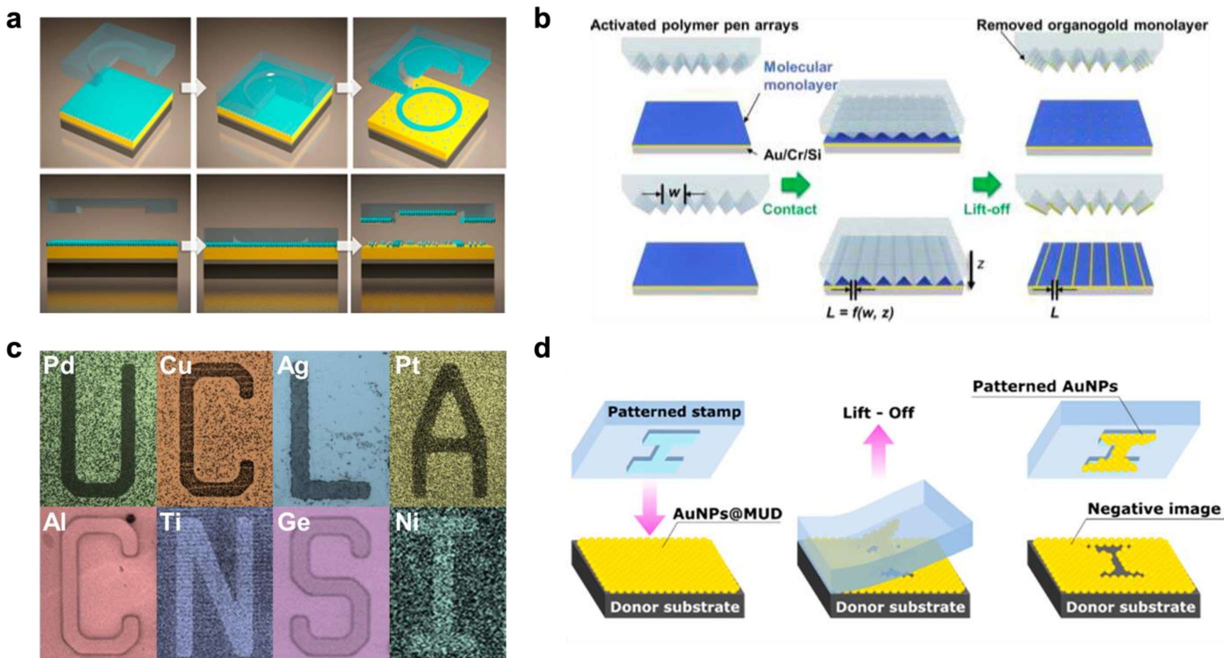

Figure 1.2. (a) Schematic illustration of self-collapse lithography (SCL). Reproduced with permission from reference 121. Copyright 2017, American Chemical Society. (b) Schematic illustrations of polymer-pen chemical lift-off lithography (PPCLL) using pyramidal (top) and V-shaped (bottom) polymer-pen arrays. Reproduced with permission from reference 122. Copyright 2017, American Chemical Society. (c) Molecular patterning on the surface of different substrates *via* chemical lift-off lithography. Reproduced with permission from reference 123. Copyright 2020, American Chemical Society. (d) The chemical lift-off process on a self-assembled monolayer of Au nanoparticles. Reproduced with permission from reference 124. Copyright 2021, American Chemical Society.

Chemical lift-off lithography, like other top-down patterning methods, requires fabricated masters to generate nanostructures on PDMS stamps. The masters are commonly fabricated with

high-cost and low-throughput EBL to achieve nanometer-scale resolution, limiting applicability.[121,122] Recently, we lowered the cost barrier of CLL by employing widely available low-cost HD-DVDs as nanostructured master patterns (**Figure 1.3a,b**).[125] We leveraged and extended the capabilities of CLL, in combination with selective etching processes, to pattern SAM molecules, metal films, and ultrathin layers of In_2O_3 successively to create periodic nanoribbon arrays with high throughput, large scale, and good uniformity (**Figure 1.3c,d**). This work provides a general approach for the facile and large-scale patterning of semiconductor 1D nanostructure arrays with high surface-to-volume ratios, which have a broad range of applications in electronic devices, optical devices, and biochemical sensors.

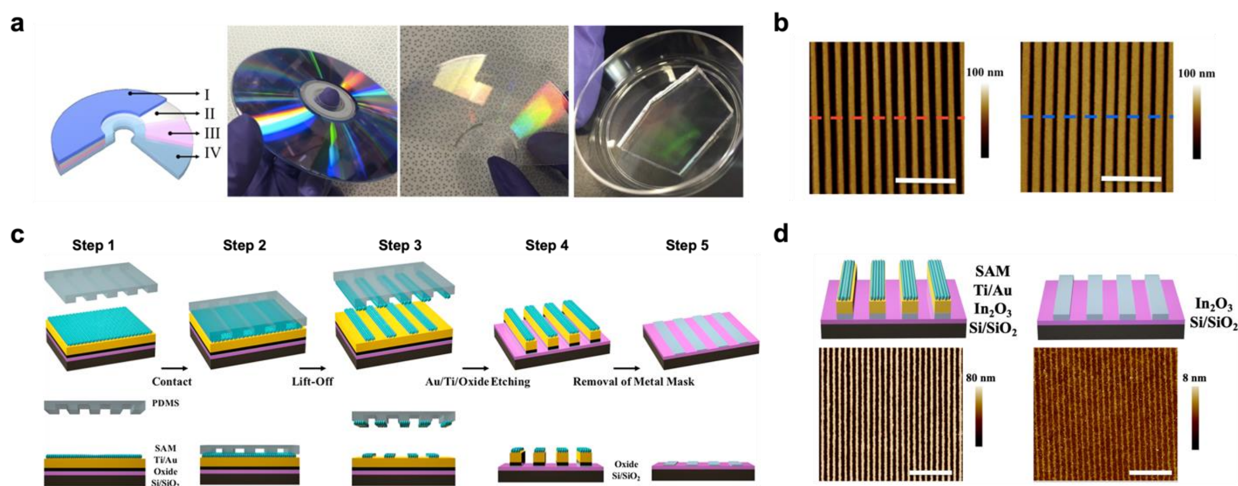

Figure 1.3. (a) Schematic architecture of a high-definition digital versatile disc (HD-DVD): layer I, polycarbonate protective layer; layer II, mirror-like metal film; layer III, data recording film; layer IV, polycarbonate layer containing concentric rings with typical widths of 250 nm and periodicities of 400 nm. Photographs of a HD-DVD, a HD-DVD master (layer IV), and a patterned polydimethylsiloxane (PDMS) stamp, respectively. (b) Atomic force micrographs of a representative HD-DVD master (left) and a patterned PDMS stamp (right). Scale bars are 2 µm. (c) Fabrication scheme for producing In_2O_3 nanoribbons using

chemical lift-off lithography. (d) (top) Topographic images measured using atomic force microscopy (AFM) and (bottom) schematic illustrations of SAM/Au/Ti/ In_2O_3 and bare In_2O_3 nanoribbons, respectively, with line widths of ~200 nm. Reproduced with permission from reference 125. Copyright 2018, American Chemical Society.

During the fabrication of In_2O_3 nanoribbons, to ensure that the etching process is complete, overetching or etching undercut of the Au/Ti layers often takes place, resulting in compromised uniformity and reproducibility of fabricated nanoribbons. By sputtering In_2O_3 into the nanochannels after Au/Ti wet etching, we addressed these shortcomings and fabricated nanoribbon field-effect transistor (FET) biosensing platforms with high sensitivity (Chapter 5).[126] Furthermore, we hybridized CLL with a double-patterning strategy to fabricate two-dimensional Au plasmonic nanostructures for photothermal intracellular delivery. By generating transient pores at the outer membrane, the platform enabled the delivery of biomolecular cargo into cells with high delivery efficiencies and cell viabilities (Chapter 6).[127]

1.3 Hybridization of Nanosphere Lithography

Nanosphere lithography (NSL) is a facile and robust unconventional nanolithographic method.[106] By using self-assembled monolayers of polymeric or oxide nanospheres, such as polystyrene (PS) and silicon oxide (SiO_2), NSL is used for scalable and periodic patterning and fabrication of underlying substrates. The periodicity, or pitch distance, is defined by the sizes (diameters) of the nanospheres, which range from less than 100 nm to over 100 microns. A typical patterning process of PS nanospheres, also known as the Langmuir-Blodgett method[128,129] (see the experimental setup in **Figure 1.4a**) involves three steps:

(1) Preparation of the PS nanosphere solution: the PS nanosphere solution with the desired concentration is prepared with several rounds of centrifugation and sonication.

(2) Self-assembly of the PS nanosphere monolayer: the prepared solution is pipetted onto the top edge of a glass slide to allow the PS nanospheres to slide down to the water surface. The nanospheres assemble into a close-packed pattern to minimize surface energy. The rainbow-like color on the water surface represents the close-packed PS monolayer (**Figure 1.4a**).

(3) Transferring the PS nanosphere monolayer to the substrates: by carefully removing the water, the high-quality close-packed monolayer of PS nanospheres are transferred from the water surface to the underlying substrates (**Figure 1.4b,c**).[130]

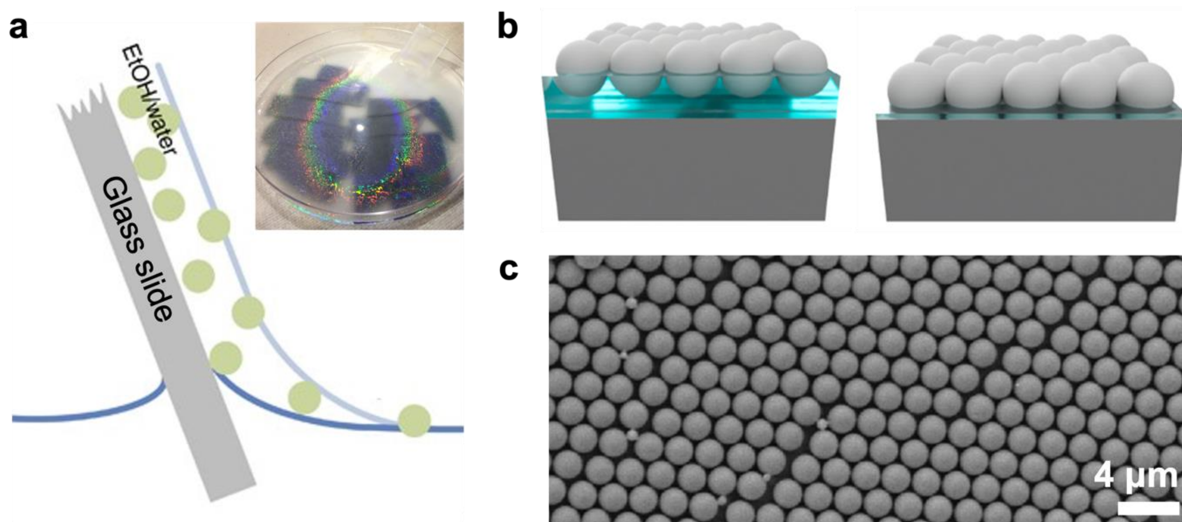

Figure 1.4. Schematics illustrating the self-assembly process of polystyrene (PS) micro-/nanospheres *via* the Langmuir-Blodgett method. (a) Addition of the PS sphere solution using a glass slide in water to form a self-assembled monolayer. (b) Drying process of the PS spheres on the substrate. (c) Scanning electronic microscopy (SEM) image of PS

sphere close-packed monolayer on a substrate. Reproduced with permission from reference 129. Copyright 2020, American Chemical Society.

Hybridized with other nanopatterning and nanofabrication techniques, NSL have been widely used for scalable fabrication of periodic arrays of 3D micro- and nanostructures.[129-131] In most cases, the sizes of the PS nanospheres are tailored *via* oxygen plasma while the pitch distance and size uniformity remain the same.[132] Decreasing the size exposes more underlying substrate for the subsequent substrate etching or material deposition step. For example, silicon nanopillars are fabricated *via* deep silicon etching using PS nanospheres as etching masks.[129] The pillar diameter can be optimized by adjusting the size of the PS nanospheres. Moreover, combined with multiple patterning strategy, PS nanospheres are used as templates in multiple-patterning nanosphere lithography (MP-NSL) to fabricate wafer-scale periodic hierarchical nanostructures.[133] We further hybridized NSL with oxide deposition and silicon wet etching for fabricating large-area ordered nanopyramid structures, which contributes to enhanced light absorption and photoelectric sensitivity for a perovskite-based photodetector (Chapter 4).[134]

1.4 Hybridization of Conventional Photolithography

Conventional photolithography, due to its scalability, robustness, and straightforward processes, has been widely applied to micro- and nanostructure manufacturing. Guided by Rayleigh's equation ($R = k_1 \cdot \lambda / NA$),[54] the resolution ($R$) of conventional photolithography has been continuously improved by reducing the wavelength (λ) of the light sources, increasing the numerical aperture (NA) of the projection systems, and/or optimizing the process factor (k_1). However, either updating the light source or changing the numerical aperture requires high primary investment and long-term development, which slows down the improvement of the resolution.

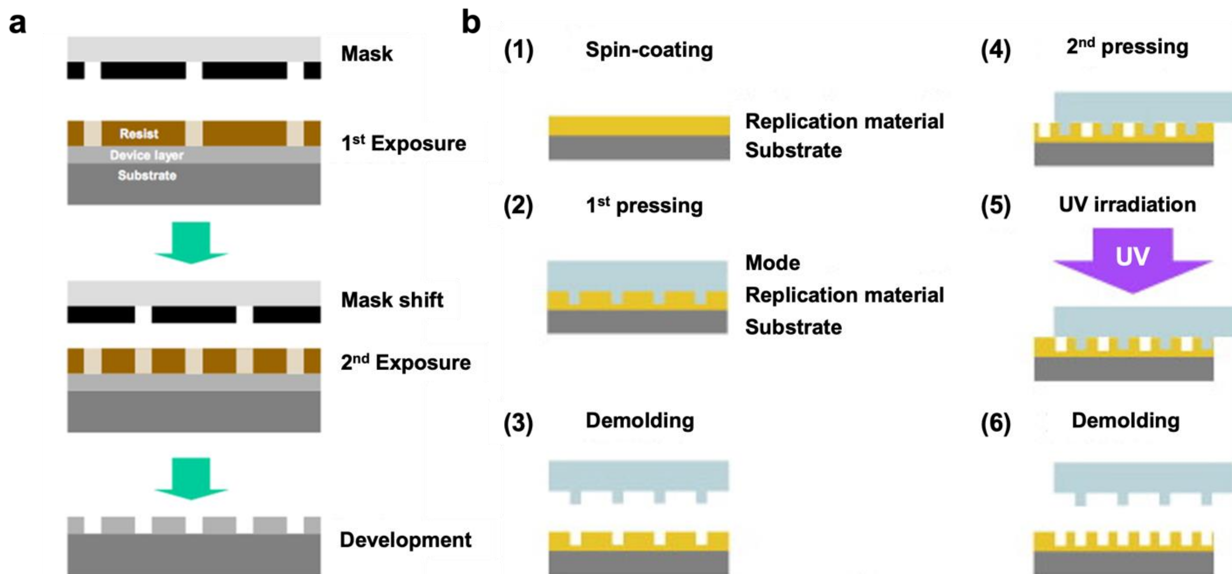

Figure 1.5. (a) Resolution improvement in conventional photolithography *via* a double exposure and patterning technique. Reproduced with permission from reference 141. Copyright 2013, ITRS. (b) Resolution improvement in nanoimprint lithography *via* a double patterning technique. Reproduced with permission from reference 142. Copyright 2013, Elsevier.

Several creative methods, such as double-patterning,[135,136] multiple-exposure,[137] phase-shifting masks (PSMs),[138,139] and off-axis illumination (OAI)[140,141] have been developed to improve the resolution to sub-micron or nanometer scales through optimization of the lithographic process. While PSMs and OAI aim to reduce the k_1, double patterning generates patterns with sizes several times smaller than the original feature size of the photomask through a "subtraction" mechanism between two sequential processes (**Figure 1.5a**).[142] Besides conventional photolithography, the double-patterning method has been applied to NIL to improve resolution and periodicity (**Figure 1.5b**).[143] However, the reproducibility and pattern quality of double patterning rely on the mask alignment between each lithographic step, which requires precise

operation and high-cost equipment. Therefore, double patterning is limited due to the trade-off between patterning throughput and alignment error.

To overcome the resolution limits of conventional photolithography and build from its versatility and practicality, we developed a high-throughput, cost-effective, and straightforward nanopatterning method, dual-layer photolithography (DLPL) (Chapter 2).[144] Systematic optimization of photolithographic parameters enabled DLPL to reach sub-200 nm patterning (Chapter 3). Combined with etching and lift-off techniques, DLPL provides a simple and economical means to fabricate various nanostructures for applications in optoelectronic devices and biotechnology.

During my graduate study, I developed high-throughput and large-scale nanolithographic techniques, hybridized with other nanopatterning and nanofabrication methods for improved patterning tunability and versatility. These hybrid techniques enabled advances in the fabrication of next-generation nanodevices and nanoplatforms for applications in electronics, optics, and biology.

1.5 References

1. Mayberry, M. The Future of Compute: How the Data Transformation is Reshaping VLSI. *2020 IEEE Symposium on VLSI Technology* **2020**, 1-4.

2. Mishra, P.; Muttreja, A.; Jha, N. K. *FinFET Circuit Design*. **2011**, 23-54.

3. Jurczak, M.; Collaert, N.; Veloso, A.; Hoffmann, T.; Biesemans, S. Review of FinFET Technology. *2009 IEEE International SOI Conference* **2009**, 1-4.

4. Nagy, D.; Indalecio, G.; Garcia-Loureiro, A. J.; Elmessary, M. A.; Kalna, K.; Seoane, N. FinFET Versus Gate-All-Around Nanowire FET: Performance, Scaling, and Variability. *IEEE J. Electron Devices Soc.* **2018,** *6*, 332-340.

5. Feng, X.; Wang, L.; Huang, X.; Chen, L.; Ang, K. W. Complementary Black Phosphorus Nanoribbons Field-Effect Transistors and Circuits. *IEEE Trans. Electron Devices* **2018,** *65*, 4122-4128.

6. Zheng, X.; Calò, A.; Albisetti, E.; Liu, X.; Alharbi, A. S. M.; Arefe, G.; Liu, X.; Spieser, M.; Yoo, W. J.; Taniguchi, T.; Watanabe, K.; Aruta, C.; Ciarrocchi, A.; Kis, A.; Lee, B. S.; Lipson, M.; Hone, J.; Shahrjerdi, D.; Riedo, E. Patterning Metal Contacts on Monolayer MoS_2 with Vanishing Schottky Barriers Using Thermal Nanolithography. *Nat. Electron.* **2019,** *2*, 17-25.

7. Huang, K.; Wu, J.; Chen, Z.; Xu, H.; Wu, Z.; Tao, K.; Yang, T.; Wu, Q.; Zhou, H.; Huang, B.; Chen, H.; Chen, J.; Liu, C. Nanostructured High-Performance Thin-Film Transistors and Phototransistors Fabricated by A High-Yield and Versatile Near-Field Nanolithography Strategy. *ACS Nano* **2019,** *13*, 6618-6630.

8. Close, G. F.; Yasuda, S.; Paul, B.; Fujita, S.; Wong, H. S. P. A 1 GHz Integrated Circuit with Carbon Nanotube Interconnects and Silicon Transistors. *Nano Lett.* **2008,** *8*, 706-709.

9. Ziaie, B.; Baldi, A.; Atashbar, M. Z. *Introduction to Micro-/Nanofabrication*. **2010**, 231-269.

10. Zeng, M.; Xiao, Y.; Liu, J.; Yang, K.; Fu, L. Exploring Two-Dimensional Materials toward the Next-Generation Circuits: From Monomer Design to Assembly Control. *Chem. Rev.* **2018,** *118*, 6236-6296.

11. Gates, B. D.; Xu, Q.; Stewart, M.; Ryan, D.; Willson, C. G.; Whitesides, G. M. New Approaches to Nanofabrication: Molding, Printing, and Other Techniques. *Chem. Rev.* **2005,** *105*, 1171-1196.

12. Liddle, J. A.; Gallatin, G. M. Nanomanufacturing: A Perspective. *ACS Nano* **2016,** *10*, 2995-3014.

13. Wu, H.; Chan, G.; Choi, J. W.; Ryu, I.; Yao, Y.; McDowell, M. T.; Lee, S. W.; Jackson, A.; Yang, Y.; Hu, L.; Cui, Y. Stable Cycling of Double-Walled Silicon Nanotube Battery Anodes through Solid–Electrolyte Interphase Control. *Nat. Nanotechnol.* **2012,** *7*, 310-315.

14. Du, F.-H.; Li, B.; Fu, W.; Xiong, Y.-J.; Wang, K.-X.; Chen, J.-S. Surface Binding of Polypyrrole on Porous Silicon Hollow Nanospheres for Li-Ion Battery Anodes with High Structure Stability. *Adv. Mater.* **2014,** *26*, 6145-6150.

15. Liu, Y.; Zhou, G.; Liu, K.; Cui, Y. Design of Complex Nanomaterials for Energy Storage: Past Success and Future Opportunity. *Acc. Chem. Res.* **2017,** *50*, 2895-2905.

16. Siddique, R. H.; Donie, Y. J.; Gomard, G.; Yalamanchili, S.; Merdzhanova, T.; Lemmer, U.; Hölscher, H. Bioinspired Phase-Separated Disordered Nanostructures for Thin Photovoltaic Absorbers. *Sci. Adv.* **2017,** *3*, e1700232.

17. Mao, J.; Sha, W. E. I.; Zhang, H.; Ren, X.; Zhuang, J.; Roy, V. A. L.; Wong, K. S.; Choy, W. C. H. Novel Direct Nanopatterning Approach to Fabricate Periodically Nanostructured Perovskite for Optoelectronic Applications. *Adv. Funct. Mater.* **2017,** *27*, 1606525.

18. Lei, Y.; Chen, Y.; Zhang, R.; Li, Y.; Yan, Q.; Lee, S.; Yu, Y.; Tsai, H.; Choi, W.; Wang, K.; Luo, Y.; Gu, Y.; Zheng, X.; Wang, C.; Wang, C.; Hu, H.; Li, Y.; Qi, B.; Lin, M.; Zhang, Z.; Dayeh, S. A.; Pharr, M.; Fenning, D. P.; Lo, Y.-H.; Luo, J.; Yang, K.; Yoo, J.; Nie, W.; Xu, S. A Fabrication Process for Flexible Single-Crystal Perovskite Devices. *Nature* **2020,** *583*, 790-795.

19. Vijselaar, W.; Westerik, P.; Veerbeek, J.; Tiggelaar, R. M.; Berenschot, E.; Tas, N. R.; Gardeniers, H.; Huskens, J. Spatial Decoupling of Light Absorption and Catalytic Activity of Ni–Mo-Loaded High-Aspect-Ratio Silicon Microwire Photocathodes. *Nat. Energy* **2018,** *3*, 185-192.

20. Su, Y.; Liu, C.; Brittman, S.; Tang, J.; Fu, A.; Kornienko, N.; Kong, Q.; Yang, P. Single-Nanowire Photoelectrochemistry. *Nat. Nanotechnol.* **2016,** *11*, 609-612.

21. Kelzenberg, M. D.; Boettcher, S. W.; Petykiewicz, J. A.; Turner-Evans, D. B.; Putnam, M. C.; Warren, E. L.; Spurgeon, J. M.; Briggs, R. M.; Lewis, N. S.; Atwater, H. A. Enhanced Absorption and Carrier Collection in Si Wire Arrays for Photovoltaic Applications. *Nat. Mater.* **2010,** *9*, 239-244.

22. Garnett, E.; Yang, P. Light Trapping in Silicon Nanowire Solar Cells. *Nano Lett.* **2010,** *10*, 1082-1087.

23. Wu, J.; Agrawal, M.; Becerril, H. A.; Bao, Z.; Liu, Z.; Chen, Y.; Peumans, P. Organic Light-Emitting Diodes on Solution-Processed Graphene Transparent Electrodes. *ACS Nano* **2009,** *4*, 43-48.

24. Kim, T.-H.; Cho, K.-S.; Lee, E. K.; Lee, S. J.; Chae, J.; Kim, J. W.; Kim, D. H.; Kwon, J.-Y.; Amaratunga, G.; Lee, S. Y.; Choi, B. L.; Kuk, Y.; Kim, J. M.; Kim, K. Full-Colour Quantum Dot Displays Fabricated by Transfer Printing. *Nat. Photonics* **2011,** *5*, 176-182.

25. Kim, J.; Shim, H. J.; Yang, J.; Choi, M. K.; Kim, D. C.; Kim, J.; Hyeon, T.; Kim, D.-H. Ultrathin Quantum Dot Display Integrated with Wearable Electronics. *Adv. Mater.* **2017,** *29*, 1700217.

26. Ho, S.-J.; Hsu, H.-C.; Yeh, C.-W.; Chen, H.-S. Inkjet-Printed Salt-Encapsulated Quantum Dot Film for UV-Based RGB Color-Converted Micro-Light Emitting Diode Displays. *ACS Appl. Mater. Interfaces* **2020,** *12*, 33346-33351.

27. Cho, C.-H.; Aspetti, C. O.; Park, J.; Agarwal, R. Silicon Coupled with Plasmon Nanocavities Generates Bright Visible Hot Luminescence. *Nat. Photonics* **2013,** *7*, 285-289.

28. Kimmerling, R. J.; Lee Szeto, G.; Li, J. W.; Genshaft, A. S.; Kazer, S. W.; Payer, K. R.; de Riba Borrajo, J.; Blainey, P. C.; Irvine, D. J.; Shalek, A. K.; Manalis, S. R. A Microfluidic Platform Enabling Single-Cell RNA-Seq of Multigenerational Lineages. *Nat. Commun.* **2016,** *7*, 10220.

29. Moolman, M. C.; Huang, Z.; Krishnan, S. T.; Kerssemakers, J. W. J.; Dekker, N. H. Electron Beam Fabrication of A Microfluidic Device for Studying Submicron-Scale Bacteria. *J. Nanobiotechnol.* **2013,** *11*, 12.

30. Sun, N.; Yang, Y.; Miao, H.; Redublo, P.; Liu, H.; Liu, W.; Huang, Y.-W.; Teng, P.-C.; Zhang, C.; Zhang, R. Y.; Smalley, M.; Yang, P.; Chou, S.-J.; Huai, K.; Zhang, Z.; Lee, Y.-T.; Wang, J. J.; Wang, J.; Liang, I. Y.; Zhang, T. X.; Zhang, D.; Liang, L.; Weiss, P. S.; Posadas, E. M.; Donahue, T.; Hecht, J. R.; Allen-Auerbach, M. S.; Bergsland, E. K.; Hope, T. A.; Pei, R.; Zhu, Y.; Tseng, H.-R.; Heaney, A. P. Discovery and Characterization of Circulating Tumor Cell Clusters in Neuroendocrine Tumor Patients Using Nanosubstrate-Embedded Microchips. *Biosens. Bioelectron.* **2022,** *199*, 113854.

31. Sun, N.; Lee, Y.-T.; Zhang, R. Y.; Kao, R.; Teng, P.-C.; Yang, Y.; Yang, P.; Wang, J. J.; Smalley, M.; Chen, P.-J.; Kim, M.; Chou, S.-J.; Bao, L.; Wang, J.; Zhang, X.; Qi, D.; Palomique, J.; Nissen, N.; Han, S.-H. B.; Sadeghi, S.; Finn, R. S.; Saab, S.; Busuttil, R. W.; Markovic, D.; Elashoff, D.; Yu, H.-h.; Li, H.; Heaney, A. P.; Posadas, E.; You, S.; Yang, J. D.; Pei, R.; Agopian, V. G.; Tseng, H.-R.; Zhu, Y. Purification of HCC-Specific Extracellular Vesicles on Nanosubstrates for Early HCC Detection by Digital Scoring. *Nat. Commun.* **2020,** *11*, 4489

32. Kim, W.; Ng, J. K.; Kunitake, M. E.; Conklin, B. R.; Yang, P. Interfacing Silicon Nanowires with Mammalian Cells. *J. Am. Chem. Soc.* **2007,** *129*, 7228-7229.

33. Boukany, P. E.; Morss, A.; Liao, W.-c.; Henslee, B.; Jung, H.; Zhang, X.; Yu, B.; Wang, X.; Wu, Y.; Li, L.; Gao, K.; Hu, X.; Zhao, X.; Hemminger, O.; Lu, W.; Lafyatis, G. P.; Lee, L. J. Nanochannel Electroporation Delivers Precise Amounts of Biomolecules into Living Cells. *Nat. Nanotechnol.* **2011,** *6*, 747-754.

34. VanDersarl, J. J.; Xu, A. M.; Melosh, N. A. Nanostraws for Direct Fluidic Intracellular Access. *Nano Lett.* **2011,** *12*, 3881-3886.

35. Shalek, A. K.; Robinson, J. T.; Karp, E. S.; Lee, J. S.; Ahn, D.-R.; Yoon, M.-H.; Sutton, A.; Jorgolli, M.; Gertner, R. S.; Gujral, T. S.; MacBeath, G.; Yang, E. G.; Park, H. Vertical Silicon Nanowires as a Universal Platform for Delivering Biomolecules into Living Cells. *Proc. Natl. Acad. Sci. U. S. A.* **2010,** *107*, 1870-1875.

36. Stewart, M. P.; Langer, R.; Jensen, K. F. Intracellular Delivery by Membrane Disruption: Mechanisms, Strategies, and Concepts. *Chem. Rev.* **2018,** *118*, 7409-7531.

37. Man, T.; Zhu, X.; Chow, Y. T.; Dawson, E. R.; Wen, X.; Patananan, A. N.; Liu, T. L.; Zhao, C.; Wu, C.; Hong, J. S.; Chung, P.-S.; Clemens, D. L.; Lee, B.-Y.; Weiss, P. S.; Teitell, M. A.; Chiou, P.-Y. Intracellular Photothermal Delivery for Suspension Cells Using Sharp Nanoscale Tips in Microwells. *ACS Nano* **2019,** *13*, 10835-10844.

38. Yang, P.; Chou, S.-J.; Li, J.; Hui, W.; Liu, W.; Sun, N.; Zhang, R. Y.; Zhu, Y.; Tsai, M.-L.; Lai, H. I.; Smalley, M.; Zhang, X.; Chen, J.; Romero, Z.; Liu, D.; Ke, Z.; Zou, C.; Lee, C.-F.; Jonas, S. J.; Ban, Q.; Weiss, P. S.; Kohn, D. B.; Chen, K.; Chiou, S.-H.; Tseng, H.-R. Supramolecular Nanosubstrate–Mediated Delivery System Enables CRISPR-Cas9 Knockin of Hemoglobin Beta Gene for Hemoglobinopathies. *Sci. Adv.* **2020,** *6*, eabb7107.

39. Miyamoto, A.; Lee, S.; Cooray, N. F.; Lee, S.; Mori, M.; Matsuhisa, N.; Jin, H.; Yoda, L.; Yokota, T.; Itoh, A.; Sekino, M.; Kawasaki, H.; Ebihara, T.; Amagai, M.; Someya, T. Inflammation-Free, Gas-Permeable, Lightweight, Stretchable On-Skin Electronics with Nanomeshes. *Nat. Nanotechnol.* **2017,** *12*, 907-913.

40. Rogers, J.; Bao, Z.; Lee, T.-W. Wearable Bioelectronics: Opportunities for Chemistry. *Acc. Chem. Res.* **2019,** *52*, 521-522.

41. Wang, S.; Xu, J.; Wang, W.; Wang, G.-J. N.; Rastak, R.; Molina-Lopez, F.; Chung, J. W.; Niu, S.; Feig, V. R.; Lopez, J.; Lei, T.; Kwon, S.-K.; Kim, Y.; Foudeh, A. M.; Ehrlich, A.; Gasperini, A.; Yun, Y.; Murmann, B.; Tok, J. B. H.; Bao, Z. Skin Electronics from Scalable Fabrication of an Intrinsically Ttretchable Transistor Array. *Nature* **2018,** *555*, 83-88.

42. Keum, K.; Eom, J.; Lee, J. H.; Heo, J. S.; Park, S. K.; Kim, Y.-H. Fully-Integrated Wearable Pressure Sensor Array Enabled by Highly Sensitive Textile-Based Capacitive Ionotronic Devices. *Nano Energy* **2021,** *79*, 105479.

43. Nayeem, M. O. G.; Lee, S.; Jin, H.; Matsuhisa, N.; Jinno, H.; Miyamoto, A.; Yokota, T.; Someya, T. All-Nanofiber–Based, Ultrasensitive, Gas-Permeable Mechanoacoustic Sensors for Continuous Long-Term Heart Monitoring. *Proc. Natl. Acad. Sci. U. S. A.* **2020,** *117*, 7063-7070.

44. Kim, J.; Campbell, A. S.; de Ávila, B. E.-F.; Wang, J. Wearable Biosensors for Healthcare Monitoring. *Nat. Biotechnol.* **2019,** *37*, 389-406.

45. Gao, W.; Emaminejad, S.; Nyein, H. Y. Y.; Challa, S.; Chen, K.; Peck, A.; Fahad, H. M.; Ota, H.; Shiraki, H.; Kiriya, D.; Lien, D.-H.; Brooks, G. A.; Davis, R. W.; Javey, A. Fully Integrated Wearable Sensor Arrays for Multiplexed *in situ* Perspiration Analysis. *Nature* **2016,** *529*, 509-514.

46. Boutry, C. M.; Beker, L.; Kaizawa, Y.; Vassos, C.; Tran, H.; Hinckley, A. C.; Pfattner, R.; Niu, S.; Li, J.; Claverie, J.; Wang, Z.; Chang, J.; Fox, P. M.; Bao, Z. Biodegradable and Flexible Arterial-Pulse Sensor for the Wireless Monitoring of Blood Flow. *Nat. Biomed. Eng.* **2019,** *3*, 47-57.

47. Liu, Z.; Qi, D.; Leow, W. R.; Yu, J.; Xiloyannnis, M.; Cappello, L.; Liu, Y.; Zhu, B.; Jiang, Y.; Chen, G.; Masia, L.; Liedberg, B.; Chen, X. 3D-Structured Stretchable Strain Sensors for Out-of-Plane Force Detection. *Adv. Mater.* **2018,** *30*, 1707285.

48. Liu, Q.; Liu, Y.; Wu, F.; Cao, X.; Li, Z.; Alharbi, M.; Abbas, A. N.; Amer, M. R.; Zhou, C. Highly Sensitive and Wearable In_2O_3 Nanoribbon Transistor Biosensors with Integrated On-Chip Gate for Glucose Monitoring in Body Fluids. *ACS Nano* **2018,** *12*, 1170-1178.

49. Zhao, C.; Xu, X.; Ferhan, A. R.; Chiang, N.; Jackman, J. A.; Yang, Q.; Liu, W.; Andrews, A. M.; Cho, N.-J.; Weiss, P. S. Scalable Fabrication of Quasi-One-Dimensional Gold Nanoribbons for Plasmonic Sensing. *Nano Lett.* **2020,** *20*, 1747-1754.

50. Nakatsuka, N.; Yang, K.-A.; Abendroth, J. M.; Cheung, K. M.; Xu, X.; Yang, H.; Zhao, C.; Zhu, B.; Rim, Y. S.; Yang, Y.; Weiss, P. S.; Stojanović, M. N.; Andrews, A. M. Aptamer–Field-Effect Transistors Overcome Debye Length Limitations for Small-Molecule Sensing. *Science* **2018,** *362*, 319-324.

51. Zhao, C.; Cheung, K. M.; Huang, I. W.; Yang, H.; Nakatsuka, N.; Liu, W.; Cao, Y.; Man, T.; Weiss, P. S.; Monbouquette, H. G.; Andrews, A. M. Implantable Aptamer–Field-Effect Transistor Neuroprobes for *in vivo* Neurotransmitter Monitoring. *Sci. Adv.* **2021,** *7*, eabj7422.

52. Wang, B.; Zhao, C.; Wang, Z.; Yang, K.-A.; Cheng, X.; Liu, W.; Yu, W.; Lin, S.; Zhao, Y.; Cheung, K. M.; Lin, H.; Hojaiji, H.; Weiss, P. S.; Stojanović, M. N.; Tomiyama, A. J.; Andrews, A. M.; Emaminejad, S. Wearable Aptamer-Field-Effect Transistor Sensing System for Noninvasive Cortisol Monitoring. *Sci. Adv.* **2022,** *8*, eabk0967.

53. Krasheninnikov, A. V.; Banhart, F. Engineering of Nanostructured Carbon Materials with Electron or Ion Beams. *Nat. Mater.* **2007,** *6*, 723-733.

54. Ito, T.; Okazaki, S. Pushing the Limits of Lithography. *Nature* **2000,** *406*, 1027-1031.

55. Okazaki, S. Resolution Limits of Optical Lithography. *J. Vac. Sci. Technol. B* **1991,** *9*, 2829.

56. Tu, M.; Xia, B.; Kravchenko, D. E.; Tietze, M. L.; Cruz, A. J.; Stassen, I.; Hauffman, T.; Teyssandier, J.; De Feyter, S.; Wang, Z.; Fischer, R. A.; Marmiroli, B.; Amenitsch, H.; Torvisco, A.; Velásquez-Hernández, M. d. J.; Falcaro, P.; Ameloot, R. Direct X-Ray and Electron-Beam Lithography of Halogenated Zeolitic Imidazolate Frameworks. *Nat. Mater.* **2020,** *20*, 93-99.

57. Palazon, F.; Akkerman, Q. A.; Prato, M.; Manna, L. X-Ray Lithography on Perovskite Nanocrystals Films: From Patterning with Anion-Exchange Reactions to Enhanced Stability in Air and Water. *ACS Nano* **2015,** *10*, 1224-1230.

58. Miszta, K.; Greullet, F.; Marras, S.; Prato, M.; Toma, A.; Arciniegas, M.; Manna, L.; Krahne, R. Nanocrystal Film Patterning by Inhibiting Cation Exchange *via* Electron-Beam or X-Ray Lithography. *Nano Lett.* **2014,** *14*, 2116-2122.

59. Goodberlet, J. G. Patterning 100 nm Features Using Deep-Ultraviolet Contact Photolithography. *Appl. Phys. Lett.* **2000,** *76*, 667-669.

60. Totzeck, M.; Ulrich, W.; Göhnermeier, A.; Kaiser, W. Pushing Deep Ultraviolet Lithography to Its Limits. *Nat. Photonics* **2007,** *1*, 629-631.

61. Wagner, C.; Harned, N. Lithography Gets Extreme. *Nat. Photonics* **2010,** *4*, 24-26.

62. Ashby, P. D.; Olynick, D. L.; Ogletree, D. F.; Naulleau, P. P. Resist Materials for Extreme Ultraviolet Lithography: Toward Low-Cost Single-Digit-Nanometer Patterning. *Adv. Mater.* **2015,** *27*, 5813-5819.

63. Vladimirsky, Y.; Silfvast, W. T.; Klosner, M.; Shimkaveg, G. M.; Bender, H.; Kubiak, G. D.; Fornaciari, N. R. High-Power Plasma Discharge Source at 13.5 nm and 11.4 nm for EUV Lithography. *Proc. SPIE* **1999,** *3676*, 272.

64. Switkes, M.; Rothschild, M. Immersion Lithography at 157 nm. *J. Vac. Sci. Technol. B* **2001,** *19*, 2353-2356.

65. Lin, B. J. Immersion Lithography and Its Impact on Semiconductor Manufacturing. *J. Micro. Nanolithogr. MEMS MOEMS* **2004,** *3*, 377-395.

66. Mason, M. E.; Ghaida, R. S.; Agarwal, K. B.; Liebmann, L. W.; Nassif, S. R.; Gupta, P. A Novel Methodology for Triple/Multiple-Patterning Layout Decomposition. *Proc. SPIE* **2012,** *8327*, 83270M.

67. Manfrinato, V. R.; Wen, J.; Zhang, L.; Yang, Y.; Hobbs, R. G.; Baker, B.; Su, D.; Zakharov, D.; Zaluzec, N. J.; Miller, D. J.; Stach, E. A.; Berggren, K. K. Determining the Resolution Limits of Electron-Beam Lithography: Direct Measurement of the Point-Spread Function. *Nano Lett.* **2014,** *14*, 4406-4412.

68. Kim, S.; Marelli, B.; Brenckle, M. A.; Mitropoulos, A. N.; Gil, E.-S.; Tsioris, K.; Tao, H.; Kaplan, D. L.; Omenetto, F. G. All-Water-Based Electron-Beam Lithography Using Silk as a Resist. *Nat. Nanotechnol.* **2014,** *9*, 306-310.

69. Chen, S.; Svedendahl, M.; Antosiewicz, T. J.; Käll, M. Plasmon-Enhanced Enzyme-Linked Immunosorbent Assay on Large Arrays of Individual Particles Made by Electron Beam Lithography. *ACS Nano* **2013,** *7*, 8824-8832.

70. Schröder, T.; Trusheim, M. E.; Walsh, M.; Li, L.; Zheng, J.; Schukraft, M.; Sipahigil, A.; Evans, R. E.; Sukachev, D. D.; Nguyen, C. T.; Pacheco, J. L.; Camacho, R. M.; Bielejec, E. S.; Lukin, M. D.; Englund, D. Scalable Focused Ion Beam Creation of Nearly Lifetime-Limited Single Quantum Emitters in Diamond Nanostructures. *Nat. Commun.* **2017,** *8*, 15376.

71. Córdoba, R.; Ibarra, A.; Mailly, D.; De Teresa, J. M. Vertical Growth of Superconducting Crystalline Hollow Nanowires by He^+ Focused Ion Beam Induced Deposition. *Nano Lett.* **2018,** *18*, 1379-1386.

72. Porrati, F.; Barth, S.; Sachser, R.; Dobrovolskiy, O. V.; Seybert, A.; Frangakis, A. S.; Huth, M. Crystalline Niobium Carbide Superconducting Nanowires Prepared by Focused Ion Beam Direct Writing. *ACS Nano* **2019,** *13*, 6287-6296.

73. Jackson, B. L.; Groves, J. T. Scanning Probe Lithography on Fluid Lipid Membranes. *J. Am. Chem. Soc.* **2004,** *126*, 13878-13879.

74. Garcia, R.; Knoll, A. W.; Riedo, E. Advanced Scanning Probe Lithography. *Nat. Nanotechnol.* **2014,** *9*, 577-587.

75. Liu, G.-Y.; Xu, S.; Qian, Y. Nanofabrication of Self-Assembled Monolayers Using Scanning Probe Lithography. *Acc. Chem. Res.* **2000,** *33*, 457-466.

76. Piner, R. D.; Zhu, J.; Xu, F.; Hong, S.; Mirkin, C. A. "Dip-Pen" Nanolithography. *Science* **1999,** *283*, 661-663.

77. Liu, J.-F.; Cruchon-Dupeyrat, S.; Garno, J. C.; Frommer, J.; Liu, G.-Y. Three-Dimensional Nanostructure Construction *via* Nanografting: Positive and Negative Pattern Transfer. *Nano Lett.* **2002,** *2*, 937-940.

78. Shi, J.; Chen, J.; Cremer, P. S. Sub-100 nm Patterning of Supported Bilayers by Nanoshaving Lithography. *J. Am. Chem. Soc.* **2008,** *130*, 2718-2719.

79. Huo, F.; Zheng, G.; Liao, X.; Giam, L. R.; Chai, J.; Chen, X.; Shim, W.; Mirkin, C. A. Beam Pen Lithography. *Nat. Nanotechnol.* **2010,** *5*, 637-640.

80. Dubois, V.; Bleiker, S. J.; Stemme, G.; Niklaus, F. Scalable Manufacturing of Nanogaps. *Adv. Mater.* **2018,** *30*, 1801124.

81. Xia, Y.; Whitesides, G. M. Soft Lithography. *Angew. Chem. Int. Ed.* **1998,** *37*, 550-575.

82. Qin, D.; Xia, Y.; Whitesides, G. M. Soft Lithography for Micro- and Nanoscale Patterning. *Nat. Protoc.* **2010,** *5*, 491-502.

83. Jackman, R. J.; Wilbur, J. L.; Whitesides, G. M. Fabrication of Submicrometer Features on Curved Substrates by Microcontact Printing. *Science* **1995,** *269*, 664-666.

84. Kumar, A.; Whitesides, G. M. Features of Gold Having Micrometer to Centimeter Dimensions Can Be Formed Through A Combination of Stamping with An Elastomeric Stamp and An Alkanethiol ''Ink'' Followed by Chemical Etching. *Appl. Phys. Lett.* **1993,** *63*, 2002-2004.

85. Gassensmith, J. J.; Erne, P. M.; Paxton, W. F.; Frasconi, M.; Donakowski, M. D.; Stoddart, J. F. Patterned Assembly of Quantum Dots onto Surfaces Modified with Click Microcontact Printing. *Adv. Mater.* **2013,** *25*, 223-226.

86. Yousaf, M. N.; Houseman, B. T.; Mrksich, M. Using Electroactive Substrates to Pattern the Attachment of Two Different Cell Populations. *Proc. Natl. Acad. Sci. U. S. A.* **2001,** *98*, 5992-5996.

87. Tian, C.; Kim, H.; Sun, W.; Kim, Y.; Yin, P.; Liu, H. DNA Nanostructures-Mediated Molecular Imprinting Lithography. *ACS Nano* **2017,** *11*, 227-238.

88. Xia, Y.; McClelland, J. J.; Gupta, R.; Qin, D.; Zhao, X.-M.; Sohn, L. L.; Celotta, R. J.; Whitesides, G. M. Replica Molding Using Polymeric Materials: A Practical Step Toward Nanomanufacturing. *Adv. Mater.* **1997,** *9*, 147-149.

89. Zheng, Z.; Daniel, W. L.; Giam, L. R.; Huo, F.; Senesi, A. J.; Zheng, G.; Mirkin, C. A. Multiplexed Protein Arrays Enabled by Polymer Pen Lithography: Addressing the Inking Challenge. *Angew. Chem.* **2009,** *121*, 7762-7765.

90. Eichelsdoerfer, D. J.; Liao, X.; Cabezas, M. D.; Morris, W.; Radha, B.; Brown, K. A.; Giam, L. R.; Braunschweig, A. B.; Mirkin, C. A. Large-Area Molecular Patterning with Polymer Pen Lithography. *Nat. Protoc.* **2013,** *8*, 2548-2560.

91. Huo, F.; Zheng, Z.; Zheng, G.; Giam, L. R.; Zhang, H.; Mirkin, C. A. Polymer Pen Lithography. *Science* **2008,** *321*, 1658-1660.

92. Loo, Y.-L.; Willett, R. L.; Baldwin, K. W.; Rogers, J. A. Interfacial Chemistries for Nanoscale Transfer Printing. *J. Am. Chem. Soc.* **2002,** *124*, 7654-7655.

93. Jeon, S.; Menard, E.; Park, J. U.; Maria, J.; Meitl, M.; Zaumseil, J.; Rogers, J. A. Three-Dimensional Nanofabrication with Rubber Stamps and Conformable Photomasks. *Adv. Mater.* **2004,** *16*, 1369-1373.

94. Childs, W. R.; Nuzzo, R. G. Decal Transfer Microlithography: A New Soft-Lithographic Patterning Method. *J. Am. Chem. Soc.* **2002,** *124*, 13583–13596.

95. Geissler, M.; McLellan, J. M.; Xia, Y. Edge-Spreading Lithography: Use of Patterned Photoresist Structures to Direct the Spreading of Alkanethiols on Gold. *Nano Lett.* **2004,** *5*, 31-36.

96. McLellan, J. M.; Geissler, M.; Xia, Y. Edge Spreading Lithography and Its Application to the Fabrication of Mesoscopic Gold and Silver Rings. *J. Am. Chem. Soc.* **2004,** *126*, 10830-10831.

97. Xia, Y.; Zhao, X.-M.; Kim, E.; Whitesides, G. M. A Selective Etching Solution for Use with Patterned Self-Assembled Monolayers of Alkanethiolates on Gold. *Chem. Mater.* **2002,** *7*, 2332-2337.

98. Delamarche, E.; Schmid, H.; Bietsch, A.; Larsen, N. B.; Rothuizen, H.; Michel, B.; Biebuyck, H. Transport Mechanisms of Alkanethiols during Microcontact Printing on Gold. *J. Phys. Chem. B* **1998,** *102*, 3324-3334.

99. Belling, J. N.; Cheung, K. M.; Jackman, J. A.; Sut, T. N.; Allen, M.; Park, J. H.; Jonas, S. J.; Cho, N.-J.; Weiss, P. S. Lipid Bicelle Micropatterning Using Chemical Lift-Off Lithography. *ACS Appl. Mater. Interfaces* **2020,** *12*, 13447-13455.

100. Bernard, A.; Renault, J. P.; Michel, B.; Bosshard, H. R.; Delamarche, E. Microcontact Printing of Proteins. *Adv. Mater.* **2000,** *12*, 1067-1070.

101. Guo, L. J. Nanoimprint Lithography: Methods and Material Requirements. *Adv. Mater.* **2007,** *19*, 495-513.

102. Chou, S. Y. Nanoimprint lithography. *J. Vac. Sci. Technol. B* **1996,** *14*, 4129.

103. Chou, S. Y.; Krauss, P. R.; Renstrom, P. J. Imprint Lithography with 25-Nanometer Resolution. *Science* **1996,** *272*, 85-87.

104. Hanarp, P.; Käll, M.; Sutherland, D. S. Optical Properties of Short Range Ordered Arrays of Nanometer Gold Disks Prepared by Colloidal Lithography. *J. Phys. Chem. B* **2003,** *107*, 5768-5772.

105. Yang, S.-M.; Jang, S. G.; Choi, D.-G.; Kim, S.; Yu, H. K. Nanomachining by Colloidal Lithography. *Small* **2006,** *2*, 458-475.

106. Hulteen, J. C.; Van Duyne, R. P. Nanosphere Lithography: A Materials General Fabrication Process for Periodic Particle Array Surfaces. *J. Vac. Sci. Technol. A* **1995,** *13*, 1553-1558.

107. Jensen, T. R.; Malinsky, M. D.; Haynes, C. L.; Van Duyne, R. P. Nanosphere Lithography: Tunable Localized Surface Plasmon Resonance Spectra of Silver Nanoparticles. *J. Phys. Chem. B* **2000,** *104*, 10549-10556.

108. Hulteen, J. C.; Treichel, D. A.; Smith, M. T.; Duval, M. L.; Jensen, T. R.; Van Duyne, R. P. Nanosphere Lithography: Size-Tunable Silver Nanoparticle and Surface Cluster Arrays. *J. Phys. Chem. B* **1999,** *103*, 3854-3863.

109. Ren, J.; Segal-Peretz, T.; Zhou, C.; Craig, G. S. W.; Nealey, P. F. Three-Dimensional Superlattice Engineering with Block Copolymer Epitaxy. *Sci. Adv.* **2020,** *6*, eaaz0002.

110. Ruiz, R.; Kang, H.; Detcheverry, F. o. A.; Dobisz, E.; Kercher, D. S.; Albrecht, T. R.; de Pablo, J. J.; Nealey, P. F. Density Multiplication and Improved Lithography by Directed Block Copolymer Assembly. *Science* **2008,** *321*, 936-939.

111. Park, M.; Harrison, C.; Chaikin, P. M.; Register, R. A.; Adamson, D. H. Block Copolymer Lithography: Periodic Arrays of ~10^{11} Holes in 1 Square Centimeter. *Science* **1997,** *276*, 1401-1404.

112. Srinivasan, C.; Mullen, T. J.; Hohman, J. N.; Anderson, M. E.; Dameron, A. A.; Andrews, A. M.; Dickey, E. C.; Horn, M. W.; Weiss, P. S. Scanning Electron Microscopy of Nanoscale Chemical Patterns. *ACS Nano* **2007,** *1*, 191-201.

113. Dameron, A. A.; Hampton, J. R.; Smith, R. K.; Mullen, T. J.; Gillmor, S. D.; Weiss, P. S. Microdisplacement Printing. *Nano Lett.* **2005,** *5*, 1834-1837.

114. Shuster, M. J.; Vaish, A.; Cao, H. H.; Guttentag, A. I.; McManigle, J. E.; Gibb, A. L.; Martinez, M. M.; Nezarati, R. M.; Hinds, J. M.; Liao, W. S.; Weiss, P. S.; Andrews, A. M. Patterning Small-Molecule Biocapture Surfaces: Microcontact Insertion Printing *vs.* Photolithography. *Chem. Commun.* **2011,** *47*, 10641.

115. Mullen, T. J.; Srinivasan, C.; Hohman, J. N.; Gillmor, S. D.; Shuster, M. J.; Horn, M. W.; Andrews, A. M.; Weiss, P. S. Microcontact Insertion Printing. *Appl. Phys. Lett.* **2007,** *90*, 063114.

116. Liao, W. S.; Cheunkar, S.; Cao, H. H.; Bednar, H. R.; Weiss, P. S.; Andrews, A. M. Subtractive Patterning *via* Chemical Lift-Off Lithography. *Science* **2012,** *337*, 1517-1521.

117. Cao, H. H.; Nakatsuka, N.; Serino, A. C.; Liao, W.-S.; Cheunkar, S.; Yang, H.; Weiss, P. S.; Andrews, A. M. Controlled DNA Patterning by Chemical Lift-Off Lithography: Matrix Matters. *ACS Nano* **2015,** *9*, 11439-11454.

118. Andrews, A. M.; Liao, W.-S.; Weiss, P. S. Double-Sided Opportunities Using Chemical Lift-Off Lithography. *Acc. Chem. Res.* **2016,** *49*, 1449-1457.

119. Kim, J.; Rim, Y. S.; Chen, H.; Cao, H. H.; Nakatsuka, N.; Hinton, H. L.; Zhao, C.; Andrews, A. M.; Yang, Y.; Weiss, P. S. Fabrication of High-Performance Ultrathin In_2O_3 Film Field-Effect Transistors and Biosensors Using Chemical Lift-Off Lithography. *ACS Nano* **2015,** *9*, 4572-4582.

120. Cao, H. H.; Nakatsuka, N.; Liao, W.-S.; Serino, A. C.; Cheunkar, S.; Yang, H.; Weiss, P. S.; Andrews, A. M. Advancing Biocapture Substrates *via* Chemical Lift-Off Lithography. *Chem. Mater.* **2017,** *29*, 6829-6839.

121. Slaughter, L. S.; Cheung, K. M.; Kaappa, S.; Cao, H. H.; Yang, Q.; Young, T. D.; Serino, A. C.; Malola, S.; Olson, J. M.; Link, S.; Häkkinen, H.; Andrews, A. M.; Weiss, P. S. Patterning of Supported Gold Monolayers *via* Chemical Lift-Off Lithography. *Beilstein J. Nanotechnol.* **2017,** *8*, 2648-2661.

122. Zhao, C.; Xu, X.; Yang, Q.; Man, T.; Jonas, S. J.; Schwartz, J. J.; Andrews, A. M.; Weiss, P. S. Self-Collapse Lithography. *Nano Lett.* **2017,** *17*, 5035-5042.

123. Xu, X.; Yang, Q.; Cheung, K. M.; Zhao, C.; Wattanatorn, N.; Belling, J. N.; Abendroth, J. M.; Slaughter, L. S.; Mirkin, C. A.; Andrews, A. M.; Weiss, P. S. Polymer-Pen Chemical Lift-Off Lithography. *Nano Lett.* **2017,** *17*, 3302-3311.

124. Cheung, K. M.; Stemer, D. M.; Zhao, C.; Young, T. D.; Belling, J. N.; Andrews, A. M.; Weiss, P. S. Chemical Lift-Off Lithography of Metal and Semiconductor Surfaces. *ACS Mater. Lett.* **2019,** *2*, 76–83.

125. Chiang, N.; Scarabelli, L.; Vinnacombe-Willson, G. A.; Pérez, L. A.; Dore, C.; Mihi, A.; Jonas, S. J.; Weiss, P. S. Large-Scale Soft-Lithographic Patterning of Plasmonic Nanoparticles. *ACS Mater. Lett.* **2021,** *3*, 282-289.

126. Zhao, C.; Xu, X.; Bae, S.-H.; Yang, Q.; Liu, W.; Belling, J. N.; Cheung, K. M.; Rim, Y. S.; Yang, Y.; Andrews, A. M.; Weiss, P. S. Large-Area, Ultrathin Metal-Oxide Semiconductor Nanoribbon Arrays Fabricated by Chemical Lift-Off Lithography. *Nano Lett.* **2018,** *18*, 5590-5595.

127. Zhao, C.; Liu, Q.; Cheung, K. M.; Liu, W.; Yang, Q.; Xu, X.; Man, T.; Weiss, P. S.; Zhou, C.; Andrews, A. M. Narrower Nanoribbon Biosensors Fabricated by Chemical Lift-off Lithography Show Higher Sensitivity. *ACS Nano* **2020,** *15*, 904-915.

128. Zhao, C.; Man, T.; Xu, X.; Yang, Q.; Liu, W.; Jonas, S. J.; Teitell, M. A.; Chiou, P.-Y.; Weiss, P. S. Photothermal Intracellular Delivery Using Gold Nanodisk Arrays. *ACS Mater. Lett.* **2020,** *2*, 1475–1483.

129. Blodgett, K. B. Monomolecular Films of Fatty Acids on Glass. *J. Am. Chem. Soc.* **1934,** *56*, 495-495.

130. Hsu, C.-M.; Connor, S. T.; Tang, M. X.; Cui, Y. Wafer-Scale Silicon Nanopillars and Nanocones by Langmuir–Blodgett Assembly and Etching. *Appl. Phys. Lett.* **2008,** *93*, 133109.

131. Cossio, G.; Yu, E. T. Zeta Potential Dependent Self-Assembly for Very Large Area Nanosphere Lithography. *Nano Lett.* **2020,** *20*, 5090-5096.

132. Cheung, C. L.; Nikolić, R. J.; Reinhardt, C. E.; Wang, T. F. Fabrication of Nanopillars by Nanosphere Lithography. *Nanotechnology* **2006,** *17*, 1339-1343.

133. Madaria, A. R.; Yao, M.; Chi, C.; Huang, N.; Lin, C.; Li, R.; Povinelli, M. L.; Dapkus, P. D.; Zhou, C. Toward Optimized Light Utilization in Nanowire Arrays Using Scalable Nanosphere Lithography and Selected Area Growth. *Nano Lett.* **2012,** *12*, 2839-2845.

134. Xu, X.; Yang, Q.; Wattanatorn, N.; Zhao, C.; Chiang, N.; Jonas, S. J.; Weiss, P. S. Multiple-Patterning Nanosphere Lithography for Fabricating Periodic Three-Dimensional Hierarchical Nanostructures. *ACS Nano* **2017,** *11*, 10384-10391.

135. Xu, X.; Liu, W.; Ji, Z.; Hao, D.; Yan, W.; Ye, Z.; Hu, Y.; Fang, M.; Wang, C.; Ma, L.; Huang, J.; Xu, X.; Weiss, P. S. Large-Area Periodic Organic–Inorganic Hybrid Perovskite Nanopyramid Arrays for High-Performance Photodetector and Image Sensor Applications. *ACS Mater. Lett.* **2021,** *3*, 1189-1196.

136. Liu, S.; Al-Shadeedi, A.; Kaphle, V.; Keum, C.-M.; Lüssem, B. Patterning Organic Transistors by Dry-Etching: The Double Layer Lithography. *Org. Electron.* **2017,** *45*, 124-130.

137. Ghaida, R. S.; Torres, G.; Gupta, P. Single-Mask Double-Patterning Lithography for Reduced Cost and Improved Overlay Control. *IEEE Trans. Semicond. Manuf.* **2011,** *24*, 93-103.

138. Moon, J. H.; Yang, S.-M.; Pine, D. J.; Chang, W.-S. Multiple-Exposure Holographic Lithography with Phase Shift. *Appl. Phys. Lett.* **2004,** *85*, 4184-4186.

139. Lin, B. J.; Terasawa, T.; Hasegawa, N.; Kurosaki, T.; Tanaka, T. 0.3-micron Optical Lithography Using A Phase-Shifting Mask. *Proc. SPIE* **1989,** *1088*, 25–33.

140. Levenson, M. D.; Viswanathan, N. S.; Simpson, R. A. Improving Resolution in Photolithography with A Phase-Shifting Mask. *IEEE Trans. Electron Devices* **1982,** *29*, 1828-1836.

141. Sugawara, M.; Chiba, A.; Nishiyama, I. Effect of Incident Angle of Off-Axis Illumination on Pattern Printability in Extreme Ultraviolet Lithography. *J. Vac. Sci. Technol. B* **2003,** *21*, 2701.

142. Garofalo, J. Mask Assisted Off-Axis Illumination Technique for Random Logic. *J. Vac. Sci. Technol. B* **1993,** *11*, 2651.

143. Hoefflinger, B. *ITRS: The International Technology Roadmap for Semiconductors*. **2011**, 161-174.

144. Okada, M.; Miyake, H.; Iyoshi, S.; Yukawa, T.; Katase, T.; Tone, K.; Haruyama, Y.; Matsui, S. Double Patterning in Nanoimprint Lithography. *Microelectron. Eng.* **2013,** *112*, 139-142.

145. Liu, W.; Wang, J.; Xu, X.; Zhao, C.; Xu, X.; Weiss, P. S. Single-Step Dual-Layer Photolithography for Tunable and Scalable Nanopatterning. *ACS Nano* **2021,** *15*, 12180-12188.

Chapter 2

Single-Step Dual Layer Photolithography for Tunable and Scalable Nanopatterning

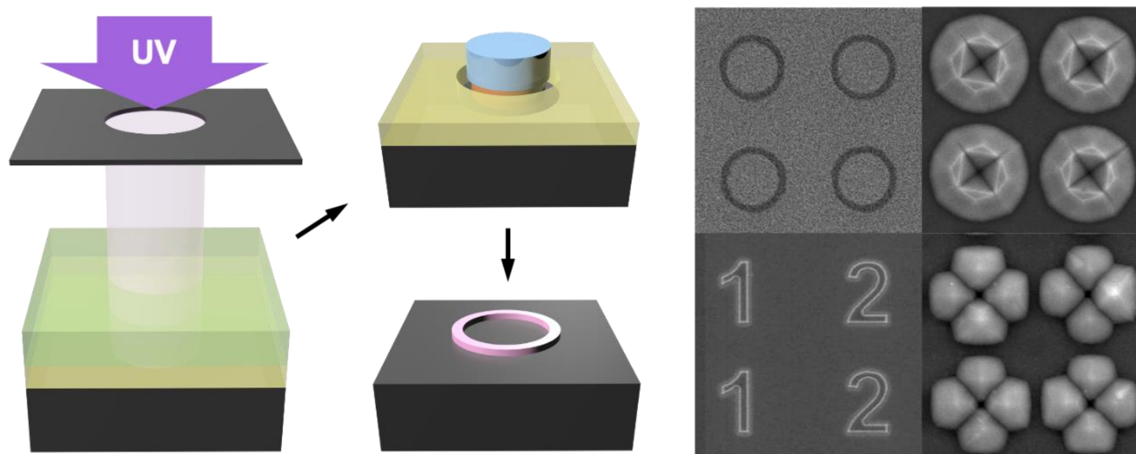

The information in this chapter is reprinted with permission from

ACS Nano **2021**, *15*, 12180-12188. Copyright (2021) American Chemical Society

Authors: **Liu, W.**; Wang, J.; Xu, X.; Zhao, C.; Xu, X.; Weiss, P. S.

2.1 Abstract

Conventional photolithography, due to its scalability, robustness, and straightforward processes, has been widely applied to micro- and nanostructure manufacturing in electronics, optics, and biology. However, optical diffraction limits the ultimate resolution of conventional photolithography, which hinders its potential in nanoscale patterning for broader applications. Here, we introduce a derivative of conventional photolithography for nanoscale patterning called dual-layer photolithography (DLPL), which is based on controlled exposure and development of overlapping positive and negative photoresists. In a typical experiment, substrates are sequentially coated by two layers of photoresists (both positive and negative). Then, we purposefully control the exposure time to generate slightly larger features in the positive photoresist than those in the negative photoresist. After development, their overlapping areas become the final features, which outline the original features. We demonstrate linewidths down to 300 nm here, which can be readily improved with more precise control. By adjusting the lithography parameters and material deposition, the feature sizes, shapes (*e.g.*, rings, numbers, letters), linewidths (300 to 900 nm), and materials (*e.g.*, SiO_2, Cr, and Ag) of these features can be independently controlled. Combined with anisotropic etching, more complex three-dimensional nanostructures can be fabricated as well, as we demonstrate here with Si. We further fabricate photodetectors as an example application to show that these nanostructures fabricated by DLPL can be used to promote light-trapping $MAPbI_3$ perovskite films to achieve good photoelectric properties. This strategy is not limited to ultraviolet photolithography and may also be incorporated into other energetic beam-based lithographic approaches, including deep and extreme ultraviolet photolithographies and electron beam lithography, to enhance their resolution.

2.2 Introduction

Nanolithography is a critical step in the fabrication processes of miniaturized electronic[1–5] and optical[6–9] devices. Conventional photolithography, using ultraviolet (UV) light to transfer features from photomasks to substrates, has been widely applied to micro- and nanoelectronics manufacturing due to its high throughput and high pattern fidelity. However, its feature resolution is limited by light diffraction and processing parameters. With recent advances in nanoscience and nanotechnology, nanometer-scale resolution is increasingly needed for emerging applications.[10,11] For example, microfluidic chips with submicron structures have been developed for advanced biomedical applications (*e.g.*, bioanalysis, cell regulation, drug delivery).[12–14] Additionally, submicron- and nanoscale structures can be integrated into optic and electric devices (*e.g.*, optoelectronic circuits, displays, plasmonic sensors) for improved performance, sensitivity, and efficiency.[15–17]

To overcome the resolution limit in conventional photolithography, advanced lithography techniques have been developed with advanced light sources with smaller wavelengths, including deep UV (DUV) and extreme UV (EUV) photolithography,[18,19] electron-beam lithography (EBL),[20–22] and focused ion beam lithography (FIB).[23–25] Although these advanced techniques have been widely used in nanoelectronics, high equipment costs (DUV, EUV) or time-consuming serial writing processes (EBL, FIB) have greatly limited their availability and practicality for laboratories in universities, research institutions, and startups,[26] while the development of low-cost and high-throughput nanolithography approaches remains a challenge.

To address this challenge, various unconventional lithographic approaches and strategies have been developed, such as nanoimprint lithography,[27–29] soft lithography,[30–32] nanosphere lithography,[33,34] molecular ruler lithography,[35] and edge spreading lithography.[36,37] For example,

large-area metal nanoring arrays can be fabricated *via* a strategy that combines colloidal lithography and nanoscale electrodeposition.[38] Moreover, by using the monolayers of self-assembled polymeric nanospheres as templates, multiple-patterning nanosphere lithography can be used to fabricate wafer-scale periodic hierarchical nanostructures.[39] Although these lithographic methods reach high resolution with relatively low cost, the pattern quality and fidelity are strongly affected by the quality of the self-assembled templates and/or the quality of the stamps.

Meanwhile, efforts also have been made to push the resolution of conventional photolithography down to the nanometer scale through the optimization of the lithography parameters and processes. For example, immersion photolithography,[40] double-patterning photolithography,[41,42] and beam-pen lithography[43] have been developed to "overcome" the resolution limit. Specifically, double-patterning lithography can generate patterns with sizes several times smaller than the original features in photomasks through a subtraction process between two sequential patterns. However, its reproducibility relies on the alignment between the photomask and the patterns produced by each photolithographic step. Such processes require high-cost equipment for mask alignment. As a result, double patterning photolithography is limited due to the trade-off between increasing yield and decreasing alignment error.

In this work, we describe and demonstrate an alternative method to double-patterning photolithography, namely, dual-layer photolithography (DLPL). Without a mask alignment process or using high-refractive-index media, we realized tunable submicron patterning at high throughput and low cost. It is based on the controlled exposure and development of overlapping positive and negative photoresists to create hollow "outline-like" patterns. Note that, instead of creating undercuts to facilitate the lift-off process as in other reported bilayer resist strategies,[44–47] DLPL is used here to scale down the feature size. The size, line width, material, and shape of the

features can all be independently controlled in DLPL. Combined with anisotropic etching of Si, complex three-dimensional (3D) structures can and have been produced.[48,49] We demonstrate the fabrication of photodetectors as an example application to show that nanostructures fabricated by DLPL can be used to promote light trapping in $MAPbI_3$ perovskite films to achieve good photoconductive properties.[50–52]

2.3 Materials and Methods

Materials. Positive photoresist BCI 3511 was purchased from Suzhou Research Materials Microtech Co., Ltd. Negative photoresist 9i was purchased from Suntific Materials (Weifang, China), Ltd. Methylammonium lead iodide ($MAPbI_3$) was purchased from Xi'an Polymer Light Technology Corp. Anhydrous potassium hydroxide (KOH) and dimethylsulphoxide (DMSO) were purchased from Sinopharm Chemical Reagent Co., Ltd. γ-butyrolactone (GBL) was purchased from Shanghai Aladdin Biochemical Technology Co., Ltd. Magnetron sputtering material SiO_2 (99.99%) and evaporation materials, including chromium (99.99%), silver (99.99%), and copper (99.99%), were purchased from ZhongNuo Advanced Material (Beijing, China) Technology Co., Ltd.

Characterization. The morphologies of the dual-layer photolithography (DLPL)-fabricated nanorings, KOH-etched 3D Si structures, and surface-coated $MAPbI_3$ thin film were measured by scanning electron microscopy (SEM, JEOL JSM-6060LA). The photoresponsivity of $MAPbI_3$-based photodetectors was measured using a source meter (Keithley 2602B) on a probe-station.

Fabrication of SiO_2 Nanorings. The SiO_2 nanorings were fabricated with DLPL. First, positive photoresist BCI 3511 was spin-coated on Si substrates at 2500 rpm followed by a 40 s soft bake. Second, negative photoresist 9i was spin-coated on the positive photoresist layer at 4000 rpm followed by a 60 s soft bake. With a mercury-xenon lamp (3500 mW/cm^2, 365 nm, Hamamatsu Corporation, JP), the dual-layer photoresists were exposed a single time for 30 s, followed by 45 s postbaking. The dual-layer photoresists were developed for 10 and 5 s in a top-down manner, and hollow nanorings were generated. Next, a SiO_2 film was deposited on the substrates *via* a DM300 magnetron sputtering System (Hefei Jusheng Vacuum Technology Inc.) at 1 nm/min. The remaining photoresists were removed by mild sonication in acetone, while the SiO_2 film on top of the photoresist was lifted off. As a result, SiO_2 nanorings were fabricated on the Si substrate.

Fabrication of Chromium (Cr) or Silver (Ag) Nanorings. The fabrication procedure followed the same fabrication scheme as SiO_2 nanorings by dual-layer photolithography except the SiO_2 deposition was changed to metal deposition *via* a DM500 thermal evaporator (Hefei Jusheng Vacuum Technology Inc.). Both Cr and Ag films were deposited at a rate of ~0.5 Å/s.

Fabrication of Complex Si Nanostructures. The complex Si nanostructures were fabricated by anisotropic etching with SiO_2 nanorings as the etching mask and 30 wt % KOH solution as the etchant. The substrate was etched at 70 °C with moderate stirring to remove the bubbles on the surface. The addition of isopropyl alcohol mediates the surface roughness of Si in wet etching. The morphology changes of the complex Si nanostructures were monitored *via* scanning electron microscopy (**Figure 2.4d-g**) and divided into four etching stages: 2, 3, 5, and 7 min.

Fabrication of $MAPbI_3$-Based Photodetectors. The substrates with desired Si complex nanostructures were deposited with ~300 nm SiO_2 at a rate of 1 Å/s *via* thermal evaporation. The perovskite precursor solution (1 M) was prepared by dissolving $MAPbI_3$ powder in a mixture of GBL and DMSO with a ratio of 7:3 and stirred for 2 h at 60 °C to ensure that the perovskite powder was fully dissolved. The mixture was filtered to remove any insoluble impurities. Then, 50 μL of the precursor solution was spin-coated on the SiO_2/Si substrate with a spin speed of 2500 rpm in the glove box under an Ar flow. The substrate was annealed at 100 °C for 10 min to form the $MAPbI_3$ film. Finally, the copper film was deposited on the $MAPbI_3$ film at a rate of 0.5 Å/s with a shadow mask to fabricate the copper electrode.

2.4. Results and Discussions

A typical process of dual-layer photolithography for fabricating SiO_2 nanorings is illustrated in **Figure 2.1**. First, one layer of positive photoresist (in yellow) and one layer of negative photoresist (in green) were sequentially spin-coated with controlled thicknesses and soft-baked on piranha-cleaned Si substrates (piranha solution is a mixture of 3:1 sulfuric acid and 30% hydrogen peroxide. *Warning: piranha solution reacts strongly with organic compounds and should be handled with caution; do not store in closed containers*). A single controlled UV exposure was applied using a photomask patterned with 5 μm hole arrays (**Figure 2.1a**). With the same amount of UV exposure, photoresponsivity variation resulted in slightly larger features on the positive photoresist than on the negative photoresist (**Figure 2.1b**). After removing the unexposed negative photoresist, circle-shaped features (in blue) were patterned on top of the positive photoresist layer (**Figure 2.1c**). The remaining negative photoresist hampered the complete removal of exposed positive photoresist (in orange) underneath, resulting in a dual-layer structure surrounded by hollow nanorings (**Figure 2.1d**). Next, a thin film of SiO_2 (~30 nm) was

deposited on the substrate *via* magnetron sputtering, resulting in the exposed Si nanoring arrays covered by SiO_2 film (**Figure 2.1e**). As the remaining SiO_2 thin film on top was lifted off with the photoresist removal, SiO_2 nanoring arrays were fabricated on Si substrates (**Figure 2.1f**).

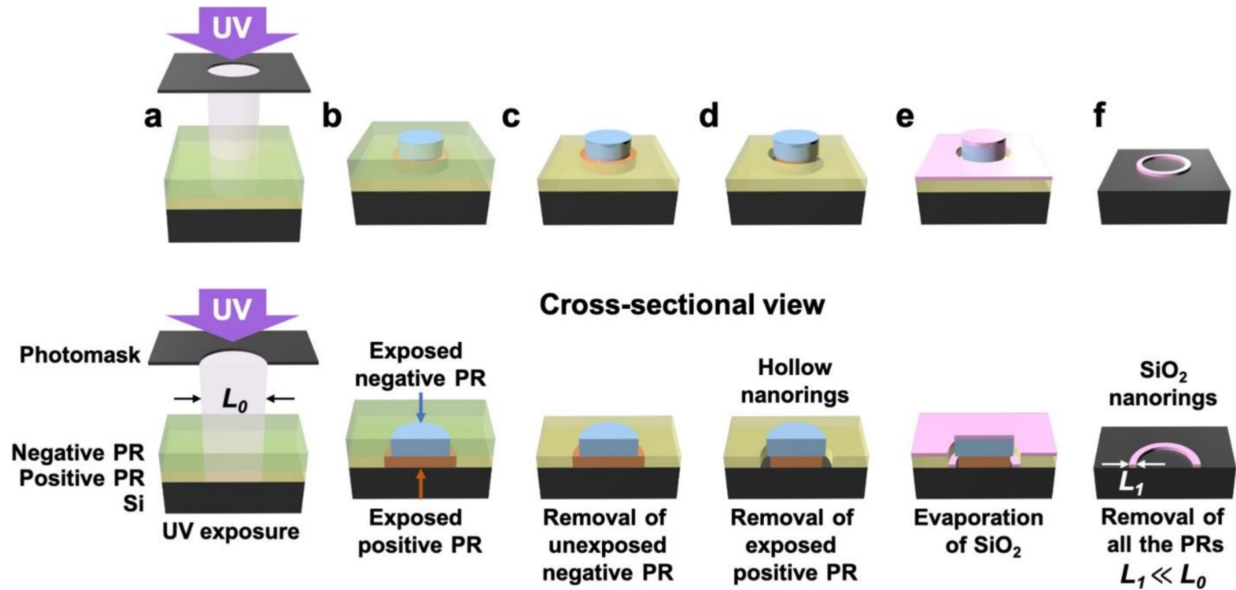

Figure 2.1. Fabrication schematics of SiO_2 nanorings by single-step dual-layer photolithography (DLPL). Top, overall process; bottom, cross-sectional view. (a) One-time ultraviolet (UV) exposure on dual-layer photoresists. (b) Postbaking after removing photomask. (c) First development of negative photoresist layer. (d) Second development of positive photoresist. (e) Deposition of SiO_2 thin film *via* magnetron sputtering. (f) Removal of dual-layer photoresists and generation of SiO_2 nanorings. PR: photoresist.

To obtain the necessary photolithography parameters suitable for DLPL, which were not listed in the datasheet, we studied the relationship between exposure time (t) and feature size (d) of each photoresist *via* designed single-layer photolithography (SLPL) using a Cr photomask with 5 μm hole arrays. While exposure time was varied, other experimental parameters (*e.g.*, UV light intensity, soft-baking time, development time) were held fixed. Theoretically, the feature sizes

should increase with the added exposure time or exposure energy.[53] As a result, features generated by both photoresists shared similar size-increasing patterns (see **Figure 2.2a,b**). Overall, as the exposure time increased from 18 to 38 s, the feature size of the positive photoresist increased by 1.8 μm (3.9–5.7 μm), whereas the feature size of the negative photoresist increased by 0.7 μm (4.2–4.9 μm) (detailed measurements are provided in **Table S2.1** of the Supporting Information). The higher feature size increase rate indicated a higher photoresponsivity of the positive photoresist than that of the negative photoresist.

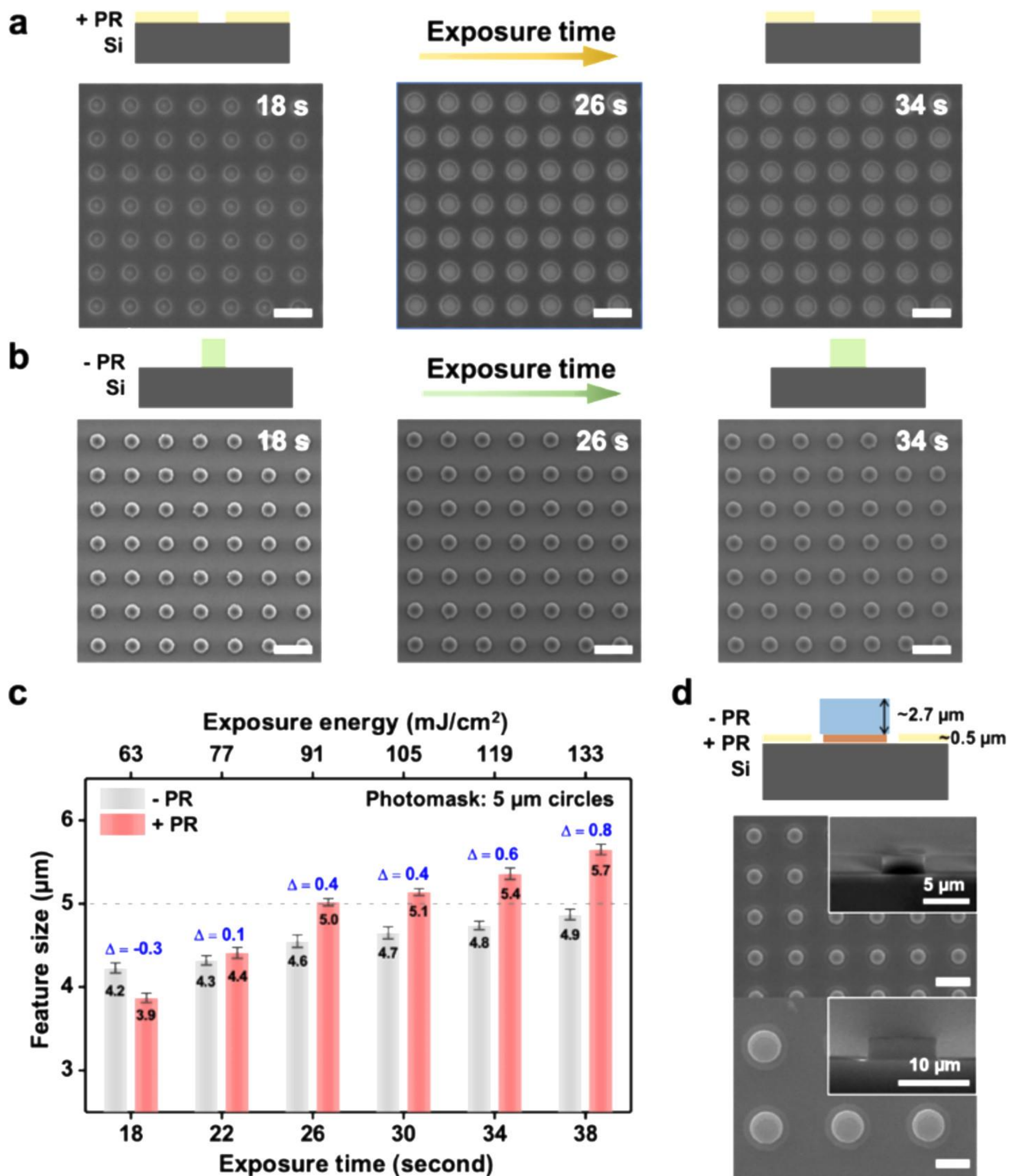

Figure 2.2. Systematic study of the pattern size dependence on the exposure time (or exposure energy) in dual-layer photolithography (DLPL). Scanning electron microscopy (SEM) images of single-layer photolithography for (a) positive photoresist and (b) negative photoresist with exposure times of 18, 26, and 34 s. Scale bar: 5 µm. (c) Histogram of the size

changes of features on positive and negative photoresists in the single-layer photolithography (SLPL) as the exposure time or corresponding exposure energy increased. (d) SEM top and side view images of the dual-layer structure after the development in DLPL with 30 s of exposure and the photomask feature sizes of 5 and 10 μm. Scale bar: 10 μm. PR: photoresist.

To understand the dynamic changes in feature size, a series of SLPL experiments were conducted in parallel with the exposure times set at 18, 22, 26, 30, 34, and 38 s (see **Figure 2.2c**; note the corresponding exposure energies shown). Note that for each condition, more than 10 samples were prepared and measured, which showed good reproducibility in feature sizes. The feature sizes of both photoresists with the same amount of exposure (d_{+PR} and d_{-PR}) were provided in pairs. The size differences ($\Delta = d_{+PR} - d_{-PR}$) were calculated to estimate the theoretical width (w) of hollow nanorings generated by DLPL under the same conditions. With 18 s of exposure, the features on the positive photoresist were smaller than those on the negative photoresist ($\Delta = -0.3$ μm). Due to the higher responsivity of the positive photoresist, the size difference narrowed as the applied exposure time or exposure energy increased. At ~21 s, the feature sizes of both photoresists were equal. At longer times (>21 s), the features on the positive photoresist became larger than those on the negative photoresist ($\Delta > 0$ μm). We thus predicted that a flip of the size difference would result in the formation of hollow nanorings in DLPL and that the theoretical ring width would increase with increasing time (t = 21–26 s). However, this increase stopped as the exposure time rose from 26 to 30 s, and the size difference remained relatively constant ($\Delta = 0.4$ μm). Within this range, the minimal size change (~0.1 μm) of both features made the size independent of the exposure time; varying the exposure time only resulted in subtle changes in the size difference. As the exposure time was increased further (t > 30 s), the size difference increased

and reached 0.8 μm (t = 38 s), which indicated that both photoresists experienced overexposure within the time range 30–38 s.

On the basis of the results of SLPL experiments, an optimal exposure time for DLPL was determined. In DLPL, since energy loss takes place when UV light penetrates the overlying negative photoresist,[53] the exposure energy received by the positive photoresist underneath is smaller compared to that of SLPL. As a result, the features generated by a positive photoresist in DLPL are equivalent to those generated with lower intensities or shorter exposure times in SLPL. Therefore, the widths of hollow nanorings obtained from DLPL are smaller than the corresponding estimates from SLPL. Although 22 s exposures produced the smallest size differences (Δ = 0.1 μm) in SLPL, hollow nanorings with widths of 0.1 μm were less likely to be realized in DLPL. According to the measured histogram (**Figure 2.2c**), both features demonstrated size uniformity as the exposure time increased from 26 to 30 s. Therefore, to minimize the size variations between SLPL and DLPL, a 30 s exposure was applied to the following DLPL experiments.

After development, the remaining photoresists formed a dual-layer 3D "cake" structure (**Figure 2.2d**). The negative photoresist layer had a thickness of ~2.7 μm, whereas the positive photoresist layer had a thickness of ~0.5 μm. As shown in **Figure 2.2d**, dual-layer structures in different sizes (5 and 10 μm) were generated using the photomasks with the corresponding feature sizes. In the top view images, the central circles corresponded to the negative photoresist, while the outer rings corresponded to the hollow nanorings. The removal of the dual-layer structure was confirmed by the topographic differences shown in the side view images. The bright spots at each side of the "cake" structure were lower than the positive photoresist layer, which indicated that the Si surface was exposed.

We tested the versatility of DLPL by modifying the photolithography parameters and the material deposition processes. The graphic changes were visualized by depositing SiO_2 or metals into the hollow "outline-like" patterns (*e.g.*, nanorings). Since the size of the hollow features depends strongly on the original features on the photomask, different feature sizes (*i.e.*, 10 and 5 μm) could be realized using different photomasks (**Figure 2.3a,b**). In addition to feature size, the line widths of the hollow patterns could be independently controlled. On the basis of the results from SLPL, the theoretical width was proportional to the exposure time in the overexposure region ($t \geq 30$ s). As a result, SiO_2 nanorings with different widths (*i.e.*, 300 and 800 nm) were fabricated with different exposure times (*i.e.*, 30 and 38 s, respectively) (**Figure 2.3b,c**).

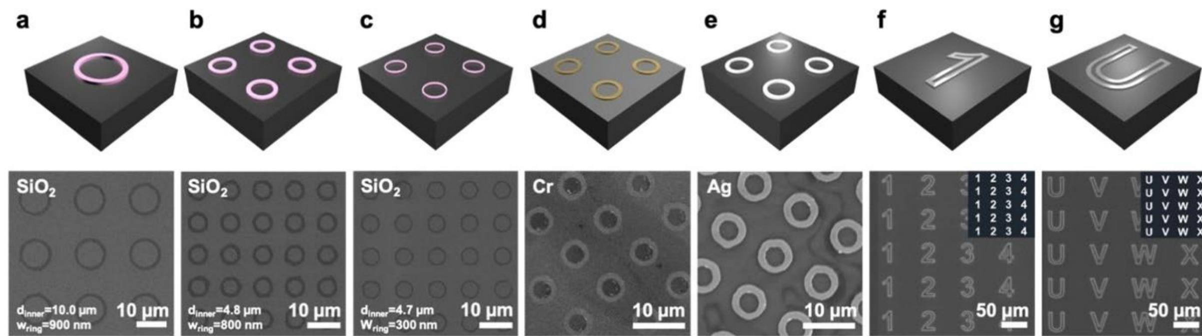

Figure 2.3. Scanning electron microscopy images of the nanopatterns fabricated by dual-layer photolithography with independent control of pattern parameters (*i.e.*, size, line width, material, and shape): (a) SiO_2 nanorings with inner diameter of 10 μm and width of 900 nm; (b) SiO_2 nanorings with inner diameter of 4.8 μm and width of 800 nm; (c) SiO_2 nanorings with inner diameter of 4.7 μm and width of 300 nm; (d) Cr nanorings; (e) Ag nanorings; (f) metal patterns in number-shaped outlines with a line width of ~10 μm; (g) metal patterns in letter-shaped outlines with a line width of ~10 μm. Original AutoCAD photomask designs of number and letter patterns are provided in (f) and (g).

Furthermore, combined with material deposition, DLPL was used to fabricate nanostructures of different materials. Besides SiO_2 nanorings, Cr nanorings were fabricated *via* thermal evaporation (**Figure 2.3d**). Ag nanorings were fabricated similarly with predeposited Cr film (~5 nm) as an adhesive layer (**Figure 2.3e**). As shown, the nanorings fabricated with different materials were consistent in shape and size, which could be further applied as etching masks for reactive ion etching[54,55] and metal-assisted chemical etching.[56,57] Notably, the widths of both Cr and Ag nanorings appeared larger than those of SiO_2 nanorings. We attribute these differences to the effects of diffusion in the thermal evaporation of metals, as compared to the magnetron sputtering of SiO_2.

To reduce the effects of diffusion, we changed the order of deposition to fabricated hollow nanorings *via* a modified DLPL procedure. In this modified fabrication scheme, a Cr film (~30 nm) was thermally deposited on the Si substrate before photoresists were coated. After the development processes, the exposed Cr surface inside the hollow nanorings was wet-etched (etchant: 15 wt % diammonium cerium(IV) nitrate and 10 wt % hydrochloric acid in deionized water). After the removal of the photoresists, hollow nanorings were patterned on the Cr layer (**Figure S2.1**). The ring width was independently controlled by adjusting the etching time. This modified procedure provided a strategy to pattern hollow features on the surface of other materials besides Si, which could be further explored to assist in the further fabrication of complex structures.

Not limited to nanorings, the shapes of hollow features generated by DLPL were also tunable by using photomasks patterned with various features. To demonstrate the versatility of feature styles, photomasks patterned with numbers and letters with line widths of ~10 μm were used. As a result, submicrometer metal patterns in the shapes of numbers and letter outlines were

fabricated with line widths of ~1 μm (**Figure 2.3f,g**). This scaling down (1:10) of various features demonstrated the effectiveness of DLPL in improving feature resolution with good pattern fidelity. Combined with the results shown above, we have achieved independent control of the feature size, line width, material, and shape in DLPL, indicating the adaptability and versatility of this nanopatterning method.

After 5 μm SiO_2 nanorings were fabricated *via* DLPL, we demonstrated its application potential as an etching mask to assist Si nanofabrication. Since SiO_2 is etched much more slowly than Si under specific etching conditions (30 wt % KOH, 70 °C), the functionality of SiO_2 nanorings was investigated *via* KOH anisotropic etching of Si(100) substrates (**Figure 2.4**). As illustrated in **Figure 2.4a**, the etching process started on the surface of Si(100), which is also the {100} plane, and the {111} planes were revealed on the edge of the area protected by the SiO_2 nanoring (in violet). The lower atomic lattice density and more dangling bonds of {100} planes compared to {111} planes led to higher etching rates along the [100] direction in Si(100).[58] Subsequently, the {100} plane was etched down faster than the {111} plane as the etching time increased (**Figure 2.4b**). Once the anisotropic etching reached completion, the {100} plane became a point where the four {111} planes intersected (**Figure 2.4c**), resulting in an inverted pyramid inscribed in the SiO_2 nanoring.[59]

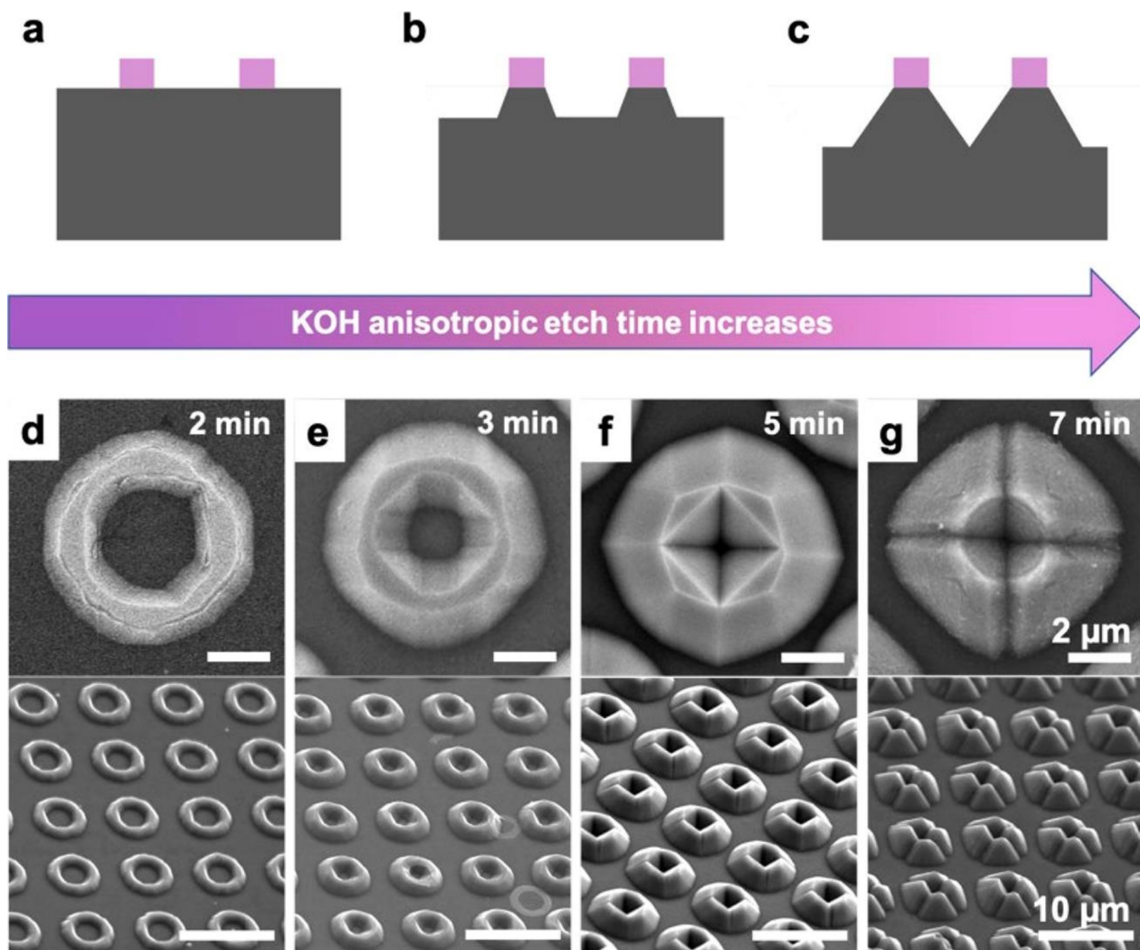

Figure 2.4. (a–c) Time-driven KOH anisotropic etching process of Si(100) substrates with a dual-layer-photolithography-fabricated SiO_2 nanoring as the etching mask. Scanning electron microscopy images of morphologic transition of Si complex three-dimensional (3D) nanostructures with etching times of (d) 2, (e) 3, (f) 5, and (g) 7 min. Top view of a single Si complex 3D nanostructure, and 45° tilt view of complex 3D nanostructure arrays.

When the substrate was immersed into the KOH etching solution, the etching processes took place both inside and outside the SiO_2 nanoring. Although the {100} plane was the primary etching plane, other planes were also etched in the anisotropic etching process. As a result, the morphology of fabricated 3D nanostructures had a dynamic transition as the etching time

increased. As shown in the SEM images, this time-driven transition was analyzed in four stages with etching durations of 2, 3, 5, and 7 min (**Figure 2.4d–g**)

At stage one (*t* = 2 min), since the etching rate varied on each plane, the shape of the inside mask window changed from circles to octagons. Meanwhile, the outside mask windows maintained the circle shape (**Figure 2.4d**). The planes with higher etching rates were removed, while the remaining planes defined the boundary of the mask window. The Si{100} planes were etched down to generate 3D nanostructures, resulting in isolated spaces inside the SiO_2 nanorings.

At stage two (*t* = 3 min), four sides on the octagon mask window were reduced while the other four were extended (**Figure 2.4e**). The decreased size of the {100} planes effectively resulted in the growth of the 3D nanostructure and the increased sizes of the exposed {111} planes. After removing the SiO_2 nanoring, the protected Si was smaller in width that at the previous stage, which indicated the growth of the undercut regions as the {111} planes were further etched.

At stage three (*t* = 5 min), as the four shorter sides of the octagon mask disappeared, the longer sides formed a square-shaped mask. Since the inside Si{100} plane was etched down to a point, the {111} planes became the principal etching planes. Inverted pyramids were formed with measured sizes of ~3 µm (**Figure 2.4f**). The presence of the undercut indicated that the inverted pyramid circumscribed the initial circle shape inside the mask window. After removing the SiO_2 nanoring, a connection at each corner of the inverted pyramid was observed. From the 45° tilt view, the inverted pyramid had a specific loading capacity isolated from the outside space due to the mask window defined (**Figure S2.2**). While anisotropic etching inside the SiO_2 nanoring reached completion, the outside etching process continued due to a larger {100} plane. As the {111} planes grew larger on the outside sidewall, the outside mask window started to transit from

a polygon to an octagon. Notably, the diagonals of the mask windows on both sides were perfectly aligned. Therefore, we anticipated that, with further etching, the connection of the top triangles would break, resulting in the loss of isolation.

At stage four (t = 7 min), the {111} planes on the outside sidewalls became the principal etching planes, which merged to form upright pyramid structures (**Figure 2.4g**). As expected, the {111} planes of both upright and inverted pyramids were further etched, resulting in valley-shaped openings along the diagonals. While the etching process of the inside {100} plane was terminated, the outside {111} planes continued, resulting in greater depths of the inverted pyramids. On the basis of the morphological transition of the etched nanostructures, we expect that the openings along the diagonals would grow larger as the etching time increased. Finally, the single Si complex nanostructure would break into four smaller nanopyramids with identical shapes and sizes. As a result, the isolated space inside the inverted pyramid no longer existed.

As shown in the top-view SEM images (**Figure S2.3a,b**), wafer-scale 3D Si complex structures at stage one (t = 2 min) and stage three (t = 5 min) were fabricated with excellent consistency and uniformity in shape and morphology. After 7 min of KOH etching, the SiO_2 nanoring on the top of the Si complex structure maintained the primary structure as fabricated by DLPL (**Figure S2.4**). Most SiO_2 nanorings were not removed even though the Si undercut was significant. The fabrication of a series of Si 3D nanostructures *via* KOH anisotropic etching demonstrated the potential of DLPL-fabricated SiO_2 nanorings in nanofabrication applications. We expect that DLPL could be used to fabricate more sophisticated patterns and structures.

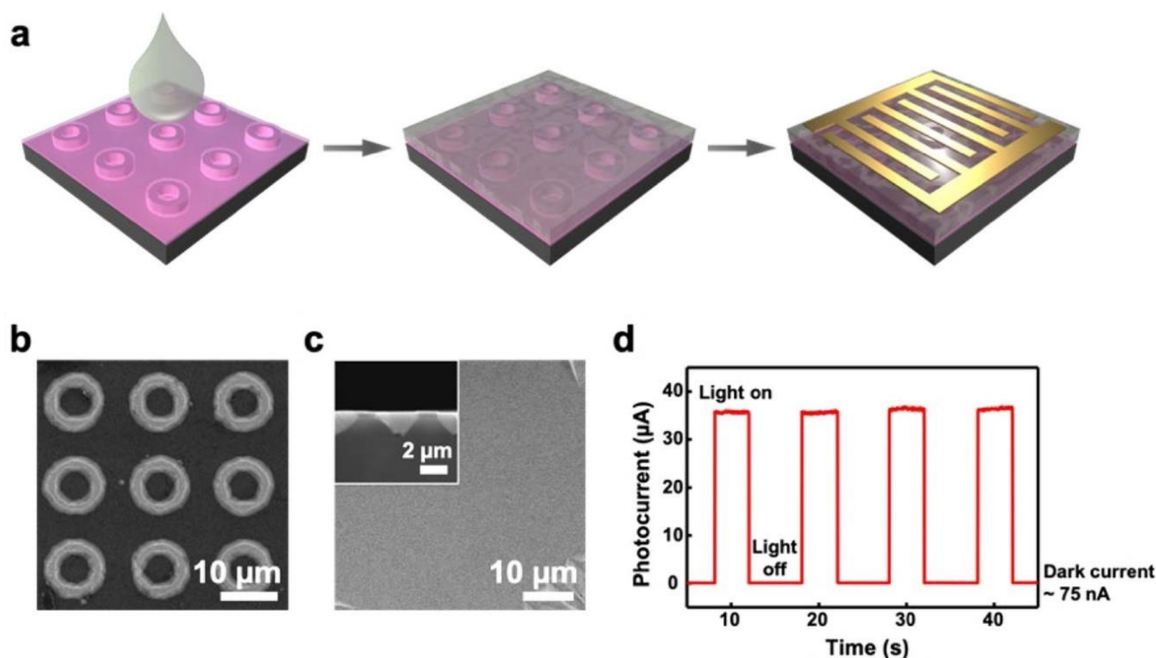

Figure 2.5. (a) Schematics of the $MAPbI_3$ film coating and interdigital electrode fabrication processes for the 2 min KOH-etched Si/SiO_2 three-dimensional (3D) complex nanostructures. (b) Scanning electron microscopy (SEM) image of the 2 min KOH-etched Si complex 3D nanostructures coated with SiO_2 for isolation. (c) Top view and side view SEM images of the $MAPbI_3$ film coated on the Si/SiO_2 substrate. (d) Time-resolved light response curve of $MAPbI_3$-based photodetector on the 2 min KOH-etched Si/SiO_2 nanostructure under a Xe lamp (10 mW/cm^2).

It has been reported that the light trapping or scattering features of Si nanostructures can enhance the photoelectric performance of perovskite-based devices due to increased light absorption.[60] Therefore, Si complex nanostructures fabricated by 2 min KOH etching were applied to fabricate $MAPbI_3$-based photodetectors. The fabrication process of the $MAPbI_3$-based photodetectors is illustrated in **Figure 2.5a**. Before the coating process, SiO_2 (~300 nm) was deposited on the Si nanostructures for insulation (**Figure 2.5b**). As shown in **Figure 2.5c**, the

uniform and flat $MAPbI_3$ film filled the isolated space inside the nanostructures. The side view confirmed that the perovskite film, with a measured thickness of 1330 ± 40 nm, fully covered the Si nanostructures, which had a measured depth of 1290 ± 50 nm. Next, copper (~200 nm) was deposited with a shadow mask to fabricate interdigitated electrodes (**Figure S2.5**). The photoresponse of the $MAPbI_3$-based photodetectors was investigated with illumination from a Xe lamp (10 mW/cm^2), for which the on/off was manually controlled (experimental details are provided in the Materials and Methods section). The periodic pattern, flat curve at top and bottom, and sharp transition times for each on/off illumination cycle from the photoresponse graph (**Figure 2.5d**) demonstrated the high stability and reproducibility of the devices. On the basis of photocurrent measurements, the device also showed 2.5 orders of magnitude increase in the photocurrent (~36 μA) compared to the dark current (~75 nA), indicating the reliable performance of the fabricated photodetectors. In addition, a $MAPbI_3$ thin film was coated on the Si complex nanostructures fabricated with 7 min KOH etching (**Figure S2.6**). Due to the longer anisotropic etching of {100} planes, the thickness of the $MAPbI_3$ thin film was smaller than the depth of the Si nanostructures. Since the inside space was no longer isolated, the $MAPbI_3$ thin film was connected on both sides. According to the reported improvement of photocurrent performance with the light-trapping structures, photodetectors fabricated with these types of nanostructures should exhibit improved performance.

2.5 Conclusions and Prospects

Our results demonstrate that DLPL is a convenient and straightforward method for nanoscale patterning with high throughput and adjustable parameters. The DLPL strategy provides a versatile and practical extension of photolithography to achieve submicron patterning at low cost with high reproducibility. This technique can be integrated into nanoscale device manufacturing for optoelectronics, nanoplasmonics, and biotechnologies, with functions that require 3D nanostructures. Furthermore, with upcoming more systematic and throughout elaborations of DLPL, the resolution could be further improved with different photoresist pairs, resulting in greater capabilities in nanoscale patterning and fabrication. Note that 300 nm is not the lower limit of DLPL; with more precise control of the lithography parameters (exposure, development, photoresist), we anticipate that much smaller features can be realized. Not limited to conventional UV photolithography, this strategy can also be incorporated into other lithographic approaches including DUV, EUV, and EBL to further enhance their resolution.

2.6 Supplementary Materials

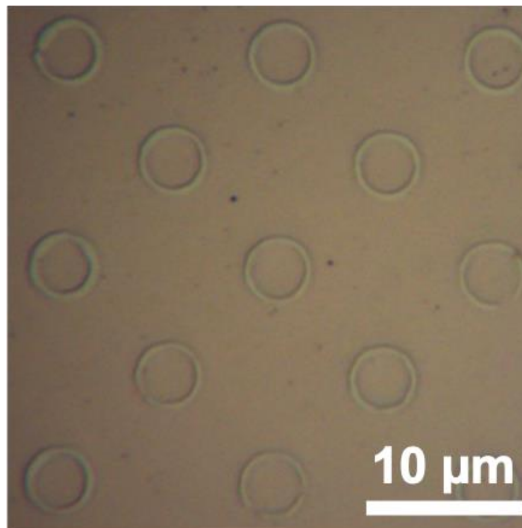

Figure S2.1. Top view optical microscopy image of 5 µm hollow nanorings fabricated by the modified dual-layer photolithography on chromium film.

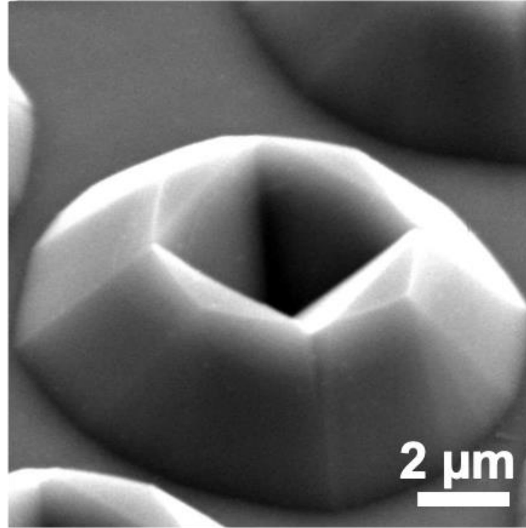

Figure S2.2. Top view scanning electron microscopy image of fabricated Si complex structure (inverted pyramid inside) with 5-min KOH anisotropic etching. Image was taken with a 45° tilt angle.

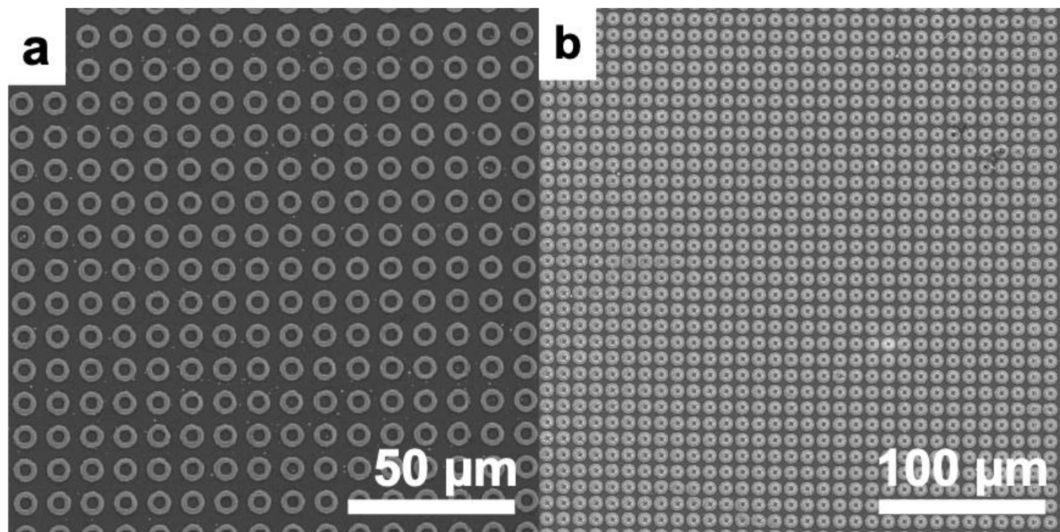

Figure S2.3. Top view scanning electron microscopy images of large-scale Si complex structure arrays fabricated with the KOH anisotropic etching time of (a) 2 min and (b) 5 min.

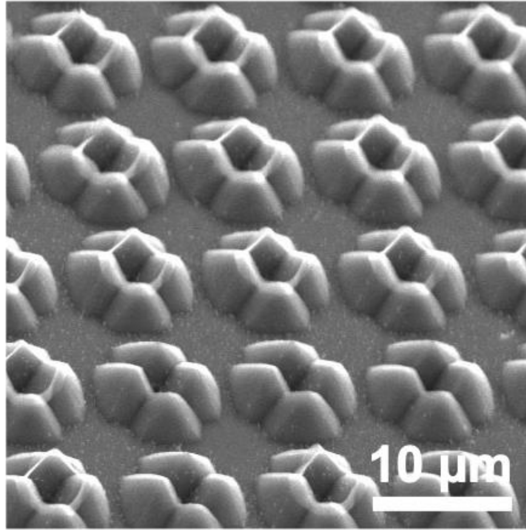

Figure S2.4. Scanning electron microscopy image of Si complex structures with 7-min KOH anisotropic etching before the removal of SiO_2 nanoring. Image was taken with a 45° tilt angle.

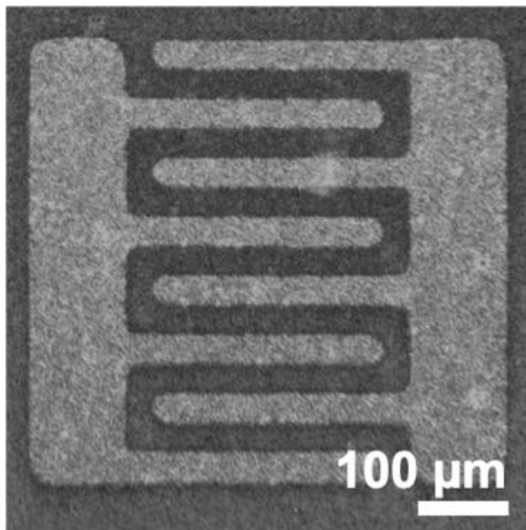

Figure S2.5. Optical image of a single $MAPbI_3$-based photodetector on SiO_2/Si substrate that was fabricated with 2-min KOH anisotropic etching.

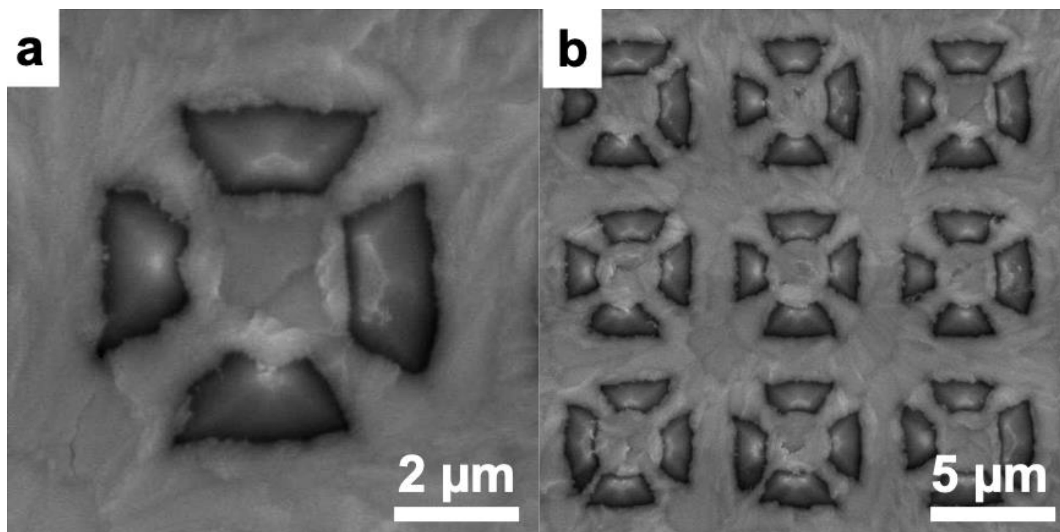

Figure S2.6. Top view scanning electron microscopy image of the $MAPbI_3$ film coated on Si/SiO_2 (a) single complex structure and (b) complex structure arrays fabricated with 7-min KOH anisotropic etching.

Table S2.1. Data of Fig. 2.2c.

Exposure time (s)	Feature size generated by positive photoresist (nm)	Feature size generated by positive photoresist (nm)
18	3870 ± 60	4230 ± 60
22	4410 ± 70	4320 ± 60
26	5020 ± 40	4550 ± 80
30	5140 ± 40	4650 ± 70
34	5360 ± 70	4740 ± 50
38	5650 ± 60	4870 ± 70

2.7 References

1. Carlson, A.; Bowen, A. M.; Huang, Y.; Nuzzo, R. G.; Rogers, J. A. Transfer Printing Techniques for Materials Assembly and Micro/Nanodevice Fabrication. *Adv. Mater.* **2012,** *24*, 5284-5318.

2. Tsai, H.; Pitera, J. W.; Miyazoe, H.; Bangsaruntip, S.; Engelmann, S. U.; Liu, C.-C.; Cheng, J. Y.; Bucchignano, J. J.; Klaus, D. P.; Joseph, E. A.; Sanders, D. P.; Colburn, M. E.; Guillorn, M. A. Two-Dimensional Pattern Formation Using Graphoepitaxy of PS-b-PMMA Block Copolymers for Advanced FinFET Device and Circuit Fabrication. *ACS Nano* **2014,** *8*, 5227-5232.

3. Shen, B.; Linko, V.; Tapio, K.; Pikker, S.; Lemma, T.; Gopinath, A.; Gothelf, K. V.; Kostiainen, M. A.; Toppari, J. J. Plasmonic Nanostructures through DNA-Assisted Lithography. *Sci. Adv.* **2018,** *4*, eaap8978.

4. Wang, C.; Linghu, C.; Nie, S.; Li, C.; Lei, Q.; Tao, X.; Zeng, Y.; Du, Y.; Zhang, S.; Yu, K.; Jin, H.; Chen, W.; Song, J. Programmable and Scalable Transfer Printing with High Reliability and Efficiency for Flexible Inorganic Electronics. *Sci. Adv.* **2020,** *6*, eabb2393.

5. Zhao, C.; Liu, Q.; Cheung, K. M.; Liu, W.; Yang, Q.; Xu, X.; Man, T.; Weiss, P. S.; Zhou, C.; Andrews, A. M. Narrower Nanoribbon Biosensors Fabricated by Chemical Lift-Off Lithography Show Higher Sensitivity. *ACS Nano* **2020,** *15*, 904-915.

6. Park, S. I.; Xiong, Y.; Kim, R. H.; Elvikis, P.; Meitl, M.; Kim, D. H.; Wu, J.; Yoon, J.; Yu, C. J.; Liu, Z.; Huang, Y.; Hwang, K. c.; Ferreira, P.; Li, X.; Choquette, K.; Rogers, J. A. Printed Assemblies of Inorganic Light-Emitting Diodes for Deformable and Semitransparent Displays. *Science* **2009,** *325*, 977-981.

7. Choi, C.; Choi, M. K.; Liu, S.; Kim, M. S.; Park, O. K.; Im, C.; Kim, J.; Qin, X.; Lee, G. J.; Cho, K. W.; Kim, M.; Joh, E.; Lee, J.; Son, D.; Kwon, S.-H.; Jeon, N. L.; Song, Y. M.; Lu, N.; Kim, D.-H. Human Eye-Inspired Soft Optoelectronic Device Using High-Density MoS_2-Graphene Curved Image Sensor Array. *Nat. Commun.* **2017,** *8*, 1664.

8. Lin, C.-H.; Cheng, B.; Li, T.-Y.; Retamal, J. R. D.; Wei, T.-C.; Fu, H.-C.; Fang, X.; He, J.-H. Orthogonal Lithography for Halide Perovskite Optoelectronic Nanodevices. *ACS Nano* **2018,** *13*, 1168–1176.

9. Lei, Y.; Chen, Y.; Zhang, R.; Li, Y.; Yan, Q.; Lee, S.; Yu, Y.; Tsai, H.; Choi, W.; Wang, K.; Luo, Y.; Gu, Y.; Zheng, X.; Wang, C.; Wang, C.; Hu, H.; Li, Y.; Qi, B.; Lin, M.; Zhang, Z.; Dayeh, S. A.; Pharr, M.; Fenning, D. P.; Lo, Y.-H.; Luo, J.; Yang, K.; Yoo, J.; Nie, W.; Xu, S. A Fabrication Process for Flexible Single-Crystal Perovskite Devices. *Nature* **2020,** *583*, 790-795.

10. Tang, Q.; Li, H.; Liu, Y.; Hu, W. High-Performance Air-Stable *n*-Type Transistors with an Asymmetrical Device Configuration Based on Organic Single-Crystalline Submicrometer/Nanometer Ribbons. *J. Am. Chem. Soc.* **2006,** *128*, 14634-14639.

11. Zhang, X.; Jie, J.; Deng, W.; Shang, Q.; Wang, J.; Wang, H.; Chen, X.; Zhang, X. Alignment and Patterning of Ordered Small-Molecule Organic Semiconductor Micro-/Nanocrystals for Device Applications. *Adv. Mater.* **2016,** *28*, 2475-2503.

12. Moolman, M.; Huang, Z.; Krishnan, S.; Kerssemakers, J. W. J.; Dekker, N. H. Electron Beam Fabrication of a Microfluidic Device for Studying Submicron-Scale Bacteria. *J. Nanobiotechnology* **2013,** *11*, 12.

13. Wang, J.; Li, W.; Zhang, L.; Ban, L.; Chen, P.; Du, W.; Feng, X.; Liu, B.-F. Chemically Edited Exosomes with Dual Ligand Purified by Microfluidic Device for Active Targeted Drug Delivery to Tumor Cells. *ACS Appl. Mater. Interfaces* **2017,** *9*, 27441-27452.

14. Nouri-Goushki, M.; Sharma, A.; Sasso, L.; Zhang, S.; Van der Eerden, B. C. J.; Staufer, U.; Fratila-Apachitei, L. E.; Zadpoor, A. A. Submicron Patterns-on-a-Chip: Fabrication of a Microfluidic Device Incorporating 3D Printed Surface Ornaments. *ACS Biomater. Sci. & Eng.* **2019,** *5*, 6127-6136.

15. Dong, P.; Chen, Y.-K.; Duan, G.-H.; Neilson, D. T. Silicon Photonic Devices and Integrated Circuits. *Nanophotonics* **2014,** *3*, 215-228.

16. Alias, M. S.; Yang, Y.; Ng, T. K.; Dursun, I.; Shi, D.; Saidaminov, M. I.; Priante, D.; Bakr, O. M.; Ooi, B. S. Enhanced Etching, Surface Damage Recovery, and Submicron Patterning of Hybrid Perovskites Using a Chemically Gas-Assisted Focused-Ion Beam for Subwavelength Grating Photonic Applications. *J. Phys. Chem. Lett.* **2015,** *7*, 137-142.

17. Higashida, R.; Funabashi, N.; Aoshima, K.-i.; Machida, K. Submicron-Scale Light Modulation Device Driven by Current-Induced Domain Wall Motion for Electro-Holography. *Jpn J. Appl. Phys.* **2020,** *59*, 053001.

18. Wagner, C.; Harned, N. Lithography Gets Extreme. *Nat. Photonics* **2010,** *4*, 24-26.

19. Ashby, P. D.; Olynick, D. L.; Ogletree, D. F.; Naulleau, P. P. Resist Materials for Extreme Ultraviolet Lithography: Toward Low-Cost Single-Digit-Nanometer Patterning. *Adv. Mater.* **2015,** *27*, 5813-5819.

20. Chen, S.; Svedendahl, M.; Antosiewicz, T. J.; Käll, M. Plasmon-Enhanced Enzyme-Linked Immunosorbent Assay on Large Arrays of Individual Particles Made by Electron Beam Lithography. *ACS Nano* **2013,** *7*, 8824-8832.

21. Manfrinato, V. R.; Zhang, L.; Su, D.; Duan, H.; Hobbs, R. G.; Stach, E. A.; Berggren, K. K. Resolution Limits of Electron-Beam Lithography toward the Atomic Scale. *Nano Lett.* **2013,** *13*, 1555-1558.

22. Kim, S.; Marelli, B.; Brenckle, M. A.; Mitropoulos, A. N.; Gil, E.-S.; Tsioris, K.; Tao, H.; Kaplan, D. L.; Omenetto, F. G. All-Water-Based Electron-Beam Lithography Using Silk as a Resist. *Nat. Nanotechnol.* **2014,** *9*, 306-310.

23. Córdoba, R.; Ibarra, A.; Mailly, D.; De Teresa, J. M. Vertical Growth of Superconducting Crystalline Hollow Nanowires by He^+ Focused Ion Beam Induced Deposition. *Nano Lett.* **2018,** *18*, 1379-1386.

24. Porrati, F.; Barth, S.; Sachser, R.; Dobrovolskiy, O. V.; Seybert, A.; Frangakis, A. S.; Huth, M. Crystalline Niobium Carbide Superconducting Nanowires Prepared by Focused Ion Beam Direct Writing. *ACS Nano* **2019,** *13*, 6287-6296.

25. Winkler, R.; Fowlkes, J. D.; Rack, P. D.; Plank, H. 3D Nanoprinting *via* Focused Electron Beams. *J. Appl. Phys.* **2019,** *125*, 210901.

26. Xu, X.; Yang, Q.; Cheung, K. M.; Zhao, C.; Wattanatorn, N.; Belling, J. N.; Abendroth, J. M.; Slaughter, L. S.; Mirkin, C. A.; Andrews, A. M.; Weiss, P. S. Polymer-Pen Chemical Lift-Off Lithography. *Nano Lett.* **2017,** *17*, 3302-3311.

27. Chou, S. Y.; Krauss, P. R.; Renstrom, P. J. Imprint Lithography with 25-Nanometer Resolution. *Science* **1996,** *272*, 85-87.

28. Mårtensson, T.; Carlberg, P.; Borgström, M.; Montelius, L.; Seifert, W.; Samuelson, L. Nanowire Arrays Defined by Nanoimprint Lithography. *Nano Lett.* **2004,** *4*, 699-702.

29. Guo, L. J. Nanoimprint Lithography: Methods and Material Requirements. *Adv. Mater.* **2007,** *19*, 495-513.

30. Huo, F.; Zheng, Z.; Zheng, G.; Giam, L. R.; Zhang, H.; Mirkin, C. A. Polymer Pen Lithography. *Science* **2008,** *321*, 1658-1660.

31. Qin, D.; Xia, Y.; Whitesides, G. M. Soft Lithography for Micro- and Nanoscale Patterning. *Nat. Protoc.* **2010,** *5*, 491-502.

32. Liao, W. S.; Cheunkar, S.; Cao, H. H.; Bednar, H. R.; Weiss, P. S.; Andrews, A. M. Subtractive Patterning *via* Chemical Lift-Off Lithography. *Science* **2012,** *337*, 1517-1521.

33. Hulteen, J. C.; Treichel, D. A.; Smith, M. T.; Duval, M. L.; Jensen, T. R.; Van Duyne, R. P. Nanosphere Lithography: Size-Tunable Silver Nanoparticle and Surface Cluster Arrays. *J. Phys. Chem. B* **1999,** *103*, 3854-3863.

34. Chen, K.; Rajeeva, B. B.; Wu, Z.; Rukavina, M.; Dao, T. D.; Ishii, S.; Aono, M.; Nagao, T.; Zheng, Y. Moiré Nanosphere Lithography. *ACS Nano* **2015,** *9*, 6031-6040.

35. Hatzor, A.; Weiss, P. S. Molecular Rulers for Scaling Down Nanostructures. *Science* **2001,** *291*, 1019-1020.

36. McLellan, J. M.; Geissler, M.; Xia, Y. Edge Spreading Lithography and Its Application to the Fabrication of Mesoscopic Gold and Silver Rings. *J. Am. Chem. Soc.* **2004,** *126*, 10830-10831.

37. Geissler, M.; McLellan, J. M.; Xia, Y. Edge-Spreading Lithography: Use of Patterned Photoresist Structures to Direct the Spreading of Alkanethiols on Gold. *Nano Lett.* **2005,** *5*, 31-36.

38. Halpern, A. R.; Corn, R. M. Lithographically Patterned Electrodeposition of Gold, Silver, and Nickel Nanoring Arrays with Widely Tunable Near-Infrared Plasmonic Resonances. *ACS Nano* **2013,** *7*, 1755-1762.

39. Xu, X.; Yang, Q.; Wattanatorn, N.; Zhao, C.; Chiang, N.; Jonas, S. J.; Weiss, P. S. Multiple-Patterning Nanosphere Lithography for Fabricating Periodic Three-Dimensional Hierarchical Nanostructures. *ACS Nano* **2017,** *11*, 10384-10391.

40. Switkes, M.; Rothschild, M. Immersion Lithography at 157 nm. *J. Vac. Sci. Technol. B* **2001,** *19*, 2353-2356.

41. Ghaida, R. S.; Torres, G.; Gupta, P. Single-Mask Double-Patterning Lithography for Reduced Cost and Improved Overlay Control. *IEEE Trans. Semicond. Manuf.* **2011,** *24*, 93-103.

42. Liu, S.; Al-Shadeedi, A.; Kaphle, V.; Keum, C.-M.; Lüssem, B. Patterning Organic Transistors by Dry-Etching: The Double Layer Lithography. *Org. Electron.* **2017,** *45*, 124-130.

43. Huo, F.; Zheng, G.; Liao, X.; Giam, L. R.; Chai, J.; Chen, X.; Shim, W.; Mirkin, C. A. Beam Pen Lithography. *Nat. Nanotechnol.* **2010,** *5*, 637-640.

44. Feng, B. C.; Feng, G. C. Two Layer Resist System. U.S. Patent 4,204,009, **1980**.

45. Lau, J. W.; Shaw, J. M. Magnetic Nanostructures for Advanced Technologies: Fabrication, Metrology and Challenges. *J. Phys. D: Appl. Phys.* **2011,** *44*, 303001.

46. Preiss, E. M.; Krauss, A.; Seidel, H. Sputtered Pt Electrode Structures with Smoothly Tapered Edges by Bi-Layer Resist Lift-Off. *Thin Solid Films* **2015,** *597*, 158-164.

47. Chiriacò, M. S.; Bianco, M.; Amato, F.; Primiceri, E.; Ferrara, F.; Arima, V.; Maruccio, G. Fabrication of Interconnected Multilevel Channels in a Monolithic SU-8 Structure Using a LOR Sacrificial Layer. *Microelectron. Eng.* **2016,** *164*, 30-35.

48. Bean, K. E. Anisotropic Etching of Silicon. *IEEE Trans. Electron Devices* **1978,** *25*, 1185-1193.

49. Yamada, K.; Yamada, M.; Maki, H.; Itoh, K. M. Fabrication of Arrays of Tapered Silicon Micro-/Nano-Pillars by Metal-Assisted Chemical Etching and Anisotropic Wet Etching. *Nanotechnology* **2018,** *29*, 28LT01.

50. Xu, X.; Liu, W.; Ji, Z.; Hao, D.; Yan, W.; Ye, Z.; Hu, Y.; Fang, M.; Wang, C.; Ma, L.; Huang, J.; Xu, X.; Weiss, P. S. Large-Area Periodic Organic-Inorganic Hybrid Perovskite Nanopyramid Arrays for High Performance Photodetector and Image Sensor Applications. **2021**, in preparation.

51. Deng, W.; Lv, Y.; Zhang, X.; Fang, X.; Lu, B.; Lu, Z.; Jie, J. High-Resolution Patterning of Organic Semiconductor Single Crystal Arrays for High-Integration Organic Field-Effect Transistors. *Mater. Today* **2020,** *40*, 82-90.

52. Deng, W.; Jie, J.; Xu, X.; Xiao, Y.; Lu, B.; Zhang, X.; Zhang, X. A Microchannel-Confined Crystallization Strategy Enables Blade Coating of Perovskite Single Crystal Arrays for Device Integration. *Adv. Mater.* **2020,** *32*, 1908340.

53. Hines, D. R.; Siwak, N. P.; Mosher, L. A.; Ghodssi, R., MEMS Lithography and Micromachining Techniques. *MEMS Materials and Processes Handbook*, **2011**, pp 667-753.

54. Morton, K. J.; Nieberg, G.; Bai, S.; Chou, S. Y. Wafer-Scale Patterning of Sub-40 nm Diameter and High Aspect Ratio (>50:1) Silicon Pillar Arrays by Nanoimprint and Etching. *Nanotechnology* **2008,** *19*, 345301.

55. Garnett, E.; Yang, P. Light Trapping in Silicon Nanowire Solar Cells. *Nano Lett.* **2010,** *10*, 1082-1087.

56. Ge, M.; Rong, J.; Fang, X.; Zhou, C. Porous Doped Silicon Nanowires for Lithium Ion Battery Anode with Long Cycle Life. *Nano Lett.* **2012,** *12*, 2318-2323.

57. Huo, C.; Wang, J.; Fu, H.; Li, X.; Yang, Y.; Wang, H.; Mateen, A.; Farid, G.; Peng, K. Q. Metal-Assisted Chemical Etching of Silicon in Oxidizing HF Solutions: Origin, Mechanism, Development, and Black Silicon Solar Cell Application. *Adv. Funct. Mater.* **2020,** *30*, 2005744.

58. Seidel, H.; Csepregi, L.; Heuberger, A.; Baumgärtel, H. Anisotropic Etching of Crystalline Silicon in Alkaline Solutions: I . Orientation Dependence and Behavior of Passivation Layers. *J. Electrochem.* **2019,** *137*, 3612-3626.

59. Mavrokefalos, A.; Han, S. E.; Yerci, S.; Branham, M. S.; Chen, G. Efficient Light Trapping in Inverted Nanopyramid Thin Crystalline Silicon Membranes for Solar Cell Applications. *Nano Lett.* **2012,** *12*, 2792-2796.

60. Mao, J.; Sha, W. E. I.; Zhang, H.; Ren, X.; Zhuang, J.; Roy, V. A. L.; Wong, K. S.; Choy, W. C. H. Novel Direct Nanopatterning Approach to Fabricate Periodically Nanostructured Perovskite for Optoelectronic Applications. *Adv. Funct. Mater.* **2017,** *27*, 1606525.

Chapter 3

Sub-200-nm Patterning by Self-Aligned Dual-Layer Photolithography

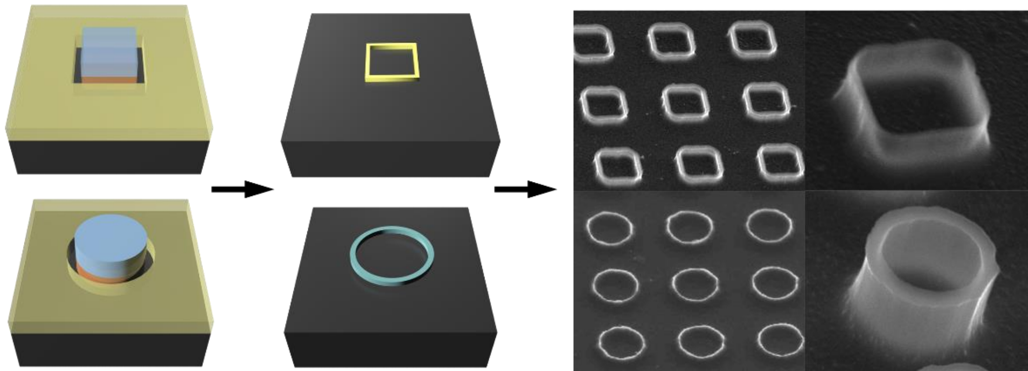

The information in this chapter is in preparation for submission and has been adapted here.

Authors: Wang, J.*; **Liu, W.***; Liu, P.; Weiss, P. S.; Xu, X.

3.1 Abstract

Recently, we reported a self-aligned double patterning strategy named dual-layer photolithography (DLPL) and applied it to ultraviolet photolithography. Dual-layer photolithography takes advantage of feature differences between positive and negative patterns to overcome the diffraction limit and to realize sub-500-nm patterning. Here, we systematically studied the interactions between the two photoresists with opposite tones to improve the resolution of DLPL. The chemical compatibility of the two photoresists and the impact on the thickness of photoresist were investigated at different thickness configurations through tuning the photoresist composition and coating conditions. We found that photoresist thinning combined with optimized exposure and development, produced linewidths down to sub-200 nm. In addition, we demonstrated the compatibility of DLPL with other fabrication processes including dry etching and lift-off. A variety of extruded and recessed micro-/nanostructures including metallic triangular/square arrays and silicon square/circular tube arrays were demonstrated.

3.2 Introduction

Conventional ultraviolet (UV) photolithography, as the primary micro-/nanomanufacturing process in the semiconductor industry, has been widely used in various applications to produce integrated circuits, sensors, wearable electronics, photonic devices, and optoelectronics, among others.[1-6] However, optical diffraction leads to resolution limits of ~λ or $\lambda/2$ in conventional UV photolithography (λ of the g-/i-line: 436/365 nm).[7-9] The resolution limit (R) is described by Rayleigh's equation $R = k_1 \cdot \lambda / NA$, where λ is wavelength, NA is numerical aperture, and k_1 is a process-related factor. The resolution limit can generally be improved through three methods: 1) decrease the wavelength of light (*e.g.*, deep ultraviolet,[10,11] extreme ultraviolet[12,13]); 2) increase the numerical aperture (*e.g.*, immersion lithography[14,15]); or 3) optimize the lithographic process. In addition, the requirements for either advanced light sources or sophisticated equipment and optical systems for the improved approaches preclude them from low-cost applications. Mask-free lithographic approaches,[16,17] such as electron-beam lithography,[18-21] focused ion-beam lithography,[22,23] and scanning-probe lithography[24-26] can achieve sub-50-nm patterning without reaching the optical diffraction limit. However, their low throughput excludes them from large-scale applications.

Without changing the light wavelength or numerical aperture of photolithography, innovations in lithographic strategies can nonetheless be utilized to overcome the resolution limit. Specifically, double or multiple patterning strategies, based on "subtraction" processes between different patterns, are important in continuously pushing the resolution limit to keep up with Moore's Law. The major challenge lies in how to improve the reproducibility and to reduce the defect rate due to the high precision requirements in pattern alignment over large areas.

Recently, we reported a self-aligned double-patterning strategy, *i.e.*, dual-layer photolithography (DLPL),[27] which eliminates the need for pattern alignment with high precision. In a typical DLPL process, two stacking layers of photoresists with opposite tones (positive and negative) were exposed to UV light with a photomask to generate opposite patterns on each layer with small differences in the feature sizes. After development, this difference was exploited through a subtractive process between the positive and negative patterns. Here, the size difference is largely determined by the degree of photo-induced polymerization and the development of photoresists instead of the optical diffraction limit. Using DLPL, we demonstrated feature linewidths down to 300 nm, smaller than the conventional UV photolithography.[27]

However, there remain unknown processes in DLPL, such as how the two opposite photoresists interact with each other, and how the photoresist configuration impacts the resolution (*e.g.*, the thickness ratio between the negative and positive photoresists).[28,29] Thus, in this work, we focus on studying the chemical compatibility of two photoresists and their thickness ratio through adjusting the photoresist composition and spin-coating speed. We found that by thinning the photoresist and optimizing the exposure and development conditions, we can realize linewidths down to sub-200 nm levels with DLPL. In addition, we demonstrate the compatibility of DLPL with dry etching and lift-off techniques,[30-35] which are commonly used in micro-/nanofabrication. A variety of micro-/nanostructures including Si square/circular tubes and metallic triangular/square arrays were fabricated.

3.3 Materials and Methods

Materials. Positive photoresist (BCI 3511) was purchased from Suzhou Research Materials Microtech Co., Ltd., China. Negative photoresist (SUN 9i) was purchased from Suntific Materials, Ltd., China. The $CsPbI_3$ was purchased from Xi'an Polymer Light Technology Corp., China. The γ-Butyrolactone (GBL) was purchased from Shanghai Aladdin Biochemical Technology Co., Ltd., China. Dimethyl sulfoxide (DMSO) was purchased from Sinopharm Chemical Reagent Co., Ltd., China. The magnetron sputtering material SiO_2 (99.99%) and nickel (99.99%) were purchased from ZhongNuo Advanced Material Technology Co., Ltd., China.

Characterization and Instruments. The morphologies of patterned photoresist, dual-layer photolithography (DLPL)-fabricated microrings, dry-etched Si microstructures, and surface-coated $CsPbI_3$ thin films were determined by scanning electron microscopy (SEM, JEOL JSM-6060LA). The UV light source for photolithography was 3500 mW/cm^2 at 365 nm (Hamamatsu Corporation, JP). Magnetron sputtering was done by a magnetron sputtering system (DM 300, Hefei Jusheng Vacuum Technology Inc.). Thermal evaporation was carried out by a thermal evaporator (DM500, Hefei Jusheng Vacuum Technology Inc.) The photoresponsivity of the $CsPbI_3$-based photodetectors was measured using a source meter (Keithley 2602B) on a probe-station.

Fabrication of SiO_2, Chromium (Cr), and Nickel (Ni) Microrings. First, DLPL experiments were conducted with the optimized photoresist composition and spin-coating speed. Second, a SiO_2 film was deposited on the substrates *via* magnetron sputtering at a rate of 1 nm/min. The Cr or Ni was deposited on the substrates *via* thermal evaporation at a rate of ~0.5 Å/s. After material deposition, the remaining photoresists were removed by mild sonication in acetone, while

the materials on top of the photoresist were lifted off. As a result, microrings of different materials were fabricated on Si substrates.

Fabrication of Si Recessed Microrings and Microtubes. The Si recessed microrings and microtubes were fabricated *via* deep reactive ion etching (DRIE) using patterned photoresists and Cr/SiO_2 microrings as the etching masks, respectively. In a typical etching process, also known as the Bosch process, SF_6 was used as the etching gas and C_4F_8 was used as the protecting gas. These gases were applied in an alternative manner (in a 10+10 s etching cycle) to etch silicon to a depth of 500 nm (SF_6 flow rate: 35 sccm; C_4F_8 flow rate: 45 sccm; working power: 650 W; bias: 45%; etching time: 10 min). After deep silicon etching, the photoresists were removed by acetone to obtain Si recessed microrings. The Cr or SiO_2 microrings were removed by hydrochloric acid or hydrofluoric acid, resulting in Si microtubes.

Fabrication of a $CsPbI_3$-Based Photodetector. A thin layer of SiO_2 (~200 nm) was deposited on the dry-etched Si microstructures. Then, 50 µL of $CsPbI_3$ precursor solution (1 M in *N*,*N*-dimethylformamide) was spin-coated on the SiO_2/Si substrates at 5000 rpm for 40 s. During the spin-coating process, 100 µL of toluene was added dropwise on the substrates. The substrates were annealed at 100 °C for 10 min to form a $CsPbI_3$ thin film. After that, Au (50 nm) electrodes were deposited *via* thermal evaporation. The channel length (l) and width (w) of the device were 50 µm and 2800 µm, respectively, with an aspect ratio of 1/56 to avoid device-to-device interference.

3.4. Results and Discussions

The thickness configuration of the dual-layer photoresists influenced the final feature sizes in DLPL. Generally, photolithography using thin photoresists (*e.g.*, <500 nm) can achieve higher resolution and smaller features due to the reduced distance between the mask and the substrate, as well as higher depth-to-width aspect ratios.

In our recent work with DLPL, the negative photoresist (-PR) layer is *ca.* 5 times thicker than the positive photoresist (+PR) layer (**Scheme 3.1a**).[27] We hypothesized that reducing the PR thickness would improve the patterning resolution of DLPL (**Scheme 3.1b**). In this study, two key parameters, *i.e.*, photoresist composition and spin-coating speed, were optimized to reduce the overall dual-layer PR thickness, as well as the thickness ratio of -PR to +PR.

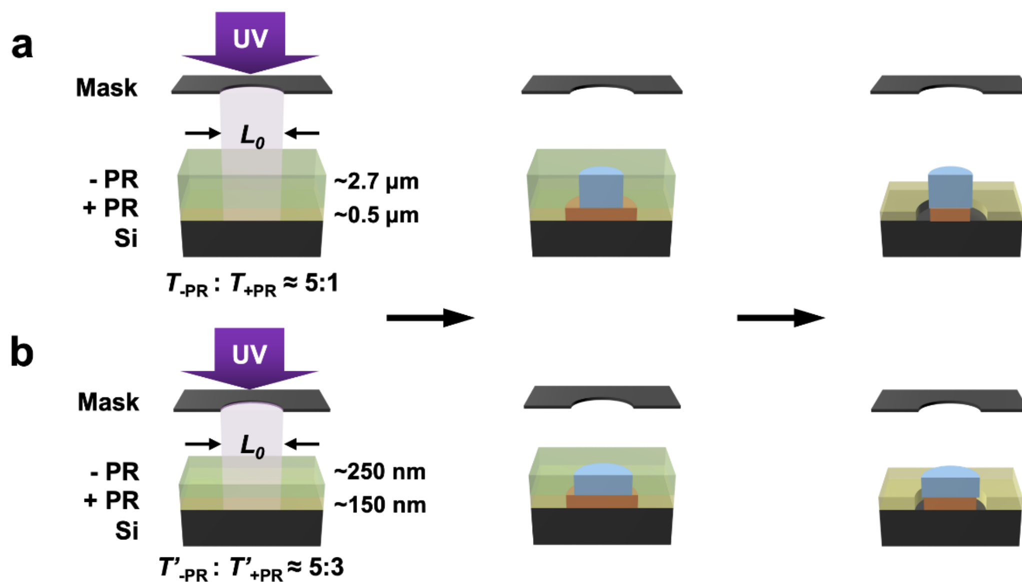

Scheme 3.1. Schematic fabrication process of (top) single-step dual-layer photolithography (DLPL) and (bottom) DLPL with optimized photoresist thickness.

3.4.1 Tuning the photoresist thickness through photoresist composition optimization

We explored the impact of the photoresist-to-solvent ratio on the photoresist thickness and feature size. Here, γ-butyrolactone was chosen as the dilution medium because it is a good solvent for -PR (SUN 9i) but not for +PR (BCI 3511). Both single-layer and dual-layer condition were studied in the following experiments.

As shown in **Figure S3.1**, the single-layer -PR was patterned into microdisk arrays with different dilution ratios by UV photolithography in which -PR and γ-butyrolactone were undiluted or diluted at a volume ratio of 3:1, 2:1, or 1:1. As the dilution ratio increased from undiluted to 1:1, the -PR thickness (T_{-PR}) decreased from ~2000 nm to 200 nm and the feature size (diameter of the microdisk pattern) increased from 3.7 μm to 4.6 μm under the same exposure dose (**Figure S3.1e**). The enlarged feature size was a result of increased relative exposure dose per unit area. The results indicated that the feature sizes could be tuned by adjusting the -PR layer thickness, which was used to guide the following study on feature size tunability under dual-layer photoresist conditions.

Based on the above results, we further investigated the PR thickness impact on DLPL through tuning the dilution ratio of -PR without changing other parameters while the spin-coating speed (ω) was fixed at 4000 rpm. Recessed microring structure were fabricated by DLPL at different PR thicknesses. Their SEM images are shown in **Figure 3.1a-d**.

Based on the equation of $T_{dual} = T_{+PR*} + T_{-PR*}$, the thickness of the PR dual layers (T_{dual}), +PR (T_{+PR*}), and -PR (T_{-PR*}) were measured and plotted in **Figure 3.1e.** As the -PR was diluted to 3:1 ratio (-PR to γ-butyrolactone), T_{dual} decreased from 2.08 μm to 0.82 μm. The increase mainly arose from a large drop in T_{-PR*} from 1.70 μm to 0.49 μm. When the dilution ratio was changed to

2:1, T_{dual} further was reduced to 0.44 µm. This decrease was attributed to two factors. First, T_{-PR*} decreased from 490 nm to 280 nm. Second, +PR was partially dissolved by the increased ratio of γ-butyrolactone in diluted -PR, which led to a reduced T_{+PR*} from 330 nm to 160 nm. When the -PR was diluted at a 1:1 ratio, +PR was completely dissolved. As a result, the 2:1 dilution ratio yielded to the smallest thickness (*i.e.,* T_{dual}= 440 nm).

Besides PR thickness, the feature sizes of the microrings (inner diameter: d_{inner}, outer diameter: d_{outer}) are summarized in **Figure 3.1f**. The linewidth (L) can be calculated based on an equation where $L = (d_{outer} - d_{inner})/2$. From the results, at the thinnest T_{dual}= 440 nm (2:1 dilution ratio of -PR), the smallest L of the recessed microrings was calculated to be 620 nm. Therefore, 2:1 dilution ratio was chosen for further optimization.

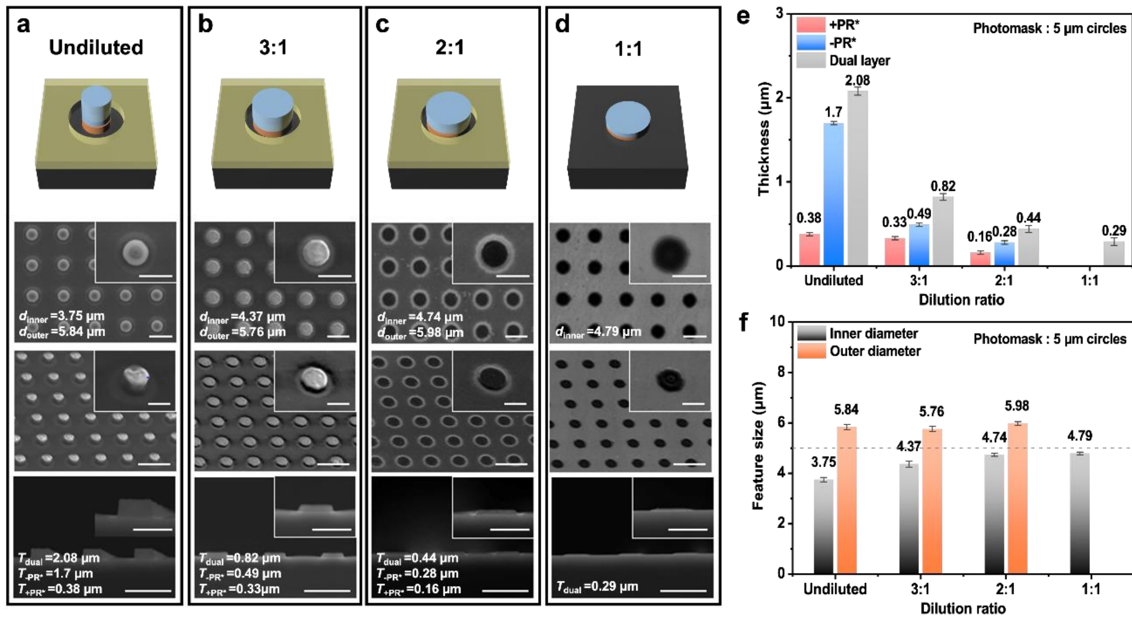

Figure 3.1. (a-d) Schematic diagrams and scanning electron microscopy images of dual-layer photolithography patterns prepared with negative photoresist (-PR) under different dilution ratios (-PR : γ-butyrolactone). From top to bottom: schematic diagram; top view; 45° view,

cross-sectional view. Scale bars: whole view 10 µm; zoom-in view 5 µm. (e) Histogram of photoresist thicknesses under different dilution ratios. (f) Histogram of inner and outer diameters under different dilution ratios.

3.4.2 Tuning the photoresist thickness through coating condition optimization

Following photoresist dilution, the spin-coating speed (ω) was adjusted. As shown in **Figure 3.2a-c**, the impact of spin coating on photoresist thickness was investigated in parallel experiments of single layer of +PR (**Figure 3.2a**), single layer of -PR (**Figure 3.2b**), and dual layer photoresists (**Figure 3.2c**). Photoresist thicknesses were measured with respect to different spin-coating speeds (**Figure 3.2d,e**). In the single-layer experiments (**Figure 3.2a,b,d**), as the spin-coating speed was increased from 2500 rpm to 5500 rpm, the thicknesses of +PR and -PR both decreased over 200 nm. Notably, both layers experienced the greater decrease (~180 nm reduction) in thickness when the spin-coating speed was increased from 2500 to 4000 rpm. When the spin-coating speed was increased further to 5500 rpm, the thickness did not decrease as much (~50 nm reduction).

In the dual-layer experiments, T_{+PR*} = 230 nm and T_{-PR*} = 440 nm at ω = 2500 rpm. Both values are much smaller than those in the single-layer experiments (*i.e.*, T_{+PR*} = 960 nm and T_{-PR*} = 700 nm) (**Figure 3.2**). We attributed this phenomenon to the partial dissolution of +PR during the coating of -PR layer on top of the +PR layer. We found that this partial dissolution phenomenon becomes more obvious, especially when the spin-coating speed of -PR is low and/or the -PR is diluted with γ-butyrolactone, which provides more interaction time or solubility between the -PR solvent and +PR.

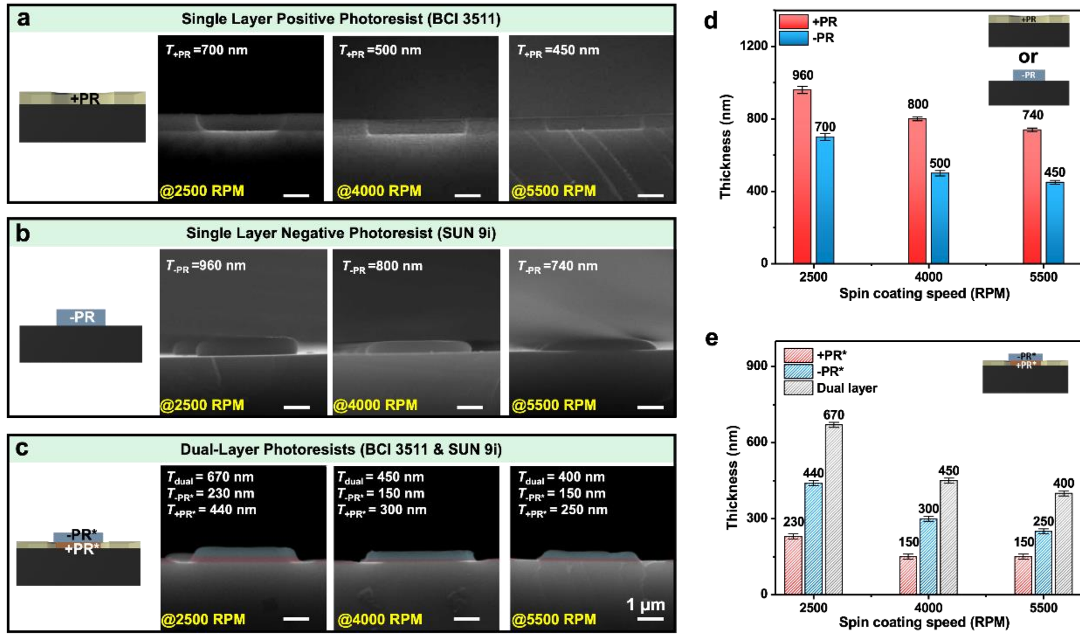

Figure 3.2. Cross-sectional scanning electron microscopy images of patterned (a) single layer positive photoresist, (b) single layer negative photoresist (-PR), and (c) dual layer photoresist at different spin-coating speeds. (d) Histogram of positive and -PRs thicknesses under different spin-coating speeds. (e) Histogram of photoresists thickness under different spin-coating speeds.

3.4.3 Tuning the exposure and development in dual-layer photolithography

The exposure time (t_{exp}) and development time (t_{dev}) are also key parameters in photolithography for feature size tuning. Increased exposure time usually generates larger feature sizes, while increased development time usually causes smaller positive features and larger negative features (**Figure 3.3a,b**).

Through sputtering and lift-off processes, DLPL patterns can be converted to microstructures of different materials (*i.e.*, SiO_2 microrings) (**Figure 3.3c**). A series of microring

arrays were patterned by DLPL at different t_{exp} (30 s, 34 s, and 38 s) and t_{dev} (10 s, 15 s, and 20 s), and converted into inverted structures with dimensions identical to the SiO_2 microrings. The measured values of inner diameter (d_{inner}), outer diameter (d_{outer}), and linewidth (L) of the SiO_2 microrings are summarized in **Figures 3.3d and S3.2**. The results show that the d_{inner} and d_{outer} values respond differently to changes in t_{exp} and t_{dev} as illustrated.

In the case of fixing t_{exp} at 38 s and increasing t_{dev} from 10 s to 20 s: d_{inner} decreased by 500 nm (from 4990 nm to 4470 nm), while d_{outer} increased by 800 nm (from 6010 nm to 6810 nm). This result agrees with the fact that the increased dissolution of PRs causes a reduction in the feature size in the -PR layer, while it increases the feature size in the +PR layer (**Figure 3.3a**). In the case of fixing t_{dev} at 15 s and increasing t_{exp} from 30 s to 38 s, only a small change was observed in d_{inner}, which increased *ca.* 200-nm (from 4740 nm to 4930 nm); the change in d_{outer} was about 6× larger as it reached 1340 nm (from 5120 nm to 6460 nm), as shown in **Figure 3.3b**. The above results demonstrated feature size tunability through adjustments in exposure times and the development times. As a result, the smallest linewidth, $L = 190$ nm, was obtained at $t_{exp} = 30$ s and $t_{dev} = 15$ s.

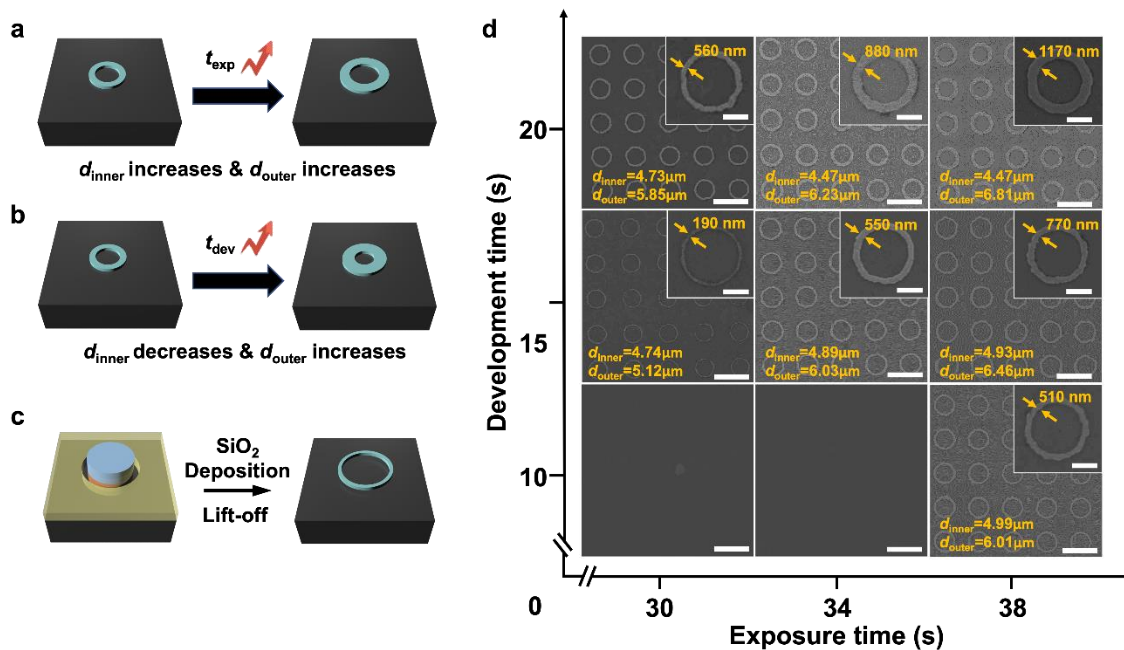

Figure 3.3. Schematic diagrams of the impact of (a) exposure and (b) development time on feature size in dual-layer photolithography. (c) Schematic of the fabrication process for SiO_2 microrings. (d) Scanning electron microscopy images of SiO_2 microrings prepared at different exposure and development times. Scale bars: whole view 10 µm; zoom-in view 2 µm.

3.4.4 Multi-purpose patterning by dual-layer photolithography

To test the multi-purpose patterning capabilities of DLPL, including those associated with different structures and materials, DLPL was further combined with deep silicon etching by RIE and metal deposition to fabricate various microstructures with different shapes and materials (**Figure 3.4a**). When using DLPL to fabricate patterned circular and triangular structures on PR (**Figure 3.4c**), as masks for RIE, we obtained recessed triangular and circular microring arrays (**Figure 3.4b**). When combining the DLPL patterned circular and triangular structures with

material deposition (*e.g.*, Cr, Ni, SiO_2), we obtained microring arrays after PR lift-off (**Figure 3.4d**).

These metallic/SiO_2 microrings arrays can further be used as hard masks for additional dry-etching steps to fabricate Si microtubes (**Figure 3.4e**). As a result, the heights of Si microtubes can be controlled by varying the etching times. (**Figure 3.4f-i**). The wall thicknesses of the Si microtubes could be reduced through tuning the RIE parameters. Finally, we applied this technique to the fabrication of perovskite-based photodetectors.[36,37] A perovskite ($CsPbI_3$) film was spin-coated on the surface containing DLPL-patterned microstructures in **Figure 3.4h**. The $CsPbI_3$ film not only showed improved crystallinity and film uniformity but also improved light sensitivity when fabricated into photodetectors. (**Figure S3.3**).

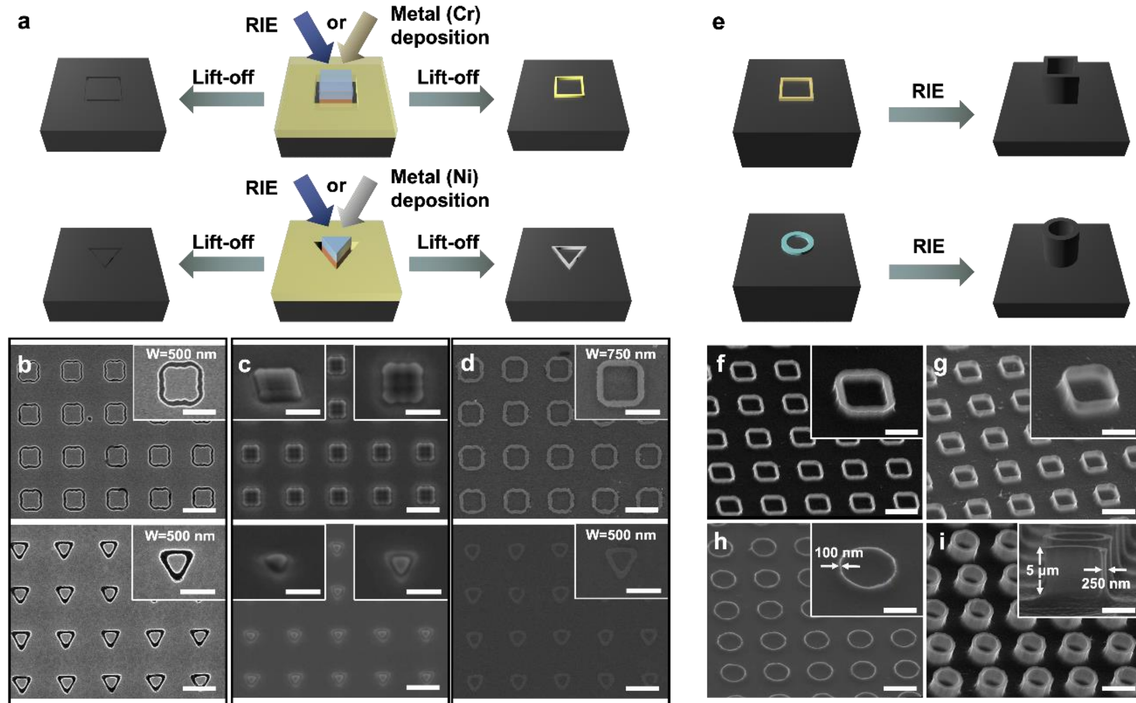

Figure 3.4. (a) Patterning scheme of dual-layer photolithography (DLPL) followed by reactive ion etching of Si (left) and metal deposition (right). Scanning electron microscopy

(SEM) images of (b) Si recessed microrings (upper: 5-μm recessed square microrings, lower: 3-μm recessed triangular microrings), (c) DLPL-patterned dual photoresist layers (zoom-in left: 45° view, zoom-in right: top view), and (d) metal microrings (upper: Cr square microrings, lower: Ni triangular microrings). (e) Fabrication scheme for Si microtubes using Cr (yellow) or SiO_2 (blue) microrings as etching masks. (f-i) SEM images of Si microtubes etched for (f) 2 min or (g) 7 min using Cr square microrings as etching masks and silicon microtubes etched for (h) 2 min or (i) 10 min using SiO_2 circular microrings as etching masks. Scale bars: whole view 5 μm; zoom-in view 2.5 μm.

3.5 Conclusions and Prospects

In summary, we systematically studied the interactions between the two photoresists with opposite tones to improve the resolution of DLPL to sub-200 nm. The chemical compatibility of the two photoresists and the impact of their thicknesses were investigated at different thickness configurations through tuning the photoresist composition and coating conditions. After the optimization of exposure and development conditions, we improved the patterning resolution of DLPL down to sub-200 nm. In addition, we demonstrated the compatibility of DLPL with common micro-/nanomanufacturing techniques such as dry etching, metal deposition, and lift-off. A variety of extruded and recessed microstructures, including Si recessed square/triangular microring arrays, metallic square/triangular ring arrays, and silicon square/circular tube arrays were fabricated. The systematic study of DLPL can be further applied to other lithographic approaches to fabricate 3D micro-/nanostructures with improved resolution and straightforward processing.

3.6 Supplementary Materials

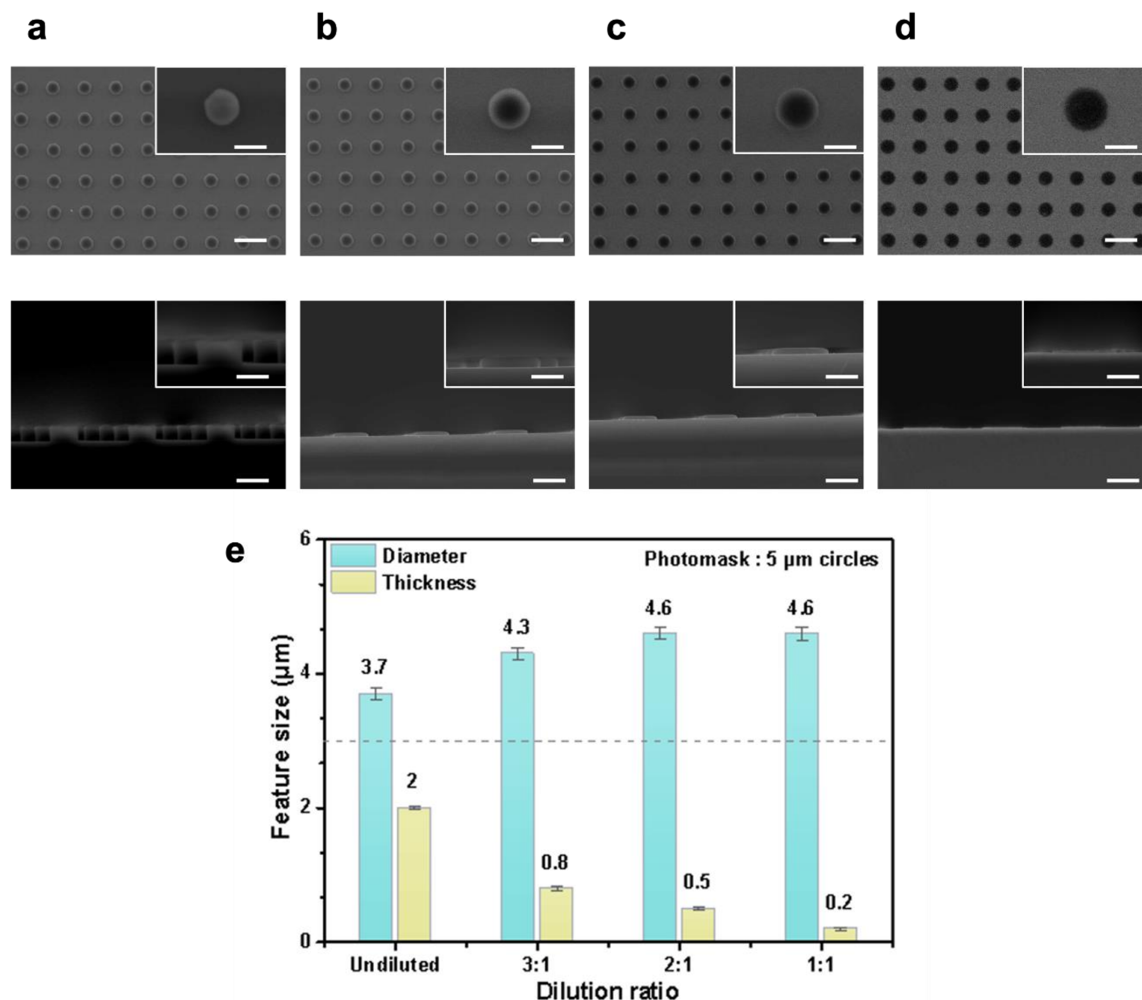

Figure S3.1. Negative photoresist (-PR) patterns prepared *via* single-layer phototlithography with different dilution ratios (-PR : γ-butyrolactone): (a) Undiluted; (b) 3:1 dilution; (c) 2:1 dilution; (d) 1:1 dilution. (e) Histogram of negative photoresist thicknesses and feature size under different dilution ratios. Scale bars: whole view 5 µm; zoom-in view 2.5 µm.

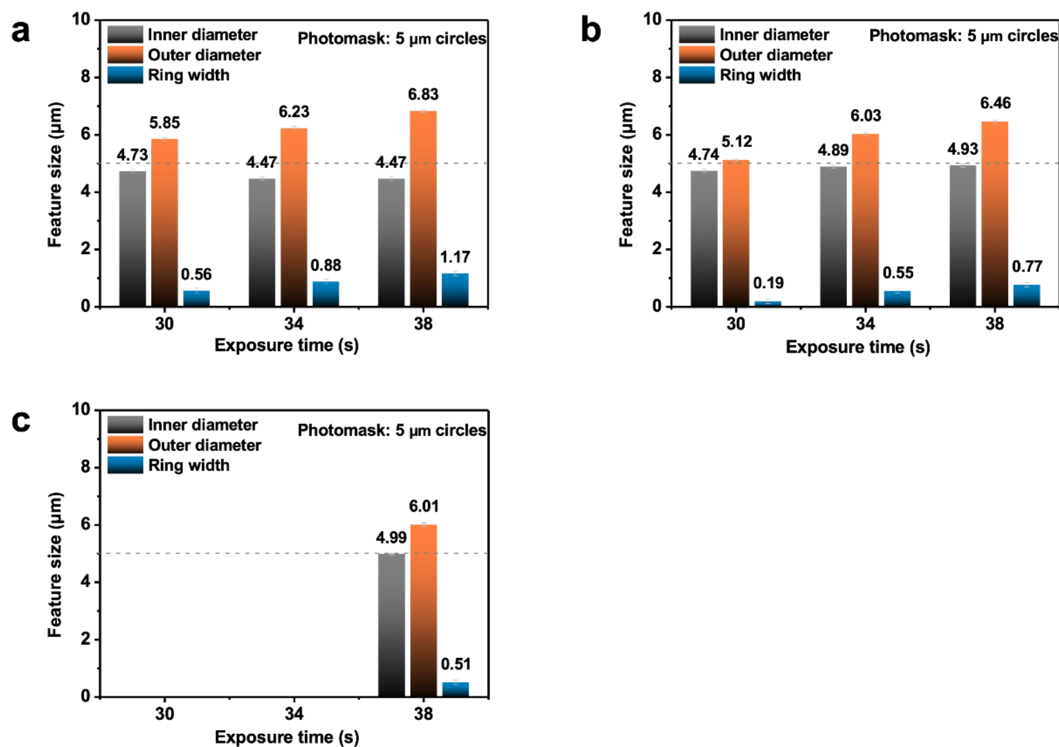

Figure S3.2. Histograms of feature sizes of the SiO_2 microrings prepared at different development time: (a) 20 s, (b) 15 s, and (c) 10 s, with exposure time varying from 30 to 38 s.

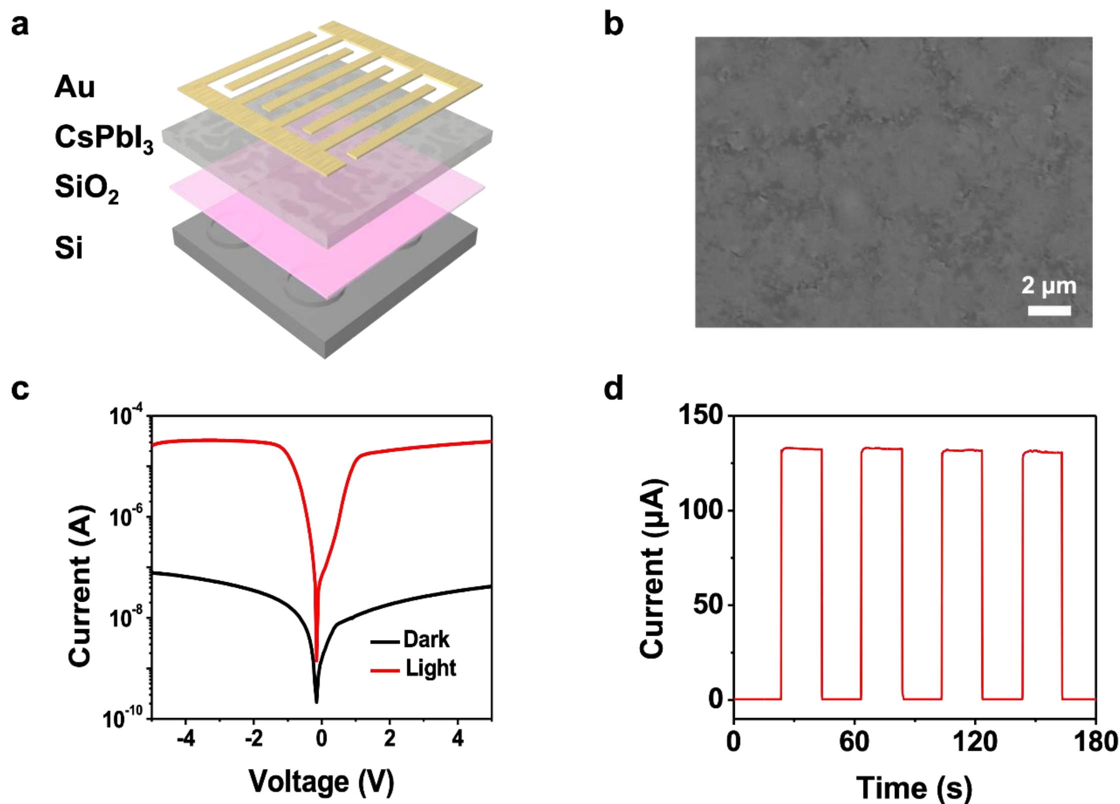

Figure S3.3. (a) Schematic illustration of the photodetector based on a $CsPbI_3$ film spin-coated on the microtube arrays. (b) Scanning electron microscopy image of the coated $CsPbI_3$ thin film on the microtube arrays. (c) Dark/photocurrent of the photodetectors under a Xe lamp (1 mW/cm^2). (d) Time-resolved light response curve of $CsPbI_3$-based photodetector.

3.7 References

1. Tu, M.; Xia, B.; Kravchenko, D. E.; Tietze, M. L.; Cruz, A. J.; Stassen, I.; Hauffman, T.; Teyssandier, J.; De Feyter, S.; Wang, Z.; Fischer, R. A.; Marmiroli, B.; Amenitsch, H.; Torvisco, A.; Velásquez-Hernández, M. d. J.; Falcaro, P.; Ameloot, R. Direct X-Ray and Electron-Beam Lithography of Halogenated Zeolitic Imidazolate Frameworks. *Nat. Mater.* **2020,** *20*, 93-99.

2. Ozel, T.; Bourret, G. R.; Mirkin, C. A. Coaxial Lithography. *Nat. Nanotechnol.* **2015,** *10*, 319-324.

3. Jeon, H.-J.; Kim, K. H.; Baek, Y.-K.; Kim, D. W.; Jung, H.-T. New Top-Down Approach for Fabricating High-Aspect-Ratio Complex Nanostructures with 10 nm Scale Features. *Nano Lett.* **2010,** *10*, 3604-3610.

4. Traub, M. C.; Longsine, W.; Truskett, V. N. Advances in Nanoimprint Lithography. *Annu. Rev. Chem. Biomol. Eng.* **2016,** *7*, 583-604.

5. Huo, F.; Zheng, G.; Liao, X.; Giam, L. R.; Chai, J.; Chen, X.; Shim, W.; Mirkin, C. A. Beam Pen Lithography. *Nat. Nanotechnol.* **2010,** *5*, 637-640.

6. Xu, X.; Yang, Q.; Cheung, K. M.; Zhao, C.; Wattanatorn, N.; Belling, J. N.; Abendroth, J. M.; Slaughter, L. S.; Mirkin, C. A.; Andrews, A. M.; Weiss, P. S. Polymer-Pen Chemical Lift-Off Lithography. *Nano Lett.* **2017,** *17*, 3302-3311.

7. Zhang, X.; Liu, Z. Superlenses to Overcome the Diffraction Limit. *Nat. Mater.* **2008,** *7*, 435-441.

8. Bratton, D.; Yang, D.; Dai, J.; Ober, C. K. Recent Progress in High Resolution Lithography. *Polym. Adv. Technol.* **2006,** *17*, 94-103.

9. Ito, T.; Okazaki, S. Pushing the Limits of Lithography. *Nature* **2000,** *406*, 1027-1031.

10. Holmes, S. J.; Mitchell, P. H.; Hakey, M. C. Manufacturing with DUV Lithography. *IBM J. Res. Dev.* **1997,** *41*, 7-19.

11. Totzeck, M.; Ulrich, W.; Göhnermeier, A.; Kaiser, W. Pushing Deep Ultraviolet Lithography to Its Limits. *Nat. Photonics* **2007,** *1*, 629-631.

12. Wagner, C.; Harned, N. Lithography Gets Extreme. *Nat. Photonics* **2010,** *4*, 24-26.

13. Langner, A.; Päivänranta, B.; Terhalle, B.; Ekinci, Y. Fabrication of Quasiperiodic Nanostructures with EUV Interference Lithography. *Nanotechnology* **2012,** *23*, 105303.

14. Hu, T.; Tseng, C.-K.; Fu, Y. H.; Xu, Z.; Dong, Y.; Wang, S.; Lai, K. H.; Bliznetsov, V.; Zhu, S.; Lin, Q.; Gu, Y. Demonstration of Color Display Metasurfaces *via* Immersion Lithography on a 12-Inch Silicon Wafer. *Opt. Express* **2018,** *26*, 19548.

15. Switkes, M.; Rothschild, M. Immersion Lithography at 157 nm. *J. Vac. Sci. Technol. B* **2001,** *19*, 2353-2356.

16. Rühe, J. And There Was Light: Prospects for the Creation of Micro- and Nanostructures through Maskless Photolithography. *ACS Nano* **2017,** *11*, 8537-8541.

17. Paul, K. E.; Breen, T. L.; Aizenberg, J.; Whitesides, G. M. Maskless Photolithography: Embossed Photoresist as Its Own Optical Element. *Appl. Phys. Lett.* **1998,** *73*, 2893-2895.

18. Manfrinato, V. R.; Wen, J.; Zhang, L.; Yang, Y.; Hobbs, R. G.; Baker, B.; Su, D.; Zakharov, D.; Zaluzec, N. J.; Miller, D. J.; Stach, E. A.; Berggren, K. K. Determining the

Resolution Limits of Electron-Beam Lithography: Direct Measurement of the Point-Spread Function. *Nano Lett.* **2014,** *14*, 4406-4412.

19. Kim, S.; Marelli, B.; Brenckle, M. A.; Mitropoulos, A. N.; Gil, E.-S.; Tsioris, K.; Tao, H.; Kaplan, D. L.; Omenetto, F. G. All-Water-Based Electron-Beam Lithography Using Silk as a Resist. *Nat. Nanotechnol.* **2014,** *9*, 306-310.

20. Cumming, D. R. S.; Thoms, S.; Weaver, J. M. R.; Beaumont, S. P. 3 nm NiCr Wires Made Using Electron Beam Lithography and PMMA Resist. *Microelectron. Eng.* **1996,** *30*, 423-425.

21. Chen, S.; Svedendahl, M.; Antosiewicz, T. J.; Käll, M. Plasmon-Enhanced Enzyme-Linked Immunosorbent Assay on Large Arrays of Individual Particles Made by Electron Beam Lithography. *ACS Nano* **2013,** *7*, 8824-8832.

22. Porrati, F.; Barth, S.; Sachser, R.; Dobrovolskiy, O. V.; Seybert, A.; Frangakis, A. S.; Huth, M. Crystalline Niobium Carbide Superconducting Nanowires Prepared by Focused Ion Beam Direct Writing. *ACS Nano* **2019,** *13*, 6287-6296.

23. Ravi Kiran, N.; Chauhan, M.; Sharma, S. K.; Ghosh, S.; Gonsalves, K. E. Resists for Helium Ion Beam Lithography: Recent Advances. *ACS Appl. Electron. Mater.* **2020,** *2*, 3805-3817.

24. Srinivasan, C.; Mullen, T. J.; Hohman, J. N.; Anderson, M. E.; Dameron, A. A.; Andrews, A. M.; Dickey, E. C.; Horn, M. W.; Weiss, P. S. Scanning Electron Microscopy of Nanoscale Chemical Patterns. *ACS Nano* **2007,** *1*, 191-201.

25. Garcia, R.; Knoll, A. W.; Riedo, E. Advanced Scanning Probe Lithography. *Nat. Nanotechnol.* **2014,** *9*, 577-587.

26. Liu, G.-Y.; Xu, S.; Qian, Y. Nanofabrication of Self-Assembled Monolayers Using Scanning Probe Lithography. *Acc. Chem. Res.* **2000,** *33*, 457-466.

27. Liu, W.; Wang, J.; Xu, X.; Zhao, C.; Xu, X.; Weiss, P. S. Single-Step Dual-Layer Photolithography for Tunable and Scalable Nanopatterning. *ACS Nano* **2021,** *15*, 12180-12188.

28. Widmann, D. W.; Binder, H. Linewidth Variations in Photoresist Patterns on Profiled Surfaces. *IEEE Trans. Electron Devices* **1975,** *22*, 467-471.

29. Lorenz, H.; Despont, M.; Fahrni, N.; Brugger, J.; Vettiger, P.; Renaud, P. High-Aspect-Ratio, Ultrathick, Negative-Tone near-UV Photoresist and Its Applications for MEMS. *Sens. Actuators A: Phys.* **1998,** *64*, 33-39.

30. Fan, R.; Wu, Y.; Li, D.; Yue, M.; Majumdar, A.; Yang, P. Fabrication of Silica Nanotube Arrays from Vertical Silicon Nanowire Templates. *J. Am. Chem. Soc.* **2003,** *125*, 5254-5255.

31. Kim, Y.-Y.; Kim, H.-J.; Jeong, J.-H.; Lee, J.; Choi, J.-H.; Jung, J.-Y.; Lee, J.-H.; Cheng, H.; Lee, K.-W.; Choi, D.-G. Facile Fabrication of Silicon Nanotube Arrays and Their Application in Lithium-Ion Batteries *Advanced Engineering Materials* **2016,** *18*, 1349-1353.

32. Bagolini, A.; Ronchin, S.; Bellutti, P.; Chiste, M.; Verotti, M.; Belfiore, N. P. Fabrication of Novel MEMS Microgrippers by Deep Reactive Ion Etching With Metal Hard Mask. *Journal of Microelectromechanical Systems* **2017,** *26*, 926-934.

33. Jansen, H.; Gardeniers, H.; Boer, M. d.; Elwenspoek, M.; Fluitman, J. A Survey on the Reactive Ion Etching of Silicon in Microtechnology. *J. Micromech. Microeng.* **1996,** *6*, 14-28.

34. Li, Y.; Zhang, H.; Yang, R.; Laffitte, Y.; Schmill, U.; Hu, W.; Kaddoura, M.; Blondeel, E. J. M.; Cui, B. Fabrication of Sharp Silicon Hollow Microneedles by Deep-Reactive Ion Etching towards Minimally Invasive Diagnostics. *Microsyst. Nanoeng.* **2019,** *5*, 41.

35. Xu, X.; Yang, Q.; Wattanatorn, N.; Zhao, C.; Chiang, N.; Jonas, S. J.; Weiss, P. S. Multiple-Patterning Nanosphere Lithography for Fabricating Periodic Three-Dimensional Hierarchical Nanostructures. *ACS Nano* **2017,** *11*, 10384-10391.

36. Chen, G.; Feng, J.; Gao, H.; Zhao, Y.; Pi, Y.; Jiang, X.; Wu, Y.; Jiang, L. Stable α-$CsPbI_3$ Perovskite Nanowire Arrays with Preferential Crystallographic Orientation for Highly Sensitive Photodetectors. *Adv. Funct. Mater.* **2019,** *29*, 1808741.

37. Du, Z.; Fu, D.; Teng, J.; Wang, L.; Gao, F.; Yang, W.; Zhang, H.; Fang, X. $CsPbI_3$ Nanotube Photodetectors with High Detectivity. *Small* **2019,** *15*, 1905253.

Chapter 4

Large-Area Periodic Organic–Inorganic Hybrid Perovskite Nanopyramid Arrays for High-Performance Photodetector and Image Sensor Applications

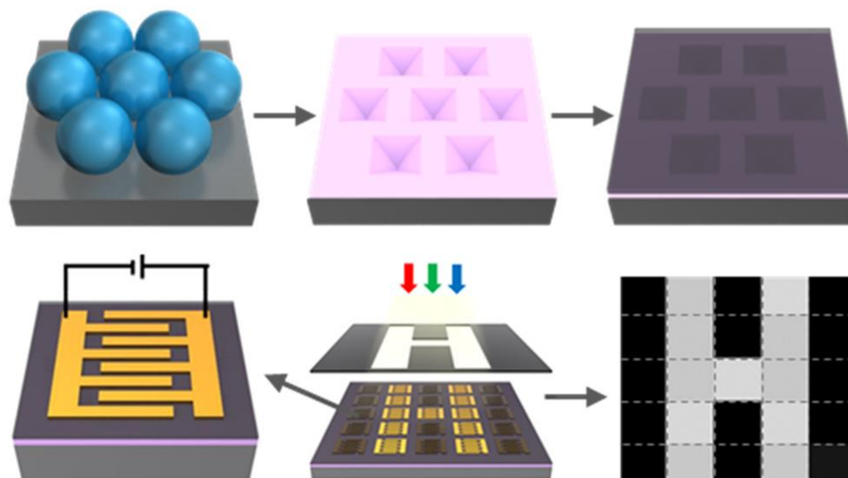

The information in this chapter is reprinted with permission from

ACS Materials Lett. **2021**, *3*, 1189–1196. Copyright (2021) American Chemical Society

Authors: Xu, X.*; **Liu, W.***; Ji, Z.; Hao, D.; Yan, W.; Ye, Z.; Hu, Y.; Fang, M.; Wang, C.; Ma, L.; Huang, J.; Xu, X.; Weiss, P. S.

4.1 Abstract

The rapidly growing interest in organic–inorganic hybrid perovskite materials (such as methylammonium lead triiodide, $MAPbI_3$) for photoelectric applications has prompted investigations of novel strategies to improve photodetection performance. Although a few surface nanofabrication methods have been applied to texture perovskite thin films to enhance light trapping, it remains challenging to pattern large-area periodic perovskite nanoarrays in a tunable and scalable manner. In this work, we report a facile and low-cost approach to fabricate large-area SiO_2/Si nanopyramids arrays through nanosphere lithography. These nanopyramids arrays are used to pattern $MAPbI_3$ thin films. We find that the introduction of nanopyramid arrays enhances the light intensity within the perovskite film, which is confirmed by light absorption tests and optical simulations. As a result, the photodetectors based on $MAPbI_3$ with nanopyramid structures show excellent responsivity of 28.8 ± 1.0 A/W and detectivity of $(3.5 \pm 0.1) \times 10^{11}$ Jones at 650 nm. The photoresponse of the photodetector to pulsed light is highly stable and reproducible, with rise and decay times of ~0.7 and 1.1 ms, respectively. They also have a broader light sensitivity range from ultraviolet to infrared light, *i.e.*, 340 nm to 1100 nm, compared to those without nanostructures. Finally, we demonstrate a prototype image sensor using these photodetector arrays.

4.2 Introduction

Photodetectors, which convert optical signals into electric signals, have been extensively used in a broad range of applications, including optical communication, biosignal sensing, bioimaging, environment monitoring, and security.[1–3] The desired characteristics of the materials for high-performance photodetectors include high optical absorption coefficients, narrow direct band gaps, high response speeds, and low cost.[4–6] Many materials have been explored for photon detection, such as zinc oxide,[7,8] graphene,[9–11] colloidal nanocrystals,[12,13] metal halide perovskites,[14–16] or their hybrids.[17–20] Among them, organic–inorganic hybrid perovskites (such as methylammonium lead trihalide, $MAPbX_3$, where MA = CH_3NH_3, X = Cl, Br, or I) is a promising material for next-generation photodetector applications, because of its high optical absorption coefficient over a wide spectral range, high carrier mobility, and long diffusion length.[21,22] In the pursuit of further improvement in the performance of organic–inorganic hybrid perovskite-based photodetectors, tremendous efforts have been applied to improve the crystallinity and light-trapping ability of organic-inorganic hybrid perovskite films.[23–26]

Organic-inorganic hybrid perovskites are unstable and can easily decompose in the atmosphere, because of the moisture and oxygen in air.[27,28] Increasing their crystallinity can slow this process by reducing material defects, thus improving device stability and performance.[29] For example, Liu *et al.* reported ultrathin single-crystalline perovskite films fabricated *via* a dynamic-flow reaction system, which showed improved optical sensitivity and quantum efficiency when used in a photodetector.[29] Other strategies, such as polymer-templated methods[30] and photolithography-assisted methods,[31] have also been reported to improve device performance.

In addition, the introduction of light scattering or trapping nanostructures to organic-inorganic hybrid perovskite films can enhance photodetector performance, because of

increased light absorption.[32] Note that ordered nanostructures usually have better reproducibility than disordered ones. However, the fabrication of ordered microstructures/nanostructures, such as pillars and lines, usually requires commercial lithographic approaches used in the semiconductor industry, such as photolithography. These methods involve high cost and complexity, especially when patterning structures with submicrometer features. Alternatives such as electron-beam lithography or focused ion beam greatly limit broad applications, because of their slow speeds and high cost. Therefore, the development of alternative large-scale economical nanofabrication approaches is highly desirable for fabricating high-performance organic-inorganic hybrid perovskite photodetectors.

Efforts have been made to find alternative low-cost and scalable nanofabrication methods for submicrometer patterning. Methods such as nanoimprinting,[33,34] nanosphere lithography,[35,36] microcontact printing,[37,38] chemical lift-off lithography,[39,40] and dual-layer photolithography[41] have been developed in the past decades. Recently, these approaches have been adapted to the fabrication of nanostructured perovskites for applications including photodetectors and solar cells. For example, recently periodic perovskites nanonets and nanobowls were fabricated by nanosphere lithography, which showed improved light absorption and photoelectric properties.[23] The enhancement in light absorption is due to increased light scattering within the rationally designed light-trapping nanostructures, which have similar dimensions to the incident light wavelengths. We note that nanostructures were found to improve the crystallinity of the perovskites. For example, perovskite nanoribbons fabricated by nanoimprinting showed both increased light absorption and crystallinity.[42]

Here, we report a strategy that combines nanosphere lithography, for fabricating large-area organic-inorganic hybrid perovskite films, with ordered nanopyramid structures. These

nanopyramids have controlled width, depth, and pitch. The as-prepared $MAPbI_3$ thin film, coated on the top of the periodic nanopyramid array, contributes to enhanced light absorption and photoelectric sensitivity for the photodetector. The role of the periodic nanopyramid array was further investigated using finite-difference time-domain (FDTD) simulations. To demonstrate our method, an image sensor composed of a 5 × 5 photodetector array was fabricated and showed excellent imaging functionality. This strategy, with great adaptivity and expansibility, provides theoretical guidance for the design and fabrication of periodic perovskite nanoarrays with enhanced photoelectric properties for high-performance photodetectors.

4.3 Materials and Methods

Materials. Polystyrene (PS) nanospheres with sizes from 500 nm to 2 μm were purchased from Rigor Bioscience Development Inc.; methylammonium iodide (CH_3NH_3I, MAI) and PbI_2 was purchased from Xi'an Polymer Light Technology Corp. All the materials and reagents were used as received.

Characterization. The morphologies of the Si nanopyramid structures were measured by scanning electron microscopy (SEM, JEOL JSM-6060LA). A Keithley 4200-Semiconductor Characterization System was used to test the photoelectric properties. A two-probe station was used to conduct the electrical measurements. The tip size of each probe was 5 μm. The voltage was set from -5 V to 5 V, and the scan interval was set to 20 mV.

Fabrication of SiO_2/Si Nanopyramid Arrays. Si substrates were cleaned with isopropanol, acetone, and deionized water in sequence for 10 min and further dried using a nitrogen gas gun. Then, the cleaned Si substrates were treated with an oxygen plasma cleaner at 100 W for 600 s and

covered with a tightly packed monolayer of PS nanospheres. The diameters of the PS nanospheres were reduced by oxygen plasma at 200 W for 30 s (for 500 nm diameter PS nanospheres), 75 s (for 1 μm diameter PS nanospheres), and 180 s (for 2 μm diameter PS nanospheres). A 30-nm thick chromium film was deposited by thermal evaporation. The substrate was immersed in a 4:1 mixture of 30% KOH aqueous solution and isopropyl alcohol at 75 °C. The wet etching time was 20 s for PS nanospheres with diameters of 500 nm, 60 s for PS nanospheres with diameters of 1 μm, and 120 s for PS nanospheres with diameters of 2 μm. The etching time for the chromium is about 120 s. Finally, silicon dioxide with a thickness of 200 nm was deposited on the surface of the Si substrate with the nanopyramid array by thermal evaporation.

Fabrication of $MAPbI_3$ on SiO_2/Si Nanopyramid Substrates. 200 nm of SiO_2 was deposited on the Si nanopyramid. Then, 50 μL of 1M $MAPbI_3$ perovskite precursor solution in γ-butyrolactone in dimethylsulphoxide (volume ratio of 7:3) was spin-coated on the SiO_2/Si nanopyramid substrate at 5,000 rpm for 40 s. During the spin-coating, 100 μL toluene was added dropwise on the substrate. Then, the sample was annealled at 100 °C for 10 min to form $MAPbI_3$ on a SiO_2/Si nanopyramid substrate.

Fabrication of Perovskite Photodetectors and Image Sensors. The electrodes of the photodetectors were fabricated by thermal evaporation of copper under a shadow mask. Copper electrodes had a thickness of 300 nm. Photodetectors based on P-1 samples, P-2 samples, P-3 samples, and Flat samples were fabricated under identical conditions.

Calculation of the Responsivity (R) of the Photodetector Based on $MAPbI_3$ Film on SiO_2/Si Nanopyramid Substrate. The R value is calculated from:

$$R = \frac{J_{ph} - J_d}{L_{light}} = \frac{I_{light} - I_{dark}}{A \times L_{light}},$$

where I_{light} is the photocurrent of the photodetector under illumination, I_{dark} is the current in the dark, A is the active area ($A = W \times L$, where W is the the channel width of the device, L is the channel length of the device) of the photodetector, and L_{light} is the light intensity. In this work, I_{light} and I_{dark} for a typical photodetector based on $MAPbI_3$ film on SiO_2/Si nanopyramid substrate were measured to be 1.24×10^{-7} A and 2.94×10^{-9} A, respectively. The wavelength of the incident light was 650 nm. Active area for the photodetector was ~1.4×10^{-3} cm^2 (W is 2800 µm and L is 50 µm). The light intensity for the incident light (650 nm) was fixed at 3 µW/cm^2, which was measured by an optical power meter. Thus the R value was estimated to be 28.78 A/W. When we used white light (the light intensity was 1 mW/cm^2) as the light source, I_{light} and I_{dark} for the photodetector based on $MAPbI_3$ film on SiO_2/Si nanopyramid substrate were measured to be 3.10×10^{-5} and 1.13×10^{-8} A, respectively. The R value was estimated to be 22.13 A/W.

4.4. Results and Discussions

To fabricate large-area periodic nanopyramid arrays as the templating substrates for $MAPbI_3$ films, we designed a patterning strategy that combines nanosphere lithography and anisotropic etching of Si, as illustrated in **Figure 4.1**.

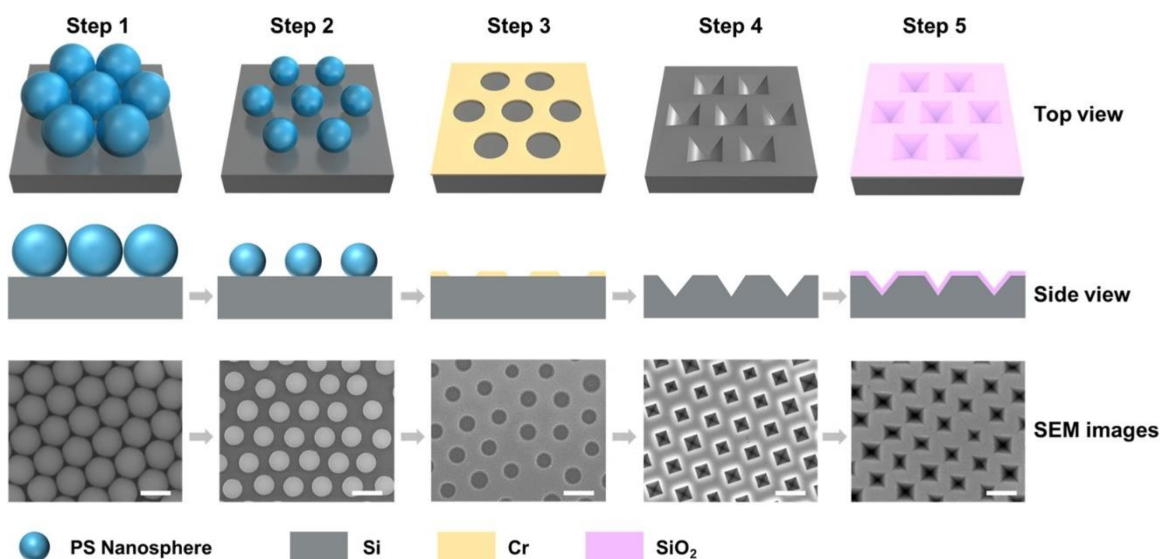

Figure 4.1. Schematic fabrication process of inverted-pyramid arrays by nanosphere lithography and related scanning electron microscopy (SEM) images. Step 1: A monolayer of close-packed polystyrene (PS) nanospheres was prepared on a Si substrate. Step 2: The sizes of PS nanospheres were reduced by O_2 plasma etching. Step 3: A 30 nm-thick Cr film was deposited followed by removal of PS nanospheres. Step 4: KOH-anisotropic etching of exposed Si and selective etching of Cr to form inverted-pyramid arrays of Si. Step 5: Thermal vapor deposition of silicon oxide film (~200 nm) on inverted-pyramid arrays of Si. Scale bars = 2 µm.

(*Step 1*) Close-packed polystyrene (PS) nanospheres were assembled into monolayers on a Si(100) substrate. In order to generate submicrometer features, the sizes of PS nanospheres were chosen to be 500 nm, 1 µm, and 2 µm.

(*Step 2*) The sizes of PS nanospheres were reduced *via* oxygen plasma. The sizes of the PS nanospheres were reduced by *ca.* 1/3 (see **Figure 4.1**, as well as **Figures S4.1** and **S4.2** in the Supporting Information).

(*Step 3*) The PS nanospheres were coated with chromium *via* thermal evaporation, then lifted off, leaving large-area periodic Cr nanoholes.

(*Step 4*) Exposed Si in the nanoholes was etched by KOH solution to form inverted nanopyramid structures. The as-fabricated inverted nanopyramids were 1000, 580, and 260 nm in base size and 690, 400, and 180 nm in depth, respectively. Afterward, the Cr film was removed, leaving a pristine Si nanopyramid array (**Figure S4.3** in the Supporting Information).

(*Step 5*) A 200-nm-thick SiO_2 film was coated on the Si nanopyramids *via* thermal vapor deposition. Then, a large area of SiO_2/Si nanopyramid arrays was fabricated.

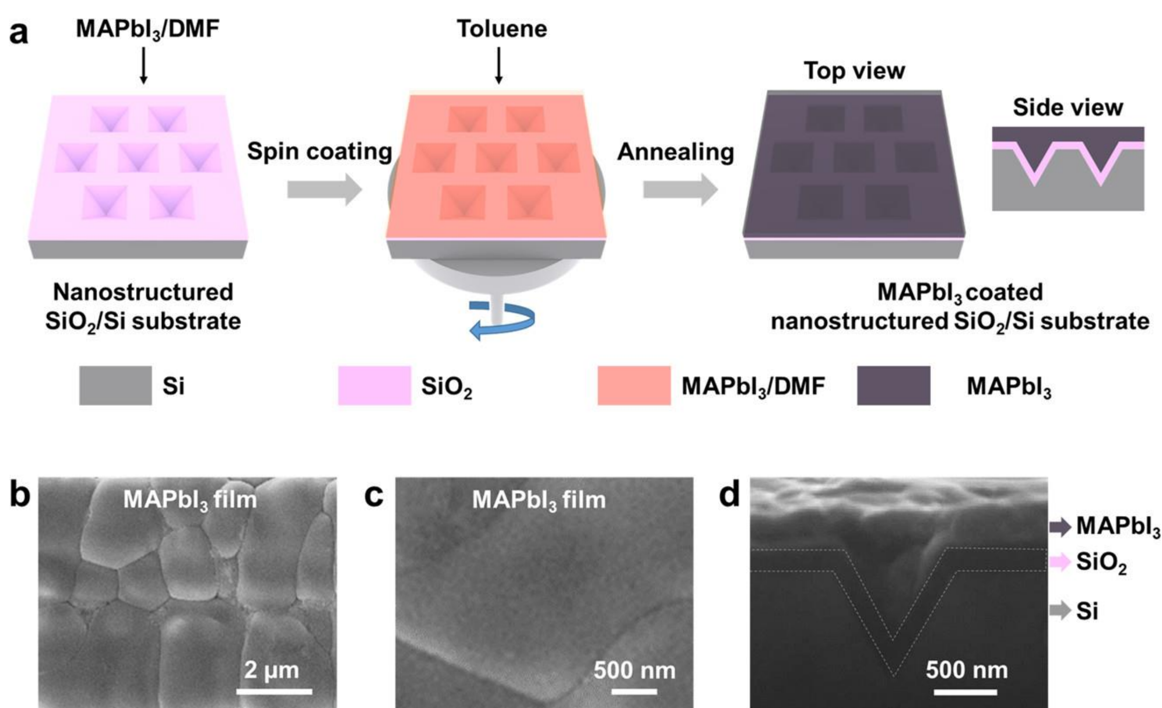

Figure 4.2. (a) Schematic coating process of $MAPbI_3$ film on inverted-pyramid arrays of SiO_2/Si. (b, c) Scanning electron microscopy (SEM) images of the $MAPbI_3$ film (top view). (d) Cross-sectional SEM image of the $MAPbI_3$ film (side view).

Next, $MAPbI_3$ film was spin-coated on SiO_2/Si nanopyramids (**Figure 4.2a**). During the spin-coating process, toluene was applied as the antisolvent[43] to facilitate the crystallization of $MAPbI_3$, followed by a thermal annealing process to increase crystallinity. (See further details in the Supporting Information.)

As shown in **Figure 4.2b**, a uniform and compact $MAPbI_3$ film was formed on the SiO_2/Si nanopyramid substrate. The SEM images (**Figures 4.2c**,**d**) confirm that the $MAPbI_3$ films on the SiO_2/Si nanopyramid substrates have flat surfaces, and thicknesses of ~200 nm, with underlying SiO_2/Si nanopyramids fully filled with $MAPbI_3$.

The absorbance spectra of $MAPbI_3$ grown on different substrates were recorded to determine their optical properties. Note that in all the tests and characterizations, at least five samples for each size of nanopyramids were fabricated and tested. The following sizes were tested: P-1 samples, nanopyramids with lateral lengths of 1000 nm and 2 μm pitch; P-2 samples, nanopyramids with lateral lengths of 580 nm and 1 μm pitch; P-3 samples, nanopyramids with lateral lengths of 260 and 500 nm pitch; and Flat samples, flat SiO_2/Si substrate (see **Figure 4.1**, as well as **Figures S4.1** and **S4.2**). From the results, we found that P-1 samples, P-2 samples, and P-3 samples showed increased light absorption across the visible light comparing to the Flat samples (**Figure 4.3a**). These results are consistent with previous reports that $MAPbI_3$ films formed on nanostructured substrates generally have higher light absorption in the visible range than those formed on flat substrates.[23,42,44]

To evaluate their optoelectronic properties, we designed and fabricated photodetector arrays. The interdigitated electrodes for the photodetectors were designed to have aspect ratios of 1/56 to prevent interference between different devices. (The channel length and width of the

photodetectors were 50 and 2800 μm, **Figure S4.4**). **Figure 4.3b** depicts the typical current versus voltage (*I-V*) curves of photodetectors measured in the dark and under white light illumination at 1 mW/cm^2. A device based on a Flat sample was also tested as a control experiment. The photodetectors based on $MAPbI_3$ films with nanopyramid structures (P-2 samples) showed significantly higher current (I_{light}) under white light illumination, *ca.* 3300 times larger (at 5 V bias) than in the darkness (I_{dark}). We also tested P-1 samples and P-3 samples, and obtained similar photocurrents to P-2 samples (the *I-V* curves are provided in **Figure S4.5**.) While the photodetectors without nanopyramid structures (Flat) only showed *ca.* 280 times larger (at 5 V bias) current under the same illumination as that in the darkness, comparable to prior reports.[45–47] Thus, the optoelectronic properties of the $MAPbI_3$ devices are improved by the introduction of nanopyramid structures.

We further studied the wavelength dependence of the photodetectors. **Figure 4.3c** shows the *I-V* curves of the photodetectors based on P-2 sample arrays measured under visible light with different wavelengths and in darkness.

In photodetectors, one key parameter is the responsivity (R), which represents the signal strength under illumination. It can be calculated using:

$$R = \frac{J_{ph} - J_{dark}}{I_{light}} \quad \textbf{Eq. (4.1)}$$

where J_{ph} is the photocurrent density, J_{dark} is the dark current density, and I_{light} is the incident light intensity.[167]

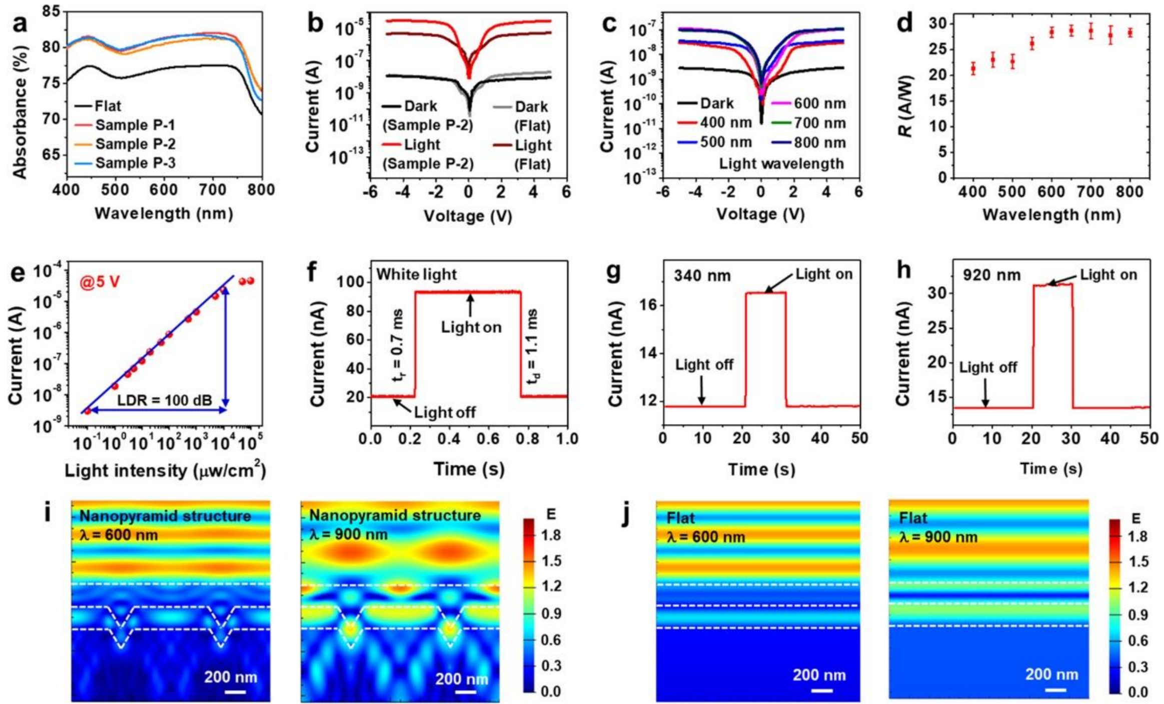

Figure 4.3. (a) Measured absorption spectra of $MAPbI_3$ films on SiO_2/Si nanopyramid substrates and flat substrates in the visible region. (b) Dark/photocurrent of the photodetectors. The incident light intensity is 1 mW/cm^2. (c) *I-V* curves of the photodetector (sample P-2, see text) measured in the dark and under illumination with a range of wavelengths. (d) Plots of responsivity of the photodetector (sample P-2) as a function of light wavelength. (e) Photocurrent-light intensity curve of the photodetector. The voltage was fixed at 5 V. (f) The rise time and decay time of the photodetector. (g, h) Time-resolved photoresponse of the photodetector at 340 and 920 nm, respectively. The incident light intensity is 3 μW/cm^2. (i) Finite-difference time-domain (FDTD) simulations for $MAPbI_3$ films on SiO_2/Si nanopyramid substrates under light illumination at 600 and 900 nm. (j) The magnitude of the electric field obtained from FDTD simulations for $MAPbI_3$ films on flat substrate under light illumination at 600 and 900 nm.

According to **eq 4.1**, the R values of the photodetectors based on $MAPbI_3$ film on SiO_2/Si nanopyramid substrates (P-2 samples) are determined to be 22.1 ± 1.3 A/W (white light) and 28.8 ± 1.0 A/W (at 650 nm), respectively. As shown in **Figure 4.3d**, across the visible light range from 400 nm to 800 nm, the R values are maintained at high levels, from 21.3 ± 1.2 A/W to 28.8 ± 1.0 A/W. We observed selectivity in the visible range, with R values that are higher in the wavelength region from 600 nm to 800 nm than those from 400 nm to 500 nm, with the peak at *ca.* 650 nm (R = 28.8 A/W). Similar phenomena have been reported previously.[48−50]

Another key parameter of photodetectors is the specific detectivity (D*), which represents the ability to detect weak signals. It can be calculated by using the expression

$$D^* = \frac{(A \cdot f)^{0.5}}{(I_n/R)} \approx \frac{R}{(2q \cdot J_{dark})^{0.5}} \qquad \textbf{Eq. (4.2)}$$

where A is the effective area of the device, f is the electrical bandwidth, and I_n is the noise current, and q is the fundamental unit of charge. The noise power spectrum of a photodetector based on a P-2 sample is provided in **Figure S4.6** in the Supporting Information. The low-frequency noise (at 1 Hz) originates mainly from mobility fluctuations caused by the scattering of acoustic phonons and ionized impurities, which also dominate the device's total noise.

The D* values of the photodetector based on P-2 samples are $(2.7 \pm 0.1) \times 10^{11}$ Jones (white light) and $(3.5 \pm 0.1) \times 10^{11}$ Jones (at 650 nm), respectively. The D* of the photodetector is distributed from $(2.6 \pm 0.1) \times 10^{11}$ Jones to $(3.5 \pm 0.1) \times 10^{11}$ Jones under a monochromatic light range from 400 nm to 800 nm (**Figure S4.7**), indicating that the device is sensitive to weak light in the visible range.

The R and D^* values of the photodetector based on perovskite films with pyramid array structures reported in this work are among the highest reported for $MAPbI_3$ film-based photodetectors (see **Table 4.1**).[23,42,51–55]

Table 4.1. Comparison of the key parameters of photodetectors based on different materials.

Materials	Light sources	R (A/W)	D^* (Jones)	Reference
$MAPbI_3$ pyramids	white light	22.1	2.7×10^{11}	this work
$MAPbI_3$ pyramids	650 nm	28.8	3.5×10^{11}	this work
$MAPbI_3$ nanoflake	265 nm	12.0	1.0×10^{11}	ref [168]
$MAPbI_3$ porous photonic crystals	white light	12.7	3.2×10^{13}	ref [169]
$MAPbI_3$ nanonet	white light	0.6	-	ref [170]
	700 nm	10.3	-	
$MAPbI_3$ network	650 nm	0.1	1.0×10^{12}	ref [171]
$MAPbI_3$ film	white light	0.2	-	ref [172]
$MAPbI_3$ film	670 nm	0.3	-	ref [173]
$MAPbI_3$ film	365 nm	3.5	-	ref [174]

To quantify the photocurrent, we performed light intensity-dependent measurements, as shown in **Figure S4.8** in the Supporting Information. The linear dynamic range (LDR) refers to the area where the photocurrent of the photodetector maintains a linear relationship with the incident light intensity, which can be obtained from the photocurrent-light intensity curve (**Figure 4.3e**). The LDR of the photodetector based on P-2 samples is calculated to be 100 dB from

$$\mathrm{LDR} = 20\log\frac{J_{upper}}{J_{lower}} = \frac{L_{upper}}{L_{lower}} \qquad \textbf{Eq. (4.3)}$$

where J and L denote the current density and light intensity, respectively.[22] A broad linear dynamic range ensures that the image sensor can work stably over a relatively wide range of light intensity.

The photoresponse of the fabricated photodetectors to pulsed light is highly stable and reproducible. The rise time (t_r) of a photodetector is defined as the time interval for the response to rise from 10% to 90% of its peak value, whereas the decay time (t_d) is defined as the time interval for the response to decay from 90% to 10% of its peak value. Here, the rise and decay times of the photodetector are determined to be ~0.7 and 1.1 ms, respectively, as shown in **Figure 4.3f**, as well as **Figure S4.9** in the Supporting Information, which are similar to previously reported values for perovskite films.[56–58] Such a high response speed of the photodetector is due to the fast carrier separation and transportation of the photogenerated carriers in the high-quality $MAPbI_3$ films on SiO_2/Si nanopyramid substrates. These photodetectors not only show high sensitivity to visible light, they also showed significant photoresponses to infrared (from 800–1100 nm) and ultraviolet (340–400 nm) light, as shown in **Figures 4.3g**,**h**, as well as **Figure S4.10** in the Supporting Information. Such a broad range of sensitivity is not typically observed for $MAPbI_3$ films grown on flat substrates. These results are due to both the increased light absorption and crystallinity of the perovskite due to the nanostructures used.

To understand the increased photoresponses of these photodetectors, we performed optical simulations *via* FDTD methods to study their optical properties. The electric field distributions of $MAPbI_3$ films on SiO_2/Si nanopyramid substrates and on flat substrates were also simulated. (Note that the incident light was set at 600 and 900 nm, and the nanopyramids had lengths of 500 nm and 1 μm pitch.) As shown in **Figure 4.3i**, the electric field fluctuates periodically along the nanopyramids, and is enhanced inside the nanopyramid structure, because the incident light can reflect multiple times inside the nanopyramids. In contrast, the electric field on flat substrates is uniformly distributed (**Figure 4.3j**). Thus, the optical simulations are consistent with the experimental results that the introduction of nanopyramid structures to the $MAPbI_3$ film increases their light absorption and light sensitivity.

Image sensors are a key application of photodetectors. In order to demonstrate their potential application in image sensing, an image sensor containing a 5 × 5 photodetector array was fabricated. Each photodetector has a size of 750 μm × 800 μm. Note that photodetectors for high-resolution sensing can be straightforwardly fabricated by using smaller electrodes. As shown schematically in **Figure 4.4a**, a 1.5 cm × 1.5 cm metallic mask with a hollow character "H" was placed on the image sensor. We first investigated the photoresponse of a single photodetector (based on a P-2 sample) under pulsed white light at a bias voltage of 5.0 V. As shown in **Figure 4.4b**, the photoresponse to pulsed light is highly stable and reproducible. Then, the image sensor was tested with light off/on at a bias voltage of 5 V. When the light is off, all the photodetectors or "pixels" showed low dark currents ($<5 \times 10^{-8}$ A), and the "H" character cannot be recognized (**Figure 4.4c**). Under illumination, all the photodetectors or pixels right under the character "H" exhibit significantly increased photocurrents ($>2 \times 10^{-6}$ A). Those pixels in the covered regions showed slight increases in current ($<1 \times 10^{-7}$ A), due to imperfect light blocking, but remain much

smaller than those under direct illumination. Thus, by mapping the photocurrent, the character “H” can be recognized (**Figure 4.4d**).

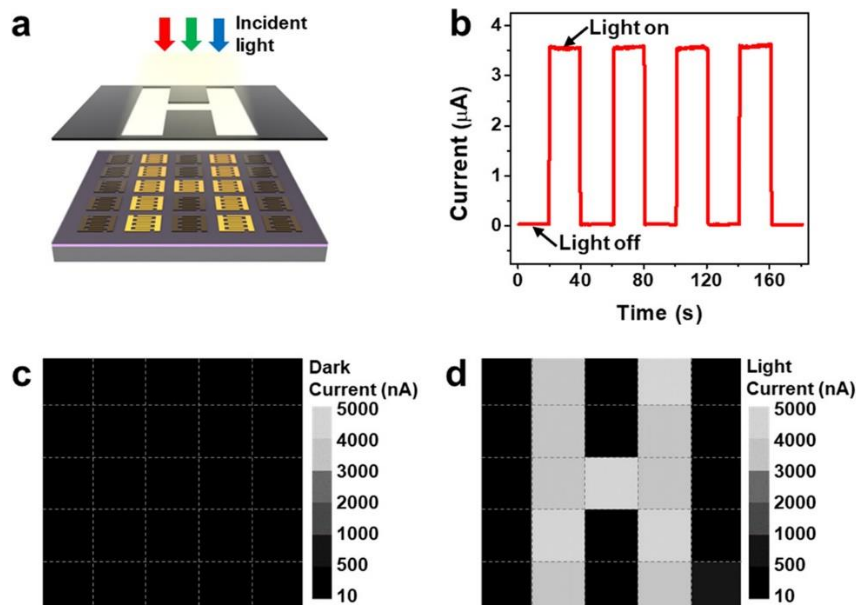

Figure 4.4. (a) Schematic illustration of a photodetector array with 5 × 5 pixels. (b) Time-resolved photoresponse of the photodetector based on a $MAPbI_3$ film on a SiO_2/Si nanopyramid substrate (P-2 sample) under white light (1 mW/cm^2). (c, d) Output results of the photodetector array in darkness and under illumination, respectively.

4.5 Conclusions and Prospects

In summary, we have successfully prepared large arrays of SiO_2/Si nanopyramids by nanosphere lithography, and we have demonstrated their application in enhancing the photosensitivity of perovskite materials. The underlying SiO_2/Si nanopyramids were found to enhance the light absorption of the coated $MAPbI_3$ films, as also supported by corresponding FDTD optical simulations. From the simulation results, we find that the electric field within the $MAPbI_3$-coated nanopyramids was enhanced, which leads to the increased photosensitivity of the $MAPbI_3$. The photodetector with nanopyramid structures exhibited high responsivity, up to 28.8 ± 1.0 A/W, large specific detectivity of $(3.5 \pm 0.1) \times 10^{11}$ Jones, and a broad linear dynamic range of 100 dB. They also showed a broader light sensitivity range from the near-ultraviolet to the infrared (*i.e.*, from 340 nm to 1100 nm), compared to those without nanostructures, which results from the combined effects of light enhancement and improved crystallinity of the $MAPbI_3$. A prototype image sensor array was fabricated and it demonstrated image sensing at high contrast. These nanopyramid arrays can be easily applied to a broad range of other light-sensing materials, such as $MAPbBr_3$, ZnO, TiO_2, and GaN. This strategy can also be readily adapted for a broad range of light-related applications, such as photovoltaics, photocatalysis, and photodriven seawater desalination.

4.6 Supplementary Materials

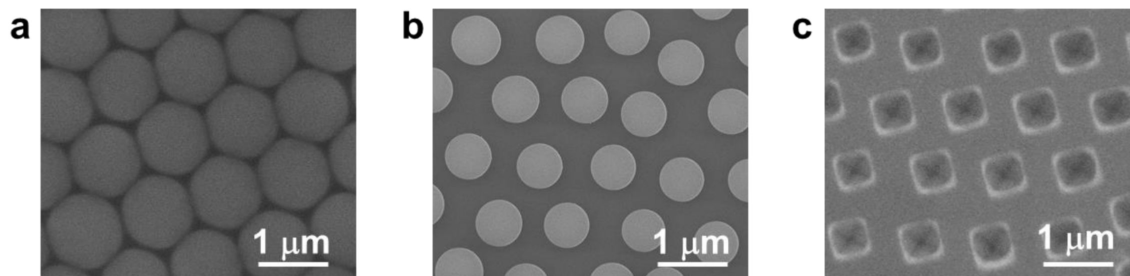

Figure S4.1. Scanning electron microscopy (SEM) images of: (a) polystyrene (PS) microspheres with 1 μm diameters, (b) size reduced PS microspheres, (c) inverted Si nanopyramid arrays.

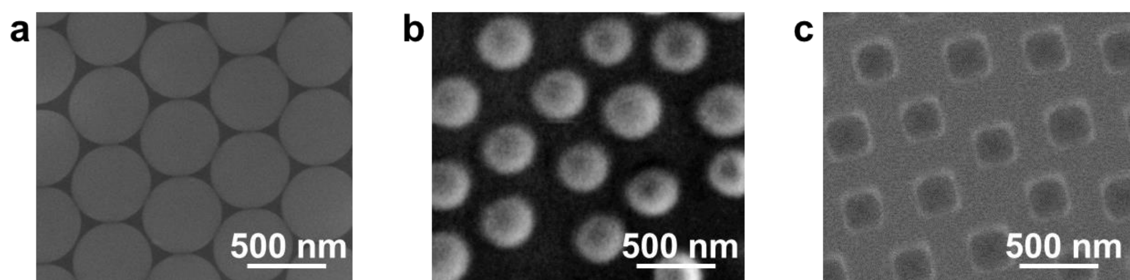

Figure S4.2. Typical scanning electron microscopy (SEM) images of: (a) polystyrene (PS) nanospheres with 500 nm diameters, (b) size reduced PS nanospheres, (c) inverted Si nanopyramid arrays.

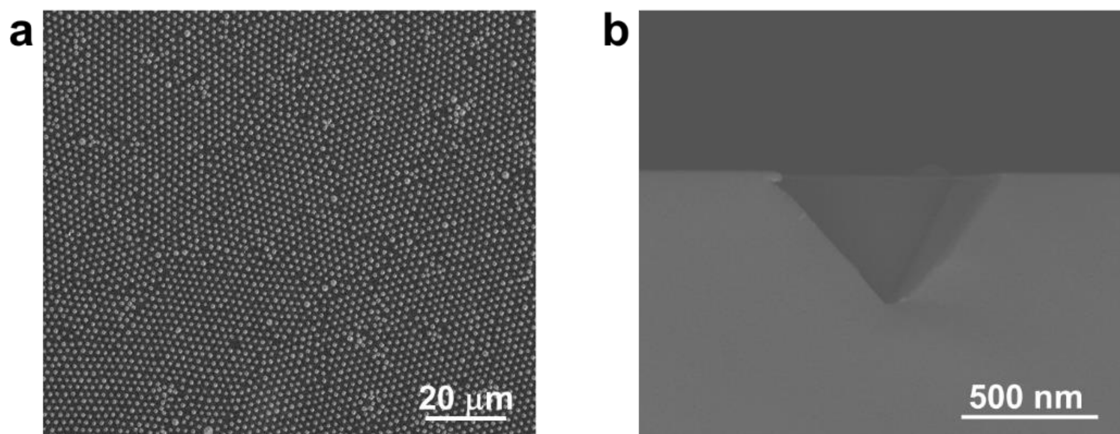

Figure S4.3. (a) Scanning electron microscopy (SEM) image of the nanopyramid array. (b) Cross-sectional SEM image of a single pyramid.

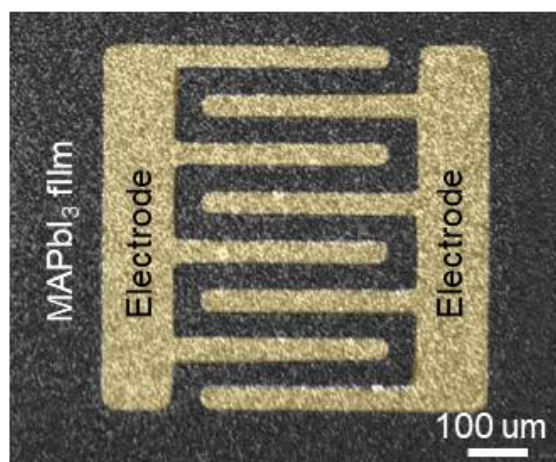

Figure S4.4. Scanning electron microscope image of the photodetector based on a $MAPbI_3$ film on a SiO_2/Si nanopyramid substrate.

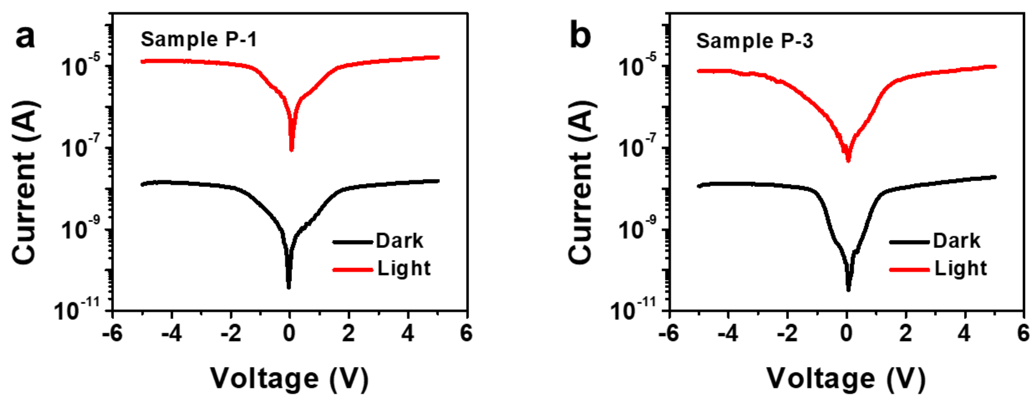

Figure S4.5. Dark/Photocurrent of the photodetector based on a $MAPbI_3$ film on a SiO_2/Si nanopyramid substrate (a P-1 sample and a P-3 sample). The incident light intensity is 1 mW/cm.

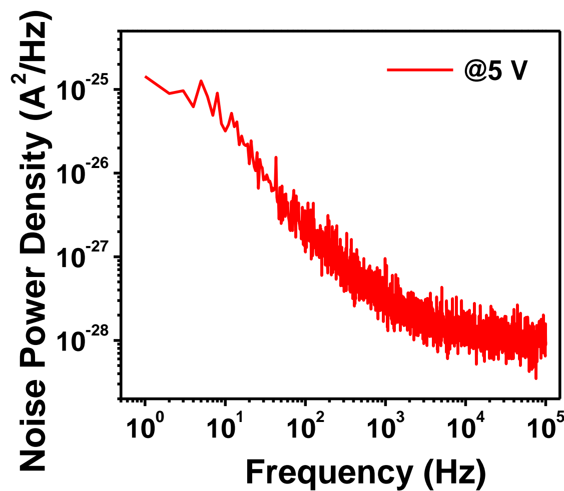

Figure S4.6. Noise power density of the photodetector based on a $MAPbI_3$ film on a SiO_2/Si nanopyramid substrate (a P-2 sample).

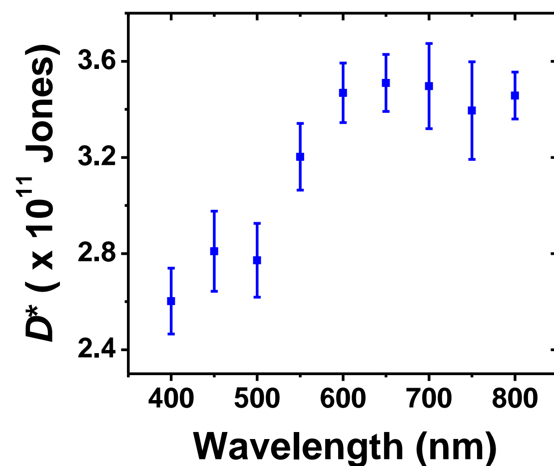

Figure S4.7. Plots of specific detectivity of the photodetector (a P-2 sample) as a function of light wavelength.

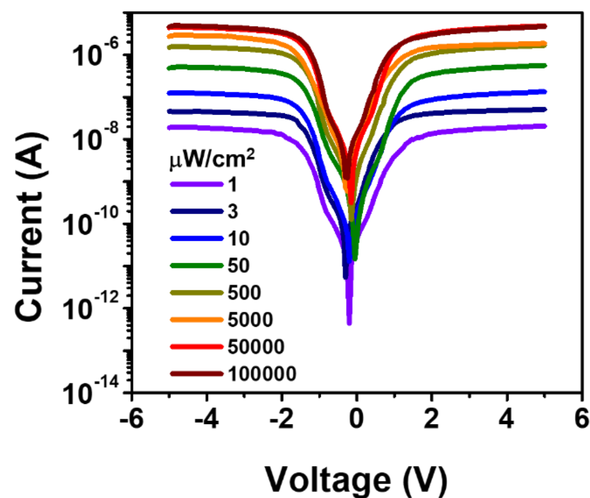

Figure S4.8. Photocurrent of the photodetector based on a $MAPbI_3$ film on a SiO_2/Si nanopyramid substrate (a P-2 sample) under white light at different light intensities.

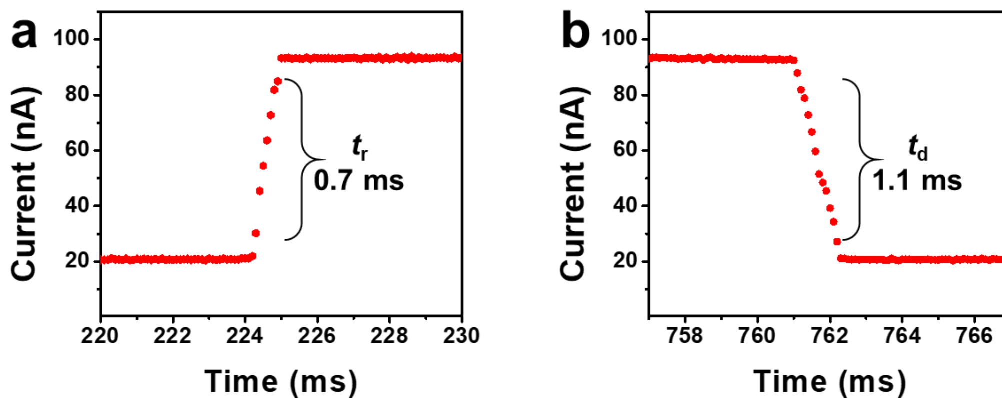

Figure S4.9. Time-resolved photoresponse of the photodetector for a $MAPbI_3$ film on SiO_2/Si nanopyramid substrate (a P-2 sample) under white light. Enlarged views of the (a) rising edge and (b) decaying edge of the photodetector.

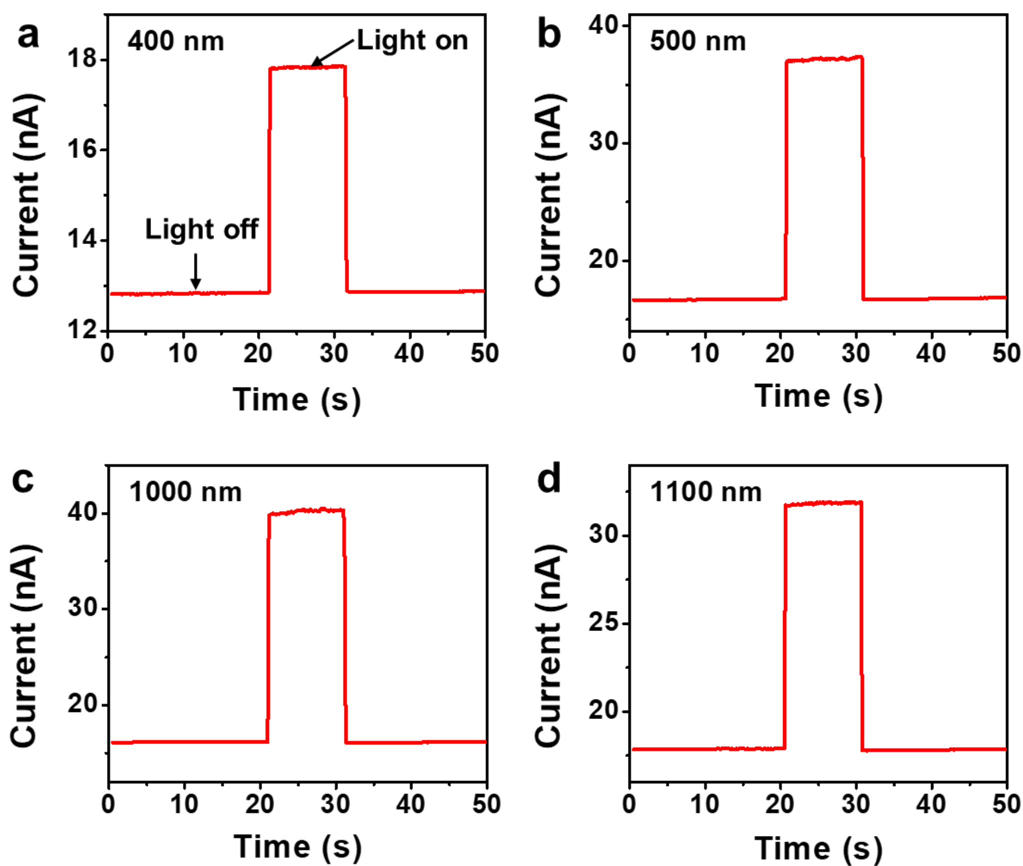

Figure S4.10. Time-resolved photoresponse of the photodetector based on a $MAPbI_3$ film on a SiO_2/Si nanopyramid substrate (a P-2 sample) under light illumination at wavelengths of: (a) 400 nm, (b) 500 nm, (c) 1000 nm, and (d) 1100 nm. The light intensity was fixed at 3 μW/cm^2.

4.7 References

1. Li, C.; Wang, H.; Wang, F.; Li, T.; Xu, M.; Wang, H.; Wang, Z.; Zhan, X.; Hu, W.; Shen, L. Ultrafast and Broadband Photodetectors Based on a Perovskite/Organic Bulk Heterojunction for Large-Dynamic-Range Imaging. *Light: Science & Applications* **2020,** *9*, 31.

2. Xu, X.; Deng, W.; Zhang, X.; Huang, L.; Wang, W.; Jia, R.; Wu, D.; Zhang, X.; Jie, J.; Lee, S.-T. Dual-Band, High-Performance Phototransistors from Hybrid Perovskite and Organic Crystal Array for Secure Communication Applications. *ACS Nano* **2019,** *13*, 5910-5919.

3. Li, Y.; Shi, Z.; Liang, W.; Wang, L.; Li, S.; Zhang, F.; Ma, Z.; Wang, Y.; Tian, Y.; Wu, D.; Li, X.; Zhang, Y.; Shan, C.; Fang, X. Highly Stable and Spectrum-Selective Ultraviolet Photodetectors Based on Lead-Free Copper-Based Perovskites. *Mater. Horiz.* **2020,** *7*, 530-540.

4. Cai, S.; Xu, X.; Yang, W.; Chen, J.; Fang, X. Materials and Designs for Wearable Photodetectors. *Adv. Mater.* **2019,** *31*, 1808138.

5. Long, M.; Wang, P.; Fang, H.; Hu, W. Progress, Challenges, and Opportunities for 2D Material Based Photodetectors. *Adv. Funct. Mater.* **2018,** *29*, 1803807.

6. Li, Y.; Zhang, X.; Huang, H.; Kershaw, S. V.; Rogach, A. L. Advances in Metal Halide Perovskite Nanocrystals: Synthetic Strategies, Growth Mechanisms, and Optoelectronic Applications. *Mater. Today* **2020,** *32*, 204-221.

7. Liu, X.; Gu, L.; Zhang, Q.; Wu, J.; Long, Y.; Fan, Z. All-Printable Band-Edge Modulated ZnO Nanowire Photodetectors with Ultra-High Detectivity. *Nat. Commun.* **2014,** *5*, 4007.

8. Yuan, Z.; Wang, W.; Wu, H.; Nie, F.; He, J. A Solution-Processed ZnO Quantum Dots Ultraviolet Photodetector with High Performance Driven by Low Operating Voltage. *Mater. Lett.* **2020,** *278*, 128413.

9. Lee, I.-H.; Yoo, D.; Avouris, P.; Low, T.; Oh, S.-H. Graphene Acoustic Plasmon Resonator for Ultrasensitive Infrared Spectroscopy. *Nat. Nanotechnol.* **2019,** *14*, 313-319.

10. Lin, H.; Sturmberg, B. C. P.; Lin, K.-T.; Yang, Y.; Zheng, X.; Chong, T. K.; de Sterke, C. M.; Jia, B. A 90-nm-Thick Graphene Metamaterial for Strong and Extremely Broadband Absorption of Unpolarized Light. *Nat. Photonics* **2019,** *13*, 270-276.

11. Xia, Z.; Li, P.; Wang, Y.; Song, T.; Zhang, Q.; Sun, B. Solution-Processed Gold Nanorods Integrated with Graphene for Near-Infrared Photodetection *via* Hot Carrier Injection. *ACS Appl. Mater. Interfaces* **2015,** *7*, 24136-24141.

12. Yin, Y.; Alivisatos, A. P. Colloidal Nanocrystal Synthesis and the Organic-Inorganic Interface. *Nature* **2004,** *437*, 664-670.

13. Saran, R.; Curry, R. J. Lead Sulphide Nanocrystal Photodetector Technologies. *Nat. Photonics* **2016,** *10*, 81-92.

14. Protesescu, L.; Yakunin, S.; Bodnarchuk, M. I.; Krieg, F.; Caputo, R.; Hendon, C. H.; Yang, R. X.; Walsh, A.; Kovalenko, M. V. Nanocrystals of Cesium Lead Halide Perovskites ($CsPbX_3$, X = Cl, Br, and I): Novel Optoelectronic Materials Showing Bright Emission with Wide Color Gamut. *Nano Lett.* **2015,** *15*, 3692-3696.

15. Wu, L.; Hu, H.; Xu, Y.; Jiang, S.; Chen, M.; Zhong, Q.; Yang, D.; Liu, Q.; Zhao, Y.; Sun, B.; Zhang, Q.; Yin, Y. From Nonluminescent Cs_4PbX_6 (X = Cl, Br, I) Nanocrystals to Highly

Luminescent $CsPbX_3$ Nanocrystals: Water-Triggered Transformation through a CsX-Stripping Mechanism. *Nano Lett.* **2017,** *17*, 5799-5804.

16. Zhou, Y.; Chen, J.; Bakr, O. M.; Mohammed, O. F. Metal Halide Perovskites for X-Ray Imaging Scintillators and Detectors. *ACS Energy Lett.* **2021,** *6*, 739-768.

17. Jin, Y.; Wang, J.; Sun, B.; Blakesley, J. C.; Greenham, N. C. Solution-Processed Ultraviolet Photodetectors Based on Colloidal ZnO Nanoparticles. *Nano Lett.* **2008,** *8*, 1649-1653.

18. Krieg, F.; Ochsenbein, S. T.; Yakunin, S.; ten Brinck, S.; Aellen, P.; Suess, A.; Clerc, B.; Guggisberg, D.; Nazarenko, O.; Shynkarenko, Y.; Kumar, S.; Shih, C. J.; Infante, I.; Kovalenko, M. V. Colloidal $CsPbX_3$ (X = Cl, Br, I) Nanocrystals 2.0: Zwitterionic Capping Ligands for Improved Durability and Stability. *ACS Energy Lett.* **2018,** *3*, 641-646.

19. Jiang, G.; Guhrenz, C.; Kirch, A.; Sonntag, L.; Bauer, C.; Fan, X.; Wang, J.; Reineke, S.; Gaponik, N.; Eychmüller, A. Highly Luminescent and Water-Resistant $CsPbBr_3$-$CsPb_2Br_5$ Perovskite Nanocrystals Coordinated with Partially Hydrolyzed Poly(Methyl Methacrylate) and Polyethylenimine. *ACS Nano* **2019,** *13*, 10386-10396.

20. El-Ballouli, A. O.; Bakr, O. M.; Mohammeed, O. F. Compositional, Processing, and Interfacial Engineering of Nanocrystal- and Quantum-Dot-Based Perovskite Solar Cells. *Chem. Mater.* **2019,** *31*, 6387-6411.

21. Chen, Q.; De Marco, N.; Yang, Y.; Song, T.-B.; Chen, C.-C.; Zhao, H.; Hong, Z.; Zhou, H.; Yang, Y. Under the Spotlight: The Organic-Inorganic Hybrid Halide Perovskite for Optoelectronic Applications. *Nano Today* **2015,** *10*, 355-396.

22. Wang, H.; Kim, D. H. Perovskite-Based Photodetectors: Materials and Devices. *Chem. Soc. Rev.* **2017,** *46*, 5204-5236.

23. Wang, W.; Ma, Y.; Qi, L. High-Performance Photodetectors Based on Organometal Halide Perovskite Nanonets. *Adv. Funct. Mater.* **2017,** *27*, 1603653.

24. Zhao, C.; Xu, X.; Ferhan, A. R.; Chiang, N.; Jackman, J. A.; Yang, Q.; Liu, W.; Andrews, A. M.; Cho, N. J.; Weiss, P. S. Scalable Fabrication of Quasi-One-Dimensional Gold Nanoribbons for Plasmonic Sensing. *Nano Lett.* **2020,** *20*, 1747-1754.

25. Siddique, R. H.; Donie, Y. J.; Gomard, G.; Yalamanchili, S.; Merdzhanova, T.; Lemmer, U.; Holscher, H. Bioinspired Phase-Separated Disordered Nanostructures for Thin Photovoltaic Absorbers. *Sci. Adv.* **2017,** *3*, e1700232.

26. Zhang, Y.; Liu, Y.; Yang, Z.; Chen, M.; Liu, S. Direct Growth of Pyramid-Textured Perovskite Single Crystals: A New Strategy for Enhanced Optoelectronic Performance. *Adv. Funct. Mater.* **2020,** *30*, 2002742.

27. Dualeh, A.; Gao, P.; Seok, S. I.; Nazeeruddin, M. K.; Graetzel, M. Thermal Behavior of Methylammonium Lead-Trihalide Perovskite Photovoltaic Light Harvesters. *Chem. Mater.* **2014,** *26*, 6160-6164.

28. Wang, R.; Mujahid, M.; Duan, Y.; Wang, Z. K.; Xue, J. J.; Yang, Y. A Review of Perovskites Solar Cell Stability. *Adv. Funct. Mater.* **2019,** *29*, 1808843.

29. Liu, Y.; Zhang, Y.; Yang, Z.; Yang, D.; Ren, X.; Pang, L.; Liu, S. F. Thinness- and Shape-Controlled Growth for Ultrathin Single-Crystalline Perovskite Wafers for Mass Production of Superior Photoelectronic Devices. *Adv. Mater.* **2016,** *28*, 9204-9209.

30. Bi, D.; Yi, C.; Luo, J.; Décoppet, J.-D.; Zhang, F.; Zakeeruddin, Shaik M.; Li, X.; Hagfeldt, A.; Grätzel, M. Polymer-Templated Nucleation and Crystal Growth of Perovskite Films for Solar Cells with Efficiency Greater than 21%. *Nat. Energy* **2016,** *1*, 16142.

31. Lei, Y.; Chen, Y.; Zhang, R.; Li, Y.; Yan, Q.; Lee, S.; Yu, Y.; Tsai, H.; Choi, W.; Wang, K.; Luo, Y.; Gu, Y.; Zheng, X.; Wang, C.; Wang, C.; Hu, H.; Li, Y.; Qi, B.; Lin, M.; Zhang, Z.; Dayeh, S. A.; Pharr, M.; Fenning, D. P.; Lo, Y.-H.; Luo, J.; Yang, K.; Yoo, J.; Nie, W.; Xu, S. A Fabrication Process for Flexible Single-Crystal Perovskite Devices. *Nature* **2020,** *583*, 790-795.

32. Mao, J.; Sha, W. E. I.; Zhang, H.; Ren, X. G.; Zhuang, J. Q.; Roy, V. A. L.; Wong, K. S.; Choy, W. C. H. Novel Direct Nanopatterning Approach to Fabricate Periodically Nanostructured Perovskite for Optoelectronic Applications. *Adv. Funct. Mater.* **2017,** *27*, 1606525.

33. Chou, S. Y.; Krauss, P. R.; Renstrom, P. J. Imprint of Sub-25 nm Vias and Trenches in Polymers. *Appl. Phys. Lett.* **1995,** *67*, 3114-3116.

34. Wang, H.; Haroldson, R.; Balachandran, B.; Zakhidov, A.; Sohal, S.; Chan, J. Y.; Zakhidov, A.; Hu, W. Nanoimprinted Perovskite Nanograting Photodetector with Improved Efficiency. *ACS Nano* **2016,** *10*, 10921-10928.

35. Haynes, C. L.; Duyne, R. P. V. Nanosphere Lithography: A Versatile Nanofabrication Tool for Studies of Size-Dependent Nanoparticle Optics. *J. Phys. Chem. B* **2001,** *105*, 5599-5611.

36. Xu, X.; Yang, Q.; Wattanatorn, N.; Zhao, C.; Chiang, N.; Jonas, S. J.; Weiss, P. S. Multiple-Patterning Nanosphere Lithography for Fabricating Periodic Three-Dimensional Hierarchical Nanostructures. *ACS Nano* **2017,** *11*, 10384-10391.

37. Xia, Y.; Whitesides, G. M. Soft Lithography. *Angew. Chem. Int. Ed.* **1998,** *37*, 550-575.

38. Qin, D.; Xia, Y.; Whitesides, G. M. Soft Lithography for Micro- and Nanoscale Patterning. *Nat. Protoc.* **2010,** *5*, 491-502.

39. Liao, W. S.; Cheunkar, S.; Cao, H. H.; Bednar, H. R.; Weiss, P. S.; Andrews, A. M. Subtractive Patterning *via* Chemical Lift-Off Lithography. *Science* **2012,** *337*, 1517-1521.

40. Zhao, C.; Liu, Q.; Cheung, K. M.; Liu, W.; Yang, Q.; Xu, X.; Man, T.; Weiss, P. S.; Zhou, C.; Andrews, A. M. Narrower Nanoribbon Biosensors Fabricated by Chemical Lift-Off Lithography Show Higher Sensitivity. *ACS Nano* **2020,** *15*, 904-915.

41. Liu, W.; Wang, J.; Xu, X.; Zhao, C.; Xu, X.; Weiss, P. S. Single-Step Dual-Layer Photolithography for Tunable and Scalable Nanopatterning. *ACS Nano* **2021**, *15*, 12180-12188 .

42. Zhan, Y.; Wang, Y.; Cheng, Q.; Li, C.; Li, K.; Li, H.; Peng, J.; Lu, B.; Wang, Y.; Song, Y.; Jiang, L.; Li, M. A Butterfly-Inspired Hierarchical Light-Trapping Structure Towards a High-Performance Polarization-Sensitive Perovskite Photodetector. *Angew. Chem. Int. Ed.* **2019,** *58*, 16456-16462.

43. Jeon, N. J.; Noh, J. H.; Kim, Y. C.; Yang, W. S.; Ryu, S.; Seok, S. I. Solvent Engineering for High-Performance Inorganic-Organic Hybrid Perovskite Solar Cells. *Nat. Mater.* **2014,** *13*, 897-903.

44. Lim, S.; Ha, M.; Lee, Y.; Ko, H. Large-Area, Solution-Processed, Hierarchical $MAPbI_3$ Nanoribbon Arrays for Self-Powered Flexible Photodetectors. *Adv. Opt. Mater.* **2018,** *6*, 1800615.

45. Jing, H.; Peng, R.; Ma, R.-M.; He, J.; Zhou, Y.; Yang, Z.; Li, C.-Y.; Liu, Y.; Guo, X.; Zhu, Y.; Wang, D.; Su, J.; Sun, C.; Bao, W.; Wang, M. Flexible Ultrathin Single-Crystalline Perovskite Photodetector. *Nano Lett.* **2020,** *20*, 7144-7151.

46. Lan, C.; Dong, R.; Zhou, Z.; Shu, L.; Li, D.; Yip, S.; Ho, J. C. Large-Scale Synthesis of Freestanding Layer-Structured PbI_2 and $MAPbI_3$ Nanosheets for High-Performance Photodetection. *Adv. Mater.* **2017,** *29*, 1702759.

47. Li, Z.; Li, J.; Ding, D.; Yao, H.; Liu, L.; Gong, X.; Tian, B.; Li, H.; Su, C.; Shi, Y. Direct Observation of Perovskite Photodetector Performance Enhancement by Atomically Thin Interface Engineering. *ACS Appl. Mater. Interfaces* **2018,** *10*, 36493-36504.

48. Wang, J.; Xiao, S.; Qian, W.; Zhang, K.; Yu, J.; Xu, X.; Wang, G.; Zheng, S.; Yang, S. Self-Driven Perovskite Narrowband Photodetectors with Tunable Spectral Responses. *Adv. Mater.* **2020,** *33*, 2005557.

49. Ding, D.; Li, H.; Yao, H.; Liu, L.; Tian, B.; Su, C.; Wang, Y.; Shi, Y. Template Growth of Perovskites on Yarn Fibers Induced by Capillarity for Flexible Photoelectric Applications. *J. Mater. Chem. C* **2019,** *7*, 9496-9503.

50. Kumar, G. S.; Sarkar, P. K.; Pradhan, B.; Hossain, M.; Rao, K. D. M.; Acharya, S. Large-Area Transparent Flexible Guanidinium Incorporated $MAPbI_3$ Microstructures for High-Performance Photodetectors with Enhanced Stability. *Nanoscale Horiz.* **2020,** *5*, 696-704.

51. Zheng, W.; Lin, R.; Zhang, Z.; Liao, Q.; Liu, J.; Huang, F. An Ultrafast-Temporally-Responsive Flexible Photodetector with High Sensitivity Based on High-Crystallinity Organic-Inorganic Perovskite Nanoflake. *Nanoscale* **2017,** *9*, 12718-12726.

52. Deng, H.; Yang, X.; Dong, D.; Li, B.; Yang, D.; Yuan, S.; Qiao, K.; Cheng, Y.-B.; Tang, J.; Song, H. Flexible and Semitransparent Organolead Triiodide Perovskite Network Photodetector Arrays with High Stability. *Nano Lett.* **2015,** *15*, 7963-7969.

53. Fang, Y.; Huang, J. Resolving Weak Light of Sub-Picowatt Per Square Centimeter by Hybrid Perovskite Photodetectors Enabled by Noise Reduction. *Adv. Mater.* **2015,** *27*, 2804-2810.

54. Bao, C.; Zhu, W.; Yang, J.; Li, F.; Gu, S.; Wang, Y.; Yu, T.; Zhu, J.; Zhou, Y.; Zou, Z. Highly Flexible Self-Powered Organolead Trihalide Perovskite Photodetectors with Gold Nanowire Networks as Transparent Electrodes. *ACS Appl. Mater. Interfaces* **2016,** *8*, 23868-23875.

55. Hu, X.; Zhang, X.; Liang, L.; Bao, J.; Li, S.; Yang, W.; Xie, Y. High-Performance Flexible Broadband Photodetector Based on Organolead Halide Perovskite. *Adv. Funct. Mater.* **2014,** *24*, 7373-7380.

56. Hu, W.; Huang, W.; Yang, S.; Wang, X.; Jiang, Z.; Zhu, X.; Zhou, H.; Liu, H.; Zhang, Q.; Zhuang, X.; Yang, J.; Kim, D. H.; Pan, A. High-Performance Flexible Photodetectors Based on High-Quality Perovskite Thin Films by a Vapor-Solution Method. *Adv. Mater.* **2017,** *29*, 1703256.

57. Wang, T.; Lian, G.; Huang, L.; Zhu, F.; Cui, D.; Wang, Q.; Meng, Q.; Jiang, H.; Zhou, G.; Wong, C.-P. A Crystal-Growth Boundary-Fusion Strategy to Prepare High-Quality $MAPbI_3$ Films for Excellent Vis-NIR Photodetectors. *Nano Energy* **2019,** *64*, 103914.

58. Chen, B.; Li, T.; Dong, Q.; Mosconi, E.; Song, J.; Chen, Z.; Deng, Y.; Liu, Y.; Ducharme, S.; Gruverman, A.; Angelis, F. D.; Huang, J. Large Electrostrictive Response in Lead Halide Perovskites. *Nat. Mater.* **2018,** *17*, 1020-1026.

Chapter 5

Narrower Nanoribbon Biosensors Fabricated by Chemical Lift-Off Lithography Show Higher Sensitivity

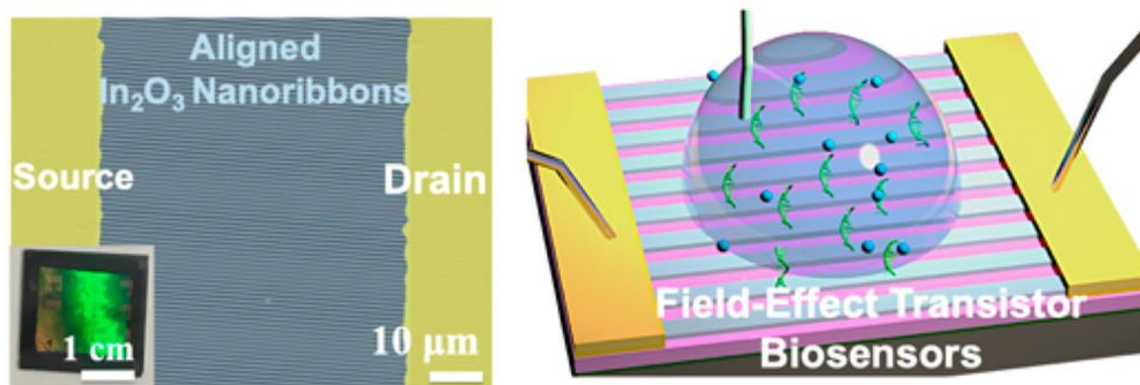

The information in this chapter is reprinted with permission from

ACS Nano **2021**, *15*, 904-915. Copyright (2021) American Chemical Society

Authors: Zhao, C.; Liu, Q.; Cheung, K. M.; **Liu, W.**; Yang, Q.; Xu, X.; Man, T.; Weiss, P. S.; Zhou, C.; Andrews, A. M.

5.1 Abstract

Wafer-scale nanoribbon field-effect transistor (FET) biosensors fabricated by straightforward top-down processes are demonstrated as sensing platforms with high sensitivity to a broad range of biological targets. Nanoribbons with 350 nm widths (700 nm pitch) were patterned by chemical lift-off lithography using high-throughput, low-cost commercial digital versatile disks (DVDs) as masters. Lift-off lithography was also used to pattern ribbons with 2 µm or 20 µm widths (4 or 40 µm pitches, respectively) using masters fabricated by photolithography. For all widths, highly aligned, quasi-one-dimensional (1D) ribbon arrays were produced over centimeter length scales by sputtering to deposit 20 nm thin-film In_2O_3 as the semiconductor. Compared to 20 µm wide microribbons, FET sensors with 350 nm wide nanoribbons showed higher sensitivity to pH over a broad range (pH 5 to 10). Nanoribbon FETs functionalized with a serotonin-specific aptamer demonstrated larger responses to equimolar serotonin in high ionic strength buffer than those of microribbon FETs. Field-effect transistors with 350 nm wide nanoribbons functionalized with single-stranded DNA showed greater sensitivity to detecting complementary DNA hybridization *vs* 20 µm microribbon FETs. In all, we illustrate facile fabrication and use of large-area, uniform In_2O_3 nanoribbon FETs for ion, small-molecule, and oligonucleotide detection where higher surface-to-volume ratios translate to better detection sensitivities.

5.2 Introduction

Label-free, ultrasensitive chemical and biological sensors that monitor biomarkers in body fluids and tissues have broad applications in healthcare and biomedical research, including cancer diagnostics,[175,176] DNA detection,[177-180] bacteria and virus detection,[181-183] and metabolite monitoring.[184-188] Developing sensors that provide accurate, real-time information regarding multiple analytes with high sensitivity and selectivity is at the heart of next-generation personalized medical devices, such as point-of-care measurements and implantable and wearable sensors.[189-199] Nanoelectronic field-effect transistor (FET) biosensors have been explored as platforms having unique properties and advantages toward the realization of these applications.

Indium oxide has been used to fabricate FET sensors with higher sensitivities, more straightforward surface functionalization, and greater stability in aqueous environments compared to other channel materials, including graphene and MoS_2.[200-202] Moreover, compared to other metal oxides, such as indium-gallium-zinc oxide, In_2O_3 is stable in buffers simulating physiological environments.[203,204] Bottom-up strategies were used to prepare In_2O_3 nanowires for use as gas sensors, chemical sensors, biosensors, and optical detectors.[205-208] However, similar to other bottom-up fabricated FETs, such as Si nanowires or carbon nanotubes, bottom-up fabricated In_2O_3 nanowire sensors suffer from poor device-to-device reproducibility due to random orientations and variable numbers of nanowires between electrodes.[209,210]

In contrast, top-down fabrication strategies, for example, soft lithography, soft lithographic molecular printing,[211-213] nanoimprint lithography,[214,215] and nanotransfer printing,[216-219] provide precise control over the morphologies and shapes of nanomaterials. Top-down In_2O_3 nanoribbons fabricated by straightforward photolithographic processes and low-temperature sputtering methods show high device uniformity and reproducibility.[204] We previously developed a

lithography-free process involving sputtering In_2O_3 through shadow masks to fabricate ribbons of 25 μm width, ~16 nm thickness, and 500 μm length over centimeter scales.[204,220,221] These devices (previously referred to as nanoribbons due to the nanoscale height of the sputtered In_2O_3) had high field-effect mobilities (>13 $cm^2 V^{-1} s^{-1}$), large current on/off ratios (>10^7),[204,220] and functioned as sensors in a variety of applications including pH sensing, cardiac biomarker detection, and wearable sensors for glucose monitoring.[204,220,221] Flexible multifunctional sensor arrays incorporating these 25-μm-wide ribbons have also been developed to measure temperature, pH, and the neurotransmitters serotonin and dopamine, simultaneously.[222] Nonetheless, ribbons fabricated *via* shadow masks are limited in lateral resolution to tens of microns.

Surface-to-volume ratio is a critical parameter impacting nanobiosensor sensitivity, where higher ratios result in greater target sensitivities.[206,210,223-229] Here, we advance a generalizable, facile, top-down strategy for fabricating highly aligned In_2O_3 nanoribbons.[230,231] We employ chemical lift-off lithography (CLL), which is a soft lithography patterning approach that is cleanroom-free, high-throughput, and high-fidelity and enables micro- and nanopatterning to produce features as small as 15 nm.[232-239] In CLL, polydimethylsiloxane (PDMS) stamps with desired patterns are used to remove molecules self-assembled on Au surfaces selectively in the stamp contact areas. The remaining molecules in the noncontacted regions act as resists during wet etching to form three-dimensional features. We used CLL to pattern Au micro- and nanostructures, including Au nanoribbon, disk, square, and circle arrays, and to pattern other metal and semiconductor surfaces.[123,200,230,236]

Here, we combined sputtering with CLL to produce 20 nm thin-film In_2O_3 ribbons at 350 nm, 2 μm, or 20 μm widths and wafer scales. As-fabricated ribbons were aligned between source and drain electrodes with controllable orientations, numbers, and sizes. Micro- and

nanoribbon FET biosensors with different aspect ratios were characterized and compared. The 350 nm wide nanoribbon FETs showed sensitivities for target detection greater than those of 20-μm-wide microribbon FETs, providing further evidence for the concept that higher surface-to-volume ratios confer greater sensitivities in nanobiosensing applications.

5.3 Materials and Methods

Materials. Prime quality 4 in. Si wafers (P/B, 0.001–0.005 Ω-cm, thickness 500 μm) were purchased from Silicon Valley Microelectronics, Inc. (Santa Clara, CA). Sylgard 184 silicone elastomer kits (lot #0008823745) were purchased from Ellsworth Adhesives (Germantown, WI). Indium(III) nitrate hydrate (99.999%), iron nitrate, thiourea, ammonium hydroxide (30% w/v in H_2O), hydrogen peroxide (30% v/v in H_2O), ethylenediaminetetraacetic acid disodium salt dihydrate (EDTA), 3-phosphonopropioninc acid, (3-aminopropyl)triethoxysilane (APTES), trimethoxy(propyl)silane, and 3-maleimidobenzoic acid *N*-hydroxysuccinimide (MBS) were purchased from Sigma-Aldrich (St. Louis, MO) and used as received. UltraPure nuclease-free distilled water was purchased from Thermo Fisher Scientific (Waltham, MA) and used as received. The masters templated for lift-off lithography were commercially available DVD-R recordable 16× speed 4.7 GB blank disks (Memorex).

Water was deionized before use (18.2 MΩ-cm) using a Milli-Q system (Millipore, Billerica, MA). The serotonin aptamer (/5ThioMC6-D/CG ACT GGT AGG CAG ATA GGG GAA GCT GAT TCG ATG CGT GGG TCG), thiolated ssDNA (/5ThioMC6-D/GG TTC TTG GAT ATA G), and complementary ssDNA (CTA TAT CCA AGA ACC) were synthesized by Integrated DNA

Technologies, Inc. (Coralville, IA). The Ag/AgCl reference electrodes were purchased from World Precision Instruments, Inc. (Sarasota, FL).

Buffer Solutions. Phosphate-buffered saline solution was purchased from Thermo Fisher Scientific (Waltham, MA, #10010023) and used as received. Artificial cerebrospinal fluid solution was NaCl (14.7 mM), KCl (0.35 mM), $CaCl_2$ (0.1 mM), NaH_2PO_4 (0.1 mM), $NaHCO_3$ (0.25 mM), and $MgCl_2$ (0.12 mM). A detailed procedure for preparation appears in the Supporting Information.

Fabrication of Masters. Photomasks for 2 µm wide and 4 µm pitch lines or 20 µm wide and 40 µm pitch lines were designed using the AutoCAD software suite (Autodesk, Inc.). Positive photoresist SPR700-1.2 (Rohm & Haas Co., Philadelphia, PA) was used for patterning Si by photolithography. The exposed Si was selectively etched using deep reactive ion etching (Plasma-Therm, LLC, Petersburg, FL). The resulting masters were then coated with trichloro(1*H*,1*H*,2*H*,2*H*-perfluorooctyl)silane as a release layer. The DVD-R masters for 350 nm wide nanoribbons were prepared by a separation and rinsing process as previously described.[56,57]

Fabrication of In_2O_3 Micro- and Nanoribbon FETs. The general fabrication process is illustrated in **Figure 5.1**. The Si substrates with 100 nm SiO_2 were coated with 30 nm Ti followed by 30 nm Au using a CHA solution electron-beam evaporator (CHA Industries, Inc., Fremont, CA) under high vacuum (10^{-8} Torr) at an evaporation rate of 0.1 nm/s. Preparation of *h*-PDMS stamps, CLL patterning, and wet etching processes for nanoribbon fabrication were carried out as previously reported.[56,57] Briefly, an ethanolic 1 mM solution of 11-mercapto-1-undecanol was used to form SAMs on Au surfaces by incubation with substrates for 12 h. Oxygen-plasma-activated DVD-templated *h*-PDMS stamps were brought into contact with SAMs. The soft PDMS stamps for CLL patterning of 2- and 20-µm ribbons were made from Si masters fabricated by conventional

photolithography, as described above. The CLL was carried out similar to patterning for 350-nm nanoribbons.

For all formats, upon stamp removal, SAM molecules in the stamp-contacted areas were selectively removed, along with monolayers of Au atoms.[58,64] After the CLL process, Au etchant composed of 20 mM iron nitrate and 30 mM thiourea was used to etch the Au films (~30 min). A Ti etchant (113 mM EDTA, 3% hydrogen peroxide (v/v in H_2O) and 1.26% ammonia hydroxide solution (w/v in H_2O)) was used to etch to Ti for ~9 min. Wet etching transferred the patterns through the metal layers. After wet etching, substrates were oxygen-plasma-treated to remove remaining SAM molecules in the noncontact areas prior to In_2O_3 sputtering.

The In_2O_3 (~20 nm) was deposited onto the patterned substrates using a radio frequency sputtering process (Denton Discovery 550 Sputtering System, Nanoelectronics Research Facility (NRF), University of California, Los Angeles (UCLA)). Sputtering is a room temperature process, which is compatible with a variety of substrates including Si, glass, polyesters, and polyimide.[30,46,47] Metal removal was then performed by immersing substrates into Ti etchant for ~9 min under ultrasonication (Branson Ultrasonics, Danbury, CT), leaving In_2O_3 micro- or nanoribbons on Si/SiO_2 substrates. Devices were cleaned with water and dried under N_2 before measurements or further functionalization. Source/drain electrodes of 10-nm-thick Ti and 50-nm-thick Au were defined by conventional photolithography and deposited using a solution electron-beam evaporator (CHA Industries, Inc., Fremont, CA) under high vacuum (10^{-8} Torr) with an evaporation rate of 0.1 nm/s. An optical microscope image of the electrode configuration with respect to In_2O_3 nanoribbons is shown in **Figure S5.2**.

Characterization. Scanning electron microscope images were obtained using a Supra 40VP scanning electron microscope with an Inlens SE Detector (Carl Zeiss Microscopy, LLC, White Plains, NY). Atomic force microscope imaging was performed using a FastScan AFM with ScanAsyst-Air tips (Bruker, Billerica, MA). Electronic FET measurements were carried out on a manual analytical probe station (Signatone, Gilroy, CA) equipped with a Keithley 4200A SCS (Tektronix, Beaverton, OR) or an Agilent 4156B semiconductor parameter analyzer (Santa Clara, CA). Optical images were taken with a digital camera attached to a Zeiss Axiotech optical microscope.

Biosensing. For pH sensing, In_2O_3 surfaces were functionalized with APTES. Real-time source–drain current measurements were performed (*i*–*t*), where the gate voltage (V_{GS}) was held at 300 mV and the drain voltage (V_D) was held at 100 mV throughout. Buffer solutions of pH 7.4 were used to obtain stable baselines. Buffer solutions from pH 10 to 5 were sequentially added and removed using pipettes.

Thiolated serotonin aptamer or thiolated ssDNA (1 μM in nuclease-free water) were immobilized onto the oxide surfaces of FETs using APTES/PTMS (1:9, v/v) and MBS ester a as linker. Serotonin (final concentration 10 fM to 100 μM) or complementary ssDNA (final concentration 1 fM to 1 μM) in 1 μL aliquots were added into the buffer solutions (39 μL) over FETs and mixed with a pipet.

Source–drain current (I_{DS}) transfer curves were obtained, wherein gate voltages (V_{GS}) were applied from −200 to 400 mV with a step voltage of 5 mV, while the drain voltage (V_D) was held at 10 mV throughout. Five gate-voltage sweeps were repeated (five sweeps at 0, 5, and 10 min). The sweeps at each time point were averaged to determine each transfer curve. Calibrated

responses were calculated by dividing the absolute sensor response (ΔI), which takes into account baseline subtraction, by the change in source–drain current with voltage sweep ($\Delta I_{DS}/\Delta V_G$).[14]

Statistics. Data for pH, serotonin, and ssDNA sensing were analyzed by two-way analysis of variance with ribbon width and target concentration as the independent variables (GraphPad Prism 7.04, San Diego, CA). Data for 10 nM, 100 nM, and 1 μM serotonin were excluded from the statistical analysis because sensor responses were saturated (**Figure 5.5c**). Two data points from the 20-μm-wide nanoribbon DNA sensing data were excluded from plotting and analysis due to external disturbance of the Ag/AgCl reference electrode noted during the measurements (**Figure 5.5f**).

Simulations. The COMSOL Multiphysics 5.2 program was used to simulate the relative responses of nanoribbons having different widths. Details for the model are from Shoorideh and Chui.[87] Here, In_2O_3 nanoribbons were designated to be 2 μm long and 20 nm thick, with widths varying from 5 nm to 20 μm. The In_2O_3 is intrinsically doped by oxygen vacancies at an estimated concentration of 2.5×10^{16} cm^{-3} *n*-type doping.[30] The substrate was 200-nm silicon dioxide. A surface charge density of 1.6×10^{-3} C/m^{-2} was added to model aptamer-induced charge change on the channels and the SiO_2 surface. Semiconductor physics was applied to compute the source–drain electric current when sweeping the gate voltage. The sensitivity was then calculated based on previous work.[14]

5.4. Results and Discussions

The general In_2O_3 micro- and nanoribbon fabrication process is shown in **Figure 5.1** and is described in detail in Materials and Methods. We fabricated ribbon features for subsequent In_2O_3 sputtering followed by a process to remove Au/Ti features, leaving behind In_2O_3 micro- or

nanoribbons. We used commercial digital versatile disks-recordable (DVD-R) as templates to fabricate 350-nm-wide nanoribbons. These disks are economical, easily accessible masters (<$0.5/disk). Blank DVD-R disks contain sub-micrometer grating features.[56,57] The DVD-R masters were prepared by a straightforward separation and rinsing process as previously described.[54,55] Hard PDMS (*h*-PDMS) was used to replicate the high-aspect-ratio DVD-R features.[56,57]

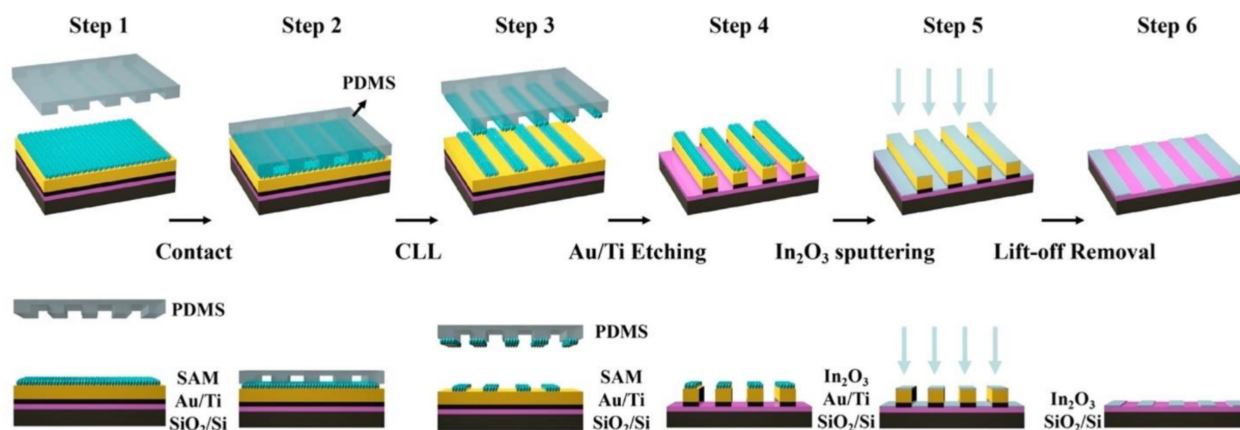

Figure 5.1. Schematic illustration of the fabrication process for In_2O_3 nanoribbons. Step 1: A Au layer (30 nm) was deposited over Ti (30 nm) on Si/SiO_2 (100 nm). A monolayer of 11-mercapto-1-undecanol was then self-assembled on the Au surface. Step 2: An oxygen plasma "activated" polydimethylsiloxane (PDMS) stamp with micro- or nanoribbon features was brought into conformal contact with the substrate. Step 3: Stamp removal from the surface (chemical lift-off lithography, CLL) lifted off self-assembled molecules in the contacted areas. Step 4: Selective etching processes removed Au and Ti in the unprotected (contacted) regions on the surface. Step 5: Sputtering was used to deposit In_2O_3 (20 nm) over the entire substrate. Step 6: The remaining Au/Ti structures were removed to obtain In_2O_3 nanoribbon arrays.

The DVD-R nanoribbon features, transfer of these features to *h*-PDMS, and further transfer to alkanethiol monolayers on Au have been characterized.[56,57] Previously, we deposited In_2O_3 *via* a sol–gel process with the Au/Ti layers deposited on top.[56] The self-assembled monolayers (SAMs) on Au were then patterned. The Au/Ti areas that were not contacted by activated *h*-PDMS served as wet etching masks. The stamp-contacted/exposed Au/Ti features were etched to expose the underlying In_2O_3.

Our previous patterning approach resulted in overetching, which limited precise patterning.[56] Even when overetching was avoided, etching undercut the protective Au/Ti features to produce In_2O_3 nanoribbons that were narrower and less reproducible compared to the features of the masters.[56,57] Further, nanoribbons patterned using the previous method had a high degree of line-edge roughness. Here, we addressed these previous shortcomings by sputtering thin-film In_2O_3 after Au/Ti etching, resulting in high-fidelity In_2O_3 nanoribbons fabricated over large areas.

Sputtering of In_2O_3 was carried out normal to the substrate surface such that undercut of the Au/Ti structures did not influence the widths of the resulting In_2O_3 nanoribbons. Nanoribbons (350 nm) were imaged before and after the lift-off process using atomic force microscopy (AFM), as shown in **Figure 5.2**. Using the present fabrication process, In_2O_3 nanoribbons had heights of ~60 nm after In_2O_3 sputtering (**Figure 5.2a**), corresponding to the sum of the heights of the underlying Au and Ti layers. Sputtering does not add to the apparent height difference as In_2O_3 was sputtered atop both the patterned Au and the interleaved Si areas.

After the Au/Ti nanoribbon structures (and the overlying In_2O_3) were removed, uniform and continuous In_2O_3 nanoribbons with 350 nm widths and 20 nm heights remained, as shown *via* AFM (**Figure 5.2b**). To compare the widths and heights of the ribbons before and after removal

of the Au templates, height profiles along the nanoribbons were analyzed (**Figure 5.2c**). The widths of In_2O_3 nanoribbons matched the spacing between the Au nanoribbons, demonstrating high-fidelity patterning and features characterized by sharp edges and high continuity.

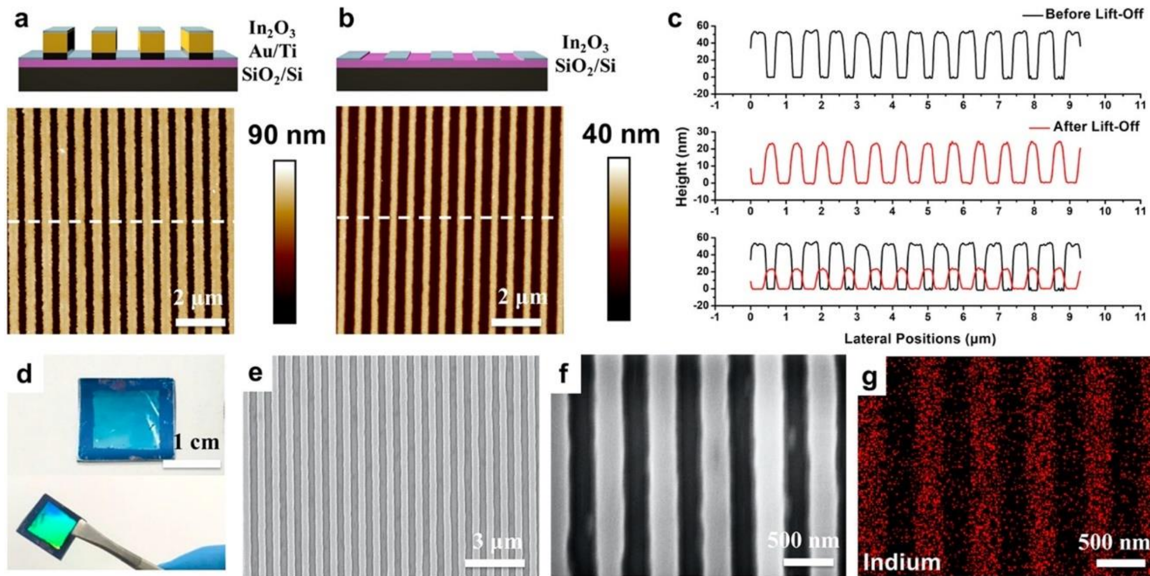

Figure 5.2. Atomic force microscope (AFM) images of 350 nm nanoribbon substrates (a) before (Step 5, Figure 5.1) and (b) after removing underlying Au structures (Step 6, Figure 5.1). (c) Height profiles from the AFM images in (a,b) across the nanoribbons. (d) Photographs of In_2O_3 nanoribbons at different viewing angles. (e,f) Scanning electron microscope (SEM) images of 350 nm wide In_2O_3 nanoribbons. (g) Energy-dispersive X-ray mapping of indium corresponding to the SEM image in (f).

Nanoribbons were fabricated on 1.5 cm × 1.5 cm Si wafers. The light blue In_2O_3 nanoribbon patterned region in the center of a representative wafer showed a strong iridescence when viewed at nonperpendicular angles under white light, indicative of periodic (diffraction) grating patterns on the surface (**Figure 5.2d**). Scanning electron microscopy (SEM) indicated that nanoribbons were continuous over tens of microns and highly defined at the single nanoribbon

scale (**Figure 5.2e,f**). Energy-dispersive X-ray (EDX) mapping was performed (**Figure 5.2g**), where the indium $L_{\alpha 1}$ energy of 3.286 keV (**Figure S5.1**) was mapped and calculated (**Table S5.1**). The EDX images showed In_2O_3 nanoribbons with ~350 nm widths, consistent with the results from AFM and SEM imaging.

To construct micro- and nanoribbon FETs, the orientations of well-aligned In_2O_3 structures were identified by AFM or SEM. Source and drain electrodes were then fabricated perpendicular to the nanoribbons (**Figure 5.3a**) or microribbons. The Au/Ti source and drain electrodes were deposited on top of as-prepared In_2O_3 ribbons *via* electron-beam (e-beam) evaporation. Interdigitated electrodes with lengths of 1300 μm and widths of 45 μm were prepared (**Figure S5.2**). Electrodes aligned well with as-fabricated 350 nm wide In_2O_3 nanoribbons, as shown in the SEM images in **Figure 5.3b,c**. Substrates with 2- or 20-μm-wide In_2O_3 microribbons similarly demonstrated well-aligned configurations between the ribbons and electrodes (**Figures 5.3d,e** and **S5.3**).

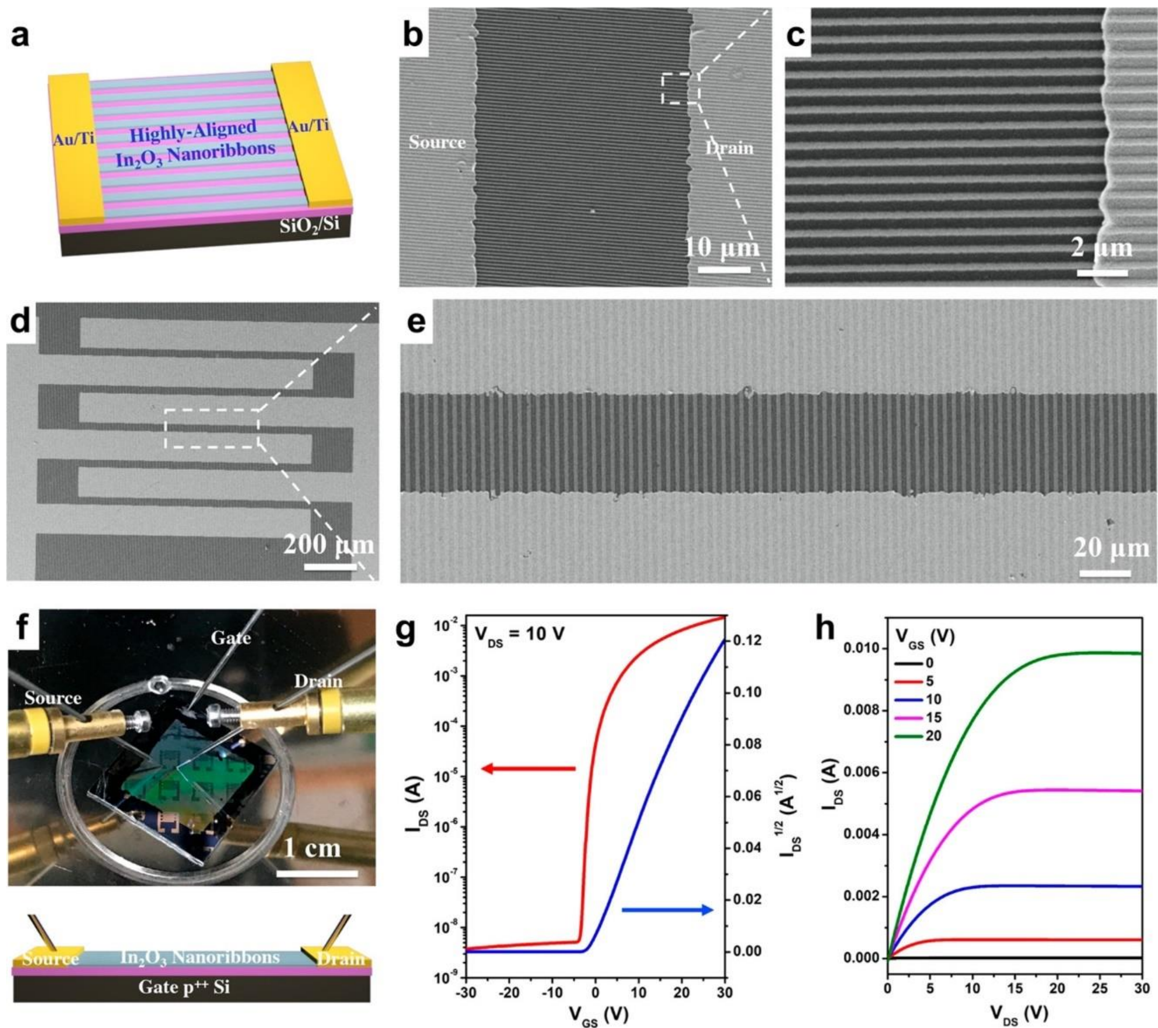

Figure 5.3. (a) Schematic illustration of the field-effect transistor (FET) configuration using In_2O_3 nanoribbons (or microribbons) as the channel material aligned perpendicular to source and drain electrodes. (b,c) Scanning electron microscope images of 350-nm-wide In_2O_3 nanoribbons with source and drain electrodes. (d,e) Scanning electron microscope images of 2-µm-wide In_2O_3 nanoribbons with source and drain electrodes. (f) Photograph (top) and schematic illustration (bottom) of the solid-state measurement setup for In_2O_3 nanoribbon (and microribbon) FETs, where p^{++} Si serves as the bottom gate. The lavender layer is SiO_2. Transfer (g) and output (h) characteristics of representative 350 nm In_2O_3 nanoribbon FETs.

As discussed above and previously reported,[35,36] the orientations and numbers of nanowires or nanoribbons are challenging to control using bottom-up approaches. By contrast, using a top-down CLL patterning approach, orientations and numbers of ribbons were straightforwardly controllable based on the widths and pitches of the ribbons and the widths of the electrodes. For example, ~1850 350-nm-wide In_2O_3 nanoribbons were incorporated and aligned with each pair of electrodes. Transistor performances were tested using a bottom-gate top-contact configuration, where p^{++} Si served as the bottom gate and SiO_2 as the gate dielectric (**Figure 5.3f**). Transfer and output curves for 350-nm-wide In_2O_3 nanoribbon FETs are shown in **Figure 5.3g,h**, respectively, demonstrating current on/off ratios $>10^6$. The FETs with 2- or 20-μm-wide ribbons, or continuous thin-film In_2O_3 FETs showed similar characteristics in solid-state measurements (**Figure S5.4**).

The electrical performance of 350-nm-wide nanoribbon FET devices in a liquid environment was tested using solution gating, which corresponds to how devices were used for biosensing (*vide infra*). Each device was covered with a PDMS well filled with an electrolyte solution (**Figure 5.4a**). A Ag/AgCl reference electrode was used to apply a bias voltage through the electrolyte solution to gate each FET. Transfer and output curves for liquid-gated 350-nm-wide In_2O_3 nanoribbon FETs in phosphate-buffered saline (PBS) are shown in **Figure 5.4b,c**, respectively. The nanoribbon FETs fabricated here operated in a liquid environment with current on/off ratios of 10^3, transfer curve saturation behavior, low gate leakage currents (**Figures 5.4d** and **S5.5**), and low driving voltages. Microribbon FETs with different widths or continuous thin-film FETs showed similar liquid-state performance characteristics (**Figure S5.6**).

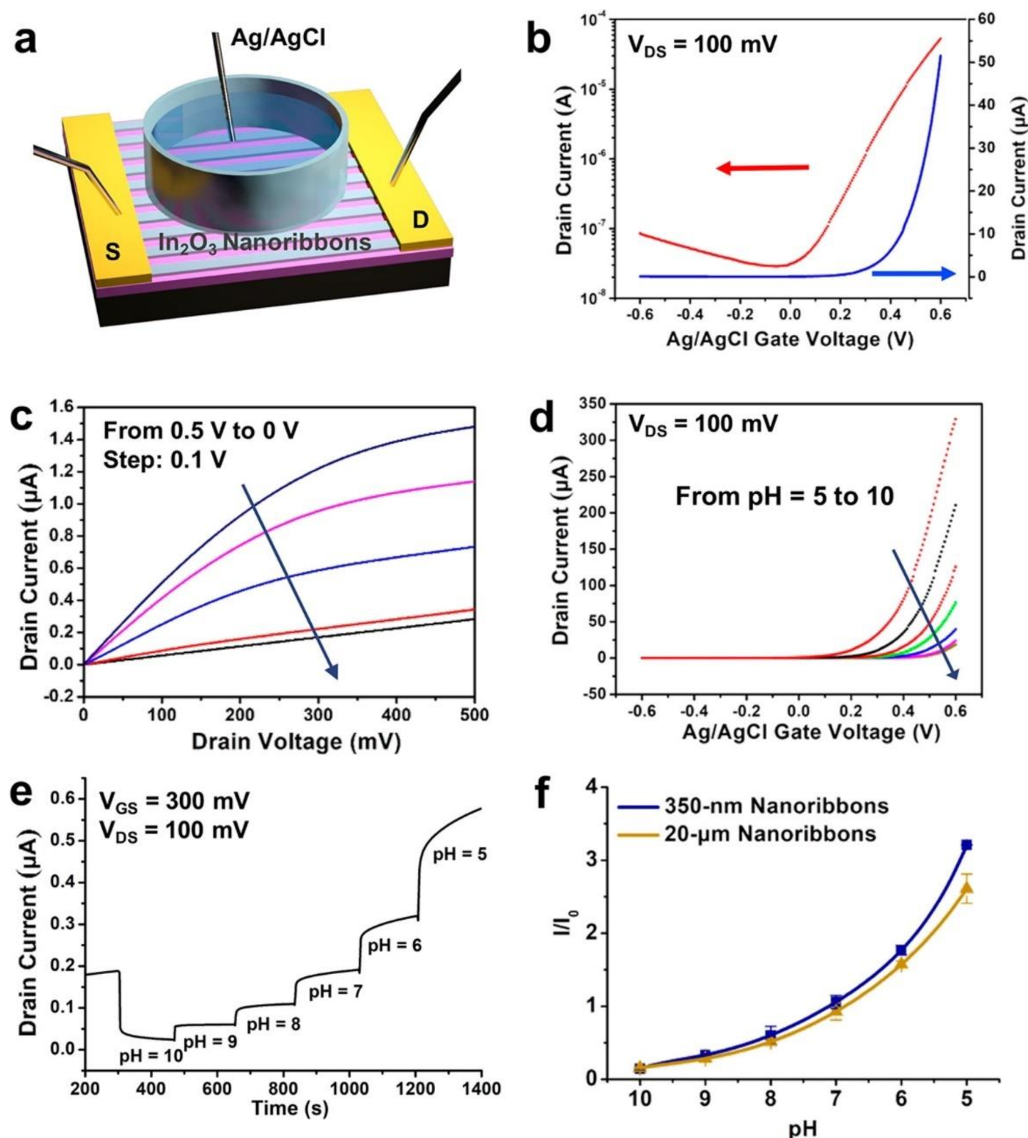

Figure 5.4. (a) Schematic illustration of a liquid state measurement where a Ag/AgCl electrode serves as the top gate. Transfer (b) and output (c) characteristics of 350-nm-wide In_2O_3 nanoribbon field-effect transistors (FETs) in the liquid-gate setup shown in (a). (d) Transfer curves of 350-nm-wide In_2O_3 nanoribbon FETs in solutions of pH 10 to 5. (e) Real-time current responses from a representative 350-nm-wide In_2O_3 nanoribbon FET exposed to commercial buffer solutions of pH 10 to 5. (f) Current responses relative to baseline for solutions of pH 10 to 5 using 350-nm- or 20-µm-wide ribbon In_2O_3 FETs. *I/I_0* is

current normalized to the baseline pH before the experiments (I_0, pH 7.4). Error bars are standard errors of the means with $N = 3$ FETs for each configuration.

Ion-sensitive FETs (ISFETs), where FETs respond to changes in environmental ion concentrations, are used for a majority of FET chemical and biological sensing applications.[67–71] To investigate the performance of In_2O_3 nanoribbon ISFETs, we conducted pH sensing by systematically increasing the hydrogen ion concentrations of the solutions contacting FETs. We previously compared the pH sensitivities of 25-μmwide In_2O_3 ribbon FET sensors having different ribbon heights.[30] Microribbons having thinner, 10- or 20-nm In_2O_3 films showed higher sensitivities to pH compared to thicker microribbons (*e.g.*, 50-nm In_2O_3 films). Here, micro- and nanoribbons with constant 20 nm heights were used to compare the effects of changing ribbon widths.

Threshold voltage changes of ISFETs were determined for 350-nm-wide nanoribbons from pH 5 to 10. Representative transfer curves (drain current to gate voltage) are shown in **Figure 5.4d**. Time-related increases in drain current were observed with decreasing pH values (**Figure 5.4e**), which is typical for *n*-type semiconductor gate-voltage modulation behavior.[27,46,47] At lower pH values, there are greater numbers of positively charged hydrogen ions in solution, leading to higher currents as more negative charge carriers are generated in *n*-type channels. Here, In_2O_3 was functionalized with (3-aminopropyl)triethoxysilane (APTES), where the terminal amine undergoes protonation and deprotonation with changes in pH. Notably, In_2O_3 FETs are less stable at low pH due to the chemical nature of metal oxides, which react with acids to form salts.[56]

Relative pH sensing responses for 350-nm *vs* 20-μm-wide In_2O_3 nanoribbon FETs were compared (**Figure 5.4f**). Device currents for both configurations increased as the $[H^+]$ increased

(*i.e.*, pH decreased). Surface-to-volume ratios for FETs with different ribbon widths were calculated (see Supporting Information, **Figure S5.7**). Ribbons with 350 nm widths had a 10% increase in surface-to-volume ratio compared to ribbons with 20 μm widths (**Table S5.2**). Yet, this modest increase in surface-to-volume ratio was sufficient to produce increased pH sensitivity, particularly at lower pH ($P < 0.01$) (see **Table S5.3** for full statistics). These findings provide evidence that FETs with nanoscale features having higher surface-to-volumes are associated with higher ion sensitivities.

Debye screening in high ionic strength solutions presents challenges for FET biosensing in physiological environments.[49,72,73] Overcoming Debye-length limitations enables the detection of biological targets *ex vivo* and *in vivo* to extend potential uses of FET biosensors for medical and biological applications, such as sensing in body fluids for point-of-care or at-home monitoring. We developed aptamer-based FET biosensors for small-molecule detection under high ionic strength conditions.[14,20,26] Aptamers, which are single-stranded oligonucleotides isolated specifically for adaptive target recognition, are functionalized on semiconductor surfaces. Upon target binding, aptamers undergo conformational rearrangements involving their negatively charged backbones (and associated solution ions), resulting in charge redistribution near semiconductor surfaces. Signal transduction arising from aptamer charge redistribution has enabled direct detection of charged as well as neutral small-molecule targets under physiological conditions.[14]

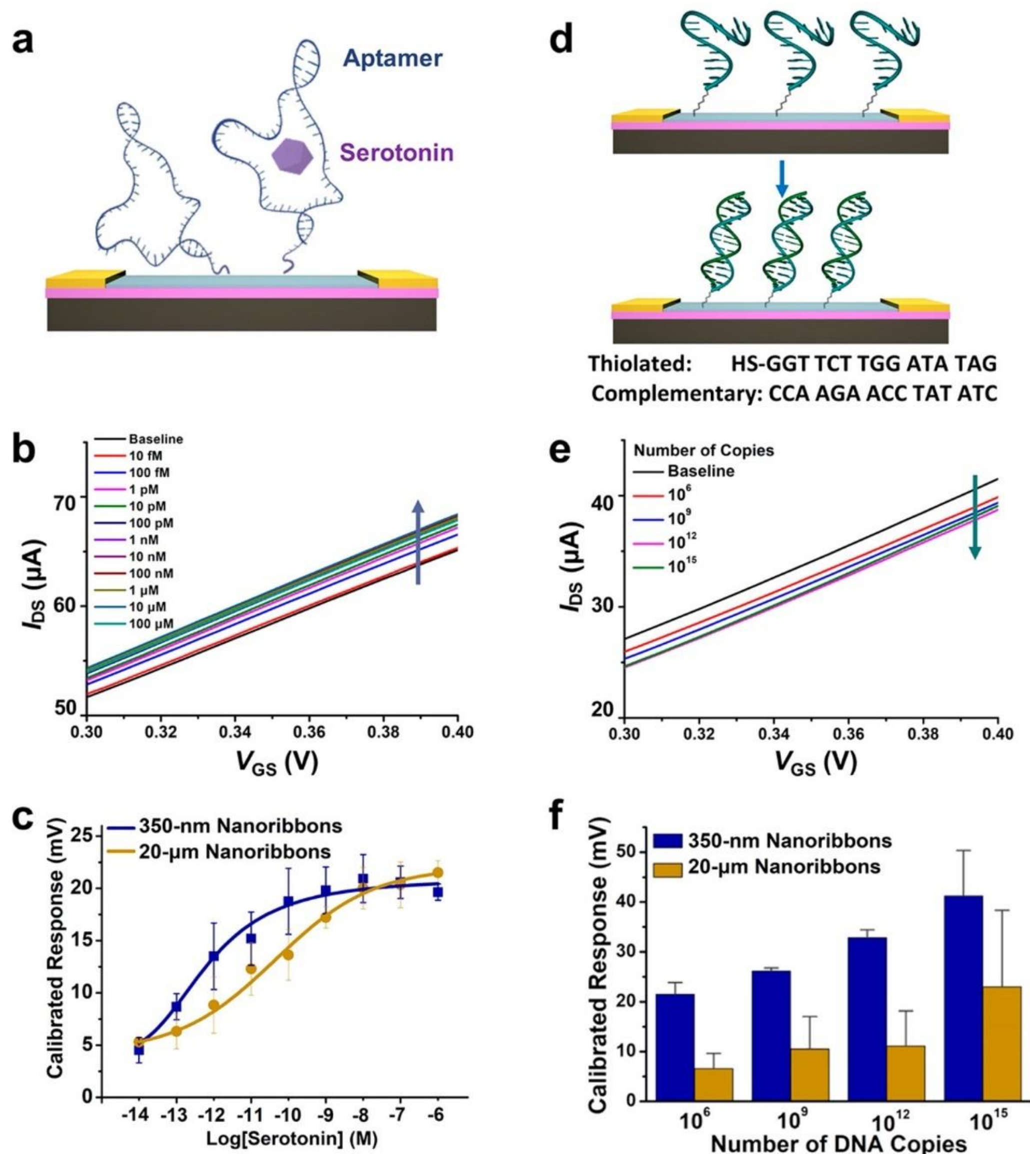

Figure 5.5. (a) Schematic illustration of serotonin detection using aptamer-functionalized In_2O_3 field-effect transistor (FET) biosensors. (b) Representative transfer curves for serotonin responses from 10 fM to 100 μM for 350-nm In_2O_3 nanoribbon FET biosensors. (c) Calibrated response curves for serotonin from 350-nm- *vs* 20-μm-wide In_2O_3 nanoribbon FET biosensors. Error bars are standard errors of the means for N = 3 350-nm-wide nanoribbon and N = 2 20-μm-wide nanoribbon devices. (d) Schematic illustration of DNA hybridization detection. (e) Representative transfer curves for responses for complementary

DNA hybridization (10^6 to 10^{15} copies) for 350-nm In_2O_3 nanoribbon FET biosensors. (f) Calibrated responses for complementary DNA hybridization for 350-nm- *vs* 20-µm-wide In_2O_3 nanoribbon FET biosensors. Error bars are standard errors of the means for *N* = 2 350-nm-wide nanoribbon and *N* = 3 20-µm-wide microribbon devices.

Aptamers that selectively recognize serotonin were covalently immobilized on In_2O_3 (and SiO_2) ribbons (**Figure 5.5a**). Aptamers on the SiO_2 dielectric contribute minimally to target-induced currents. We conducted neurotransmitter sensing by adding increasing concentrations of serotonin into the PBS solutions above FETs. Representative transfer curves for 350-nm-wide In_2O_3 nanoribbon FETs at different serotonin concentrations are shown in **Figure 5.5b**. Calibrated response curves comparing the performance of 350-nm- *vs* 20-µm-wide ribbons both having 20-nm thin-film In_2O_3 are shown in **Figure 5.5c**.

Nanoribbons with 350 nm widths showed a trend toward larger calibrated responses to serotonin compared to those of 20-µm-wide nanoribbons ($0.1 < P < 0.05$). Differences in performance for the two FET configurations were apparent at serotonin concentrations between 100 fM and 1 nM, where sensor responses were linear for both configurations but left-shifted for 350-nm-wide nanoribbons. Tuning nanoribbon widths provides another strategy for shifting overall device sensitivities, in addition to truncating or destabilizing aptamer stems and/or changing aptamer surface densities.[14,20] These strategies will be important for translation to *in vivo* sensing applications where target concentrations vary widely, such as serotonin concentrations in the gut (micromolar range)[74] *vs* the brain extracellular space (nanomolar range).[75]

Previously, we found that even small changes in pH affect aptamer–FET sensor responses.[48] This effect was attributed to H^+-associated changes in charge redistribution around

aptamers and near FET surfaces. For *in vivo* applications where the environmental pH varies, for example, in conjunction with neuronal burst firing, we showed that incorporation of a separate pH sensor as part of a multiplexed device differentiated changes in pH from changes in neurotransmitter concentrations.[48] In previous work, we also carried out control experiments to determine target-specific detection using unfunctionalized FETs and FETs functionalized with a scrambled serotonin aptamer sequence, as well sensing in the presence of structurally similar interferants, which indicated that serotonin-aptamer FETs are highly selective.[14,48] Moreover, we have investigated real-time serotonin sensing (femtomolar-micromolar) with a temporal resolution of ≤5 s, which was limited by the measurement system response time.[48]

In addition to ions and small molecules, oligonucleotide sensing is important for clinical diagnostics, such as genotyping for cancer immunotherapy and for diagnosing infectious diseases.[5,6,77–80] Here, label-free DNA detection was performed on micro- and nanoribbon FET biosensors. Thiolated single-stranded DNA (ssDNA) was covalently immobilized onto In_2O_3 (and SiO_2). Solutions containing 10^6 to 10^{15} copies of complementary oligonucleotide (~1 fM to ~1 µM) were added to the sensing environment in artificial cerebrospinal fluid (aCSF) (**Figure 5.5d**). The aCSF was diluted 10-fold to increase the Debye length and thereby to maximize low copy-number detection.

Representative transfer curves for 350-nm-wide In_2O_3 nanoribbon FETs at different target DNA copy numbers are shown in **Figure 5.5e**. Calibrated responses are compared in **Figure 5.5f** for the performance of 350-nm nanoribbon *vs* 20-µm microribbon In_2O_3 FETs. Nanoribbons with 350 nm widths showed higher sensitivity to DNA hybridization than that of the 20-µm-wide microribbons ($P < 0.05$).

The direction of change for n-type In_2O_3 FET transfer characteristics is due to gating effects associated with negatively charged oligonucleotides.[14,20] For aptamer-based sensing, the serotonin aptamers used here reorient away from FET surfaces upon target binding, resulting in increases in concentration-related currents in i–V sweeps due to increased transconductance.[14] For DNA hybridization, decreases in currents in the i–V sweeps with increasing DNA concentrations are due to the accumulation of net negative surface charge, which occurs upon DNA hybridization.[77] In a previous study, we observed negligible sensor responses to noncomplementary target sequences.[77] We differentiated sequences with single-base mismatches. The highly sensitive platform developed here and in our recent work[77] portends a reagentless strategy for oligonucleotide (DNA, RNA) sensing, which can be developed for the detection of a wide variety of infectious agents, including the severe acute respiratory-related coronavirus 2 (SARS-CoV-2).[80,81]

Relationships between FET sensitivity and surface-to-volume ratio have been investigated using different types of channel materials.[32,36,49–55] Silicon nanowires with dimensions ≥50 nm have been most often investigated.[36,50,54] Silicon nanowires with higher surface-to-volume ratios have higher sensitivities toward pH, protein, and DNA detection.[36,50,54] For example, Linnros and colleagues studied silicon-on-insulator (SOI) nanowires with widths of 50–170 nm fabricated by electron-beam lithography having a 100-nm semiconductor layer.[54] For their smallest, 50-nm nanowires, the surface-to-volume ratio was only 2/100 nm^{-1} (*i.e.*, 0.4/20 nm^{-1}), which is 60% less than the surface-to-volume ratio of our 20-nm thin-film In_2O_3 FETs (*i.e.*, 1/20 nm^{-1}; see Supporting Information for calculations and **Table S5.2**).

For bottom-up fabricated cylindrical nanowires, the surface-to-volume ratio is related to $2/r$, where r is the nanowire radius. In principle, Si nanowires with diameters larger than 80 nm (*i.e.*, surface-to-volume ratio 1/20 nm^{-1}) have surface-to-volume ratios lower than those in the

microribbon, nanoribbon, and thin-film FETs investigated here. For instance, Sun and co-workers produced Si nanowire devices for sensing protein adsorption.[36] Fabrication involved nanowire contract printing and SEM to select and to remove nanowires, individually producing devices with specific numbers and diameters of nanowires. Single nanowire devices were grouped by diameter ranges (*i.e.*, 60–80, 81–100, and 101–120 nm). The smallest, 60-nm nanowires had surface-to-volume ratios of 2/30 nm^{-1} (*i.e.*, 1.3/20 nm^{-1})—a 17% increase over the surface-to-volume ratio of the 350-nm nanoribbons investigated here (**Table S5.2**).

Williams and co-authors explored the effects of surface-to-volume ratio in the context of ssDNA hybridization with complementary single-stranded peptide nucleic acids functionalized on Si nanowire FETs having widths of 50, 100, 200, 400, and 800 nm.[50] The Si semiconductor layer was 50 nm. For these sensors, the signal-to-volume ratios were 3/50, 2/50, 1.5/50, 1.25/50, and 1.125/50 nm^{-1}, respectively (*i.e.*, 1.2/20, 0.8/20. 0.6/20, 0.5/20, and 0.45/20 nm^{-1}, respectively). Hybridization sensitivity was linear for nanowires with widths between 800 and 100 nm. A sharp increase in sensitivity to DNA hybridization for the 50-nm-wide Si nanowires was attributed to nonlinear increases in conductance at small nanowire diameters, which was determined experimentally and *via* simulation.

For In_2O_3 nanoribbon FETs, sensor sensitivity can be increased by reducing nanoribbon dimensions using In_2O_3 sol-gel processing to produce thinner semiconductor layers[26,27,56] and/or *via* CLL with masters fabricated by e-beam lithography to pattern features as small as 15 nm.[58–65] To extend our findings beyond the feature sizes investigated experimentally, we performed finite element analysis simulations to predict FET sensitivities with respect to a number of different nanoribbon widths. As shown in **Figure S5.8**, increased sensitivity was predicted for FETs with smaller widths given the same In_2O_3 thickness (20 nm), which is attributed to higher

surface-to-volume ratios. Similar to the findings of Williams and colleagues, we observed the greatest increases in FET responses for features with widths <100 nm.[50]

Here, we focused on top-down approaches using soft lithography. Traditional top-down approaches, such as e-beam lithography (EBL), also offer precise control over the orientations, sizes, and numbers of quasi-1D nanostructures, thereby enabling fabrication of biosensors with high reproducibility.[82] Nonetheless, top-down fabrication of sub-micrometer features needed to achieve high surface-to-volume ratios requires techniques that are challenging to translate for broad applications. For example, commonly used EBL methods are low-throughput and suffer from high equipment and usage costs.

Bottom-up approaches involving 1D nanomaterials (*e.g.*, Si nanowires, SiNWs) have also been used to fabricate FETs with high surface-to-volume ratios, which increased device sensitivities.[83–85] However, fabrication of Si-based nanomaterials, including SiNWs, often relies on silicon-on-insulator wafers, which are considerably more expensive (>$500 per 4 in. wafer) than standard Si wafers (<$50 per 4 in. wafer).[86] Together, these drawbacks present significant barriers to the use of many types of nanomaterials in actual biomedical applications and necessitate the development of high-throughput, cost-effective, and precise fabrication strategies for biosensors, such as the method described herein.

5.5 Conclusions and Prospects

Highly aligned In_2O_3 nanoribbon FETs were fabricated by chemical lift-off lithography using commercially available DVD-R disks as nanostructured templates and low-temperature sputtering to produce 20-nm In_2O_3thin films. Nanoribbon FET sensors have high surface-to-volume ratios that imparted greater sensitivity for ion, small-molecule, and oligonucleotide detection, all other factors being equal. The fabrication and sensing approaches reported herein represent generalizable strategies for improving electronic biosensing by fabricating high surface-to-volume ratio nanoscale features for applications where high and/or tunable sensitivities are critical.

This top-down, large-scale nanolithography strategy to fabricate metal-oxide nanoribbons can be implemented as a high-throughput, cost-effective, cleanroom-free means of production. Even so, nanostructure surface-to-volume ratio is only one of many parameters that impacts nanobiosensor sensitivity. Other factors include semiconductor material, doping, and nanowire/nanostructure densities. If surface receptors are employed for selective biosensing, receptor type (*e.g.*, protein, nucleic acid), density, and target affinity, as well as the ionic strength of the sensing environment and biofouling will influence performance. Nonetheless, we demonstrate unequivocally through experimentation and simulation that surface-to-volume ratio impacts biosensor responses under physiologically relevant conditions.

5.6 Supplementary Materials

Artificial cerebrospinal fluid (aCSF) was prepared from stock solutions. The 10× base stock contains NaCl (1470 mM), KCl (35 mM), NaH_2PO_4 (10 mM), and $NaHCO_3$ (25 mM) in deionized distilled water. The base stock is aliquoted and stored at room temperature. It is stable for at least one year. **Preparation note**: Neither $CaCl_2$ nor $MgCl_2$ should be added directly to the 10× base stock solution due to their low solubility in aqueous solution at pH >7.5. The Mg^{2+} and Ca^{2+} precipitate as $Mg(OH)_2$ and $Ca(OH)_2$ causing the stock solution to appear cloudy and/or for a visible precipitate to form. Stock solutions of $CaCl_2$ (901.063 mM) and $MgCl_2$ (1050.31 mM) in deionized distilled water are each prepared separately. **Safety note**: The addition of $CaCl_2$ or $MgCl_2$ to water is exothermic. Use caution, cold water, and slow stirring when preparing these solutions. The $CaCl_2$ and $MgCl_2$ stocks are aliquoted into 1-mL Eppendorf tubes and stored at -80 °C indefinitely.

Before experiments, the working aCSF solution (physiological concentration, "1×") was prepared. One aliquot each of the $CaCl_2$ and $MgCl_2$ stocks was thawed. Deionized distilled water was added to a beaker at ~80% of the final volume of the working solution. The 10× base stock was added, *e.g.*, 50 mL 10× base stock was added to ~400 mL water for 500 mL final volume of working solution. The pH was initially adjusted to 7.4-7.5 with ~1% HCl. The $CaCl_2$ stock was then added dropwise slowly using a pipette. The working solution was constantly stirred to avoid precipitation for a final concentration of 1.0 mM $CaCl_2$, *e.g.*, 555 µL for a final volume of 500 mL working solution. Next, the $MgCl_2$ stock solution was added dropwise slowly while stirring, for a final concentration of 1.2 mM, *e.g.*, 571 µL for a final volume of 500 mL working solution. The pH of the working solution was adjusted to 7.30 ± 0.03 using ~1% HCl. Finally, the solution was brought to the final volume with deionized distilled water, *e.g.*, final volume 500 mL. The final

concentrations of the working aCSF solution (1×) were NaCl (147 mM), KCl (3.5 mM), NaH_2PO_4 (1.0 mM), $NaHCO_3$ (2.5 mM), $CaCl_2$ (1.0 mM), and $MgCl_2$ (1.2 mM). The working solution was stored at 4 °C for ≤2 weeks.

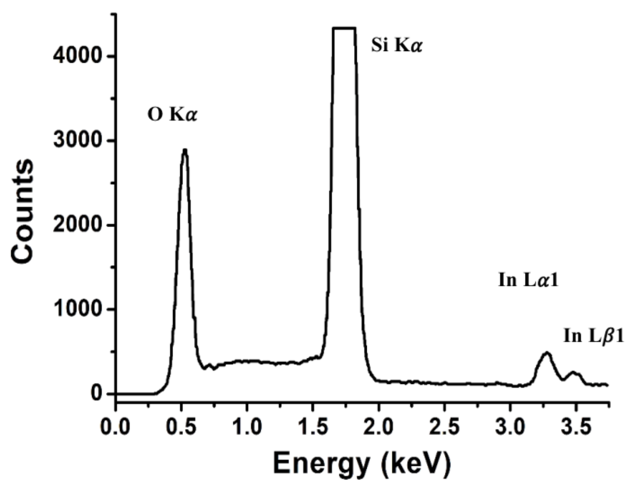

Figure S5.1. **Elemental energy spectrum for In_2O_3 nanoribbons from energy-dispersive X-ray mapping.**

Table S5.1. Elemental quantification analysis of In_2O_3 nanoribbons by energy-dispersive X-ray mapping.

Element line	Net counts	Element wt %	Element wt % error	Atom%	Atom% error
O K	26915	50.60	---	66.48	± 0.51
Si L	0	---	---	---	---
Si K	213374	43.30	± 0.14	32.40	± 0.11
In M	0	---	---	---	---
In L	10378	6.10	± 0.26	1.12	± 0.05
Total		100.0		100.0	

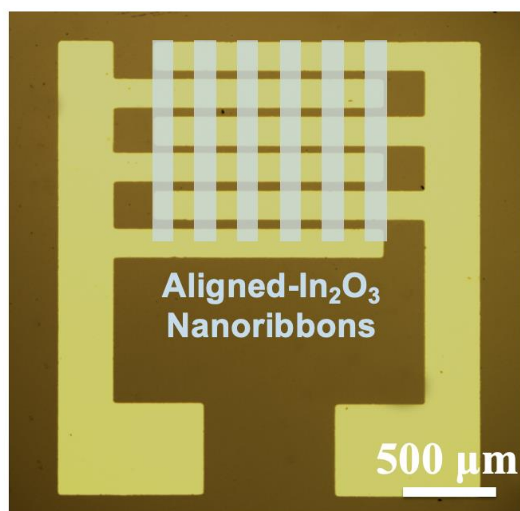

Figure S5.2. Optical microscope image of interdigitated electrodes (yellow). Orientations of In_2O_3 nanoribbons are depicted in overlay (light blue).

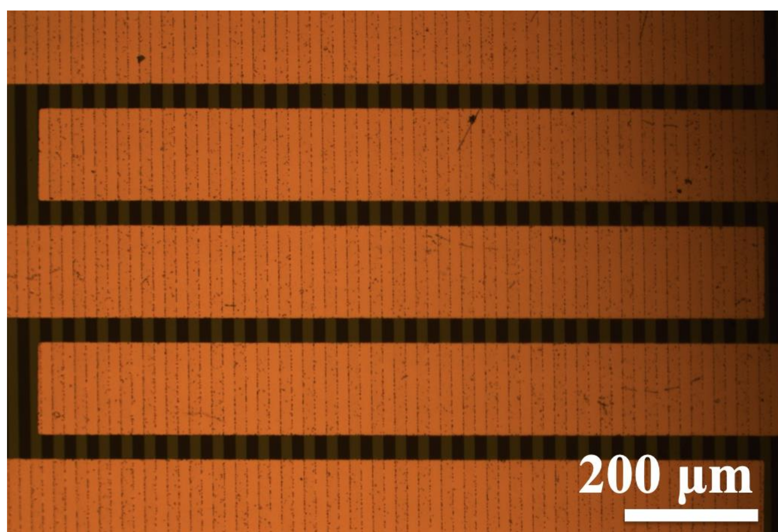

Figure S5.3. Optical microscope images of 20-µm-wide In_2O_3 nanoribbons with source and drain electrodes.

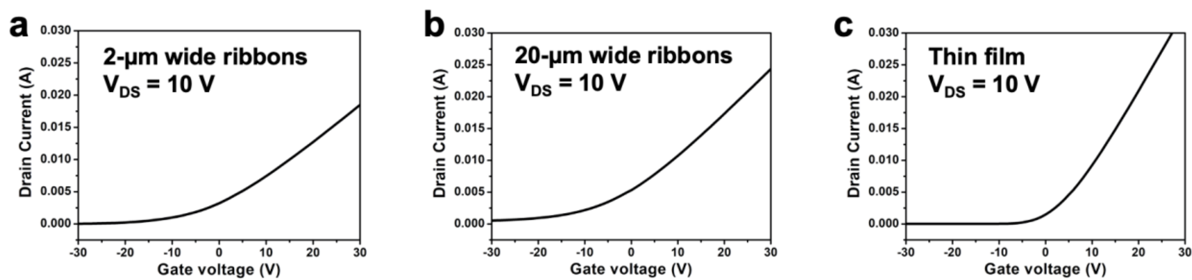

Figure S5.4. Solid-state transfer characteristics of In_2O_3 FETs with different nanoribbon widths, (a) 2 μm, (b) 20 μm, and (c) thin film.

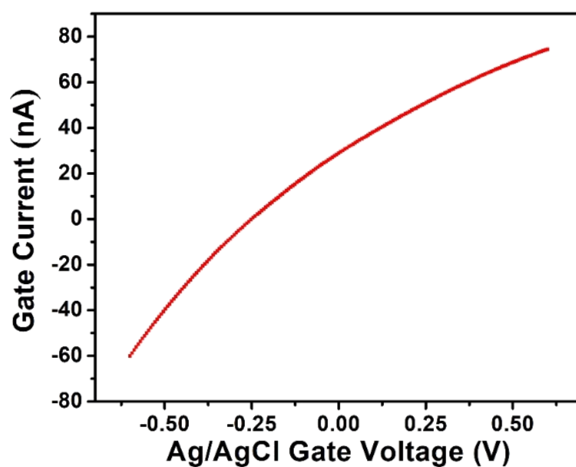

Figure S5.5. Gate leakage current (gate current to gate voltage) in buffer solution (pH = 7.4) at V_{DS} = 100 mV.

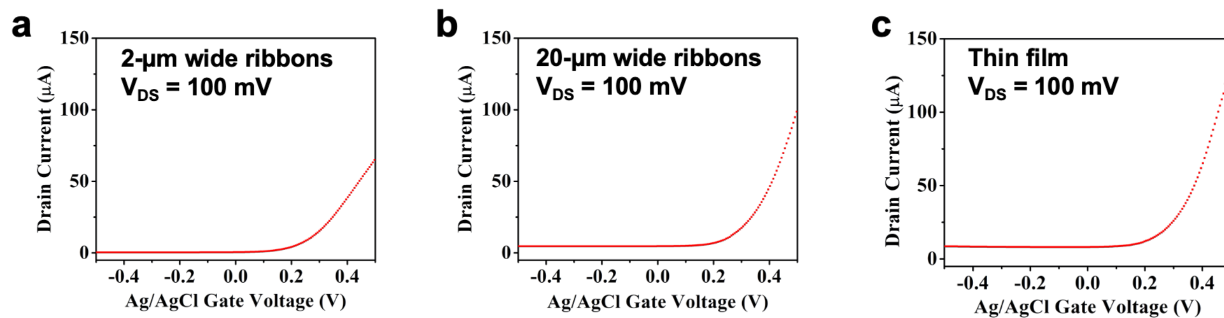

Figure S5.6. Liquid-state transfer characteristics of In_2O_3 FETs with nanoribbon different widths, (a) 2 µm, (b) 20 µm, or (c) thin film.

Calculation of surface-to-volume ratios

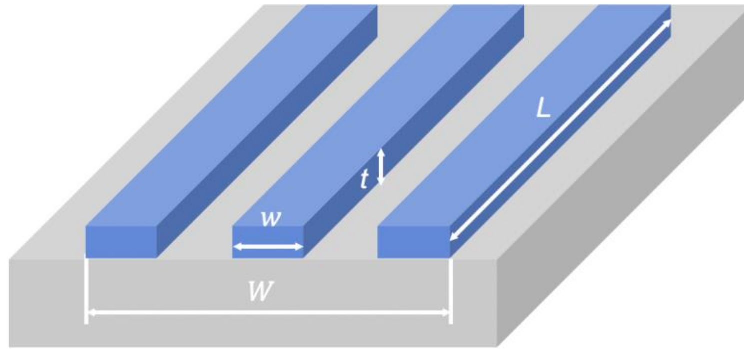

Figure S5.7. Schematic of nanoribbons for calculation of surface-to-volume ratio.

Consider a nanoribbon array, where the surface-to-volume ratio of an arbitrary area with width W is calculated. For each In_2O_3 nanoribbon, the length is denoted as L, width as w, and thickness as t. The pitch of the nanoribbons is $2w$ for different widths of nanoribbons. For nanoribbon surface area calculations, only the top surface and the two side surfaces are included. Results are summarized in **Table S5.2**.

Number of ribbons (per arbitrary area): $N = \frac{W}{2w}$ **Eq. (S5.1)**

Surface area: $S = (w * L) + (2 * L * t)$ **Eq. (S5.2)**

Volume: $V = w * L * t$ **Eq. (S5.3)**

Surface-to-volume ratio (per nanoribbon): $\frac{S}{V} = \frac{w*L+2*L*t}{w*L*t} = \frac{w+2*t}{w*t} = \frac{1+2*\frac{t}{w}}{t}$ **Eq. (S5.4)**

Surface-to-volume ratio (per arbitrary area): $\frac{S}{V} = \frac{(w*L+2*L*t)*N}{(w*L*t)*N} = \frac{(w*L+2*L*t)}{(w*L*t)} = \frac{1+2*\frac{t}{w}}{t}$ **Eq. (S5.5)**

For w_1 = 350 nm:

$$\frac{S}{V} = \frac{1+2*\frac{t}{w}}{t} = \frac{1+2*\frac{20\,nm}{350\,nm}}{20\,nm} = \frac{1+0.11}{20} nm^{-1} = \frac{1.11}{20} nm^{-1}$$

For w_2 = 2 µm:

$$\frac{S}{V} = \frac{1+2*\frac{t}{w}}{t} = \frac{1+2*\frac{20\,nm}{2000\,nm}}{20\,nm} = \frac{1+0.02}{20} nm^{-1} = \frac{1.02}{20} nm^{-1}$$

For w_3 = 20 µm:

$$\frac{S}{V} = \frac{1+2*\frac{t}{w}}{t} = \frac{1+2*\frac{20\,nm}{20000\,nm}}{20\,nm} = \frac{1+0.002}{20} nm^{-1} = \frac{1.002}{20} nm^{-1}$$

For thin-films:

$$\frac{t}{w} \to 0, \frac{S}{V} = \frac{1+2*\frac{t}{w}}{t} = \frac{1}{20} nm^{-1}$$

Table S5.2. Surface-to-volume ratios calculated for different configurations of In_2O_3 FETs.

Width	Pitch	Thickness	Surface-to-volume ratio	Surface-to-volume ratio increase *vs* thin film
350 nm	700 nm	20 nm	$\frac{1.11}{20} nm^{-1}$	11%
2 µm	4 µm	20 nm	$\frac{1.02}{20} nm^{-1}$	2%
20 µm	40 µm	20 nm	$\frac{1.002}{20} nm^{-1}$	0.2%
Thin film	---	20 nm	$\frac{1}{20} nm^{-1}$	---

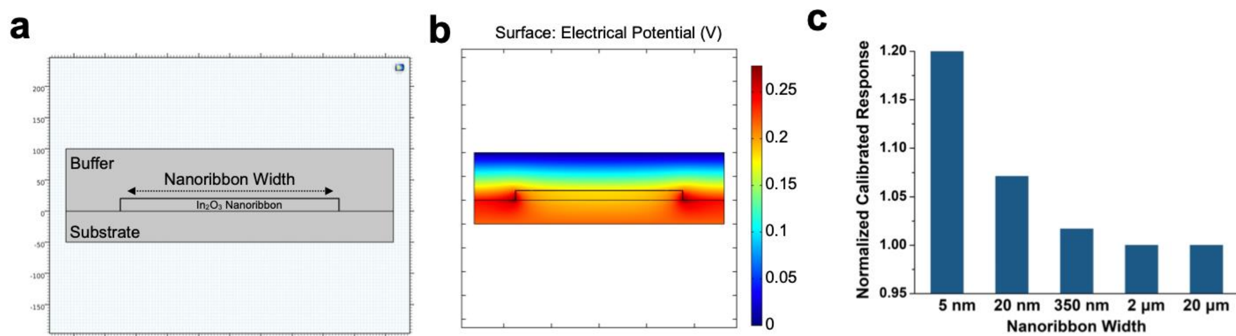

Figure S5.8. COMSOL simulations of effects of nanoribbon width on surface-to-volume ratio. (a) Model used in the simulation, where nanoribbons are 20-nm-thick with widths varying from 5 nm to 20 µm. (b) Simulation results of the electrostatic potential due to the charge of the biomolecules. (c) Simulated normalized calibrated responses at different ribbon widths showing that the sensitivity of In_2O_3 nanoribbon FETs is predicted to increase at widths below 2 µm. Simulated calibrated response values were normalized to responses for 20-µm microribbons. Simulated responses are not directly comparable with experimental results in the main text due to the nature of the simulation complexity for the semiconductor system under study.

Table S5.3. Concentration-dependent field-effect transistor data were analyzed by two-way analysis of variance with nanoribbon sizes and target concentration as the independent variables.

Type	Figure	Interaction term	Nanoribbon width	Concentration
pH	Fig. 5.4f	$F(5,24) = 3.395$ $P = 0.019$	$F(1,24) = 13.09$ $P = 0.001$	$F(5,24) = 307.0$ $P < 0.0001$
Serotonin	Fig. 5.5c	$F(5,18) = 0.375$ $P = 0.859$	$F(1,18) = 4.010$ $P = 0.061$	$F(5,18) = 9.107$ $P = 0.0002$
DNA	Fig. 5.5f	$F(3,10) = 0.054$ $P = 0.982$	$F(1,10) = 7.293$ $P = 0.022$	$F(3,10) = 1.518$ $P = 0.269$

5.7 References

1. Arya, S. K.; Bhansali, S. Lung Cancer and Its Early Detection Using Biomarker-Based Biosensors. *Chem. Rev.* **2011,** *111*, 6783–6809.

2. Huang, X.; Liu, Y.; Yung, B.; Xiong, Y.; Chen, X. Nanotechnology-Enhanced No-Wash Biosensors for *in Vitro* Diagnostics of Cancer. *ACS Nano* **2017,** *11*, 5238–5292.

3. Hahm, J.-i.; Lieber, C. M. Direct Ultrasensitive Electrical Detection of DNA and DNA Sequence Variations Using Nanowire Nanosensors. *Nano Lett.* **2004,** *4*, 51–54.

4. Sorgenfrei, S.; Chiu, C. Y.; Gonzalez, R. L., Jr.; Yu, Y. J.; Kim, P.; Nuckolls, C.; Shepard, K. L. Label-Free Single-Molecule Detection of DNA-Hybridization Kinetics with a Carbon Nanotube Field-Effect Transistor. *Nat. Nanotechnol.* **2011,** *6*, 126–132.

5. Ping, J.; Vishnubhotla, R.; Vrudhula, A.; Johnson, A. T. Scalable Production of High-Sensitivity, Label-Free DNA Biosensors Based on Back-Gated Graphene Field Effect Transistors. *ACS Nano* **2016,** *10*, 8700–8704.

6. Blair, E. O.; Corrigan, D. K. A Review of Microfabricated Electrochemical Biosensors for DNA Detection. *Biosens. Bioelectron.* **2019,** *134*, 57–67.

7. Patolsky, F.; Zheng, G.; Hayden, O.; Lakadamyali, M.; Zhuang, X.; Lieber, C. M. Electrical Detection of Single Viruses. *Proc. Natl. Acad. Sci. U. S. A.* **2004,** *101*, 14017–14022.

8. Miranda, O. R.; Li, X.; Garcia-Gonzalez, L.; Zhu, Z. J.; Yan, B.; Bunz, U. H.; Rotello, V. M. Colorimetric Bacteria Sensing Using a Supramolecular Enzyme-Nanoparticle Biosensor. *J. Am. Chem. Soc.* **2011,** *133*, 9650–9653.

9. Seo, G.; Lee, G.; Kim, M. J.; Baek, S. H.; Choi, M.; Ku, K. B.; Lee, C. S.; Jun, S.; Park, D.; Kim, H. G.; Kim, S. J.; Lee, J. O.; Kim, B. T.; Park, E. C.; Kim, S. I. Rapid Detection of COVID-19 Causative Virus (SARS-CoV-2) in Human Nasopharyngeal Swab Specimens Using Field-Effect Transistor-Based Biosensor. *ACS Nano* **2020,** *14*, 5135–5142.

10. Gao, W.; Emaminejad, S.; Nyein, H. Y. Y.; Challa, S.; Chen, K.; Peck, A.; Fahad, H. M.; Ota, H.; Shiraki, H.; Kiriya, D.; Lien, D. H.; Brooks, G. A.; Davis, R. W.; Javey, A. Fully Integrated Wearable Sensor Arrays for Multiplexed *in Situ* Perspiration Analysis. *Nature* **2016,** *529*, 509–514.

11. Koh, A.; Kang, D.; Xue, Y.; Lee, S.; Pielak, R. M.; Kim, J.; Hwang, T.; Min, S.; Banks, A.; Bastien, P.; Manco, M. C.; Wang, L.; Ammann, K. R.; Jang, K. I.; Won, P.; Han, S.; Ghaffari, R.; Paik, U.; Slepian, M. J.; Balooch, G.; et al. A Soft, Wearable Microfluidic Device for the Capture, Storage, and Colorimetric Sensing of Sweat. *Sci. Transl. Med.* **2016,** *8*, 366ra165.

12. Zhang, Y.; Clausmeyer, J.; Babakinejad, B.; Cordoba, A. L.; Ali, T.; Shevchuk, A.; Takahashi, Y.; Novak, P.; Edwards, C.; Lab, M.; Gopal, S.; Chiappini, C.; Anand, U.; Magnani, L.; Coombes, R. C.; Gorelik, J.; Matsue, T.; Schuhmann, W.; Klenerman, D.; Sviderskaya, E. V.; et al. Spearhead Nanometric Field-Effect Transistor Sensors for Single-Cell Analysis. *ACS Nano* **2016,** *10*, 3214–3221.

13. Emaminejad, S.; Gao, W.; Wu, E.; Davies, Z. A.; Yin Yin Nyein, H.; Challa, S.; Ryan, S. P.; Fahad, H. M.; Chen, K.; Shahpar, Z.; Talebi, S.; Milla, C.; Javey, A.; Davis, R. W. Autonomous Sweat Extraction and Analysis Applied to Cystic Fibrosis and Glucose Monitoring Using a Fully Integrated Wearable Platform. *Proc. Natl. Acad. Sci. U. S. A.* **2017,** *114*, 4625–4630.

14. Nakatsuka, N.; Yang, K. A.; Abendroth, J. M.; Cheung, K. M.; Xu, X.; Yang, H.; Zhao, C.; Zhu, B.; Rim, Y. S.; Yang, Y.; Weiss, P. S.; Stojanovic, M. N.; Andrews, A. M. Aptamer–Field-Effect Transistors Overcome Debye Length Limitations for Small-Molecule Sensing. *Science* **2018,** *362*, 319–324.

15. Pollock, N. R.; Rolland, J. P.; Kumar, S.; Beattie, P. D.; Jain, S.; Noubary, F.; Wong, V. L.; Pohlmann, R. A.; Ryan, U. S.; Whitesides, G. M. A Paper-Based Multiplexed Transaminase Test for Low-Cost, Point-Of-Care Liver Function Testing. *Sci. Transl. Med.* **2012,** *4*, 152ra129.

16. Kim, J.; Lee, M.; Shim, H. J.; Ghaffari, R.; Cho, H. R.; Son, D.; Jung, Y. H.; Soh, M.; Choi, C.; Jung, S.; Chu, K.; Jeon, D.; Lee, S. T.; Kim, J. H.; Choi, S. H.; Hyeon, T.; Kim, D. H. Stretchable Silicon Nanoribbon Electronics for Skin Prosthesis. *Nat. Commun.* **2014,** *5*, 5747.

17. Liu, R.; Chen, R.; Elthakeb, A. T.; Lee, S. H.; Hinckley, S.; Khraiche, M. L.; Scott, J.; Pre, D.; Hwang, Y.; Tanaka, A.; Ro, Y. G.; Matsushita, A. K.; Dai, X.; Soci, C.; Biesmans, S.; James, A.; Nogan, J.; Jungjohann, K. L.; Pete, D. V.; Webb, D. B.; et al. High Density Individually Addressable Nanowire Arrays Record Intracellular Activity from Primary Rodent and Human Stem Cell Derived Neurons. *Nano Lett.* **2017,** *17*, 2757–2764.

18. Taylor, I. M.; Du, Z.; Bigelow, E. T.; Eles, J. R.; Horner, A. R.; Catt, K. A.; Weber, S. G.; Jamieson, B. G.; Cui, X. T. Aptamer-Functionalized Neural Recording Electrodes for the Direct Measurement of Cocaine *in Vivo*. *J. Mater. Chem. B* **2017,** *5*, 2445–2458.

19. Bariya, M.; Nyein, H. Y. Y.; Javey, A. Wearable Sweat Sensors. *Nat. Electron.* **2018,** *1*, 160–171.

20. Cheung, K. M.; Yang, K. A.; Nakatsuka, N.; Zhao, C.; Ye, M.; Jung, M. E.; Yang, H.; Weiss, P. S.; Stojanovic, M. N.; Andrews, A. M. Phenylalanine Monitoring *via* Aptamer–Field-Effect Transistor Sensors. *ACS Sens.* **2019,** *4*, 3308–3317.

21. Kim, J.; Campbell, A. S.; de Avila, B. E.; Wang, J. Wearable Biosensors for Healthcare Monitoring. *Nat. Biotechnol.* **2019,** *37*, 389–406.

22. Gao, W.; Ota, H.; Kiriya, D.; Takei, K.; Javey, A. Flexible Electronics toward Wearable Sensing. *Acc. Chem. Res.* **2019,** *52*, 523–533.

23. Wen, X.; Wang, B.; Huang, S.; Liu, T. L.; Lee, M. S.; Chung, P. S.; Chow, Y. T.; Huang, I. W.; Monbouquette, H. G.; Maidment, N. T.; Chiou, P. Y. Flexible, Multifunctional Neural Probe with Liquid Metal Enabled, Ultra-Large Tunable Stiffness for Deep-Brain Chemical Sensing and Agent Delivery. *Biosens. Bioelectron.* **2019,** *131*, 37–45.

24. Scida, K.; Plaxco, K. W.; Jamieson, B. G. High Frequency, Real-Time Neurochemical and Neuropharmacological Measurements *in Situ* in the Living Body. *Transl. Res.* **2019,** *213*, 50–66.

25. He, X.; Yang, S.; Pei, Q.; Song, Y.; Liu, C.; Xu, T.; Zhang, X. Integrated Smart Janus Textile Bands for Self-Pumping Sweat Sampling and Analysis. *ACS Sens.* **2020,** *5*, 1548–1554.

26. Kim, J.; Rim, Y. S.; Chen, H.; Cao, H. H.; Nakatsuka, N.; Hinton, H. L.; Zhao, C.; Andrews, A. M.; Yang, Y.; Weiss, P. S. Fabrication of High-Performance Ultrathin In_2O_3 Film Field-Effect Transistors and Biosensors Using Chemical Lift-Off Lithography. *ACS Nano* **2015,** *9*, 4572–4582.

27. Rim, Y. S.; Bae, S. H.; Chen, H.; Yang, J. L.; Kim, J.; Andrews, A. M.; Weiss, P. S.; Yang, Y.; Tseng, H. R. Printable Ultrathin Metal Oxide Semiconductor-Based Conformal Biosensors. *ACS Nano* **2015,** *9*, 12174–12181.

28. Chen, H.; Rim, Y. S.; Wang, I. C.; Li, C.; Zhu, B.; Sun, M.; Goorsky, M. S.; He, X.; Yang, Y. Quasi-Two-Dimensional Metal Oxide Semiconductors Based Ultrasensitive Potentiometric Biosensors. *ACS Nano* **2017,** *11*, 4710–4718.

29. Jin, S. H.; Kang, S. K.; Cho, I. T.; Han, S. Y.; Chung, H. U.; Lee, D. J.; Shin, J.; Baek, G. W.; Kim, T. I.; Lee, J. H.; Rogers, J. A. Water-Soluble Thin Film Transistors and Circuits Based on Amorphous Indium-Gallium-Zinc Oxide. *ACS Appl. Mater. Interfaces* **2015,** *7*, 8268–8274.

30. Aroonyadet, N.; Wang, X.; Song, Y.; Chen, H.; Cote, R. J.; Thompson, M. E.; Datar, R. H.; Zhou, C. Highly Scalable, Uniform, and Sensitive Biosensors Based on Top-Down Indium Oxide Nanoribbons and Electronic Enzyme-Linked Immunosorbent Assay. *Nano Lett.* **2015,** *15*, 1943-1951.

31. Li, C.; Zhang, D.; Liu, X.; Han, S.; Tang, T.; Han, J.; Zhou, C. In_2O_3 Nanowires as Chemical Sensors. *Appl. Phys. Lett.* **2003,** *82*, 1613–1615.

32. Zhang, D.; Liu, Z.; Li, C.; Tang, T.; Liu, X.; Han, S.; Lei, B.; Zhou, C. Detection of NO_2 Down to ppb Levels Using Individual and Multiple In_2O_3 Nanowire Devices. *Nano Lett.* **2004,** *4*, 1919–1924.

33. Tang, T.; Liu, X.; Li, C.; Lei, B.; Zhang, D.; Rouhanizadeh, M.; Hsiai, T.; Zhou, C. Complementary Response of In_2O_3 Nanowires and Carbon Nanotubes to Low-Density Lipoprotein Chemical Gating. *Appl. Phys. Lett.* **2005,** *86*, 103903.

34. Curreli, M.; Li, C.; Sun, Y.; Lei, B.; Gundersen, M. A.; Thompson, M. E.; Zhou, C. Selective Functionalization of In_2O_3 Nanowire Mat Devices for Biosensing Applications. *J. Am. Chem. Soc.* **2005,** *127*, 6922–6923.

35. Lee, B. Y.; Sung, M. G.; Lee, J.; Baik, K. Y.; Kwon, Y. K.; Lee, M. S.; Hong, S. Universal Parameters for Carbon Nanotube Network-Based Sensors: Can Nanotube Sensors Be Reproducible? *ACS Nano* **2011,** *5*, 4373–4379.

36. Li, J.; Zhang, Y.; To, S.; You, L.; Sun, Y. Effect of Nanowire Number, Diameter, and Doping Density on nano-FET Biosensor Sensitivity. *ACS Nano* **2011,** *5*, 6661–6668.

37. Xia, Y.; Rogers, J. A.; Paul, K. E.; Whitesides, G. M. Unconventional Methods for Fabricating and Patterning Nanostructures. *Chem. Rev.* **1999,** *99*, 1823–1848.

38. Mizuno, H.; Buriak, J. M. Catalytic Stamp Lithography for Sub-100 nm Patterning of Organic Monolayers. *J. Am. Chem. Soc.* **2008,** *130*, 17656–17657.

39. Braunschweig, A. B.; Huo, F.; Mirkin, C. A. Molecular Printing. *Nat. Chem.* **2009,** *1*, 353–358.

40. Wang, H.; Haroldson, R.; Balachandran, B.; Zakhidov, A.; Sohal, S.; Chan, J. Y.; Zakhidov, A.; Hu, W. Nanoimprinted Perovskite Nanograting Photodetector with Improved Efficiency. *ACS Nano* **2016,** *10*, 10921–10928.

41. Wang, C.; Shao, J.; Lai, D.; Tian, H.; Li, X. Suspended-Template Electric-Assisted Nanoimprinting for Hierarchical Micro-Nanostructures on a Fragile Substrate. *ACS Nano* **2019,** *13*, 10333–10342.

42. Meitl, M. A.; Zhu, Z.-T.; Kumar, V.; Lee, K. J.; Feng, X.; Huang, Y. Y.; Adesida, I.; Nuzzo, R. G.; Rogers, J. A. Transfer Printing by Kinetic Control of Adhesion to an Elastomeric Stamp. *Nat. Mater.* **2005,** *5*, 33–38.

43. Seo, M. H.; Yoo, J. Y.; Choi, S. Y.; Lee, J. S.; Choi, K. W.; Jeong, C. K.; Lee, K. J.; Yoon, J. B. Versatile Transfer of an Ultralong and Seamless Nanowire Array Crystallized at High Temperature for Use in High-Performance Flexible Devices. *ACS Nano* **2017,** *11*, 1520–1529.

44. Han, H. J.; Jeong, J. W.; Yang, S. R.; Kim, C.; Yoo, H. G.; Yoon, J. B.; Park, J. H.; Lee, K. J.; Kim, T. S.; Kim, S. W.; Jung, Y. S. Nanotransplantation Printing of Crystallographic-Orientation-Controlled Single-Crystalline Nanowire Arrays on Diverse Surfaces. *ACS Nano* **2017,** *11*, 11642–11652.

45. Lee, S. H.; Shin, S. H.; Madsen, M.; Takei, K.; Nah, J.; Lee, M. H. A Soft Lithographic Approach to Fabricate InAs Nanowire Field-Effect Transistors. *Sci. Rep.* **2018,** *8*, 3204.

46. Liu, Q.; Aroonyadet, N.; Song, Y.; Wang, X.; Cao, X.; Liu, Y.; Cong, S.; Wu, F.; Thompson, M. E.; Zhou, C. Highly Sensitive and Quick Detection of Acute Myocardial Infarction Biomarkers Using In_2O_3 Nanoribbon Biosensors Fabricated Using Shadow Masks. *ACS Nano* **2016,** *10*, 10117–10125.

47. Liu, Q.; Liu, Y.; Wu, F.; Cao, X.; Li, Z.; Alharbi, M.; Abbas, A. N.; Amer, M. R.; Zhou, C. Highly Sensitive and Wearable In_2O_3 Nanoribbon Transistor Biosensors with Integrated On-Chip Gate for Glucose Monitoring in Body Fluids. *ACS Nano* **2018,** *12*, 1170–1178.

48. Liu, Q.; Zhao, C.; Chen, M.; Liu, Y.; Zhao, Z.; Wu, F.; Li, Z.; Weiss, P. S.; Andrews, A. M.; Zhou, C. Flexible Multifunctional In_2O_3 Nanoribbon Aptamer-Field-Effect Transistor Biosensing. *iScience* **2020,** *23*, 101469.

49. Nair, P. R.; Alam, M. A. Screening-Limited Response of Nanobiosensors. *Nano Lett.* **2008,** *8*, 1281-1285.

50. Li, Z.; Rajendran, B.; Kamins, T. I.; Li, X.; Chen, Y.; Williams, R. S. Silicon Nanowires for Sequence-Specific DNA Sensing: Device Fabrication and Simulation. *Appl. Phys. A* **2005,** *80*, 1257–1263.

51. Sheehan, P. E.; Whitman, L. J. Detection Limits for Nanoscale Biosensors. *Nano Lett.* **2005,** *5*, 803-807.

52. Zhiyong, F.; Lu, J. G. Chemical Sensing with ZnO Nanowire Field-Effect Transistor. *IEEE Trans. Nanotechnol.* **2006,** *5*, 393–396.

53. Stern, E.; Klemic, J. F.; Routenberg, D. A.; Wyrembak, P. N.; Turner-Evans, D. B.; Hamilton, A. D.; LaVan, D. A.; Fahmy, T. M.; Reed, M. A. Label-Free Immunodetection with CMOS-Compatible Semiconducting Nanowires. *Nature* **2007,** *445*, 519–522.

54. Elfstrom, N.; Juhasz, R.; Sychugov, I.; Engfeldt, T.; Karlstrom, A. E.; Linnros, J. Surface Charge Sensitivity of Silicon Nanowires: Size Dependence. *Nano Lett.* **2007,** *7*, 2608–2612.

55. Elfstrom, N.; Karlstrom, A. E.; Linnros, J. Silicon Nanoribbons for Electrical Detection of Biomolecules. *Nano Lett.* **2008,** *8*, 945–949.

56. Zhao, C.; Xu, X.; Bae, S. H.; Yang, Q.; Liu, W.; Belling, J. N.; Cheung, K. M.; Rim, Y. S.; Yang, Y.; Andrews, A. M.; Weiss, P. S. Large-Area, Ultrathin Metal-Oxide Semiconductor

Nanoribbon Arrays Fabricated by Chemical Lift-Off Lithography. *Nano Lett.* **2018,** *18*, 5590–5595.

57. Zhao, C.; Xu, X.; Ferhan, A. R.; Chiang, N.; Jackman, J. A.; Yang, Q.; Liu, W.; Andrews, A. M.; Cho, N. J.; Weiss, P. S. Scalable Fabrication of Quasi-One-Dimensional Gold Nanoribbons for Plasmonic Sensing. *Nano Lett.* **2020,** *20*, 1747–1754.

58. Liao, W. S.; Cheunkar, S.; Cao, H. H.; Bednar, H. R.; Weiss, P. S.; Andrews, A. M. Subtractive Patterning *via* Chemical Lift-Off Lithography. *Science* **2012,** *337*, 1517–1521.

59. Cao, H. H.; Nakatsuka, N.; Serino, A. C.; Liao, W.-S.; Cheunkar, S.; Yang, H.; Weiss, P. S.; Andrews, A. M. Controlled DNA Patterning by Chemical Lift-Off Lithography: Matrix Matters. *ACS Nano* **2015,** *9*, 11439–11454.

60. Andrews, A. M.; Liao, W. S.; Weiss, P. S. Double-Sided Opportunities Using Chemical Lift-Off Lithography. *Acc. Chem. Res.* **2016,** *49*, 1449–1457.

61. Xu, X.; Yang, Q.; Cheung, K. M.; Zhao, C.; Wattanatorn, N.; Belling, J. N.; Abendroth, J. M.; Slaughter, L. S.; Mirkin, C. A.; Andrews, A. M.; Weiss, P. S. Polymer-Pen Chemical Lift-Off Lithography. *Nano Lett.* **2017,** *17*, 3302–3311.

62. Zhao, C.; Xu, X.; Yang, Q.; Man, T.; Jonas, S. J.; Schwartz, J. J.; Andrews, A. M.; Weiss, P. S. Self-Collapse Lithography. *Nano Lett.* **2017,** *17*, 5035–5042.

63. Cao, H. H.; Nakatsuka, N.; Liao, W.-S.; Serino, A. C.; Cheunkar, S.; Yang, H.; Weiss, P. S.; Andrews, A. M. Advancing Biocapture Substrates *via* Chemical Lift-Off Lithography. *Chem. Mater.* **2017,** *29*, 6829–6839.

64. Slaughter, L. S.; Cheung, K. M.; Kaappa, S.; Cao, H. H.; Yang, Q.; Young, T. D.; Serino, A. C.; Malola, S.; Olson, J. M.; Link, S.; Hakkinen, H.; Andrews, A. M.; Weiss, P. S. Patterning of Supported Gold Monolayers *via* Chemical Lift-Off Lithography. *Beilstein J. Nanotechnol.* **2017,** *8*, 2648–2661.

65. Cao, H. H.; Nakatsuka, N.; Serino, A. C.; Liao, W.-S.; Cheunkar, S.; Yang, H.; Weiss, P. S.; Andrews, A. M. Small-Molecule Patterning *via* Prefunctionalized Alkanethiols. *Chem. Mater.* **2018,** *30*, 4017–4030.

66. Cheung, K. M.; Stemer, D. M.; Zhao, C.; Young, T. D.; Belling, J. N.; Andrews, A. M.; Weiss, P. S. Chemical Lift-Off Lithography of Metal and Semiconductor Surfaces. *ACS Mater. Lett.* **2019,** *2*, 76–83.

67. Zayats, M.; Huang, Y.; Gill, R.; Ma, C. A.; Willner, I. Label-Free and Reagentless Aptamer-Based Sensors for Small Molecules. *J. Am. Chem. Soc.* **2006,** *128*, 13666–13667.

68. Lee, C. S.; Kim, S. K.; Kim, M. Ion-Sensitive Field-Effect Transistor for Biological Sensing. *Sensors (Basel)* **2009,** *9*, 7111–7131.

69. Zhang, J.; Rupakula, M.; Bellando, F.; Garcia Cordero, E.; Longo, J.; Wildhaber, F.; Herment, G.; Guerin, H.; Ionescu, A. M. Sweat Biomarker Sensor Incorporating Picowatt, Three-Dimensional Extended Metal Gate Ion Sensitive Field Effect Transistors. *ACS Sens.* **2019,** *4*, 2039–2047.

70. Keeble, L.; Moser, N.; Rodriguez-Manzano, J.; Georgiou, P. ISFET-Based Sensing and Electric Field Actuation of DNA for On-Chip Detection: A Review. *IEEE Sens. J.* **2020**.

71. Jeon, J. H.; Cho, W. J. Ultrasensitive Coplanar Dual-Gate ISFETs for Point-Of-Care Biomedical Applications. *ACS Omega* **2020,** *5*, 12809–12815.

72. Stern, E.; Wagner, R.; Sigworth, F. J.; Breaker, R.; Fahmy, T. M.; Reed, M. A. Importance of the Debye Screening Length on Nanowire Field Effect Transistor Sensors. *Nano Lett.* **2007,** *7*, 3405–3409.

73. Lee, K.; Nair, P. R.; Scott, A.; Alam, M. A.; Janes, D. B. Device Considerations for Development of Conductance-Based Biosensors. *J. Appl. Phys.* **2009,** *105*, 102046.

74. Patel, B. A. Continuous Amperometric Detection of Co-Released Serotonin and Melatonin from the Mucosa in the Ileum. *Analyst* **2008,** *133*, 516–524.

75. Yang, H.; Thompson, A. B.; McIntosh, B. J.; Altieri, S. C.; Andrews, A. M. Physiologically Relevant Changes in Serotonin Resolved by Fast Microdialysis. *ACS Chem. Neurosci.* **2013,** *4*, 790–798.

76. Zhao, C.; Cheung, K. M.; Huang, I-W.; Yang, H.; Nakatsuka, N.; Liu, W.; Cao, Y.; Man, T.; Weiss, P. S.; Monbouquette, H. G.; Andrews, A. M. Implantable Aptamer–Field-Effect Transistor Neuroprobes for *in Vivo* Neurotransmitter Monitoring. *Sci. Adv.* **2021,** *7*, eabj7422.

77. Cheung, K. M.; Abendroth, J. M.; Nakatsuka, N.; Zhu, B.; Yang, Y.; Andrews, A. M.; Weiss, P. S. Detecting DNA and RNA and Differentiating Single-Nucleotide Variations *via* Field-Effect Transistors. *Nano Lett.* **2020,** *20*, 5982–5990.

78. Xiao, Y.; Qu, X.; Plaxco, K. W.; Heeger, A. J. Label-Free Electrochemical Detection of DNA in Blood Serum *via* Target-Induced Resolution of an Electrode-Bound DNA Pseudoknot. *J. Am. Chem. Soc.* **2007,** *129*, 11896–11897.

79. Sassolas, A.; Leca-Bouvier, B. D.; Blum, L. J. DNA Biosensors and Microarrays. *Chem. Rev.* **2008,** *108*, 109–139.

80. Chu, D. K. W.; Pan, Y.; Cheng, S. M. S.; Hui, K. P. Y.; Krishnan, P.; Liu, Y.; Ng, D. Y. M.; Wan, C. K. C.; Yang, P.; Wang, Q.; Peiris, M.; Poon, L. L. M. Molecular Diagnosis of a Novel Coronavirus (2019-nCoV) Causing an Outbreak of Pneumonia. *Clin. Chem.* **2020,** *66*, 549–555.

81. Fauci, A. S.; Lane, H. C.; Redfield, R. R. Covid-19–Navigating the Uncharted. *N. Engl. J. Med.* **2020,** *382*, 1268–1269.

82. Behzadirad, M.; Nami, M.; Wostbrock, N.; Zamani Kouhpanji, M. R.; Feezell, D. F.; Brueck, S. R. J.; Busani, T. Scalable Top-Down Approach Tailored by Interferometric Lithography to Achieve Large-Area Single-Mode Gan Nanowire Laser Arrays on Sapphire Substrate. *ACS Nano* **2018**, *12*, 2373– 2380.

83. Cui, Y.; Wei, Q.; Park, H.; Lieber, C. M. Nanowire Nanosensors for Highly Sensitive and Selective Detection of Biological and Chemical Species. *Science* **2001,** *293*, 1289–1292.

84. Patolsky, F.; Zheng, G.; Lieber, C. M. Fabrication of Silicon Nanowire Devices for Ultrasensitive, Label-Free, Real-Time Detection of Biological and Chemical Species. *Nat. Protoc.* **2006,** *1*, 1711–1724.

85. Hu, P.; Yan, M.; Wang, X.; Han, C.; He, L.; Wei, X.; Niu, C.; Zhao, K.; Tian, X.; Wei, Q.; Li, Z.; Mai, L. Single-Nanowire Electrochemical Probe Detection for Internally Optimized Mechanism of Porous Graphene in Electrochemical Devices. *Nano Lett.* **2016,** *16*, 1523–1529.

86. Knopfmacher, O.; Tarasov, A.; Fu, W.; Wipf, M.; Niesen, B.; Calame, M.; Schonenberger, C. Nernst Limit in Dual-Gated Si-Nanowire FET Sensors. *Nano Lett.* **2010,** *10*, 2268–2274.

87. Shoorideh, K.; Chui, C. O. On the Origin of Enhanced Sensitivity in Nanoscale FET-Based Biosensors. *Proc. Natl. Acad. Sci. U. S. A.* **2014,** *111*, 5111–5116.

Chapter 6

Photothermal Intracellular Delivery Using Gold Nanodisk Arrays

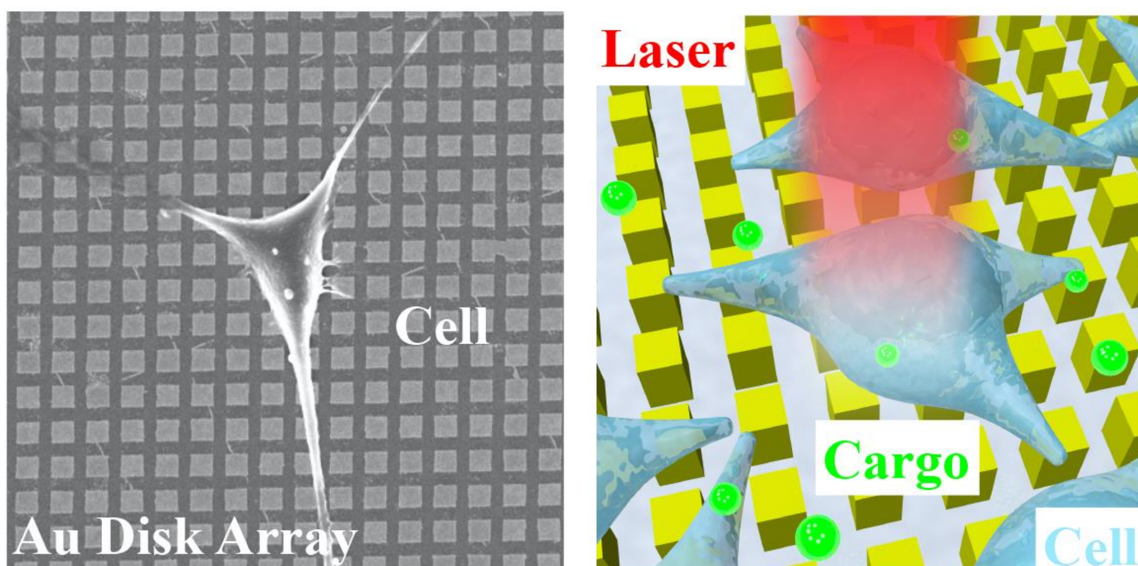

The information in this chapter is reprinted with permission from

ACS Mater. Lett. **2020**, *2*, 1475–1483 Copyright (2021) American Chemical Society

Authors: Zhao, C.; Man, T.; Xu, X.; Yang, Q.; **Liu, W.**; Jonas, S. J.; Teitell, M. A.;

Chiou, P. Y.; Weiss, P. S.

6.1 Abstract

Local heating using pulsed laser-induced photothermal effects on plasmonic nanostructured substrates can be used for intracellular delivery applications. However, the fabrication of plasmonic nanostructured interfaces is hampered by complex nanomanufacturing schemes. Here, we demonstrate the fabrication of large-area plasmonic gold (Au) nanodisk arrays that enable photothermal intracellular delivery of biomolecular cargo at high efficiency. The Au nanodisks (350 nm in diameter) were fabricated using chemical lift-off lithography (CLL). Nanosecond laser pulses were used to excite the plasmonic nanostructures, thereby generating transient pores at the outer membranes of targeted cells that enable the delivery of biomolecules *via* diffusion. Delivery efficiencies of >98% were achieved using the cell impermeable dye calcein (0.6 kDa) as a model payload, while maintaining cell viabilities at >98%. The highly efficient intracellular delivery approach demonstrated in this work will facilitate translational studies targeting molecular screening and drug testing that bridge laboratory and clinical investigations.

6.2 Introduction

Intracellular delivery of exogenous cargo, such as nucleic acids,[240-243] proteins,[244,245] and membrane-impermeable drugs,[245-247] is of great importance across a spectrum of biomedical and therapeutic applications, including precision gene modification,[248-251] immunotherapy,[252-254] intracellular imaging/sensing,[255,256] drug delivery,[245,247,257,258] and regenerative medicine.[259,260] To date, efforts towards intracellular delivery have been advanced by carrier-based and membrane-disruption-based approaches.[261-263] Viral-vector-based methods remain the most clinically advanced carrier-based strategies, achieving nucleic acid delivery with high efficiencies and specificities.[264,265] However, challenges associated with their potential immunogenicity, safety concerns from off-target effects, complexity, and high costs have limited their broader application.[264] Moreover, viral-based carrier systems suffer from intrinsic limitations in their cargo-carrying capacity, which preclude effective complex biomolecules or mixtures of components. Membrane-disruption-based approaches,[262,266,267] where transient pores are created in cell membranes *via* mechanical,[263,268-274] electrical,[275,276] or photothermal methods,[277-283] are less dependent on cargo and cell type.[284] Electroporation-based methods yield appropriate efficiencies but suffer from low viability and require specialized equipment and reagents.[261,285-288] Strategies using nanostructures, such as nanowires,[289,290] nanostraws,[291-293] and nanoneedles[269,294-297] to create pores in cell membranes, have also been shown to have suitable efficiencies and viabilities for intracellular delivery, but are limited by poor reproducibility, slow processing throughputs, and complicated fabrication processes.

Photothermal strategies that utilize the generation of cavitation bubbles induced by laser irradiation of noble metal nanoparticles or metal plasmonic structures represent another promising membrane-disruption method.[298,299] Upon laser irradiation, metallic nanostructures absorb incident

photon energy through electron oscillations, which results in abrupt temperature increases in the surrounding aqueous medium.[300,301] Explosive cavitation bubbles nucleate when the temperature exceeds the critical temperature of the aqueous medium.[282] Large fluid shear stress induced by the rapid expansion and collapse of cavitation generates transient and localized pores an adjacent cell membrane.[302] The size of cavitation bubbles dependents on the laser fluences radiated, which has been previously studied to be in the range of 100 nm to 1 μm.[303] Previous studies have demonstrated that noble metal nanoparticles, such as Au nanoparticles, are well suited to serve as high-efficiency delivery agents.[277-283,304,305] However, the cytotoxicity of Au nanoparticles is still under investigation, and this method also suffers from limitations in reproducibility. For example, it has been shown that the number and the location of pores created on each cell is not well controlled due to the random distribution of nanoparticles. Moreover, high delivery efficiencies achieved with increased nanoparticle concentration typically resulted in compromised cell viability.[306] Alternatively, substrate-supported plasmonic structures, fabricated using micro- and nanolithography techniques, serve as promising platforms for high-efficiency and high-viability intracellular delivery.[245,247,258,307] In addition, because of the physical separation of the nanostructures, the stoichiometry of the interactions with the cells can be controlled precisely (as compared to the case for plasmonic nanoparticles). Current methods of producing plasmonic architectures for photothermal delivery applications are limited by time consuming and costly conventional nanolithographic fabrication processes (*e.g.*, electron-beam lithography) used to pattern metal layers, which hinder the scalability of these techniques and represent a critical barrier to applying these technologies to clinical targets. Alternatively, nanofabrication approaches that yield repeatable, scalable, and economical processing of plasmonic nanostructures could facilitate consideration of this approach for wide-scale clinical applications. Recent advances have been

made in producing plasmonic structures using template-stripping processes. For example, nanopyramid structures have been fabricated in an economical and high-throughput manner.[247] However, challenges remain for a facile fabrication process as the template stripping process requires the fabrication on a polymer layer and an extra transfer process.

Soft lithography uses soft polymeric stamps to fabricate a range of micro- and nanoscale features in a high-throughput, large-scale, and cost-effective manner.[308,309] Microcontact printing (μCP), as a representative soft lithography method, transfers molecular inks, such as alkanethiols, from stamp to target surfaces.[309,310] A complementary, subtractive soft-lithography process, chemical lift-off lithography (CLL), uses oxygen plasma-activated polydimethylsiloxane (PDMS) stamps to remove self-assembled monolayer (SAM) molecules selectively from contacted areas on surfaces to create patterns over large areas, and may be used to achieve high-fidelity chemical patterns with line widths approaching 5 nm (corresponding to patterns ~10 molecules across).[233,311-317] The remaining SAM molecules in the non-lifted-off regions can act as resists to enable selective etching of exposed Au to produce Au nanostructures, such as Au nanolines, nanocircles, and nanosquares.[236,312,317,318]

In this work, we apply CLL to achieve fabrication of Au plasmonic nanostructures over large areas for photothermal intracellular delivery. Large-area two-dimensional (2D) Au nanodisk arrays are fabricated across centimeter length scales on a variety of substrates, such as silicon wafers, glass slices, and plastic petri dishes, which provides a significant advantage for versatile intracellular delivery environments and creates opportunities for integration with medical devices. Nanodisk arrays of different sizes have been fabricated in this study to measure delivery efficiencies and cell viabilities as a function of nanostructure surface density per cell. Upon excitation of the nanodisks with a nanosecond laser, delivery efficiencies of >98% and cell

viabilities of >98% were achieved using 0.6 kDa cell membrane-impermeable calcein as a model cargo molecule, which is comparable with current photothermal intracellular delivery platforms. This work demonstrates a promising economical and reproducible intracellular delivery approach, with widespread applicability for drug delivery, nanoparticle delivery, and regenerative medicine.

6.3 Materials and Methods

Materials. Prime quality 4″ silicon (Si) wafers (P/B, 0.001-0.005 Ω·cm, thickness 500 μm) were purchased from Silicon Valley Microelectronics, Inc. (Santa Clara, CA, USA). Sylgard 184® silicone elastomer kits were purchased from Ellsworth Adhesives (Germantown, WI, USA). Iron nitrate, and thiourea were purchased from Sigma-Aldrich (St. Louis, MO, USA) and used as received. Deionized water (18.2 MΩ·cm) from a Milli-Q system (Millipore, Billerica, MA) was used in all experiments.

Chemical lift-off lithography. Gold nanodisk substrates were prepared *via* chemical lift-off lithography (CLL).[79] Briefly**,** a CHA solution electron-beam evaporator was used to first deposit a 10-nm-thick titanium (Ti) adhesion layer followed by a 30-nm gold (Au) film onto desired substrates. The substrates were then annealed in a hydrogen flame for ~10 s before immersion into 1 mM 11-mercapto-1-undecanol solution for over 12 h. Polydimethylsiloxane (PDMS) stamps[S317] were exposed to oxygen plasma (Harrick Plasma, Ithaca, NY) for 40 s at a power of 18 W and a pressure of 10 psi for activation before contact with the substrate for over 12 h. After the PDMS stamps were lifted-off, the substrate was then immersed into an aqueous solution of 20 mM iron nitrate and 30 mM thiourea for 30 min to etch the Au film selectively within the exposed area. The etch rate was ~1 nm/min. Substrates were then rinsed with deionized

water, dried under a stream of N_2 before use, and sterilized *via* ultraviolet (UV) irradiation overnight.

Characterization. Scanning electron microscope (SEM) images were obtained using a Zeiss Supra 40VP scanning electron microscope with an Inlens SE Detector (Inlens secondary electron detector). Atomic force microscope (AFM) imaging was performed on a Bruker FastScan system using peak force tapping mode with ScanAsyst-Air tips. Optical images were taken with a Zeiss Axiotech optical microscope. Fluorescence images were taken with an upright fluorescence microscope (Axio Scope.A1, Carl Zeiss) equipped with a 10× objective lens.

Cell Seeding and Culture on Substrate. HeLa cells (ATCC) were maintained in Dulbecco's modified essential medium (DMEM, Corning) supplemented with 10% (vol/vol) fetal bovine serum (FBS, Thermo Scientific), 1% penicillin/streptomycin (Mediatech), and 1% sodium pyruvate (Corning). Chips were coated with fibronectin (Sigma, 40 µg/mL in phosphate-buffered saline, PBS) to promote cell adhesion. HeLa cells were seeded on to the chip and kept in an incubator at 37 °C and 5% CO_2 for 24 h. Cells were stained with 1 µg/mL Calcein AM (Invitrogen) to show cell seeding results.

Cell Fixation. Chips with HeLa cells were rinsed with PBS three times and soaked in 4% paraformaldehyde in PBS for 20 min at room temperature. The chips were then removed from the paraformaldehyde solution and were then rinsed with PBS three times prior to immersion in ethanol of graded concentrations (50%, 70%, 90%, and 100%) for 5 min each. And then hexamethyldisilazane (HMDS) three times for 7 min each. Samples were then air dried overnight prior to analysis.

Laser-Scanning and Delivery Setup. A Q-switched Nd:YAG laser (Minilite I, Continuum) with wavelength of 532 nm, beam diameter of 3 mm, and pulse duration of 6 ns was used to scan each sample. A half-wave polarizer and polarizing beam splitter designed for a 532 nm laser was used to adjust the power splitting ratio of the two beams. Laser energy was checked prior to each experiment using a laser energy meter (Nova II, Ophir). Sample were placed on an automated X Y translation stage to expose their entire 1 cm2 area to the laser beam (**Figure S1**). As shown in the schematic, the laser beam was directed from the top of the sample. We used 35-mm petri dishes to hold the sample in the center during the laser pulsing, which mitigates the effect of the meniscus. The laser beam is 3 mm in diameter, while the HeLa cell sizes are in the range of tens of microns. In our experiments, cells were treated with single laser pulses to obtain the current results.

Fluorescence Microscopy and Cell Counting. Scanning cells were incubated in 37 °C and 5% CO2 for 90 min before checking delivery efficiency and viability. The cell permeable nuclear dye Hoechst 33342 was used to label all processed cells for ease of quantifying the total number of cells present on each chip. HeLa cells that retained the cell-impermeable calcein molecules represented successful delivery. Cell viability was determined using propidium iodide (5 µg/mL), which is permeable to dead cells. Cell number was determined using both the automatic counting algorithm of the Fiji image processing software package and manual counting to double check. Each data point in **Figure 6.5e-g** represents the mean value of at least 3 randomly selected fields of view with at least 200 cells; error bars represent standard deviation.

Numerical Simulations. Temperature distributions from the plasmonic structures were modeled using a finite element method (COMSOL, Multiphysics 5.3) to calculate substrate-light interactions. The geometry was constructed based on the dimensions of the actual nanodisk chips. Electromagnetic wave with linear polarization in diagonal direction was applied, which is

consistent with experimental configurations. Electromagnetic interaction was calculated using a scattered field formulation method in the z direction (wavelength = 532 nm, fluence = 11 mJ/cm^2) and the resistive loss was used as the heat source for transient heat transfer. Perfectly matched layers were applied to truncate the modeling domain.

6.4. Results and Discussions

We exploit the plasmonic properties of the gold nanodisks whereby exposure to nanosecond laser pulses generates cavitation bubbles with energies sufficient to puncture cellular membranes, forming pores that facilitate intracellular delivery of desired cargo (**Figure 6.1**). HeLa cells, used as a model cell line, were cultured onto CLL-patterned nanodisk substrates and placed in a growth medium containing calcein. By scanning the laser across the wafer-scale Au plasmonic substrate, plasmonic hotspots formed upon illumination. Cavitation bubbles generated at these local regions in contacting the plasma membranes of the target HeLa cells serve as projectiles that render the cells transiently permeable. Cargo molecules within the surrounding medium are able to enter the cytoplasm *via* diffusion.[245] Precision control of the pulsed-laser spot position across the substrate is maintained with a pair of X-Y scanning mirrors. It takes 10 s to scan across the entire 25-mm^2 chip, with over 10^4 cells per chip.

The fabrication of periodic metal nanostructures with micron-scale features can be achieved readily *via* conventional photolithography, while producing sub-micron features often requires specialized tools such as electron beam lithography (EBL) and focused ion beam lithography (FIB). However, these serial writing processes systems are time consuming and costly to operate, leading to extremely limited production yields and output. Transfer printing techniques, such as nanotransfer printing, provide an alternative solution for nanofabrication over large areas while achieving higher processing throughputs.[319] Existing nanoscale printing approaches are

limited to certain substrates based on surface energy constraints that are critical for successful and reproducible pattern transfer. In this study, we extend the applications of CLL for biomedical applications. Double-patterning CLL has been recently reported as a means of fabricating Au plasmonic nanodisk arrays (**Figure 6.2a**).[318] Polydimethylsiloxane stamps, textured with lines of different widths and pitches are activated by exposure to oxygen plasma to generate hydrophilic silanol groups at the stamp surface. Substrates for CLL (*e.g.*, silicon wafers) are coated with a thin layer of Au (30 nm) that is functionalized with a hydroxyl-terminated alkanethiol (11-mercapto-1-undecanol) SAM. Conformal contact between the stamp and the substrate leads to condensation reactions between OH-groups of SAM and the silanol groups of activated PDMS, leading to the formation of covalent bonds (Si–O–SAM). Lifting the stamp from the substrate results in selective removal of the SAM corresponding to the stamp's pattern, leaving SAM molecules within the non-contacted regions that establish a series of nanoscale lines. A second CLL step was then carried out using a re-activated stamp that is rotated 90° and registered to the initial pattern. After the second patterning step, arrays comprised of SAM nanosquares are produced, which serve as molecular resists during the subsequent wet etching to generate 2D Au nanodisk substrates.

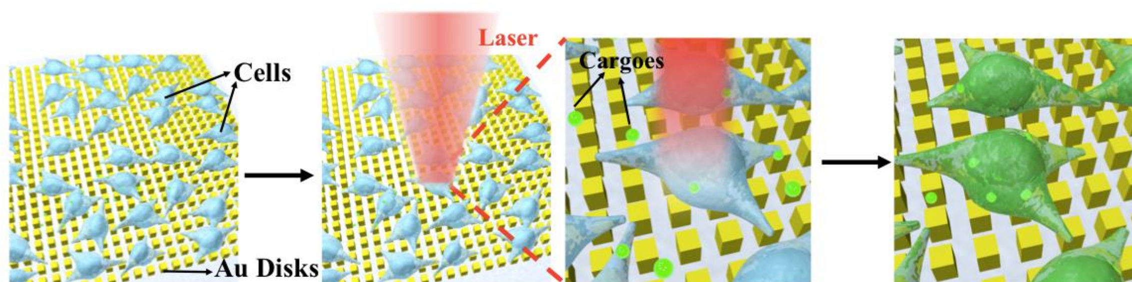

Figure 6.1. (a) Illustration of photothermal intracellular delivery enabled by localized surface plasmon resonance (LSPR) of gold nanodisks excited by a nanosecond laser. After cell seeding, the laser was rastered over cells seeded onto the nanostructures and cultured in a medium containing membrane impermeable biomolecules. Upon irradiation, the gold plasmonic structures heat up rapidly and generate cavitation bubbles, which facilitate the delivery of the biomolecular cargo into targeted cells by creating transient pores along nearby their outer membranes.

A representative image of a Au nanodisk array on a petri dish is shown in **Figure 6.2b**, where the central area contains uniformly patterned plasmonic nanostructures over cm scales. We extend the capabilities of this technique by demonstrating fabrication on multiple materials (*e.g.*, plastic petri dishes) that are easily coated with Au thin films and then modified *via* CLL patterning (**Figure 6.2c**). The ease of integration with commercially available cell culture products demonstrates the potential of our platform to add new functionality to existing medical devices, enabling opportunities for controlled *in situ* drug delivery and molecular screening. Stamps with periodic lines of different feature sizes were used in this study, with widths ranging from 350 nm to 10 μm and pitches ranging from 700 nm to 20 μm. To create sub-micron features, we used commercial optical storage products, such as DVDs (~ $1 each), as masters that contain large-area, periodic gratings with 350 nm wide at 700 nm pitch to circumvent the need for expensive and slow

lithographic techniques such as EBL. Atomic force microscope (AFM) images show the morphology of the fabricated Au nanodisks, with widths of 350 nm (**Figure 6.2d**), 1 μm (**Figure 6.2e**), and 2 μm (**Figure 6.2f**). The nanostructures maintain uniform shape with sharp edges, as seen in the AFM images. Corresponding optical microscope images that demonstrate the capability to tune the microscale widths of the patterned structures at 350 nm (**Figure S6.1**), 1 μm (**Figure 6.2g**), 2 μm (**Figure 6.2h**), and 10 μm (**Figure 6.2i**).

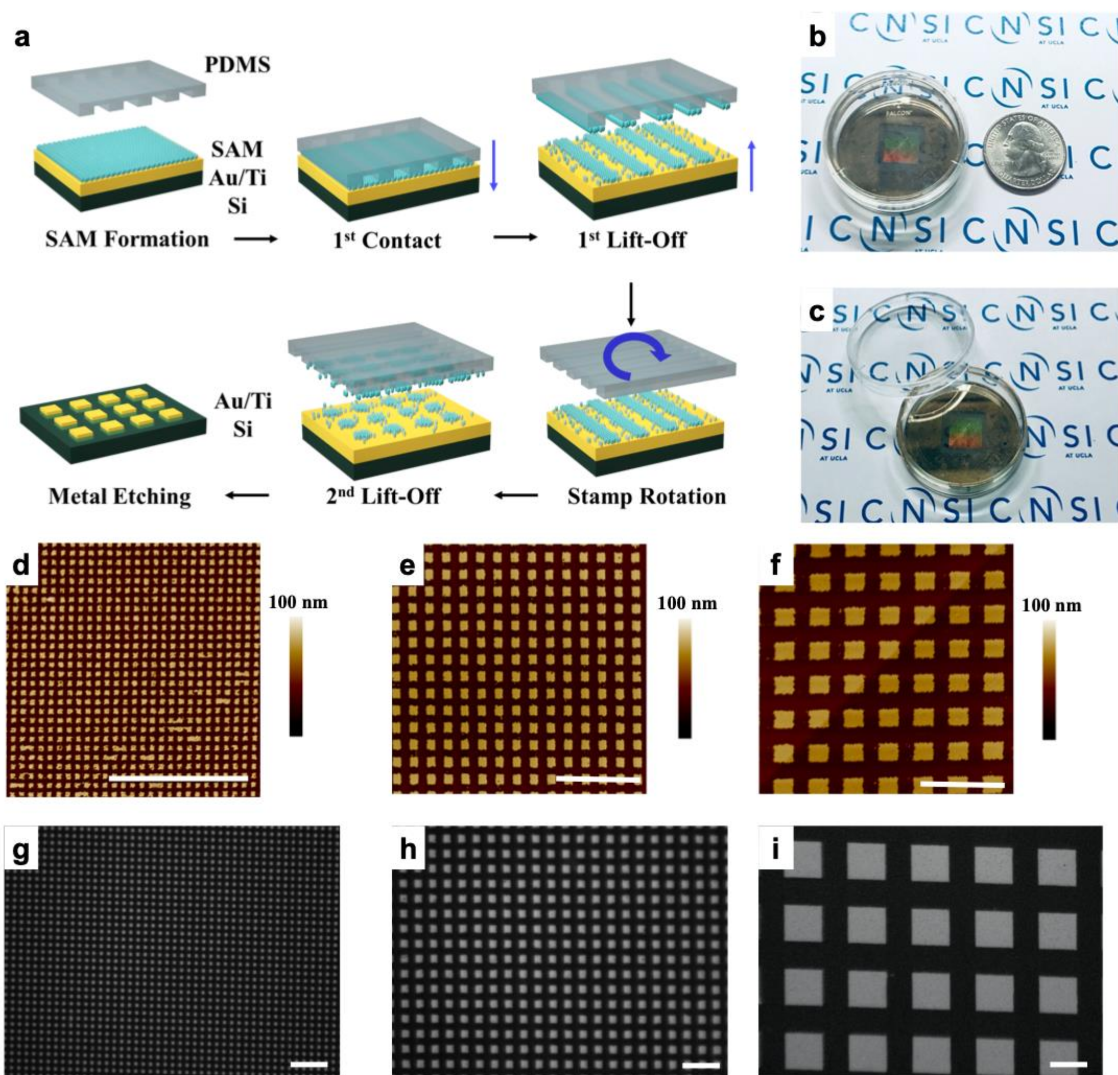

Figure 6.2. Gold plasmonic disk arrays fabricated by double-patterning chemical lift-off lithography (CLL). (a) Schematic of the patterning process. Substrates were coated with gold (Au) before being functionalized with self-assembled monolayers (SAMs). Polydimethylsiloxane (PDMS) stamps with line patterns were "activated" by exposure to an oxygen plasma to generate hydrophilic silanol groups on their surfaces. The stamps were then placed in conformal contact with the substrate. Molecules were selectively removed in the contact region upon lifting the stamp. A second patterning step was then performed by rotating the stamp 90° to generate two dimensional (2D) nanosquare chemical patterns.

Exposed metal was removed *via* wet etching to generate Au 2D nanodisk arrays. (b,c) Representative images of large-area 350-nm-wide Au nanodisk arrays on a plastic petri dish. (d-f) Atomic force microscope images of Au nanodisk arrays comprised of (d) 350-nm wide, (e) 1-µm wide, and (f) 2-µm wide features. (g-i) Optical microscope images of gold nanodisk arrays with feature widths (g) 1 µm, (h) 2 µm, and (i) 10 µm. Scale bars: 10 µm. CNSI at UCLA logo used with permission.

Plasmonic nanodisk arrays fabricated in this manner are promising candidates for substrates for surface plasmonic resonance (SPR) measurements.[318] Surface plasmon resonance properties of Au nanodisks have been studied in separate work.[318] We hypothesized that these plasmonic structures could be applied for photothermal delivery, where sharp edges concentrate effectively laser energy to generate cavitation bubbles in the cell culture medium.[307] Explosive boiling of water will occur when the temperature reaches 80–90% of its critical temperature (~650 K) that enables the bubbles formed in close proximity to a cell to puncture its outer membrane discretely.[245,247] Finite element analysis simulations (COMSOL, Multiphysics 4.4) were conducted that estimate that the aqueous cell culture medium reaches above 640 K (~360 °C) locally at laser irradiances of 11 mJ/cm^2 (**Figure 6.3h,i**), which is sufficient to initiate cavitation bubble formation. We have performed the simulations on different dimensions of Au nanodisk arrays, which show temperature increases between 636 and 644 K upon laser radiation across different nanodisk array sizes (**Figure S6.2**). Calcein AM (AM = acetoxymethyl), a cell membrane permeable variant of calcein, was used for short-term labeling of HeLa cells, as shown in **Figure 6.3a**, prior to fixation on a 1-µm wide nanodisk array. A scanning electron microscope (SEM) image of same region after cell fixation (**Figure 6.3b)** illustrates that cells are able to adhere to the Au nanodisk arrays substrates. An overlay of the optical and SEM images, within the green

box (**Figure 6.3b**), is presented in **Figure 6.3c** with matching cell distribution and morphology. Results of florescence image of calcein, cell fixation, and an image overlay on 2-μm wide nanodisk arrays are shown in **Figure 6.3d-3f**, respectively. Single cell morphology on a 2-μm wide nanodisk array was shown in **Figure 6.3g** with diameters of *ca*. 20 μm.

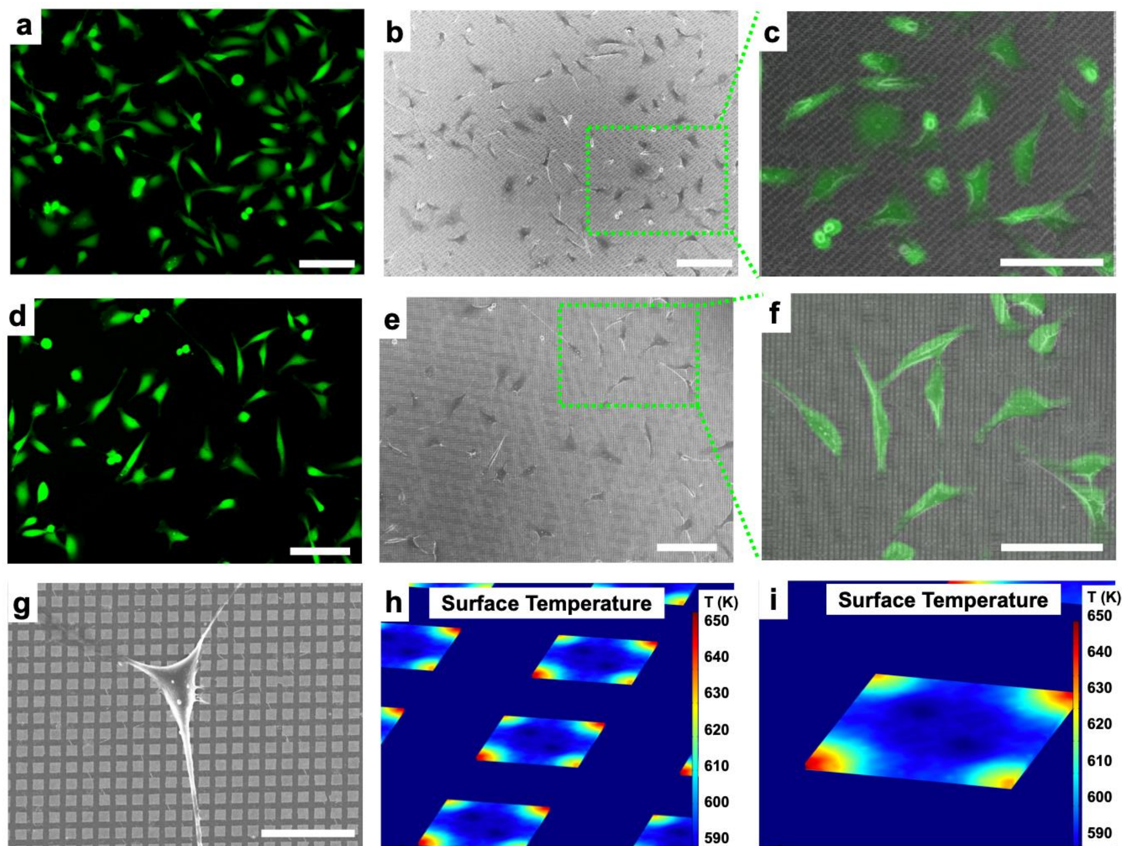

Figure 6.3. (a) Fluorescence microscope images of HeLa cells on 1-µm-wide gold (Au) nanodisk arrays labeled with a cell membrane-impermeable dye (Calcein AM). (b) Scanning electron microscope images of fixed cells on a substrate. (c) Overlay of the green-box-designated region seen in (b) with (a). (d) Fluorescence microscope images of HeLa cells on 2-µm-wide gold (Au) nanodisk arrays labeled with a cell membrane impermeable dye (Calcein AM). (e) Scanning electron microscope images of fixed cells on a substrate. (f) Overlay of the green box-designated region seen in (b) with (a). (g) Scanning electron microscope image of single Hela cell on 2-µm-wide Au nanodisk array substrate. (h,i) Simulation results of surface temperature at the gold nanodisk array (1-µm wide) interface in water. Scale bars: (a-f) 100 µm, (g) 20 µm.

We next demonstrated delivery of Calcein green (0.6 kDa membrane impermeable cargo) with high efficiency and high viability. A schematic of optical setup is shown in **Figure S6.3**. Calcein delivery using Au nanodisks (1 μm radius, 2 μm pitch, 30 nm thick) under 11 mJ/cm^2 laser irradiation can be seen in **Figure 6.4a**. Hoechst 33342, a cell-permeable nucleus fluorescence dye that emits at 497 nm, was used to label cell nuclei to quantify the total number of cells (**Figure 6.4b**). Propidium iodide (PI), which is not permeable to live cells, was used to detect dead cells (**Figure 6.4c**). Overlaid images of Calcein green fluorescence, Hoechst 33342 nucleus staining, and PI staining were taken 90 min after laser pulsing and are shown in **Figure 6.4d**. Efficiency was determined to be 98 ± 1%, with a viability of 99 ± 1% under the conditions described above, with three independent experiments of ~740 cells in total. Control experiments were performed on uniformly flat gold films (30 nm thick) under the same conditions show negligible delivery efficiency, which verifies the critical role of the Au nanostructure in the intracellular delivery of Calcein green under laser irradiation. It has been shown previously for similar systems that the cells will have minimal Au residue after laser radiation.[247]

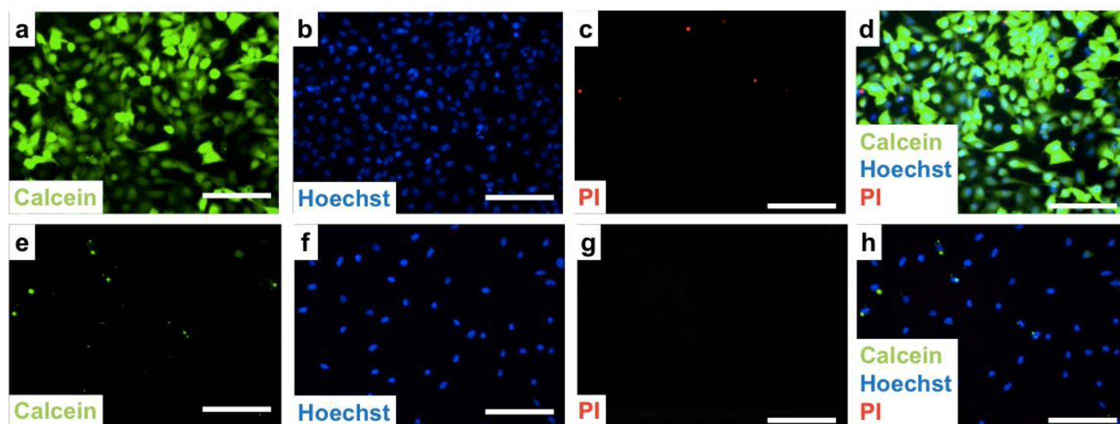

Figure 6.4. (a) Delivery efficiency and cell viability testing. (a-d) Delivery of calcein to HeLa cells using gold nanodisk arrays (1 µm wide, 2 µm pitch, 30 nm thickness) under laser irradiation with 11 mJ/cm^2 fluence. (a) Representative image of delivery of calcein (green) to targeted cells. (b) Cell nuclei are stained with Hoechst 33342 to label both live and dead cells (blue). (c) Propidium iodide (PI) assay to identify dead cells (red). (d) Overlaid image of calcein, Hoechst 33342, and PI dyes. Efficiency was found to be 98 ± 1%, and viability to be 99 ± 1%. (e–h) Control experiment using flat gold thin film under the same laser irradiation of 11 mJ/cm^2 fluence, where (e) corresponds to the calcein channel, (f) is the Hoechst dye, (g) is the PI dye, and (h) is the overlaid image of (e–g). Scale bars: 100 µm.

Different laser fluences, ranging from 7 to 21 mJ/cm^2, were studied to optimize delivery performance (**Figure 6.5a,b**). We observed that the number of cells receiving the calcein cargo (green) decreased while cytotoxicity (red) increased with increasing laser fluence. Additional experiments studying the effect of different laser fluences were performed with results plotted in **Figure 6.5e**. Over 2,500 cells were counted for each sample tested. Delivery efficiencies increased when the laser fluence was increased from the minimum laser intensity up to 11 mJ/cm^2, reaching 98 ± 1% efficiency. At higher laser fluences, both cell viability and efficiency decreased

significantly (with viability decreasing to 16 ± 2% and 6 ± 1% efficiency at 21 mJ/cm^2). We attribute this cytotoxicity to irrecoverable membrane disruption occurring at the higher laser intensities.[245,247,258,320] The delivery efficiency decrease with cell viability is expected, as calcein will only remain in live cells with intact plasma membranes.

We also studied the effects of width and pitch of the periodic nanodisk arrays on delivery performance. Fewer calcein-delivered cells were observed as the sizes of Au nanodisks were increased from 2 μm to 10 μm (**Figure 6.5c,d**) while the numbers of dead cells (red) remained the same relative to the total number of cells (blue). This phenomenon can be explained by the density of cavitation bubbles induced by the gold plasmonic structures per cell.[245] Results from our simulations of photothermal response (**Figure 6.3f**) indicate that hotspots occur at the corner of each nanodisk where the pitch of nanodisk array is twice the width of an individual disk. Disk arrays with larger disk widths have fewer hotspots and thus form fewer cavitation bubbles. Delivery efficiency therefore decreases on these substrates, due to the smaller numbers of cavitation bubbles. Our data indicate that the delivery efficiency is maximized for disks with widths smaller than 2 μm. Delivery efficiency and cell viability results on nanodisk arrays with different feature widths are shown in **Figure 6.5f**. Cargoes with different sizes were also studied, including 0.6 kDa calcein, 4 kDa calcein, and a 150 kDa dextran (**Figure 6.5g**). Delivery efficiencies of 98 ± 1% and 94 ± 1% were achieved for 0.6 kDa and 4 kDa calcein, respectively. Decreased efficiency of 36 ± 5% was observed for the dextran, which we infer is related to its lower diffusion coefficient. Note that the gold nanodisk substrates have the added benefit of being reusable as we did not notice any drop in performance after five experiments **(Figure S6.4).**

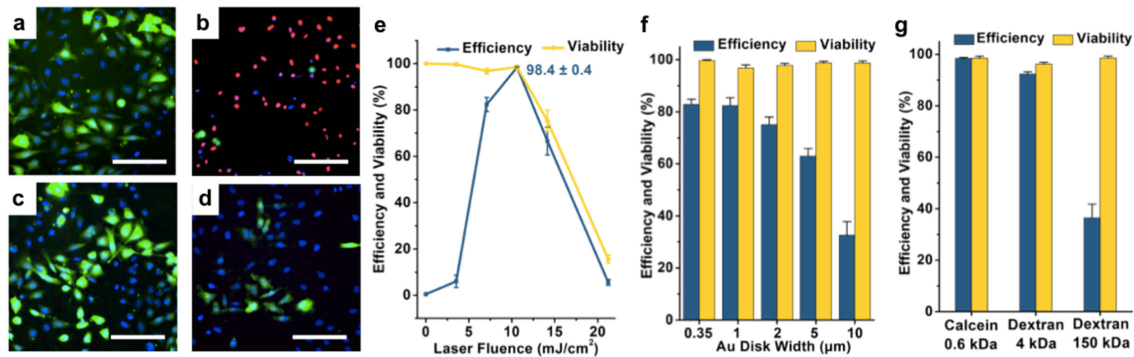

Figure 6.5. (a) Delivery efficiency and cell viability at different laser fluences and gold disk sizes are shown in overlaid images (a-d) of 0.6 kDa calcein delivery (green), Hoechst dye (blue), and PI dye (red). Delivery results under different laser fluence at (a) 7 mJ/cm^2, and (b) 21.2 mJ/cm^2, respectively, both on 1-µm wide nanodisk arrays. Delivery results using different sizes of gold nanodisk arrays of (c) 2 µm and (d) 10 µm widths, respectively, both under laser fluence of 7 mJ/cm^2. (e) Delivery efficiencies and viabilities after 90 min as a function of laser fluence on 1-µm wide nanodisk arrays. Error bars represented standard error mean (s.e.m.) (n = ~2,500 cells for all tests). (f) Delivery efficiencies and viabilities with different sizes of gold nanodisk arrays at 7 mJ/cm^2. Error bars, s.e.m. (n = ~1,900 cells for all tests). (g) Delivery efficiencies and viabilities with different cargoes at 11 mJ/cm^2 on 1-µm-wide nanodisk arrays. Error bars, s.e.m. (n = ~2,000 cells for all tests). Scale bars: 100 µm.

6.5 Conclusions and Prospects

In summary, effective and safe delivery of biomolecular cargos intracellularly was achieved by exposing large-area gold plasmonic substrates fabricated using double-patterning CLL to nanosecond-laser pulses. Gold surfaces patterned with 2D SAM nanosquare arrays were used to create sub-micron nanostructures. Illuminating the gold nanostructures with nanosecond laser pulses induced cavitation bubbles at the plasmonic hotspots through a photothermal effect. Cells seeded on the nanostructures were rendered transiently porous upon contact with the bubbles, enabling delivery of exogenous biomolecular cargo. Laser fluences and nanodisk sizes were optimized to achieve delivery efficiencies of over 98% for 0.6 kDa calcein with cell viability maintained at over 98%. Note that we attribute the photothermal delivery predominantly to the sheer force generated by the formation and collapse of the cavitation bubble, but we do not exclude the effects of local thermal heating of the plasma membrane.

Desirable features of this CLL-based strategy include: (1) cost-effective and high-throughput fabrication of uniform nanostructures over large (square centimeter) areas, (2) versatile substrate selection, (3) scalability and reproducibility, and (4) economical setup that does not require specialized instrumentation. Efficient delivery of membrane impermeant small molecules to HeLa cells with minimal cell death was achieved, which opens new opportunities for testing and manipulating in disease-relevant cellular targets and potential integration with medical devices. Both the PDMS stamps and the fabricated plasmonic substrates are reusable, enabling scale-up to larger formats. Compared with femtosecond lasers sometimes used in laboratory studies, the nanosecond pulsed laser used here is economical and straightforward to operate. This study demonstrates a promising method for high-efficiency intracellular delivery for cellular therapeutic and drug-discovery applications. In this work, we focused on delivery of small molecules into

HeLa cells. Previously, we have shown that our photothermal delivery platform can be applied to deliver large functional cargoes, such as live bacteria, proteins, and plasmids, into a variety of cell types, including primary normal human dermal fibroblasts and human B lymphocyte cells.[261,307] Future optimization and investigations of the Au nanodisk arrays will focus on advancing this technique so as to enable clinical applications, such as gene therapy and cancer immunotherapy.

6.6 Supplementary Materials

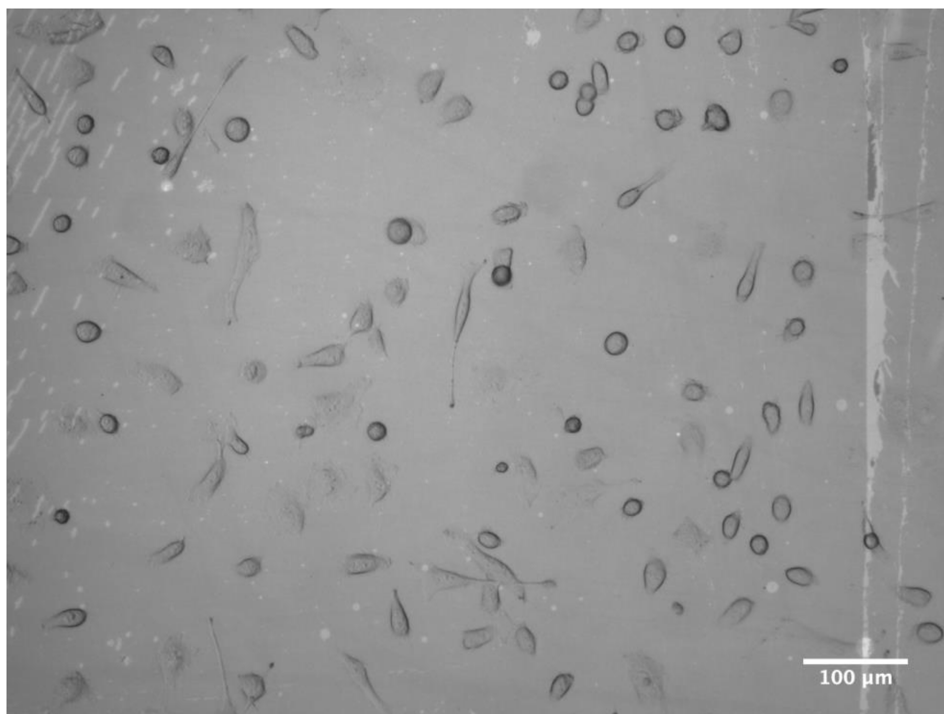

Figure S6.1. Optical microscope image of cells on 350-nm Au nanodisk arrays. The Au nanodisks are not visible in the optical microscope due to their sub-micron features.

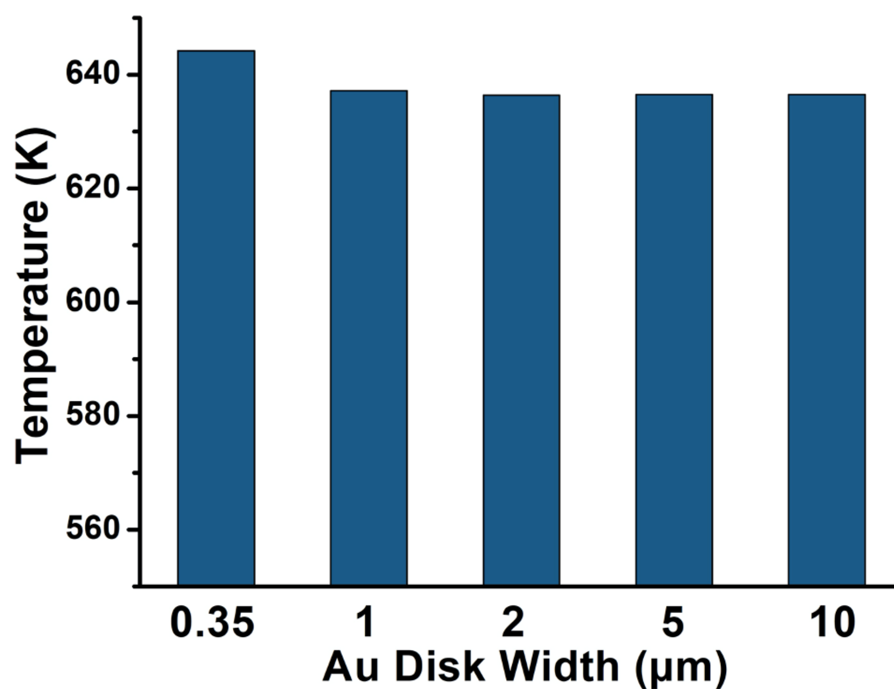

Figure S6.2. Simulation results for tip temperature on different dimensions of Au nanodisk arrays upon laser radiation of 11 mJ/cm^2.

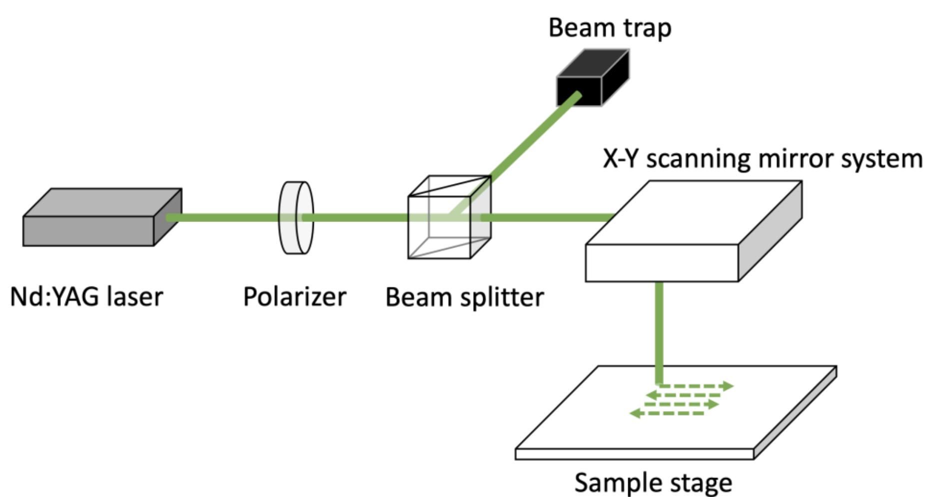

Figure S6.3. Schematic diagram of the optical setup.

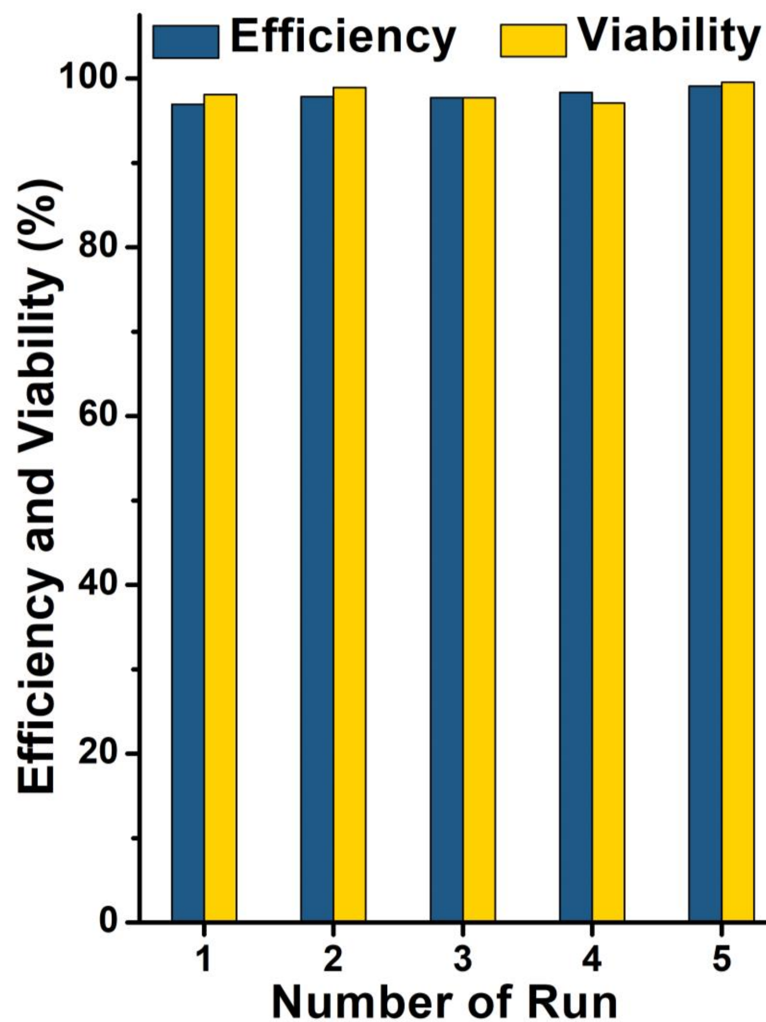

Figure S6.4. Delivery efficiency and cell viability results of 0.6 kDa calcein AM using a 1-µm-wide gold (Au) nanodisk arrays chip after five runs under 11 mJ/cm^2 laser fluence.

6.7 References

1. Esteban-Fernández de Ávila, B.; Angell, C.; Soto, F.; Lopez-Ramirez, M. A.; Báez, D. F.; Xie, S.; Wang, J.; Chen, Y. Acoustically Propelled Nanomotors for Intracellular siRNA Delivery. ACS Nano 2016, 10, 4997–5005.

2. Ding, X.; Stewart, M.; Sharei, A.; Weaver, J. C.; Langer, R. S.; Jensen, K. F. High-Throughput Nuclear Delivery and Rapid Expression of DNA *via* Mechanical and Electrical Cell-Membrane Disruption. *Nat. Biomed. Eng.* **2017,** *1*, 0039.

3. Xu, X.; Hou, S.; Wattanatorn, N.; Wang, F.; Yang, Q.; Zhao, C.; Yu, X.; Tseng, H. R.; Jonas, S. J.; Weiss, P. S. Precision-Guided Nanospears for Targeted and High-Throughput Intracellular Gene Delivery. *ACS Nano* **2018,** *12*, 4503–4511.

4. Ball, R. L.; Hajj, K. A.; Vizelman, J.; Bajaj, P.; Whitehead, K. A. Lipid Nanoparticle Formulations for Enhanced Co-Delivery of siRNA and mRNA. *Nano Lett.* **2018,** *18*, 3814–3822.

5. Yan, M.; Du, J.; Gu, Z.; Liang, M.; Hu, Y.; Zhang, W.; Priceman, S.; Wu, L.; Zhou, Z. H.; Liu, Z.; Segura, T.; Tang, Y.; Lu, Y. A Novel Intracellular Protein Delivery Platform Based on Single-Protein Nanocapsules. *Nat. Nanotechnol.* **2010,** *5*, 48–53.

6. Wu, Y. C.; Wu, T. H.; Clemens, D. L.; Lee, B. Y.; Wen, X.; Horwitz, M. A.; Teitell, M. A.; Chiou, P. Y. Massively Parallel Delivery of Large Cargo into Mammalian Cells with Light Pulses. *Nat. Methods* **2015,** *12*, 439–444.

7. Chou, L. Y.; Ming, K.; Chan, W. C. Strategies for the Intracellular Delivery of Nanoparticles. *Chem. Soc. Rev.* **2011,** *40*, 233–245.

8. Saklayen, N.; Huber, M.; Madrid, M.; Nuzzo, V.; Vulis, D. I.; Shen, W.; Nelson, J.; McClelland, A. A.; Heisterkamp, A.; Mazur, E. Intracellular Delivery Using Nanosecond-Laser Excitation of Large-Area Plasmonic Substrates. *ACS Nano* **2017,** *11*, 3671–3680.

9. Yin, H.; Kanasty, R. L.; Eltoukhy, A. A.; Vegas, A. J.; Dorkin, J. R.; Anderson, D. G. Non-Viral Vectors for Gene-Based Therapy. *Nat. Rev. Genet.* **2014,** *15*, 541–555.

10. Wang, H. X.; Li, M.; Lee, C. M.; Chakraborty, S.; Kim, H. W.; Bao, G.; Leong, K. W. CRISPR/Cas9-Based Genome Editing for Disease Modeling and Therapy: Challenges and Opportunities for Nonviral Delivery. *Chem. Rev.* **2017,** *117*, 9874–9906.

11. Zhu, H.; Zhang, L.; Tong, S.; Lee, C. M.; Deshmukh, H.; Bao, G. Spatial Control of *in vivo* CRISPR-Cas9 Genome Editing *via* Nanomagnets. *Nat. Biomed. Eng.* **2019,** *3*, 126–136.

12. Fang, J.; Hsueh, Y. Y.; Soto, J.; Sun, W.; Wang, J.; Gu, Z.; Khademhosseini, A.; Li, S. Engineering Biomaterials with Micro/Nanotechnologies for Cell Reprogramming. *ACS Nano* **2020,** *14*, 1296–1318.

13. Qin, X.-F.; An, D. S.; Chen, I. S. Y.; Baltimore, D. Inhibiting HIV-1 Infection in Human T Cells by Lentiviral-Mediated Delivery of Small Interfering RNA against CCR5. *Proc. Natl. Acad. Sci. U. S. A.* **2003,** *100*, 183–188.

14. Tebas, P.; Stein, D.; Tang, W. W.; Frank, I.; Wang, S. Q.; Lee, G.; Spratt, S. K.; Surosky, R. T.; Giedlin, M. A.; Nichol, G.; Holmes, M. C.; Gregory, P. D.; Ando, D. G.; Kalos, M.; Collman, R. G.; Binder-Scholl, G.; Plesa, G.; Hwang, W. T.; Levine, B. L.; June, C. H. Gene Editing of CCR5 in Autologous CD4 T Cells of Persons Infected with HIV. *N. Engl. J. Med.* **2014,** *370*, 901–910.

15. Rosenberg, S. A.; Restifo, N. P. Adoptive Cell Transfer as Personalized Immunotherapy for Human Cancer. *Science* **2015,** *348*, 62–68.

16. Zhao, C.; Bai, Z.; Liu, X.; Zhang, Y.; Zou, B.; Zhong, H. Small GSH-Capped $CuInS_2$ Quantum Dots: MPA-Assisted Aqueous Phase Transfer and Bioimaging Applications. *ACS Appl. Mater. Inter.* **2015,** *7*, 17623–17629.

17. Syed, A. M.; Sindhwani, S.; Wilhelm, S.; Kingston, B. R.; Lee, D. S. W.; Gommerman, J. L.; Chan, W. C. W. Three-Dimensional Imaging of Transparent Tissues *via* Metal Nanoparticle Labeling. *J. Am. Chem. Soc.* **2017,** *139*, 9961–9971.

18. Fox, C. B.; Cao, Y.; Nemeth, C. L.; Chirra, H. D.; Chevalier, R. W.; Xu, A. M.; Melosh, N. A.; Desai, T. A. Fabrication of Sealed Nanostraw Microdevices for Oral Drug Delivery. *ACS Nano* **2016,** *10*, 5873–5881.

19. Madrid, M.; Saklayen, N.; Shen, W.; Huber, M.; Vogel, N.; Mazur, E. Laser-Activated Self-Assembled Thermoplasmonic Nanocavity Substrates for Intracellular Delivery. *ACS Appl. Bio. Mater.* **2018,** *1*, 1793–1799.

20. Naldini, L. *Ex vivo* Gene Transfer and Correction for Cell-Based Therapies. *Nat. Rev. Genet.* **2011,** *12*, 301–315.

21. Cavazzana-Calvo, M.; Payen, E.; Negre, O.; Wang, G.; Hehir, K.; Fusil, F.; Down, J.; Denaro, M.; Brady, T.; Westerman, K.; Cavallesco, R.; Gillet-Legrand, B.; Caccavelli, L.; Sgarra, R.; Maouche-Chrétien, L.; Bernaudin, F.; Girot, R.; Dorazio, R.; Mulder, G.-J.; Polack, A.; Bank, A.; Soulier, J.; Larghero, J.; Kabbara, N.; Dalle, B.; Gourmel, B.; Socie, G.; Chrétien, S.; Cartier, N.; Aubourg, P.; Fischer, A.; Cornetta, K.; Galacteros, F.; Beuzard, Y.; Gluckman, E.; Bushman,

F.; Hacein-Bey-Abina, S.; Leboulch, P. Transfusion Independence and HMGA2 Activation after Gene Therapy of Human β-Thalassaemia. *Nature* **2010,** *467*, 318–322.

22. Stewart, M. P.; Sharei, A.; Ding, X.; Sahay, G.; Langer, R.; Jensen, K. F. *In Vitro* and *ex Vivo* Strategies for Intracellular Delivery. *Nature* **2016,** *538*, 183–192.

23. Stewart, M. P.; Langer, R.; Jensen, K. F. Intracellular Delivery by Membrane Disruption: Mechanisms, Strategies, and Concepts. *Chem. Rev.* **2018,** *118*, 7409–7531.

24. Belling, J. N.; Heidenreich, L. K.; Tian, Z.; Mendoza, A. M.; Chiou, T. T.; Gong, Y.; Chen, N. Y.; Young, T. D.; Wattanatorn, N.; Park, J. H.; Scarabelli, L.; Chiang, N.; Takahashi, J.; Young, S. G.; Stieg, A. Z.; De Oliveira, S.; Huang, T. J.; Weiss, P. S.; Jonas, S. J. Acoustofluidic Sonoporation for Gene Delivery to Human Hematopoietic Stem and Progenitor Cells. *Proc. Natl. Acad. Sci. U. S. A.* **2020,** *117*, 10976–10982.

25. Thomas, C. E.; Ehrhardt, A.; Kay, M. A. Progress and Problems with the Use of Viral Vectors for Gene Therapy. *Nat. Rev. Genet.* **2003,** *4*, 346–358.

26. Kotterman, M. A.; Chalberg, T. W.; Schaffer, D. V. Viral Vectors for Gene Therapy: Translational and Clinical Outlook. *Annu. Rev. Biomed. Eng.* **2015,** *17*, 63–89.

27. Qu, Y.; Zhang, Y.; Yu, Q.; Chen, H. Surface-Mediated Intracellular Delivery by Physical Membrane Disruption. *ACS Appl. Mater. Inter.* **2020,** *12*, 31054–31078.

28. Tay, A. The Benefits of Going Small: Nanostructures for Mammalian Cell Transfection. *ACS Nano* **2020**, *14*, 7714.

29. Sharei, A.; Zoldan, J.; Adamo, A.; Sim, W. Y.; Cho, N.; Jackson, E.; Mao, S.; Schneider, S.; Han, M.-J.; Lytton-Jean, A.; Basto, P. A.; Jhunjhunwala, S.; Lee, J.; Heller, D. A.; Kang, J. W.;

Hartoularos, G. C.; Kim, K.-S.; Anderson, D. G.; Langer, R.; Jensen, K. F. A Vector-Free Microfluidic Platform for Intracellular Delivery. *Proc. Natl. Acad. Sci. U. S. A.* **2013,** *110*, 2082–2087.

30. Chiappini, C.; Campagnolo, P.; Almeida, C. S.; Abbassi-Ghadi, N.; Chow, L. W.; Hanna, G. B.; Stevens, M. M. Mapping Local Cytosolic Enzymatic Activity in Human Esophageal Mucosa with Porous Silicon Nanoneedles. *Adv. Mater.* **2015,** *27*, 5147–5152.

31. Seong, H.; Higgins, S. G.; Penders, J.; Armstrong, J. P. K.; Crowder, S. W.; Moore, A. C.; Sero, J. E.; Becce, M.; Stevens, M. M. Size-Tunable Nanoneedle Arrays for Influencing Stem Cell Morphology, Gene Expression, and Nuclear Membrane Curvature. *ACS Nano* **2020,** *14*, 5371–5381.

32. Kang, G.; Carlson, D. W.; Kang, T. H.; Lee, S.; Haward, S. J.; Choi, I.; Shen, A. Q.; Chung, A. J. Intracellular Nanomaterial Delivery *via* Spiral Hydroporation. *ACS Nano* **2020,** *14*, 3048–3058.

33. Tay, A.; Melosh, N. Nanostructured Materials for Intracellular Cargo Delivery. *Acc. Chem. Res.* **2019,** *52*, 2462–2471.

34. Dixit, H. G.; Starr, R.; Dundon, M. L.; Pairs, P. I.; Yang, X.; Zhang, Y.; Nampe, D.; Ballas, C. B.; Tsutsui, H.; Forman, S. J.; Brown, C. E.; Rao, M. P. Massively-Parallelized, Deterministic Mechanoporation for Intracellular Delivery. *Nano Lett.* **2020,** *20*, 860–867.

35. Deng, Y.; Kizer, M.; Rada, M.; Sage, J.; Wang, X.; Cheon, D. J.; Chung, A. J. Intracellular Delivery of Nanomaterials *via* an Inertial Microfluidic Cell Hydroporator. *Nano Lett.* **2018,** *18*, 2705–2710.

36. Chopra, A.; Krishnan, S.; Simmel, F. C. Electrotransfection of Polyamine Folded DNA Origami Structures. *Nano Lett.* **2016,** *16*, 6683–6690.

37. Geng, T.; Zhan, Y. H.; Wang, J.; Lu, C. Transfection of Cells Using Flow-through Electroporation Based on Constant Voltage. *Nat. Protoc.* **2011,** *6*, 1192–1208.

38. Lukianova-Hleb, E. Y.; Mutonga, M. B. G.; Lapotko, D. O. Cell-Specific Multifunctional Processing of Heterogeneous Cell Systems in a Single Laser Pulse Treatment. *ACS Nano* **2012,** *6*, 10973–10981.

39. Xiong, R. H.; Raemdonck, K.; Peynshaert, K.; Lentacker, I.; De Cock, I.; Demeester, J.; De Smedt, S. C.; Skirtach, A. G.; Braeckmans, K. Comparison of Gold Nanoparticle Mediated Photoporation: Vapor Nanobubbles Outperform Direct Heating for Delivering Macromolecules in Live Cells. *ACS Nano* **2014,** *8*, 6288–6296.

40. Sengupta, A.; Kelly, S. C.; Dwivedi, N.; Thadhani, N.; Prausnitz, M. R. Efficient Intracellular Delivery of Molecules with High Cell Viability Using Nanosecond-Pulsed Laser-Activated Carbon Nanoparticles. *ACS Nano* **2014,** *8*, 2889–2899.

41. Kalies, S.; Heinemann, D.; Schomaker, M.; Gentemann, L.; Meyer, H.; Ripken, T. Immobilization of Gold Nanoparticles on Cell Culture Surfaces for Safe and Enhanced Gold Nanoparticle-Mediated Laser Transfection. *J. Biomed. Opt.* **2014,** *19*. 070505.

42. Li, M.; Lohmuller, T.; Feldmann, J. Optical Injection of Gold Nanoparticles into Living Cells. *Nano Lett.* **2015,** *15*, 770–775.

43. Lukianova-Hleb, E.; Hu, Y.; Latterini, L.; Tarpani, L.; Lee, S.; Drezek, R. A.; Hafner, J. H.; Lapotko, D. O. Plasmonic Nanobubbles as Transient Vapor Nanobubbles Generated around Plasmonic Nanoparticles. *ACS Nano* **2010,** *4*, 2109–2123.

44. Lyu, Z. L.; Zhou, F.; Liu, Q.; Xue, H.; Yu, Q.; Chen, H. A Universal Platform for Macromolecular Delivery into Cells Using Gold Nanoparticle Layers *via* the Photoporation Effect. *Adv. Funct. Mater.* **2016,** *26*, 5787–5795.

45. Tong, S.; Moyo, B.; Lee, C. M.; Leong, K.; Bao, G. Engineered Materials for *in vivo* Delivery of Genome-Editing Machinery. *Nat. Rev. Mater.* **2019,** *4*, 726–737.

46. Lee, W. G.; Demirci, U.; Khademhosseini, A. Microscale Electroporation: Challenges and Perspectives for Clinical Applications. *Integr. Biol.* **2009,** *1*, 242–251.

47. Priceman, S. J.; Tilakawardane, D.; Jeang, B.; Aguilar, B.; Murad, J. P.; Park, A. K.; Chang, W. C.; Ostberg, J. R.; Neman, J.; Jandial, R.; Portnow, J.; Forman, S. J.; Brown, C. E. Regional Delivery of Chimeric Antigen Receptor-Engineered T Cells Effectively Targets HER2(+) Breast Cancer Metastasis to the Brain. *Clin. Cancer Res.* **2018,** *24*, 95–105.

48. Shi, J.; Ma, Y.; Zhu, J.; Chen, Y.; Sun, Y.; Yao, Y.; Yang, Z.; Xie, J. A Review on Electroporation-Based Intracellular Delivery. *Molecules* **2018,** *23*, 3044.

49. Stewart, M. P.; Langer, R.; Jensen, K. F. Intracellular Delivery by Membrane Disruption: Mechanisms, Strategies, and Concepts. *Chem. Rev.* **2018,** *118*, 7409–7531.

50. Xu, X. B.; Liu, C.; Kim, K.; Fan, D. L. Electric-Driven Rotation of Silicon Nanowires and Silicon Nanowire Motors. *Adv. Funct. Mater.* **2014,** *24*, 4843–4850.

51. Kim, W.; Ng, J. K.; Kunitake, M. E.; Conklin, B. R.; Yang, P. Interfacing Silicon Nanowires with Mammalian Cells. *J. Am. Chem. Soc.* **2007,** *129*, 7228–7229.

52. Xie, X.; Xu, A. M.; Leal-Ortiz, S.; Cao, Y.; Garner, C. C.; Melosh, N. A. Nanostraw–Electroporation System for Highly Efficient Intracellular Delivery and Transfection. *ACS Nano* **2013,** *7*, 4351–4358.

53. VanDersarl, J. J.; Xu, A. M.; Melosh, N. A. Nanostraws for Direct Fluidic Intracellular Access. *Nano Lett.* **2012,** *12*, 3881–3886.

54. He, G.; Feng, J.; Zhang, A.; Zhou, L.; Wen, R.; Wu, J.; Yang, C.; Yang, J.; Li, C.; Chen, D.; Wang, J.; Hu, N.; Xie, X. Multifunctional Branched Nanostraw-Electroporation Platform for Intracellular Regulation and Monitoring of Circulating Tumor Cells. *Nano Lett.* **2019,** *19*, 7201–7209.

55. Chiappini, C.; De Rosa, E.; Martinez, J. O.; Liu, X.; Steele, J.; Stevens, M. M.; Tasciotti, E. Biodegradable Silicon Nanoneedles Delivering Nucleic Acids Intracellularly Induce Localized *in Vivo* Neovascularization. *Nat. Mater.* **2015,** *14*, 532–539.

56. Peer, E.; Artzy-Schnirman, A.; Gepstein, L.; Sivan, U. Hollow Nanoneedle Array and Its Utilization for Repeated Administration of Biomolecules to the Same Cells. *ACS Nano* **2012,** *6*, 4940–4946.

57. Xie, X.; Xu, A. M.; Angle, M. R.; Tayebi, N.; Verma, P.; Melosh, N. A. Mechanical Model of Vertical Nanowire Cell Penetration. *Nano Lett.* **2013,** *13*, 6002–6008.

58. Wang, Y.; Yang, Y.; Yan, L.; Kwok, S. Y.; Li, W.; Wang, Z.; Zhu, X.; Zhu, G.; Zhang, W.; Chen, X.; Shi, P. Poking Cells for Efficient Vector-Free Intracellular Delivery. *Nat. Commun.* **2014,** *5*, 4466.

59. Lee, S. E.; Sasaki, D. Y.; Park, Y.; Xu, R.; Brennan, J. S.; Bissell, M. J.; Lee, L. P. Photonic Gene Circuits by Optically Addressable siRNA-Au Nanoantennas. *ACS Nano* **2012,** *6*, 7770–7780.

60. Xin, H.; Namgung, B.; Lee, L. P. Nanoplasmonic Optical Antennas for Life Sciences and Medicine. *Nat. Rev. Mater.* **2018,** *3*, 228–243.

61. Boulais, E.; Lachaine, R.; Meunier, M. Plasma Mediated Off-Resonance Plasmonic Enhanced Ultrafast Laser-Induced Nanocavitation. *Nano Lett.* **2012,** *12*, 4763–4769.

62. Furlani, E. P.; Karampelas, I. H.; Xie, Q. Analysis of Pulsed Laser Plasmon-Assisted Photothermal Heating and Bubble Generation at the Nanoscale. *Lab Chip* **2012,** *12*, 3707–3719.

63. Prentice, P.; Cuschieri, A.; Dholakia, K.; Prausnitz, M.; Campbell, P. Membrane Disruption by Optically Controlled Microbubble Cavitation. *Nat. Phys.* **2005,** *1*, 107–110.

64. Wu, T. H.; Teslaa, T.; Kalim, S.; French, C. T.; Moghadam, S.; Wall, R.; Miller, J. F.; Witte, O. N.; Teitell, M. A.; Chiou, P. Y. Photothermal Nanoblade for Large Cargo Delivery into Mammalian Cells. *Anal. Chem.* **2011,** *83*, 1321–1327.

65. Ghosh, P.; Han, G.; De, M.; Kim, C. K.; Rotello, V. M. Gold Nanoparticles in Delivery Applications. *Adv. Drug. Deliver. Rev.* **2008,** *60*, 1307–1315.

66. Peng, T.; Li, X.; Li, K.; Nie, Z.; Tan, W. DNA-Modulated Plasmon Resonance: Methods and Optical Applications. *ACS Appl. Mater. Inter.* **2020,** *12*, 14741–14760.

67. Pitsillides, C. M.; Joe, E. K.; Wei, X.; Anderson, R. R.; Lin, C. P. Selective Cell Targeting with Light-Absorbing Microparticles and Nanoparticles. *Biophys. J.* **2003,** *84*, 4023–4032.

68. Man, T.; Zhu, X.; Chow, Y. T.; Dawson, E. R.; Wen, X.; Patananan, A. N.; Liu, T. L.; Zhao, C.; Wu, C.; Hong, J. S.; Chung, P. S.; Clemens, D. L.; Lee, B. Y.; Weiss, P. S.; Teitell, M. A.; Chiou, P. Y. Intracellular Photothermal Delivery for Suspension Cells Using Sharp Nanoscale Tips in Microwells. *ACS Nano* **2019,** *13*, 10835–10844.

69. Odom, T. W.; Love, J. C.; Wolfe, D. B.; Paul, K. E.; Whitesides, G. M. Improved Pattern Transfer in Soft Lithography Using Composite Stamps. *Langmuir* **2002,** *18*, 5314–5320.

70. Qin, D.; Xia, Y.; Whitesides, G. M. Soft Lithography for Micro- and Nanoscale Patterning. *Nat. Protocols* **2010,** *5*, 491–502.

71. Kumar, A.; Whitesides, G. M. Features of Gold Having Micrometer to Centimeter Dimensions Can Be Formed through a Combination of Stamping with an Elastomeric Stamp and an Alkanethiol ''Ink'' Followed by Chemical Etching. *Appl. Phys. Lett.* **1993,** *63*, 2002–2004.

72. Andrews, A. M.; Liao, W. S.; Weiss, P. S. Double-Sided Opportunities Using Chemical Lift-Off Lithography. *Acc. Chem. Res.* **2016,** *49*, 1449-1457.

73. Cao, H. H.; Nakatsuka, N.; Serino, A. C.; Liao, W.-S.; Cheunkar, S.; Yang, H.; Weiss, P. S.; Andrews, A. M. Controlled DNA Patterning by Chemical Lift-Off Lithography: Matrix Matters. *ACS Nano* **2015,** *9*, 11439–11454.

74. Kim, J.; Rim, Y. S.; Chen, H.; Cao, H. H.; Nakatsuka, N.; Hinton, H. L.; Zhao, C.; Andrews, A. M.; Yang, Y.; Weiss, P. S. Fabrication of High-Performance Ultrathin In_2O_3 Film

Field-Effect Transistors and Biosensors Using Chemical Lift-Off Lithography. *ACS Nano* **2015,** *9*, 4572–4582.

75. Srinivasan, C.; Mullen, T. J.; Hohman, J. N.; Anderson, M. E.; Dameron, A. A.; Andrews, A. M.; Dickey, E. C.; Horn, M. W.; Weiss, P. S. Scanning Electron Microscopy of Nanoscale Chemical Patterns. *ACS Nano* **2007,** *1*, 191–201.

76. Smith, R. K.; Lewis, P. A.; Weiss, P. S. Patterning Self-Assembled Monolayers. *Prog. Surf. Sci.* **2004,** *75*, 1–68.

77. Liao, W. S.; Cheunkar, S.; Cao, H. H.; Bednar, H. R.; Weiss, P. S.; Andrews, A. M. Subtractive Patterning *via* Chemical Lift-Off Lithography. *Science* **2012,** *337*, 1517–1521.

78. Vaish, A.; Shuster, M. J.; Cheunkar, S.; Weiss, P. S.; Andrews, A. M. Tuning Stamp Surface Energy for Soft Lithography of Polar Molecules to Fabricate Bioactive Small-Molecule Microarrays. *Small* **2011,** *7*, 1471–1479.

79. Zhao, C.; Xu, X.; Bae, S. H.; Yang, Q.; Liu, W.; Belling, J. N.; Cheung, K. M.; Rim, Y. S.; Yang, Y.; Andrews, A. M.; Weiss, P. S. Large-Area, Ultrathin Metal-Oxide Semiconductor Nanoribbon Arrays Fabricated by Chemical Lift-Off Lithography. *Nano Lett.* **2018,** *18*, 5590–5595.

80. Zhao, C.; Xu, X.; Yang, Q.; Man, T.; Jonas, S. J.; Schwartz, J. J.; Andrews, A. M.; Weiss, P. S. Self-Collapse Lithography. *Nano Lett.* **2017,** *17*, 5035–5042.

81. Zhao, C.; Xu, X.; Chiang, N.; Yang, Q.; Liu, W.; Schwartz, J. J.; Andrews, A. M.; Weiss, P. S. Two-Dimensional Plasmonic Nanostructure Arrays Fabricated by Double-Patterning Chemical Lift-Off Lithography. **2020,** *In prep*.

82. Carlson, A.; Bowen, A. M.; Huang, Y.; Nuzzo, R. G.; Rogers, J. A. Transfer Printing Techniques for Materials Assembly and Micro/Nanodevice Fabrication. *Adv. Mater.* **2012,** *24*, 5284–5318.

83. Raun, A.; Saklayen, N.; Zgrabik, C.; Shen, W.; Madrid, M.; Huber, M.; Hu, E.; Mazur, E. A Comparison of Inverted and Upright Laser-Activated Titanium Nitride Micropyramids for Intracellular Delivery. *Sci. Rep.* **2018,** *8*, 15595.

Chapter 7

Conclusions and Future Prospects

My graduate research focused on developing hybrid nanolithographic techniques that have advantages associated with high throughput, large scale, and low cost, to fabricate one-, two-, and three-dimensional submicron and nanostructures of various materials. The resulting scalable and ordered structures have been used in the design and assembly of next-generation electronic and biomedical devices and platforms.

Conventional photolithography, a robust, high-throughput, and straightforward patterning technique has been widely used in microstructure manufacturing. To overcome the resolution limit for broader applications, I developed dual-layer photolithography (DLPL) to realize scalable and tunable sub-micron patterning without mask alignment or high-refractive index media. By purposely controlling the time of single-step exposure, “outline-like” features were generated at the overlapping region of the dual photoresist layers. Through serial optimization of photoresist composition and photolithographic parameters, we further improved the patterning resolution of the DLPL process to 180 nm, which is approximately 25 times smaller than the original feature sizes of the photomask. Combined with Si etching, metal deposition, and other nanofabrication techniques, DLPL can be used to fabricate various three-dimensional (3D) nanostructures for applications in optoelectronic devices. Not limited to conventional photolithography, this strategy can also be incorporated into other lithographic techniques using photoresists, such as deep ultraviolet photolithography and electron-beam lithography.

Previously, DLPL has been used to generate two-dimensional (2D) “outline-like” patterns, such as circular and triangular patterns, depending on the photomask features. Nonetheless, patterning one-dimensional (1D) nanostructures had not been explored yet had the potential for additional applications. Our recent progress extended the capability of DLPL to fabricate 1D Si nanotrenches and SiO_2 nanoribbons. Combined with thin-layer deposition, DLPL could be used to

fabricate high-aspect-ratio metal and semiconductor nanoribbons, which have application potential in plasmonic sensing and field-effect-transistor biosensing. Another exciting opportunity afforded by DLPL is using recessed "outline-like" features for directed self-assembly. For example, combined with block-copolymer lithography, DLPL-fabricated Si nanotrenches could serve as self-assembly templates to achieve sub-nanometer patterning.

We also advanced chemical lift-off lithography (CLL), a high-throughput and large-scale soft lithographic technique developed by our groups. Previously, CLL has been used to pattern self-assembled monolayers (SAMs) of alkanethiol molecules on Au and other surfaces through conformal contact. Combined with chemical etching, the SAM molecules remaining in the non-contacted regions serve as etch resists for the fabrication of various nanostructures. Previously, our group demonstrated the capability of CLL for pattering source/drain electrodes for field-effect transistor biosensors. Using commercially available DVDs as nanoribbon templates, we can lower the cost of master fabrication for CLL and make CLL a cleanroom-free process, improving its practicality and accessibility.

To increase surface-to-volume ratios, we used CLL-fabricated Au nanoribbons as wet-etching masks to produce In_2O_3 ribbons with <200 nm widths and ~3-nm thicknesses. To solve the over-etching problem through the underlying In_2O_3 layer, we developed a fabrication strategy that combined wet etching and sputtering to fabricate large-scale and high-fidelity In_2O_3 nanoribbons. Incorporated with a double-patterning strategy, CLL can be used to achieve plaid-like patterns. The differences in the molecular densities of two different types of SAM molecules led to the fabrication of various 2D gold nanostructures. Gold nanodisk arrays fabricated by 90° rotation between the two CLL processes have been used as photothermal intracellular delivery platforms, resulting in >98% delivery efficiency of calcein with >98% cell viability.

Promisingly, by combining a triple-pattering strategy and/or adjusting the rotation angles between processing steps, various Au nanostructures, with plasmonic properties, could be patterned *via* CLL. Furthermore, CLL can also be used to pattern and fabricate nanostructures on soft polymeric substrates, which have the potential for use as wearable skin electronics for health monitoring or FET probes for biomarker sensing in body fluids.

Finally, as a facile and robust unconventional nanolithographic technique, nanosphere lithography (NSL) utilizes the self-assembly of nanospheres to realize scalable nanostructure array patterning on underlying substrates. Combined with dry etching and metal deposition, NSL was used to fabricate various extruded and recessed 3D micro-/nanostructures such as pillar and hole arrays. We further demonstrated the compatibility of NSL with Si anisotropic etching and sputtering, to fabricate nanopyramid arrays that contribute to enhanced light absorption of as-prepared $MAPbI_3$ perovskite films. The assembled photodetectors with nanopyramid structures showed excellent responsivity of 28.8±1.0 $A \cdot W^{-1}$. Besides optoelectronics devices, NSL-fabricated nanostructures, due to their high periodicity and uniformity, could serve as biomedical platforms for cell culture, cell regulation, and drug delivery. Combined with multiple-pattering and nanoimprint strategies, various 3D nanostructures such as nanotubes, nanoneedles, nanobowls, and others can be fabricated for broader applications.

Nanolithography is an extraordinary field that can revolutionize manufacturing in electronics, optics, and biology, advancing our lifestyle and human society. I spent my graduate career developing hybrid nanolithographic techniques to advance our patterning and fabrication capabilities. The three hybrid nanolithographic techniques introduced in this dissertation foretell a fruitful and remarkable advancement pathway for nanolithography. I anticipate there will be many more exciting discoveries forthcoming in this field.